

DYNAMIC STABILITY AND SLIDER-LUBRICANT INTERACTIONS

IN HARD- DISK DRIVES

BY

ROHIT PRADEEP AMBEKAR

B.TECH. (INDIAN INSTITUTE OF TECHNOLOGY, MUMBAI, INDIA) 2002

M. S. (UNIVERSITY OF CALIFORNIA, BERKELEY) 2005

A DISSERTATION SUBMITTED IN PARTIAL SATISFACTION OF THE

REQUIREMENTS FOR THE DEGREE OF

DOCTOR OF PHILOSOPHY

IN

ENGINEERING – MECHANICAL ENGINEERING

IN THE

GRADUATE DIVISION

OF THE

UNIVERSITY OF CALIFORNIA, BERKELEY

COMMITTEE IN CHARGE:

PROFESSOR DAVID B. BOGY, CHAIR

PROFESSOR KYRIAKOS KOMVOPOULOS

PROFESSOR THOMAS M. DEVINE

SPRING 2007

This dissertation of Rohit Pradeep Ambekar is approved.

Chair

Date

Date

Date

University of California, Berkeley

Spring 2007

DYNAMIC STABILITY AND SLIDER-LUBRICANT INTERACTIONS IN HARD- DISK DRIVES

COPYRIGHT © 2007

BY

ROHIT PRADEEP AMBEKAR

ABSTRACT

DYNAMIC STABILITY AND SLIDER-LUBRICANT INTERACTIONS IN HARD- DISK DRIVES

By

Rohit Pradeep Ambekar

Doctor of Philosophy in Engineering – Mechanical Engineering

University of California, Berkeley

Professor David B. Bogy, Chair

Hard disk drives (HDD) have played a significant role in the current information age and have become the backbone of storage. The soaring demand for mass data storage drives the necessity for increasing capacity of the drives and hence the areal density on the disks as well as the reliability of the HDD. To achieve greater areal density in hard disk drives, the flying height of the airbearing slider continually decreases. Different proximity forces and interactions influence the air bearing slider resulting in fly height modulation and instability. This poses several challenges to increasing the areal density (current goal is 2Tb/in.²) as well as making the head-disk interface (HDI) more reliable. Identifying and characterizing these forces or interactions has become important for achieving a stable fly height at proximity and realizing the goals of areal density and reliability.

Several proximity forces or interactions influencing the slider are identified through the study of touchdown-takeoff hysteresis. Slider-lubricant interaction which causes meniscus force between the slider and disk as well as airbearing surface contamination seems to be the most important factor affecting stability and reliability at

proximity. In addition, intermolecular forces and disk topography are identified as important factors.

Disk-to-slider lubricant transfer leads to lubricant pickup on the slider and also causes depletion of lubricant on the disk, affecting stability and reliability of the HDI. Experimental and numerical investigation as well as a parametric study of the process of lubricant transfer has been done using a half-delubed disk. In the first part of this parametric study, dependence on the disk lubricant thickness, lubricant type and slider ABS design has been investigated. It is concluded that the lubricant transfer can occur without slider-disk contact and there can be more than one timescale associated with the transfer. Further, the transfer increases non-linearly with increasing disk lubricant thickness. Also, the transfer depends on the type of lubricant used, and is less for Ztetraol than for Zdol. The slider ABS design also plays an important role, and a few suggestions are made to improve the ABS design for better lubricant performance.

In the second part of the parametric study, the effect of carbon overcoat, lubricant molecular weight and inclusion of X-1P and A20H on the slider-lubricant interactions is investigated using a half-delubed disk approach. Based on the results, it is concluded that there exists a critical head-disk clearance above which there is negligible slider-lubricant interaction. The interaction starts at this critical clearance and increases in intensity as the head-disk clearance is further decreased below the critical clearance. Using shear stress simulations and previously published work a theory is developed to support the experimental observations. The critical clearance depends on various HDI parameters and hence can be reduced through proper design of the interface. Comparison of critical clearance on CH_x and CH_xN_y media indicates that presence of nitrogen is better for

HDI as it reduces the critical clearance, which is found to increase with increasing lubricant molecular weight and in presence of additives X-1P and A20H. Further experiments maintaining a fixed slider-disk clearance suggest that two different mechanisms dominate the disk-to-slider and slider-to-disk lubricant transfer.

One of the key factors influencing the slider stability at proximity is the disk topography, since it provides dynamic excitation to the low-flying sliders and strongly influences its dynamics. The effect of circumferential as well as radial disk topography is investigated using a new method to measure the 2-D (true) disk topography. Simulations using CMLAir dynamic simulator indicate a strong dependence on the circumferential roughness and waviness features as well as radial features, which have not been studied intensively till now. The simulations with 2-D disk topography are viewed as more realistic than the 1-D simulations. Further, it is also seen that the effect of the radial features can be reduced through effective ABS design.

Finally, an attempt has been made to establish correlations between some of the proximity interactions as well as others which may affect the HDI reliability by creating a relational chart. Such an organization serves to give a bigger picture of the various efforts being made in the field of HDI reliability and link them together. From this chart, a causal relationship is suggested between the electrostatic, intermolecular and meniscus forces.

Professor David B. Bogy,
Dissertation Chair

DEDICATION

To my Parents, Sister and Wife

TABLE OF CONTENTS

DEDICATION	i
TABLE OF CONTENTS.....	ii
LIST OF FIGURES.....	v
LIST OF TABLES.....	xii
ABBREVIATIONS	xiii
ACKNOWLEDGEMENTS	xv
CHAPTER 1	1
INTRODUCTION.....	1
1.1 Evolution of the hard disk drive.....	1
1.2 Mechanics of the head-disk interface.....	2
1.3 Motivation	3
1.4 Objective	4
1.5 Dissertation outline.....	4
CHAPTER 2	10
EXPERIMENTAL AND NUMERICAL INVESTIGATION OF DYNAMIC INSTABILITY AT THE HEAD DISK INTERFACE AT PROXIMITY	10
2.1 Introduction	10
2.2 Rationale:.....	12
2.3 Experimental Setup:	13
2.3.1 Dependence on humidity:.....	13
2.3.2 Dependence on lubricant thickness:	14
2.3.3 Dependence on slider design	16
2.4 Results:	16
2.4.1 Dependence on humidity:.....	16
2.4.2 Dependence on lubricant thickness:	17
2.4.3 Dependence on slider design.....	18
2.5 Modeling of Intermolecular Forces:.....	19
2.6 Discussion:	24
2.7 Conclusions:	25
CHAPTER 3	37
FURTHER STUDIES ON THE TOUCHDOWN-TAKEOFF HYSTERESIS	37
3.1 Introduction:	37
3.2 Experiments.....	38
3.2.1 Touchdown-takeoff tests	38
3.2.2 Stability tests for effect of lube pickup	38
3.2.3 Stability tests for effect of disk topography	39
3.2.4 Dependence on velocity profile (experimental bias).....	39
3.3 Results:	40

3.3.1	Touchdown-takeoff tests	40
3.3.2	Stability tests for the effect of lube pickup.....	41
3.3.3	Stability tests for the effect of disk topography	41
3.3.4	Dependence on velocity profile.....	42
3.4	Discussion:	43
3.4.1	Intermolecular Forces.....	43
3.4.2	Lubricant Pickup	44
3.4.3	Disk Topography	47
3.4.4	Inherent Hysteresis.....	48
3.5	Conclusions	49
CHAPTER 4	59
SLIDER-LUBRICANT INTERACTIONS AT THE HEAD-DISK INTERFACE	59
4.1	Introduction:	59
4.2	Experiments.....	60
4.3	Simulations.....	61
4.3.1	Using lubricant profiles from experiments.....	61
4.3.2	Calculating the lubricant depletion profile.....	62
4.3.3	Using calculated lubricant profiles.....	66
4.4	Results:	67
4.4.1	Experimental lubricant depletion profile.....	67
4.4.2	Numerical lubricant depletion profile	68
4.4.3	Comparison of flying attitudes with and without the inclusion of lubricant 69	
4.5	Discussion:	69
4.6	Experiments.....	70
4.7	Results:	71
4.8	Discussion:	75
4.9	Conclusions	76
CHAPTER 5	96
LUBRICANT DEPLETION AND DISK-TO-SLIDER TRANSFER	96
5.1	Introduction:	96
5.2	Experimental:	98
5.3	Results and Discussion:.....	99
5.3.1	Dynamics of Lubricant Transfer	99
5.3.2	Dependence on Disk Lubricant Thickness.....	104
5.3.3	Dependence on Lubricant Type.....	108
5.3.4	Dependence on ABS Design	109
5.4	Conclusions	117
CHAPTER 6	138
CRITICAL CLEARANCE FOR SLIDER-LUBRICANT INTERACTIONS	138
6.1	Introduction:	138
6.2	Experimental:	138
6.3	Results	139
6.4	Simulations:.....	140

6.5	Discussion:	141
6.6	Conclusions	144
CHAPTER 7		150
SLIDER-LUBRICANT INTERACTIONS: EFFECT OF MEDIA-TYPE, LUBRICANT MOLECULAR WEIGHT AND ADDITIVES		150
7.1	Introduction:	150
7.2	Experimental:	150
7.2.1	Determination of Critical Clearance:	151
7.2.2	Fixed Clearance tests:	151
7.2.3	Parametric Dependence	152
7.3	Results and Discussion:	153
7.3.1	Dependence on media type:	153
7.3.2	Dependence on lubricant molecular weight:	155
7.3.3	Dependence on additives:	160
7.4	Conclusions:	162
CHAPTER 8		172
EFFECTS OF RADIAL AND CIRCUMFERENTIAL DISK FEATURES ON SLIDER DYNAMICS		172
8.1	Introduction:	172
8.2	Experimental and Numerical Procedure:	173
8.3	Results and Discussion:	175
8.4	Conclusions:	181
CHAPTER 9		191
CORRELATIONS BETWEEN DIFFERENT PHENOMENA AT THE HEAD DISK INTERFACE		191
9.1	Introduction:	191
9.2	Chart Organization:	192
9.3	Correlations:	193
9.4	Discussion:	201
9.5	Conclusions:	202
CHAPTER 10		205
CONCLUSIONS AND FUTURE WORK		205
10.1	Conclusions	205
10.2	Current and Future Work	210
REFERENCES		213
APPENDIX A		229
2-D disk topography input in CMLAir Dynamic Simulator		229
APPENDIX B		231
Guidelines to use CML – Parameter Identification Program (PIP) 2.0:		231

LIST OF FIGURES

Figure 1.1: Fifty years of progress: (a) A 1957 50x24” IBM RAMAC with 5MB storage capacity; (b) A 2007 5x3.5” Hitachi UltraStar with 1TB storage capacity. (Source: Hitachi Global Storage Technologies)	6
Figure 1.2: Increase in the areal density of hard drives since its inception in 1957. (Source: Seagate Technologies)	6
Figure 1.3: Parts of a Hard Disk Drive (HDD)	7
Figure 1.4: Various layers of the recording disk in HDD (Source: Hitachi Global Storage Technologies)	8
Figure 1.5: Head-Gimbal Assembly- slider airbearing surface (ABS) and suspension (Source: Hitachi Global Storage Technologies).....	8
Figure 1.6: Reduction in the head-disk physical spacing (Source: Hitachi Global Storage Technologies)	9
Figure 2.1: (a) Belljar apparatus; (b) Modified environmental chamber with N ₂ gas cylinder.	28
Figure 2.2: (a) Candela Optical Surface Analyzer (OSA); (b) Olympus Optical Microscope	29
Figure 2.3: (a) 18 nm (pico) slider; (b) 7 nm CML (pico) slider	30
Figure 2.4: Velocity profile for Hysteresis tests.....	30
Figure 2.5: Hysteresis observed at zero humidity for 18nm slider.	31
Figure 2.6: Dependence on ambient humidity	31
Figure 2.7: High hysteresis at high humidity: Lubricant pickup.....	32
Figure 2.8: Hysteresis observed for various lubricant thicknesses (Red arm of velocity profile is spindown while the black arm corresponds to spin up.).....	32
Figure 2.9: Comparison between AE and LDV signals for detection of contact.....	33
Figure 2.10: Variation of Touchdown rpm as a function of lubricant thickness for various slider designs (Experimental Results).	33
Figure 2.11: Multilayer model for modeling intermolecular forces.....	34
Figure 2.12: Variation of intermolecular forces as a function of lubricant thickness	34

Figure 2.13: Fly height diagram (Simulations)	35
Figure 2.14: Variation of Touchdown rpm as a function of lubricant thickness for various slider designs (Simulation results)	35
Figure 2.15: Sliders used for simulations – high-damped design: (a) Pico slider and (b) Femto slider	36
Figure 2.16: IMF between slider and disk for high-damped slider designs when simulated over actual and DFHT interfaces.	36
Figure 3.1: Disk velocity profile during touchdown-takeoff tests	51
Figure 3.2: Sliders used (a) CML 7nm : For tests A, B, C and D ; (b) CML 5 nm: For test D	51
Figure 3.3: Increased takeoff velocity due to lubricant pickup (dashed curve).	52
Figure 3.4: Effect of lubricant pickup on stability	52
Figure 3.5: (a) ABS contamination during stability tests; (b) Lubricant pickup behind the trailing pad.....	53
Figure 3.6: Schematic of the lube-lube interaction in the event of lubricant pickup by the slider.	53
Figure 3.7: (a) Inverse hysteresis; (b) Effect of burnishing	53
Figure 3.8: Contact in the Takeoff Leg (Effect of contamination).....	54
Figure 3.9: Shifting of the hysteresis to the right	54
Figure 3.10: Steady State Hysteresis for CML-7nm slider	55
Figure 3.11: Steady State Hysteresis for CML-5nm slider	56
Figure 3.12: Dependence of Acceleration/Deceleration	57
Figure 3.13: Dependence of Acceleration/Deceleration	57
Figure 3.14: Plot of combined compatibility index as a function of the degree of lubrication or contamination, for use when at least one of the two contacting materials is non-metallic.	58
Figure 3.15: Inherent hysteresis	58
Figure 4.1: OSA Calibration for Zdol 4000	80

Figure 4.2: ABS designs used for experiments: (a) CML Pico 7nm; (b) CML Femto 3.5nm.....	80
Figure 4.3: Adding the lube profile on the disk to the slider.....	80
Figure 4.4: Experimentally measured lube profiles at 30 mins after smoothing for (a) CML Femto and (b)CML Pico slider. These profiles were used for static simulations.....	81
Figure 4.5: Waterfall plot of cross-section of lube profile at various angles along the circumferential direction for showing uniformity in lube depletion.	82
Figure 4.6: Model 1 used for predicting lube depletion: (a) Data fit to experimental measurements of disjoining pressure [9]; (b) Lube profile for 1nm thick lube with CML Pico slider; (c) Lube profile for 2nm thick lube with CML Pico slider	83
Figure 4.7: Model 2 used for predicting lube depletion: (a) Data fit to experimental measurements of dispersive surface energy [10]; (b) Data fit to experimental measurements of polar surface energy [10]; (c) Plot of polar, dispersive and total disjoining pressure using data fits obtained from (a) and (b); (d) Lube profile for 1nm thick lube; (e) Lube profile for 2nm thick lube	84
Figure 4.8: Model 3 used for predicting lube depletion: (a) Data fits to experimental measurements of disjoining pressure [11]. Black and blue lines correspond to models 3A and 3B respectively; (b) Lube profile for 1nm thick lube using model 3A (c) Lube profile for 2nm thick lube using model 3A; (d) Lube profile for 1nm thick lube using model 3B (e) Lube profile for 2nm thick lube using model 3B; (f) Lube profile for 1nm thick lube using model 3B/10; (g) Lube profile for 2nm thick lube using model 3B/10.....	86
Figure 4.9: Extruding the lube profile: (a) Lube profile estimated by model 2; (b) Extruded lube profile added to slider profile for static simulations	86
Figure 4.10: Algorithm for static simulations for inclusion of the effect of lube	86
Figure 4.11: ABS designs used for simulations: (a) CML Pico; (b) CML Femto; (c) DSI Femto; (d) High Damped (HD) Pico; (e) HD Femto	87
Figure 4.12: Convergence for simulation procedure outlined in Figure 4.10; (a) Convergence for CML Pico slider; (b) Convergence for CML Femto slider	87
Figure 4.13: Comparison between experimental and numerical lube profile: (a) For CML pico slider ; (b) For CML Femto slider;	88
Figure 4.14: Lubricant profile as a result of slider-disk partial contact: (a) OSA scan of the experimental track; (b) Lubricant profiles corresponding to each of the black squares in (a).	90

Figure 4.15: Physical explanation for experimentally observed lube profiles during slider-disk partial contact: (a) Lube depletion due to downward motion of the slider; (b) Lube buildup due to upward motion of the slider; (c) Lube modulation due to bouncing of the slider	91
Figure 4.16: AE(blue) and LDV (green) signals with corresponding lube profile observed during experiments: (a) and (b) Lube depletion observed when substantial slider-disk contact; (c) and (d) Lube modulation observed when light slider-disk contact.	92
Figure 4.17: Lube modulation under slider trailing pad observed for disks with different lube thicknesses	93
Figure 4.18: Frequency content of lube modulation for (a) 8Å; (b) 12Å and (c) 20Å disks	94
Figure 4.19: Slider dynamics corresponding to observed lube modulations: (a) Time history during light contact; (b) Frequency content during light contact.....	95
Figure 5.1: OSA trace showing depletion and transfer in lubed and delubed zones respectively.....	120
Figure 5.2: OSA Calibration: (a) Zdol and (b) Ztetrol	120
Figure 5.3: ABS designs used for experiments: (a) Femto A; (b) Femto B.....	120
Figure 5.4: Successive operations on the OSA trace to obtain lubricant transfer volume: (a) Radial averaging to OSA trace; (b) Filtering the data (blue) obtained from (a) to get smooth data (red); (c) Further smoothing and changing the background reflectivity to zero by tilting; (d) Integrating area under the reflectivity curve.....	121
Figure 5.5: Time history of (a) Lubricant depletion volume; (b) Lubricant transfer volume; (c) Net depletion volume for Femto A with Zdol lubricant	122
Figure 5.6: Angular distribution of the lubricant (a) Original data from OSA; (b) Conditioned data of (a).....	123
Figure 5.7: Schematic of lubricant flow between the slider and the disk	124
Figure 5.8: Data fit to lubricant depletion volume showing two time scales	124
Figure 5.9: (a),(b) Angular distribution and transfer history for low value of K_1 , respectively;.....	125
Figure 5.10: Lubricant depletion and transfer for different thicknesses of Zdol:	127
Figure 5.11: Total lubricant depletion and transfer after 30 minutes along with data fits	128

Figure 5.12: Volume rate of lube transfer as a function of disk lubricant thickness as predicted by evaporation model of [5]	128
Figure 5.13: Dependence of disjoining pressure lubricant thickness for Zdol 4000 [8].	129
Figure 5.14: Effect of lubricant type on the lubricant depletion and transfer	129
Figure 5.15: Effect of ABS design on the lubricant depletion and transfer	130
Figure 5.16: (a), (b): ABS of Femto A and B, respectively, as seen under optical microscope after experiments;.....	131
Figure 5.17: (a),(c),(e) Pressure distribution, shear stress and shear/unit width for Femto A, respectively; (b),(d),(f) Pressure distribution, shear stress and shear/unit width for Femto B, respectively	132
Figure 5.18: Schematic of sudden expansion of air under the airbearing	133
Figure 5.19: Maximum expansion ratios for Femto A and B	133
Figure 5.20: Lubricant depletion volume and RMS AE signal at different rpms : (a) Femto A ; (b) Femto B	134
Figure 5.21: Frequency content of slider dynamics as measured by LDV at different rpms for (a) Femto A and (b) Femto B.....	135
Figure 5.22: (a): Critical clearance and Minimum fly height for Femto A and B;	136
Figure 5.23: (a) ,(c): Femto A and B above critical rpm showing less depletion and transfer, respectively;	137
Figure 6.1: Experimental setup for studying slider-lubricant interaction	146
Figure 6.2: OSA images showing lube change at various rpms.....	147
Figure 6.3: Critical clearance as a function of lubricant molecular weight, additives and carbon overcoat type.....	148
Figure 6.4: Variation of shear force and maximum shear rate with disk velocity	148
Figure 6.5: Molecular view of disk lubricant	149
Figure 7.1: ABS designs used for experiments: (a) Femto A; (b) Femto B.....	166
Figure 7.2: Slider (Femto A) response to disk topography, FHM and frequency spectra for slider and disk for (a) Media A and (b) Media B.....	166
Figure 7.3: Lubricant volume depleted in 5 minutes at various rpms along with corresponding AE signal with Femto A slider for (a) Media A and (b) Media B..	167

Figure 7.4: Determination of critical clearance from critical rpm and touchdown rpm for Media A (CHx) and Media B (CHxNy) for Femto B slider.....	168
Figure 7.5: (a) Different airbearing forces acting on lubricant at point A on the disk: (1) Positive airbearing pressure, (2) Negative airbearing pressure, (3) Intermolecular force and (4) airbearing shear;.....	168
Figure 7.6: Dependence of critical clearance on lubricant molecular weight for Zdol for Femto B slider.	169
Figure 7.7:Depiction of molecular roughness for lower and higher lubricant molecular weights [14]. Directions of airbearing shear and intermolecular forces due to slider are also shown.	169
Figure 7.8: Fixed clearance tests: Dependence of lubricant volume depleted, transferred and the net lubricant accumulation on slider on lubricant molecular weight for Zdol with Femto B slider.	170
Figure 7.9: Lubricant transfer volume as a percentage of the lubricant depletion volume (Figure 7.8) for different molecular weights of Zdol for Femto B slider.....	170
Figure 7.10: Dependence of critical clearance on inclusion of additives X-1P and A20H in Zdol 2000 for Femto B slider.	171
Figure 7.11: Fixed clearance tests: Dependence of lubricant volume depleted, transferred and the net lubricant accumulation on slider on inclusion of additives in Zdol with Femto B slider.	171
Figure 8.1: Candela 6300 surface topography measurement technique (Source: KLA-Tencor /Candela)	184
Figure 8.2: ABS Designs used for simulations; (a) Slider A (Pico) and (b) Slider B (Femto) design.....	184
Figure 8.3: Circumferential topography (1-D) of three disks measured at MD by Candela 6300	185
Figure 8.4: (a) 1-D disk topography of the center track; (b) 2-D disk topography obtained from integrating the slope in radial direction and “weaving” it with the center track profile.	185
Figure 8.5: Modal diagram for Slider A.....	186
Figure 8.6: Modal diagram for Slider B.....	186
Figure 8.7: (a) Slider following the disk profile; (b) Net fly height of the slider above the disk	187

Figure 8.8: (a) Fly height modulation of Slider A relative to 1-D disk topographies; (b) Frequency content of the response of Slider A	187
Figure 8.9: (a) Fly height modulation of Slider B relative to 1-D disk topographies; (b) Frequency content of the response of Slider B.....	188
Figure 8.10: (a) Fly height modulation of Slider A relative to 1-D and 2-D disk topographies; (b) Frequency content of the response of Slider A	188
Figure 8.11: (a) Fly height modulation of Slider B relative to 1-D and 2-D disk topographies; (b) Frequency content of the response of Slider B	189
Figure 8.12: (a) Pressure distribution of Slider A; (b) Pressure distribution of Slider B.	189
Figure 8.13: Difference in topography of the track corresponding to maximum airbearing pressure and the center track for (a) Slider A and (b) Slider B	190
Figure 8.14: At skew angle of 17.6° : (a) Fly height modulation of Slider A relative to 1-D and 2-D disk topographies; (b) Frequency content of the response of Slider A	190
Figure 9.1: Chart for correlation between different phenomena at the head-disk interface	204
Figure 10.1: Dynamic coupling scheme between CML and lube dynamic simulators..	212

LIST OF TABLES

Table 2.1: Properties of different layers at the Head Disk Interface (as used for simulations) [4, 18].....	27
Table 2.2: Hamaker Constants for Head Disk Interface.....	27
Table 2.3: Interface material properties for “actual” and DFHT interfaces.....	27
Table 4.1: Maximum and minimum lube height predicted by different models for original lube thicknesses of 1nm and 2nm.	78
Table 4.2: Comparison between static simulation results with and without the effect of lube depletion	78
Table 4.3: Static simulation results for different ABS designs to show maximum effect of lube depletion on the flying attitude of the slider.	79
Table 5.1: Lubricant thicknesses of various disks used for experiments	119
Table 5.2: Chemical structures of Zdol and Ztetraol.....	119
Table 7.1: Media properties.....	164
Table 7.2: Lubricant thickness for disks corresponding to different lubricant molecular weight used in the experiments	164
Table 7.3: Lubricant thickness for disks corresponding to different additives used in the experiments	165
Table 7.4: Chemical structures of Zdol, X-1P and A20H	165
Table 8.1: State state flying attitude of sliders	183
Table 8.2: Standard deviation (3σ) values of FHM for different slider disk combinations (in nm)	183
Table 8.3: Standard deviation (3σ) values of FHM corresponding to 1-D and 2-D disk topographies (in nm)	183

ABBREVIATIONS

ABS	Air Bearing Surface
AE	Accoutic Emission
AFM	Atomic Force Microscopy
BPI	Bits Per Inch
CC	Critical Clearance
CDS	CMLAir Dynamic Simulator
CML	Computer Mechanics Laboratory
CMLPIP	CML Parameter Identification Program
CSS	Contact Start Stop
DFHT	Dynamic Fly Height Tester
DLC	Diamond-Like Carbon
DOF	Degree Of Freedom
DSI	Data Storage Institute (Singapore)
DSLTT	Disk-to-Slider Lubricant Transfer
ESF	Electro-Static Force
FH	Fly Height
FHM	Flying Height Modulation
HAMR	Heat Assisted Magnetic Recording
HDD	Hard Disk Drive
HDI	Head-Disk Interface
HGST	Hitachi Global Storage Technologies
ID	Inner Diameter

IMF	Inter-Molecular Force
INSIC	INformation Storage Industry Consortium (formerly NSIC, National Storage Industry Consortium)
LDV	Laser Doppler Vibrometry
LDS	Lubricant Dynamic Simulator
L/UL	Load Un-Load
MD	Middle Diameter
OD	Outer Diameter
OSA	Optical Surface Analyzer
PFPE	Per-Fluoro Poly-Ether
RAMAC	Random Access Method of Accounting and Control
RH	Relative Humidity
RMS	Root Mean Square
RPM	Revolutions Per Minute
SDLT	Slider-to-Disk Lubricant Transfer
SDS	Spindown-Dwell-Spinup
TFC	Thermal Flyheight Control
TPI	Tracks Per Inch
UDG	User Defined Geometry

ACKNOWLEDGEMENTS

I would like to express my deepest gratitude towards my advisor Prof. David B. Bogy, who provided me with a balanced environment for research and exploration throughout my career as a graduate student. His thoroughness and keen for detail has made this dissertation a better piece of work. Close association with him has taught me so much! His personality, attitude and thoughts will always serve as a guideline for me.

I am deeply indebted to Dr. C. Singh Bhatia of Hitachi GST, who has been very important in shaping my research path and for helping me at every stage of my Ph.D. Without his infectious enthusiasm and vast wealth of experience, it would not have been possible to finish this dissertation on time.

During these CML years, I have also had a unique opportunity of close interaction with the industry. I would like to specially thank Drs. R.J. Waltman and B. Marchon of HitachiGST for the helpful discussions and Mr. T. Watanabe of Fuji Electric Device Co. for providing excellent disks for research. Thanks are also due to Drs. Q.H. Zeng and F.-Y. Huang of HitachiGST, Drs. V. Prabhakaran and L. Zheng of Western Digital and Mr. S. Venkatram of KLA-Tencor/Candela for the knowledge as well as unique opportunities I received during internships.

I received rich academic training at Berkeley thanks to the great professors here. I thank Profs. P. Papadopoulos, A. Szeri, O. O'Reilly and A. Chorin for serving on my qualifying exam committee. I am also thankful to Profs. K. Komvopoulos and T.M. Devine for carefully reviewing this dissertation and to Prof. S. McMains for supporting me during my initial stay.

A big vote of thanks is due to fellow CMLers. Technical discussions with them have helped me gain a broader education. Brendan Cox, Puneet Bhargava, Sujit Kirpekar and Vineet Gupta deserve special thanks. Five years at Berkeley having been transforming, academically as well as personally. My roommates- Vineet Gupta, Rohit Karnik and Nihar Shah, and all my friends have enriched my life and made these years memorable.

Finally, I attribute all my success to my wonderful family. I am indebted to them for their sacrifices and unconditional love not only during my graduate career but throughout my entire life. I thank my parents for their endless support and for inculcating the deepest values in me since my childhood, which has made me what I am today. I thank my sister for all the wonderful times and my in-laws for their support. Lastly, I wish to acknowledge the titanic role of my wife Manasi in my success as a graduate student. I thank her for the immense emotional and financial support she gave me, while being a constant source of inspiration and energy in all aspects of life.

The research presented in this dissertation was supported by the Computer Mechanics Laboratory at the University of California, Berkeley, and the Information Storage Industry Consortium's (INSIC) extremely high density recording (EHDR) program.

May 14, 2007
Berkeley, CA.

CHAPTER 1

INTRODUCTION

1.1 Evolution of the hard disk drive

Introduced in 1956 [1], the IBM-made Random Access Method of Accounting and Control (RAMAC) was the first disk drive. It consisted of 50 magnetic disks 24” in diameter (Figure 1.1(a)) with a storage capacity of 5 MB (megabyte) and could be leased for \$3200 per month. Almost fifty-one years later, at the time of writing this dissertation, a 1 TB (terabyte = 10^6 MB) drive has been announced [2], which consists of only 4-5 magnetic disks 3.5” in diameter (Figure 1.1(b)) and costs under \$500!

This demonstrates the gigantic strides made by the hard disk drives (HDDs) over the past half century, which has enabled continuous increase in the areal density¹ from 2 Kbit/in.² to 160 Gbit/in.² (Figure 1.2), an 80-million fold increase! Correspondingly, the cost of storage has continuously decreased (from \$10,000 per MB to \$0.0005 per MB), which has enabled the HDD to be at the heart of every computer today and has played a key role in the information revolution.

Initially used only in special applications like supercomputing and military/space operations, the HDDs have now also found a multitude of applications in consumer electronics. Innovations and interdisciplinary research over the years has been responsible for the success of this magnetic recording technology. An excellent historical account of magnetic storage has been provided in [3].

¹ *Areal recording density* is defined as the amount of data that can be stored on a unit area of the recording medium and is usually expressed as bits per square inch (bits/in.²). In HDD, areal density is the product of the *linear bit density* (bits per inch, BPI) along the circumferential direction and the *track density* (tracks per inch, TPI) along the radial direction.

1.2 Mechanics of the head-disk interface

Though the areal density of the HDD has increased and its size has reduced, the fundamental basis of magnetic recording has not changed much since its introduction half a century ago. Figure 1.3 shows a picture of a modern HDD with its top cover off, exposing its components. Information is written on (and read back from) concentric data “tracks” on each disk surface in the stack of co-rotating disks (platters) by corresponding read-write transducer/head which is located at the trailing edge of a slider. A suspension and an actuator arm connect each slider to the voice-coil actuator, which provides rotary motion to the slider (and head) about the actuator axis so that the head can access all the data tracks. This dissertation focuses mainly on the mechanics of the interface between slider and the disk, otherwise called head-disk interface (HDI). Hence, it is necessary to have a closer look at the disk and slider technology.

The disks used in HDD are ultra-smooth (rms roughness ~ 0.2 nm) and have multiple layers as shown in Figure 1.4. The data is stored in magnetic layer which is about 30 nm thick. A hard diamond-like carbon (DLC) overcoat layer of thickness 1-3 nm exists on top of the magnetic layer to provide wear and corrosion protection to the data. Above the DLC layer is a thin layer (1-2 nm) of lubricant necessary for wear protection and reliability. Figure 1.5 shows the head-gimbal assembly, which consists of the slider and the suspension. The slider has an air-bearing surface (ABS) with specific etches (referred to as ABS design). The suspension applies a fixed “preload” on the slider to press it against the disk. When the disks spin, an air-bearing is formed between the slider ABS and the disk, and the slider “flies” on the disk maintaining a particular flying height, dictated by the ABS design which regulates the air flow in the airbearing.

1.3 Motivation

To achieve a growth in the areal density, the size of the magnetic bits has to be reduced, which decreases the intensity of its magnetic field. Further, the intensity of the magnetic field also decreases exponentially with increase in head-disk spacing, according to the Wallace spacing law [4]. Hence, for a smaller bit with a lower magnetic intensity, the head-disk spacing has to be reduced. Figure 1.6 shows the trend of reduction in the head-disk spacing with time due to the increase in areal density. It is seen that in the past fifteen years, the spacing has reduced from 100 nm to less than 10 nm.

. With the current areal density goal of $1\text{Tb}/\text{in}^2$, the magnetic spacing between the head and the disk has to be reduced to about 5 nm. This includes thicknesses for necessary overcoat layers – disk DLC, disk lubricant and slider DLC (provides corrosion protection to transducer), which leaves only about 2.5 nm for the mechanical slider-disk spacing. At such small slider-disk spacing, proximity interactions like intermolecular, meniscus and electrostatic forces and factors such as disk topography limit the ability of the slider to fly stably over the disk. Smaller spacing also increases the chance of intermittent slider-disk contact. This, in addition to reducing the HDI stability, leads to slider vibrations in the vertical (out-of-plane) direction or fly height modulation (FHM) resulting in loss of magnetic signal and causing errors due to read/write skip. Thus, identification and characterization of these proximity interactions is very important to achieve small slider-disk spacing and realize the areal density goal of $1\text{Tb}/\text{in}^2$. This has been the motivation for the research presented in this dissertation.

1.4 Objective

Briefly, the objective of this research is to investigate interactions or phenomena, in particular the slider-lubricant interactions, which are responsible for the dynamic instability at the head-disk interface at proximity.

1.5 Dissertation outline

This dissertation is divided into ten chapters. Chapter 1 is an introduction that covers evolution of the disk drive, dissertation objective and outline. Chapter 2 presents the study of touchdown-takeoff hysteresis in which intermolecular force (IMF) is identified as one of the factors affecting stability at proximity. Multilayer modeling of IMF has been done to explain the experimental trends. Chapter 3 continues the study of hysteresis, and lubricant pickup, disk topography, contamination and slider dynamics are identified as other factors causing hysteresis. Lubricant pickup due to slider-lubricant interactions is found to significantly affect stability. Chapter 4 covers some numerical efforts to model lubricant depletion as well as some experimental effort to understand slider-lubricant interactions in partial contact. In Chapter 5, experimental and numerical investigation of the process of disk-to-slider lubricant transfer (DSLTT) is presented along with a parametric study of its dependence on some HDI parameters – disk lubricant thickness, lubricant type and slider ABS design. Chapter 6 reports experiments suggesting the existence of a critical head-disk clearance above which there is negligible slider-lubricant interaction. A theory is developed to support the experimental observations using shear stress simulations and previously published work. Chapter 7

covers the second part of the parametric study of DSLT – effect of media-type (carbon overcoat), lubricant molecular weight and inclusion of X-1P and A20H. Chapter 8 presents the effect of the circumferential and radial disk topography on the slider dynamics, wherein a new method is used to measure the 2-D (true) disk topography. Chapter 9 attempts to establish correlations between some of the proximity interactions as well as others which may affect the HDI reliability by creating a relational chart. From this chart, a causal relationship is suggested between the electrostatic, intermolecular and meniscus forces. Chapter 10 concludes the dissertation by summarizing the significant findings and indicating avenues for future research.

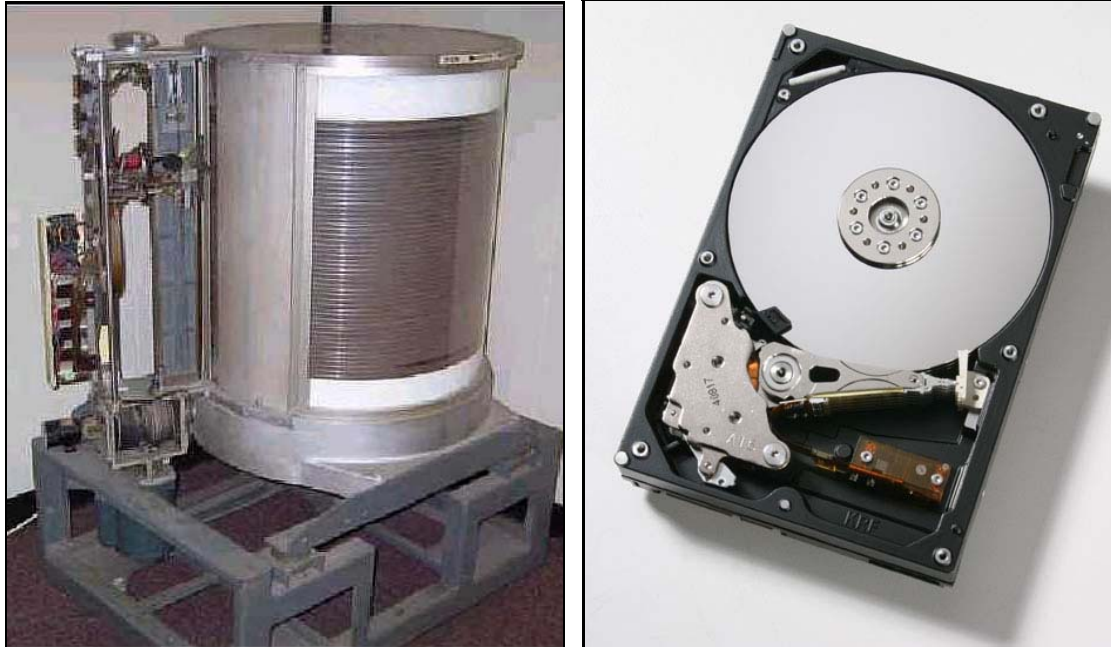


Figure 1.1: Fifty years of progress: (a) A 1957 50x24" IBM RAMAC with 5MB storage capacity; (b) A 2007 5x3.5" Hitachi UltraStar with 1TB storage capacity. (Source: Hitachi Global Storage Technologies)

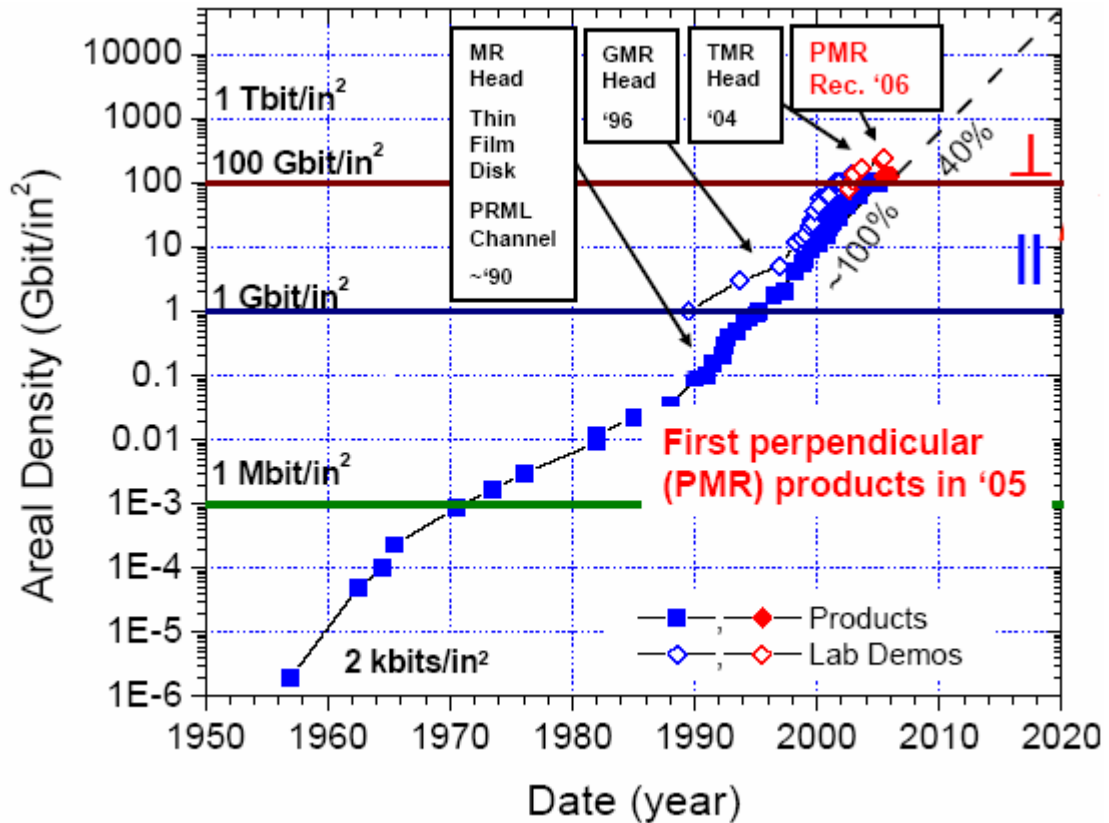
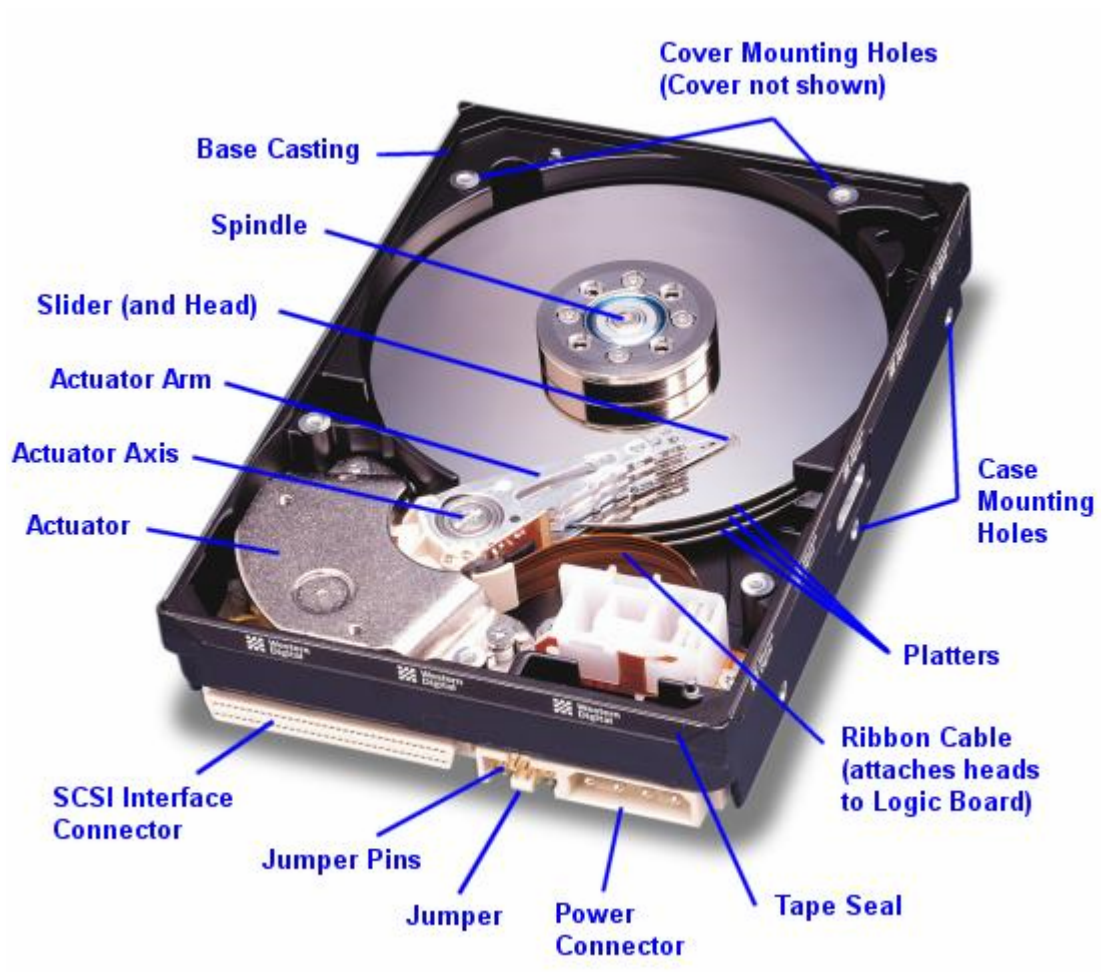


Figure 1.2: Increase in the areal density of hard drives since its inception in 1957. (Source: Seagate Technologies)



<http://www.storagereview.com/guide2000/ref/hdd/op/index.html>

Figure 1.3: Parts of a Hard Disk Drive (HDD)

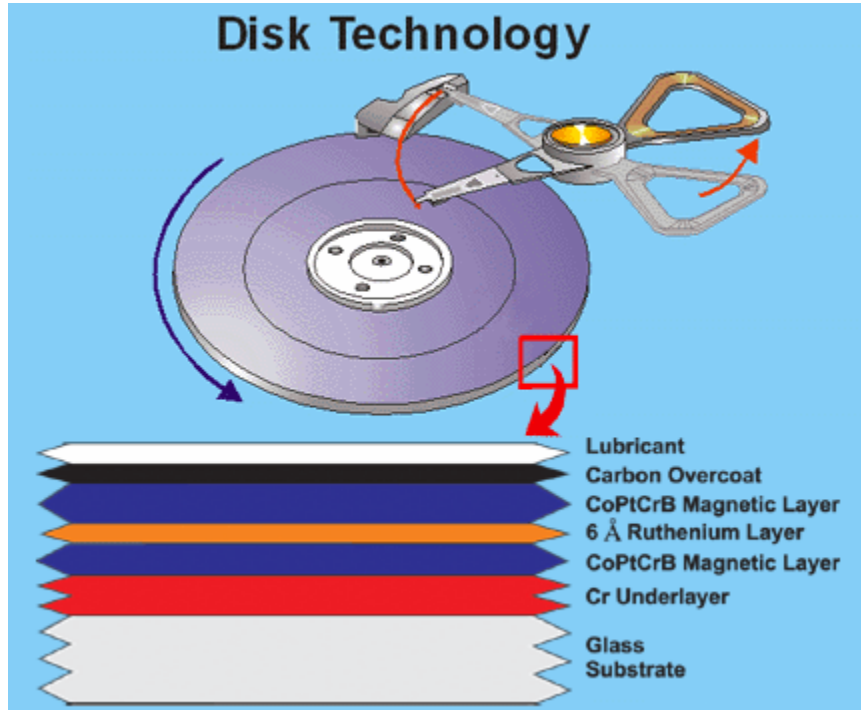


Figure 1.4: Various layers of the recording disk in HDD (Source: Hitachi Global Storage Technologies)

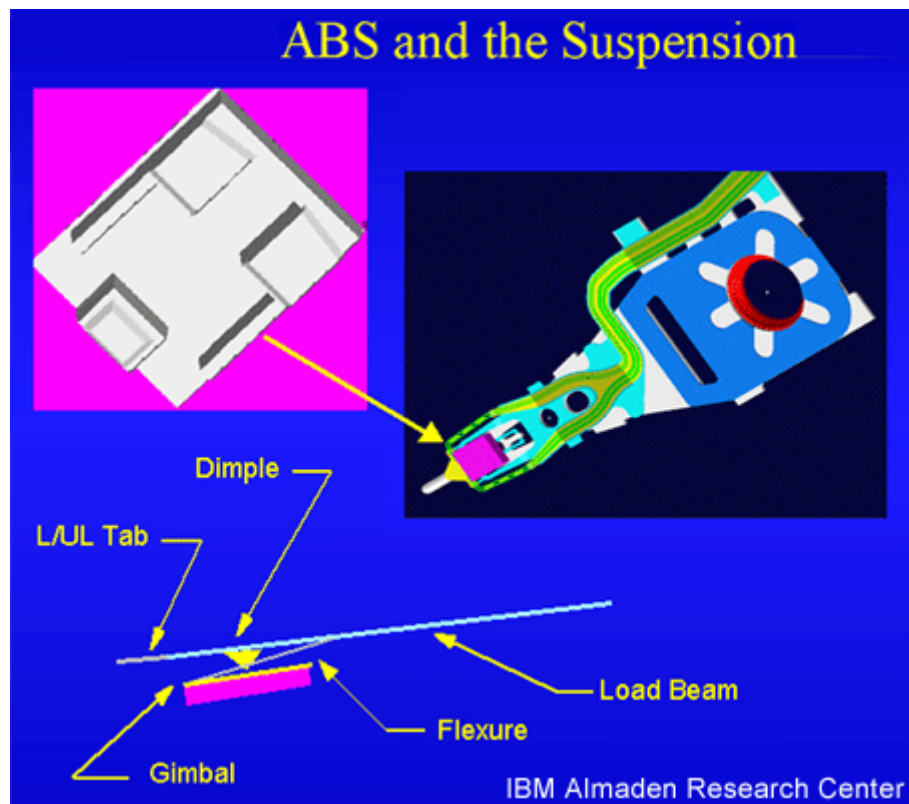


Figure 1.5: Head-Gimbal Assembly- slider airbearing surface (ABS) and suspension (Source: Hitachi Global Storage Technologies)

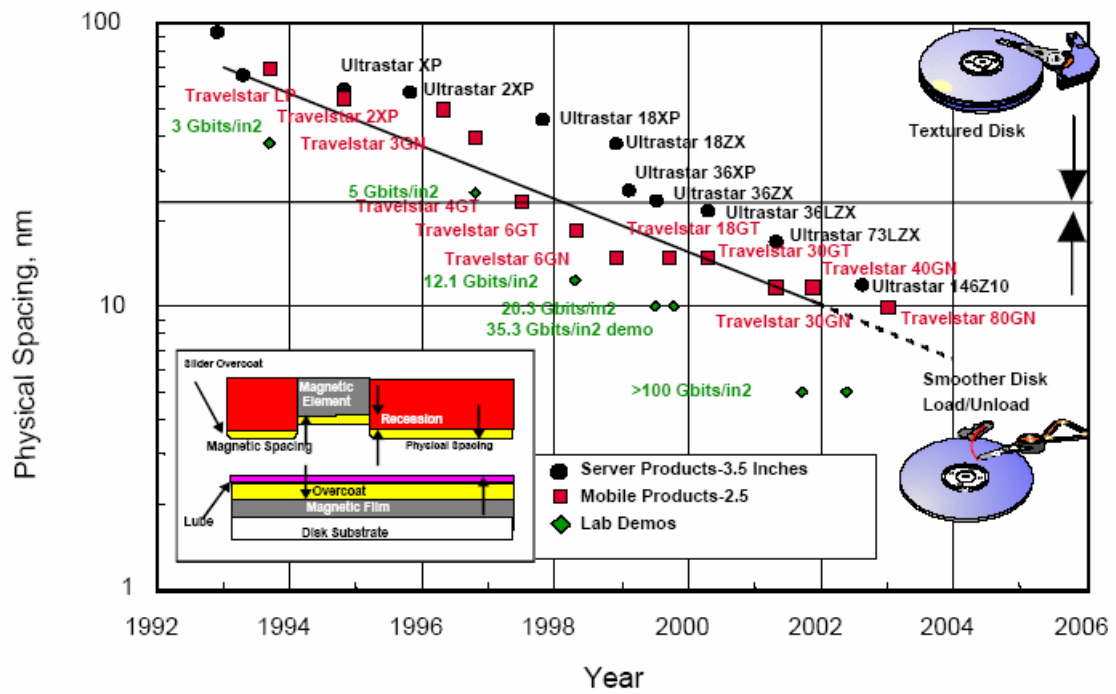


Figure 1.6: Reduction in the head-disk physical spacing (Source: Hitachi Global Storage Technologies)

CHAPTER 2

EXPERIMENTAL AND NUMERICAL INVESTIGATION OF DYNAMIC INSTABILITY AT THE HEAD DISK INTERFACE AT PROXIMITY

2.1 Introduction

One of the major roadblocks in achieving the goal of higher areal density [1] is the dynamic instability of the HDI. It has been experimentally observed that a dynamic instability occurs in the fly height in the sub 5nm flying regime. The observed phenomena have been modeled primarily as resulting from intermolecular forces [2]-[3] and meniscus forces [4]-[8]. The objective of this research is to investigate this fly height instability in detail and determine the contributing factors.

Extensive research has been conducted in the past few years on the dynamic instability of air bearing sliders in HDD at proximity to understand the various phenomena occurring and to achieve a stable flying height in the sub 5nm regime. Different analytical models have been developed. One goal of the many models has been to predict the experimentally observed fly height hysteresis.

Hysteresis is a common phenomenon in a variety of materials and processes. It is prominent in Atomic Force Microscopy (AFM) [9], and analytical models explain this hysteresis by the presence of meniscus forces, where the liquid (absorbed water on the surface of the material) forms a meniscus bridge when the AFM tip comes into contact with the sample. This meniscus exerts an attractive force on the tip and it ruptures at a much larger spacing when the tip retracts, thus demonstrating hysteresis [9]. In HDI, the presence of a lubricant / adsorbed water layer creates a similar situation. Hence, bridge

models have been proposed using the meniscus force to explain the touchdown-takeoff hysteresis observed in HDD [8].

However, the lubricant layer in the HDI is very thin (\sim monolayer), strongly bonded to the protective carbon overcoat and has only a small fraction of free mobile lubricant to form the meniscus. Also, the average time of contact during the “bouncing” is of the order of 10^{-9} seconds, and this is far from the equilibrium state predicted by the kinetic meniscus formation model [4].

A variety of proximity phenomena have been explained by intermolecular adhesion force models. These forces are primarily a result of electrostatic attraction between two atoms/ molecules due to their unbalanced electron clouds, leading to a dipole formation [16]. These forces can be very large when two surfaces are in close proximity (\sim atomic distances).

The effect of intermolecular forces on HDI dynamic performance was first considered by Wu and Bogy [2] . Thornton and Bogy [3] demonstrated the observed experimental instability at proximity and hysteresis by a 1-DOF model using intermolecular forces (Lennard-Jones potential). Thus, hysteresis has been analytically demonstrated as a result of meniscus forces as well as intermolecular force. Hence, experimental investigation is needed to determine the various factors/ interactions that cause this hysteresis and the dynamic instability. This was achieved in the research presented here by conducting spindown-dwell-spinup (SDS) tests under varying conditions of humidity and lubricant thickness. The touchdown-takeoff rpm (hysteresis) was monitored, and correlation was established between the observed phenomena and the variation in the experimental parameters.

2.2 Rationale:

Different forces act on the slider in proximity that influence the dynamic stability of the head-disk interface. Some of these forces may arise from contact of the slider and the disk, such as the development of menisci, while some may be non-contact short range forces, such as the external excitation of the low flying slider by lubricant modulation, or the presence of intermolecular forces.

The phenomenon of hysteresis has two components – touchdown and takeoff. Care is taken so that the slider is never in contact before the touchdown occurs, so the variation in the touchdown can be attributed to the variation in non-contact forces. The two major non-contact forces are considered to be the intermolecular forces and the external excitation caused by the lubricant modulation [10]. If further, the touchdown variation is studied keeping the lubricant modulation variation to the minimum (achieved by using a disk with high bonded lubricant ratio, and dwelling on the experimental track on the disk for not more than 10 seconds), the other non-contact force (intermolecular force) can be investigated for its existence and its effect can be studied on the dynamic instability.

Using this rationale, the presence of intermolecular forces can be determined by monitoring the touchdown rpm while the meniscus forces can be determined by takeoff rpm. The variation in the touchdown and takeoff rpm can be used to study the effects of intermolecular and meniscus forces, respectively.

In this report we describe an experiment to identify the factors contributing to the dynamic instability and present the experimental results. Experimental evidence of the presence of intermolecular forces is established.

The experiment was carried out in a controlled environmental chamber (Figure 2.1) with the CETR tester equipped with a wide bandwidth acoustic emission (AE) sensor. The effect of hysteresis was studied for different values of humidity, slider design and lubricant thickness, and inferences were made from the observations.

It is concluded that the touchdown velocity is affected by the thickness of the lubricant on the disk. Further, the hysteresis is affected by other phenomena such as lubricant pickup by the flying slider. The change in the ambient humidity (0-60% RH) did not show any particular trend in the hysteresis observed.

2.3 Experimental Setup:

Figure 2.1(a),(b) and Figure 2.2(a),(b) show the various apparatus used to conduct the experiment. Figure 2.1(a) shows an apparatus to achieve the controlled environment. A low pressure of 5 mTorr is achievable. A CETR tester was modified, and set up inside the environmental chamber. First, a load-unload (L/UL) test was conducted with an 18nm FH (fly height) slider using the velocity profile shown in Figure 2.4. Disks of various lubricant thicknesses were used for the experiments (described in Table 2.1). The touchdown-takeoff hysteresis process was monitored by an AE sensor. This is a very reliable method of detecting contact [11].

2.3.1 Dependence on humidity:

In the presence of ambient humidity water is adsorbed onto the disk surface [11]. This, as well as the mobile lubricant layer may aid in the formation of a meniscus and thereby contribute to the meniscus forces. The spindown-spinup tests were conducted

for disks with a high ratio of bonded lubricant at zero humidity and at ambient humidity. The procedure of the tests is briefly described as follows:

The 18nm FH slider (Figure 2.3 (a)) was loaded on to the rotating disk with the designed z-height. The slider was then unloaded onto a L/UL ramp, and the chamber was closed with the belljar. The disk rotation was stopped and the chamber was pumped down to a lower pressure depending upon the final humidity desired in the chamber. To achieve zero humidity in the environmental chamber, N₂ gas (ultra high pure-UHP) was pumped into the chamber. The final experimental conditions were ambient pressure and temperature and the desired humidity.

In the tests conducted later, low flying sliders (5nm and 7nm CML) of the CSS (contact start-stop) type were used. Since the pressure in the belljar could not be pumped down very low, a different CSS tester with its hood was modified into an environmental chamber (Figure 2.1 (b)), in which N₂ gas could be pumped into the chamber through a pipe. The chamber was provided with a small aperture at the opposite end to force the excess gas out. The pumped gas mixed with the ambient gas in the chamber decreasing the humidity, and forcing the ambient gas out from the chamber. A humidity sensor kept inside the chamber measured the humidity.

In the tests conducted, the same slider was used on different tracks on a disk and without cleaning. After a test sequence, the slider was observed with a microscope to observe lubricant/debris pickup.

2.3.2 Dependence on lubricant thickness:

While keeping the humidity constant (ambient ~ 40%RH), we conducted the tests using INSIC CML sliders (7nm and 5nm) for various values of lubricant thickness. Each

run was conducted on a different track, and with a clean slider. The slider and the disk were monitored after the tests using the microscope and the Candela OSA (Figure 2.2 (a),(b)) respectively. The tests were conducted in the order of lubricant thicknesses of 1.2nm – 0.8nm – 2.0nm or 1.2nm – 2.0nm – 0.8nm.

First, the tests were conducted using the CETR and the actual AE signal amplitudes (filtered with a high order filter in MATLAB) were plotted against the velocity (Figure 2.5-Figure 2.8). The test was programmed with the software of the CETR. The disk starts rotating and attains a speed of 8000 rpm, at which time the slider is lowered onto the disk at 1.6” with the required z-height. The actuator then seeks to the required track (being used for the run), and the disk speed is lowered to a value such that a slight slider-disk contact is expected. (This value of rpm is set by performing sample runs on a particular slider-disk combination.) The disk dwells at the minimum rpm for 1 second, and then it is accelerated at the same rate at which it was decelerated (symmetric velocity profile). After reaching the final speed of 8000 rpm, the actuator seeks to the 1.6” track and is loaded off the disk, while the disk is dwelling at 8000 rpm. The disk is then decelerated to a halt. Both the slider and the disk are then removed from the CETR tester. The slider is observed under the microscope for lubricant pickup and the disk is observed on the Candela OSA for lube depletion and modulation.

In order to verify that the AE signal corresponds to the slider-disk contact, similar tests were performed on a TTi tester having both AE and LDV measurement capabilities. The AE and LDV signals both showed spikes at the same instant indicating most likely contact (Figure 2.9).

The disks used in these tests were 95 mm ultra smooth disks (~0.2 nm RMS roughness), with aluminum substrate, magnetic layer, 3nm CHN overcoat and lubricant of varying thickness, with a bonded-mobile ratio of about 1:1. The disks were of the same make, and hence were expected to have same waviness.

2.3.3 Dependence on slider design

The dependence of the hysteresis on slider design was also studied along with the effect of lubricant thickness. The various sliders used in these tests are shown in Figure 2.3. They had fly heights of 18nm (pico), 7nm (pico) and 5nm (pico, with new suspension and old).

2.4 Results:

The results of the previously described experiments are presented in this section:

2.4.1 Dependence on humidity:

The results of the SDS test conducted at zero humidity are shown in Figure 2.5. As can be seen there, a hysteresis occurs at zero humidity for lubricant with a high bonded ratio and in absence of slider lubricant pickup. This is a case in which formation of a meniscus is very difficult, and it implies that meniscus forces, if they affect at all, cannot be the only contributing factor to the hysteresis observed.

The effect of humidity on the mobility of the lubricant and its bonding to the carbon overcoat has been studied previously [13]-[14]. An increase in humidity may weaken the lubricant-carbon overcoat bonding because the adsorbed water may diffuse into the carbon surface and form bonds with the active sites on the carbon surface. This also reduces the diffusion energy barrier (due to intermolecular and lubricant-disk

interactions) that the lubricant molecules have to overcome in order to move from one area to another, thereby increasing the lubricant mobility.

The effect of humidity also depends on the terminal group reactivity of the lubricant. The lubricant-overcoat bonding is stronger in the case of a more reactive terminal group [13].

However, from the tests conducted, it appears that hysteresis does not have a strong dependence on humidity (Figure 2.6). Figure 2.7 shows extreme hysteresis (solid curve). This was attributed to severe lubricant pickup by the slider as observed under the microscope. Thus, other factors such as lubricant pickup appear to have some bearing on the hysteresis observed.

2.4.2 Dependence on lubricant thickness:

Experiments for studying the effect of lubricant thickness on the hysteresis were conducted on the CETR tester at ambient humidity (40% RH). It was observed that the touchdown speeds were greater for low flying sliders. A plot of AE signal versus the disk velocity (rpm) for various lubricant thicknesses is shown in Figure 2.8. It is seen that the touchdown velocity is higher for lower lubricant thickness. These results are opposite to what has been obtained by other authors [15]. Therefore, to verify the results, similar tests were conducted on a variety of other slider designs. The same trend was obtained for each ABS design. Figure 2.10 shows the touchdown variation for various slider designs for tests conducted at 0° skew at radius of 1.45”.

This observed trend in the variation of the touchdown rpm is believed to be a result of a variation in non-contact forces, which are, in turn, a result of slider-lubricant interactions (causing lubricant modulation/depletion) and intermolecular forces.

Lubricant modulation provides external excitation to the low flying slider which may cause a touchdown at higher rpm.

Lubricant modulation profiles before touchdown cannot be observed, as there is severe contact of the slider and the disk, which causes lubricant depletion. Lubricant depletion provides some estimate of the amount of mobile lubricant on the track before the touchdown occurs. It also relates to the severity of contact during the SDS test. Larger lubricant thickness with more mobile lubricant will have more lubricant modulation and depletion. Hence, the touchdown velocity is expected to be higher for thicker lubricants.

There was some difference in the lubricant depletion profiles. For example, the 8 Å, 12 Å and 20 Å disks had lubricant depletion of 5 Å, 3.3 Å and 10 Å respectively for the 5nm, and 2.5 Å, -3.3 Å and 5 Å, respectively, for the 7nm (negative sign indicates a lubricant buildup). The important observation to be made is that even though more modulation can be expected for higher lubricant thickness which should cause a higher touchdown velocity, the observed results should show a contrary trend. Hence, there must be present a strong attractive non-contact force which overcomes the effect of lubricant modulation and influences the observed trend. These evidences lead us to conclude the presence of a strong attractive intermolecular force at proximity.

2.4.3 Dependence on slider design

The touchdown velocity was observed to be dependent on the slider design. It was found to be higher for low flying sliders (Figure 2.10). The effect of intermolecular force is stronger for low flying sliders. Hence, the touchdown velocity is expected to be higher. Furthermore, less lubricant depletion was observed. Also it does not vary much

with the lubricant thickness variation. Hence, the variation in the touchdown rpm can be correlated with the fly height of a slider as a function of rpm.

After obtaining the experimental trends, simulations were done to see if the inclusion of intermolecular forces in the presence of different lubricant thicknesses yielded similar trends to those observed in experiments.

2.5 Modeling of Intermolecular Forces:

Intermolecular forces are close range forces. They constitute of a (relatively) long range attractive force and a short range repulsive force and can be modeled by the Lennard-Jones Potential.

$$F(r) = -\frac{A}{r^6} + \frac{B}{r^{12}} \quad (2.1)$$

where, r = distance between the particles/ molecules /atoms
 A, B = Hamaker constants ($A \sim 10^{-19}$ J and $B \sim 10^{-76}$ Jm⁶)
 $F(r)$ = Intermolecular force (function of distance, r)

The intermolecular force model was incorporated into the CML Air software. In this software, the calculation of intermolecular forces between the slider and disk surfaces is done at every node in the mesh, and attractive and repulsive forces are calculated by summing the individual forces on the nodes to give the value of the total intermolecular force. From Eq. (2.1), it is seen that the attractive component of the intermolecular force depends on the Hamaker constant A . This constant, is specific to material combinations.

Typically, the range of action of this force is ~ 10 nm. Hence, for low flying sliders, it is not only interaction between the topmost layers (lubricant on the disk and

DLC on the slider) that counts, but other layers in both, disk and slider influence the interaction. Since both, the slider and the disk are layered, there is a multilayer interaction (Figure 2.11), and the method for calculating the Hamaker constant A is given by Lifshitz theory [16]. According to this theory, the Hamaker constant for two materials, 1 and 2, interacting across a medium 3 is given by:

$$A_{132} = \frac{3}{4} k\bar{T} \left(\frac{\varepsilon_1 - \varepsilon_3}{\varepsilon_1 + \varepsilon_3} \right) \left(\frac{\varepsilon_2 - \varepsilon_3}{\varepsilon_2 + \varepsilon_3} \right) + \frac{3h\nu_e}{8\sqrt{2}} \frac{(n_1^2 - n_3^2)(n_2^2 - n_3^2)}{(n_1^2 + n_3^2)^{1/2} (n_2^2 + n_3^2)^{1/2} \{ (n_1^2 + n_3^2)^{1/2} + (n_2^2 + n_3^2)^{1/2} \}} \quad (2.2)$$

where,

- ε_i = permittivity of material i ($C^2J^{-1}m^{-1}$),
- n_i = refractive index of material i ,
- ν_e = 3×10^{15} Hz (ionization frequency),
- h = $(2\pi\hbar)$ = Planck's constant, ($6.626 \times 10^{-34} Js$),
- k = $1.381 \times 10^{-23} JK^{-1}$ (Boltzmann's constant), and
- \bar{T} ~ 300 K (Temperature at the interface)

The Hamaker constant, and thus the intermolecular forces depend on the refractive index and the permittivity of a material. Changes in these properties, cause an increase or decrease of intermolecular forces between the slider and the disk. However, since both the slider and the disk have multiple layers, and further, they are thin enough (~2-20 nm) to contribute to the intermolecular forces, multilayer effects have to be considered. The multilayer model (Eqn. 11.37) derived in [16] is not applicable to the Head Disk Interface because the sign of the combining relations used in order to derive it

has to be changed by the combination of materials [16]. The equation for a multilayer model is derived for a 4 layer model by Matsuoka et. al. [16] as:

$$F(D_l) = -\frac{1}{6\pi} \left[\frac{A_{232'3}}{D_l^3} + \frac{A_{2'312}}{(D_l + T)^3} + \frac{A_{231'2'}}{(D_l + T')^3} + \frac{A_{121'2'}}{(D_l + T + T')^3} \right] \Delta x \Delta y \quad (2.3)$$

where,

$$A_{ijkl} = \frac{3h\nu_e}{8\sqrt{2}} \frac{(n_i^2 - n_j^2)(n_k^2 - n_l^2)}{(n_i^2 + n_j^2)^{1/2} (n_k^2 + n_l^2)^{1/2} \{ (n_i^2 + n_j^2)^{1/2} + (n_k^2 + n_l^2)^{1/2} \}} \quad (2.4)$$

and,

D_l = Fly height of the slider (nm)

T = Thickness of disk lube (nm)

T' = Thickness of head DLC (nm)

And the rest of the symbols have their meaning as explained above (after Eq. (2.2)). Note that the first term in Eq. (2.2) containing permittivity is not included in Eq. (2.4) as it is an order of magnitude smaller than the second term.

This equation was used to calculate the intermolecular force between the slider and the disk in the CML Air software. For the head disk interaction two layers on the disk (lube, DLC) and two layers on the slider (DLC, Al₂O₃-TiC), i.e. a total of 4 layers were considered to be interacting across air as the medium. Thus, the 4-layer model was used to obtain the results. The Hamaker constants were calculated using the permittivities and refractive indices of the various layers (Table 2.1). It was found that the Hamaker constant for DLC was greater than that of lubricant. Hence, the less thick

the lubricant, the more the influence of disk DLC on the head disk interface. Thus, an increase in the intermolecular force maybe expected when lubricant thickness is reduced.

Using the thicknesses given in Table 2.1, and varying the thickness of the lubricant, we completed simulations at a radius of 1.45” (36.8 mm) and 0° skew with the CML Air software.

The results are shown in Figure 2.12, 15 and 16. In Figure 2.12, it is seen that as the lubricant thickness increases, the magnitude of intermolecular force decreases. Also, as the fly height decreases there is more of an increase in the intermolecular forces with decreasing lubricant thickness, i.e., the effect of change in lubricant thickness will have a larger effect on flyability of the slider for lower flying heights.

This can be explained on the basis of the values of the Hamaker constants calculated (Table 2.2). We note that $A_{232'3}$ and $A_{2'312}$ are dominant as compared to $A_{231'2'}$ and $A_{121'2'}$. $A_{232'3}$ corresponds to disk lube – head DLC interaction through air while $A_{2'312}$ corresponds to disk DLC – head DLC interaction with multilayer effect of air and disk lube included. When D_1 and T are equal, we see that $(D_1+T)^3 = 8*D_1^3$. Thus, $A_{232'3}$ will be the dominant term whenever there is more lubricant. This is consistent with the physical explanation that the properties of the closest layers at the interface will be more dominant. The thicker these layers become, the further away from the interface the back layers ($1'$ and 1) are, and the less will be the influence they wield. However, this also indicates that as the lubricant layer gets thinner, the effect of disk DLC will be dominant, esp. because it has a higher Hamaker constant value associated with it. From Figure 2.12, it is seen that at $FH=1.5$ nm, IMF (lube=0 nm) = -0.66 gm and IMF (lube=2.0 nm)

= -0.42 gm, an increase of 57% in the intermolecular forces. These forces are significant as they are comparable to the gram loads applied to the sliders (1.5 gm for pico).

For higher fly heights, when $D_1 \gg T$, $(D_1+T) \approx D_1$. Thus, the effect of $A_{232'3} < A_{2'312}$ is not as acute as when $D_1 \approx T$ holds, and hence, there is only a small variation in the intermolecular forces due to change in the lubricant thickness for higher flying heights, as seen in Figure 2.12.

In Figure 2.13, the fly height diagrams obtained from the simulations are plotted. The upper curves correspond to stable flying heights, while the lower ones correspond to unstable flying heights [3]. During spindown, as the rpm reduces, the fly-height of the slider reduces along the upper (stable) curve. At the bifurcation point shown in the graph, there is a transition of the slider from a stable regime to a contact. The rpm at which this transition takes place is defined as the touchdown rpm for the simulation results and it has been plotted for two sliders corresponding to various lubricant thicknesses in Figure 2.14. It is seen that the experimental (Figure 2.10) and simulation (Figure 2.14) results exhibit similar trends: the touchdown velocity is higher for thinner lubricants and low flying sliders. This is primarily the result of the increase in the intermolecular forces due to reduction in the lubricant thickness.

From the above simulations and analysis, it is seen that the IMF at the head-disk interface is affected by the material properties at the interface. Thus, the IMF and hence the slider fly height can change if the interface materials are changed. One such important scenario is the optical fly height measurement by Dynamic Fly Height Tester (DFHT), where the slider flies over a thick glass disk. Since this interface is slightly different than that in an actual drive, the fly height measured on DFHT may be different

than that in an actual drive. Hence, we conducted simulations to determine the effect of this change of interface on the actual fly height and the IMF between slider and disk. The material properties and layer thicknesses used for the DFHT and “actual” interface are shown in Table 2.3. When steady state calculations were done with CML 5nm slider, not much difference in fly height was found (5.02 nm for actual and 5.09 nm for DFHT interface). The fly height for the actual interface was slightly lower as the IMF was calculated to be slightly higher when fly height was close to 5 nm. Subsequently, fixed attitude simulations were done for high-damped pico and femto slider designs as shown in Figure 2.15. In these simulations, the pitch and roll values were set at $100\mu\text{rad}$ and $-1\mu\text{rad}$, respectively, while the fly height was reduced from 10nm to contact. It was found that the IMF was slightly less for DFHT interface for higher fly heights. However, as the fly heights reduced, the IMF for DFHT increased in magnitude faster and surpassed the IMF for the actual interface as shown in Figure 2.16. This indicates that a slider with a very low flying height ($< 5\text{ nm}$) could fly significantly lower on DFHT. Since IMF contributes to head-disk adhesion, higher IMF also implies stronger head-disk interaction which could lead to greater wear in case of DFHT. From Figure 2.16, we also note that the IMF is much less for the femto slider as compared to pico. This is because greater area of the slider is in close proximity to the disk in case of a pico slider and certain features on the trailing pad of the pico slider fly lower in presence of the small roll due to wider trailing pad.

2.6 Discussion:

The differences in the touchdown rpm relate to the variation in non-contact forces, which for the head disk interface have been primarily identified as the

intermolecular forces and external excitation due to lubricant modulation or changes in the flying conditions due to lubricant depletion (lubricant non-uniformity). In the experiments conducted, care was taken to keep the variation of the lubricant modulation/depletion limited. Hence, the variation of the touchdown rpm (which was counter to the trend meniscus forces would predict) was attributed to the presence of the other proximity non-contact forces, the intermolecular forces.

In an SDS test, as the disk rpm reduces, the slider flies lower. Hence, an increase in the attractive force due to a decrease in lubricant thickness may lead to early touchdown. Simulations using a multilayer model, varying the lubricant thickness, indicate that as the lubricant thickness decreases, there is more adhesion force due to intermolecular forces. This explains the experimentally observed phenomenon: The touchdown rpm is higher for thinner lubricants.

2.7 Conclusions:

Monitoring the touchdown and takeoff velocity while varying the parameters such as lubricant thickness and humidity can give information about various head disk interactions at proximity. The experimental trends obtained were correlated with the possible factors that could cause them, and the presence of intermolecular forces was concluded as a primary cause on the basis of the following observations:

- (a) Hysteresis can be a result of many phenomena occurring at the head-disk interface.

Hence, to make conclusions about the effects of a particular interaction, it is necessary to isolate each interaction on the basis of its nature (contact or non-contact) and its domain of operation.

- (b) Hysteresis was observed at zero humidity for a lubricant with a high bonded ratio, leading to a conclusion that a meniscus force may not be the primary contributor to the observed hysteresis.
- (c) Most importantly, the variation in the touchdown rpm is due to a non-contact force. Since lubricant non-uniformity is small, the variation must be due to a variation in the intermolecular forces. Thus, we conclude that IMF is a contributor to the hysteresis.
- (d) Simulations conducted with the inclusion of a multilayer model of intermolecular forces into CMLAir predicted results consistent with the observed experimental trends.
- (e) Simulations conducted to study the difference between DFHT and actual interfaces indicate that there may be significant reduction in fly height over the DFHT interface as compared to actual at very small fly heights (< 5 nm).

Layer	Permittivity (ϵ_i)	Refractive Index (n)	Layer Thickness (nm)
Head Al ₂ O ₃ -TiC	11.54	1.75	∞
Head DLC	2.418	1.9	2.5
Air	1.0	1.0	Fly height
Disk Lubricant	2.2	1.3	0 - 2 <varied>
Disk DLC	2.418	1.9	∞

Table 2.1: Properties of different layers at the Head Disk Interface (as used for simulations) [4, 18].

Hamaker Constants ($\times 10^{-20}$ J)			
$A_{232'3}$	$A_{2'312}$	$A_{231'2'}$	$A_{121'2'}$
7.1176	12.010	-1.1129	-1.9072

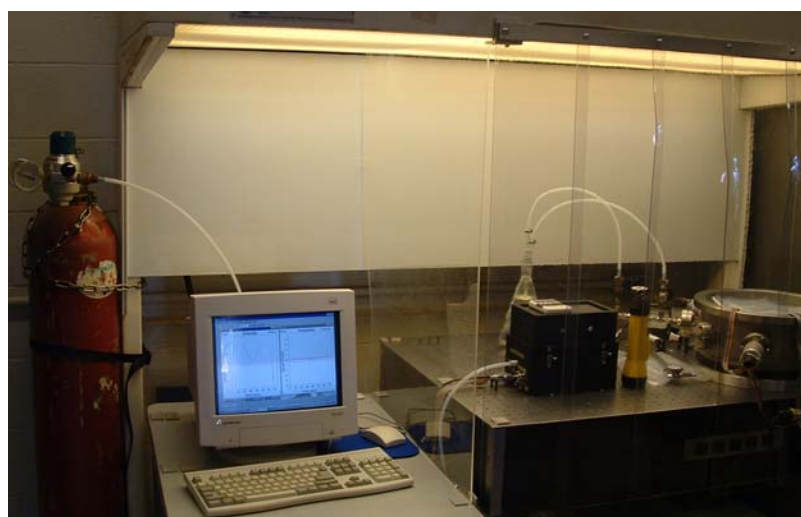
Table 2.2: Hamaker Constants for Head Disk Interface

Actual			DFHT		
Layer	Refractive Index (n)	Thickness (nm)	Layer	Refractive Index (n)	Thickness (nm)
Head Al ₂ O ₃ -TiC	1.75	∞	Head Al ₂ O ₃ -TiC	1.75	∞
Head DLC	1.9	2.5	Head DLC	1.9	2.5
Air	1.0	Fly height	Air	1.0	Fly height
Disk Lubricant	1.3	1	Disk Lubricant	1.3	0
Disk DLC	1.9	∞	Glass	1.5	∞

Table 2.3: Interface material properties for “actual” and DFHT interfaces

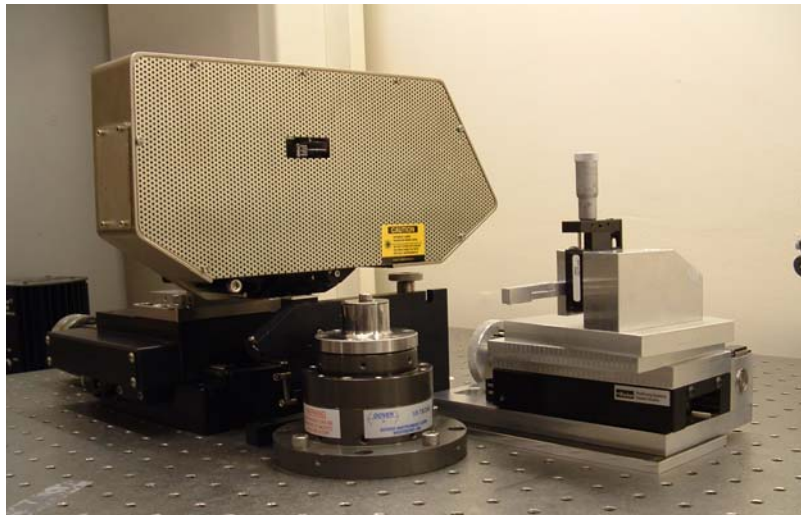


(a)



(b)

Figure 2.1: (a) Belljar apparatus; (b) Modified environmental chamber with N₂ gas cylinder.



(a)



(b)

Figure 2.2: (a) Candela Optical Surface Analyzer (OSA); (b) Olympus Optical Microscope

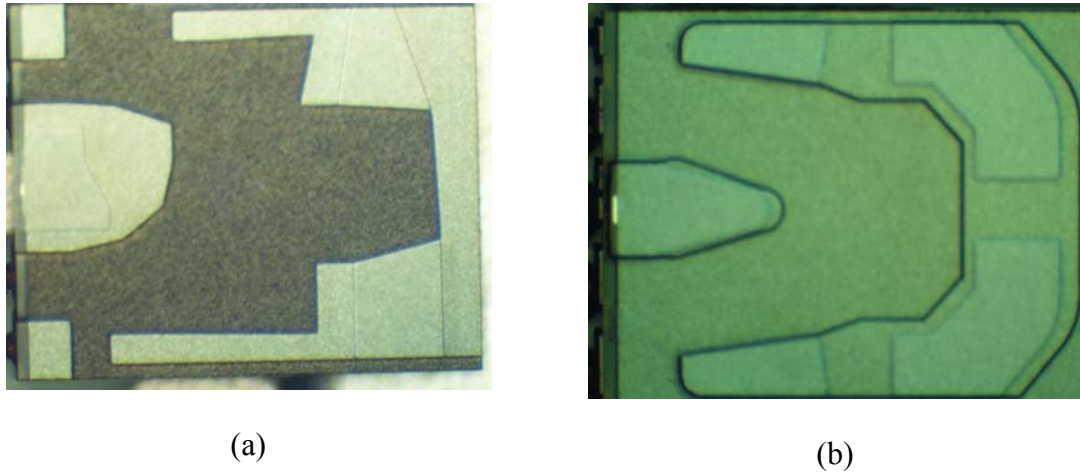


Figure 2.3: (a) 18 nm (pico) slider; (b) 7 nm CML (pico) slider
 (Note: The ABS of 5nm design is very similar to 7 nm design)

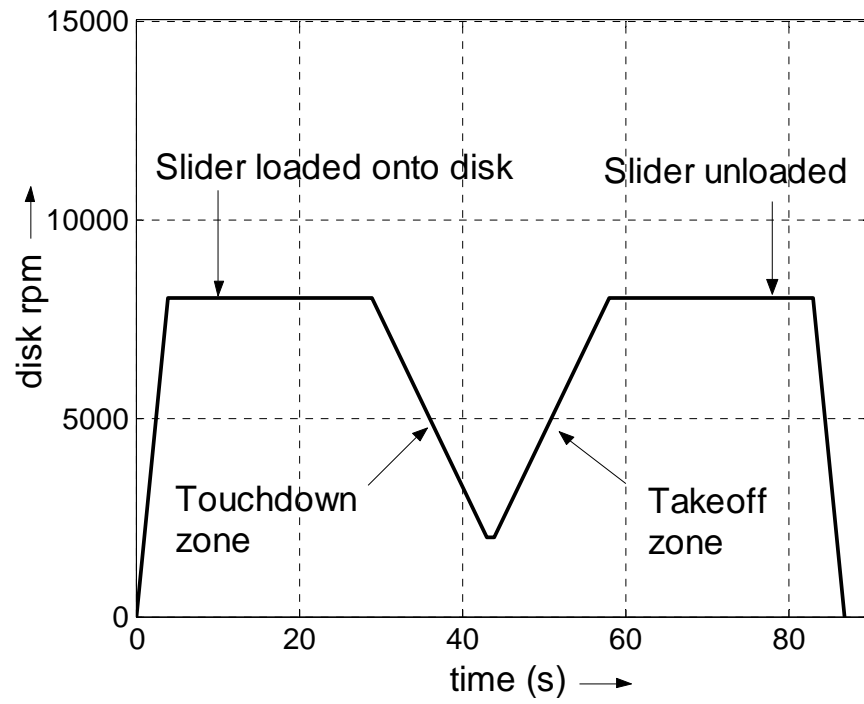


Figure 2.4: Velocity profile for Hysteresis tests

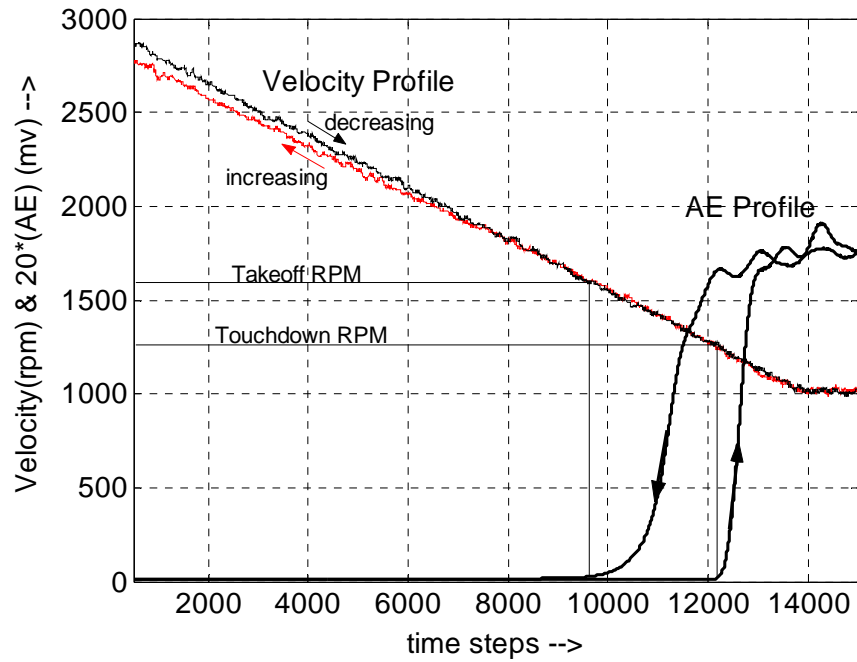


Figure 2.5: Hysteresis observed at zero humidity for 18nm slider.

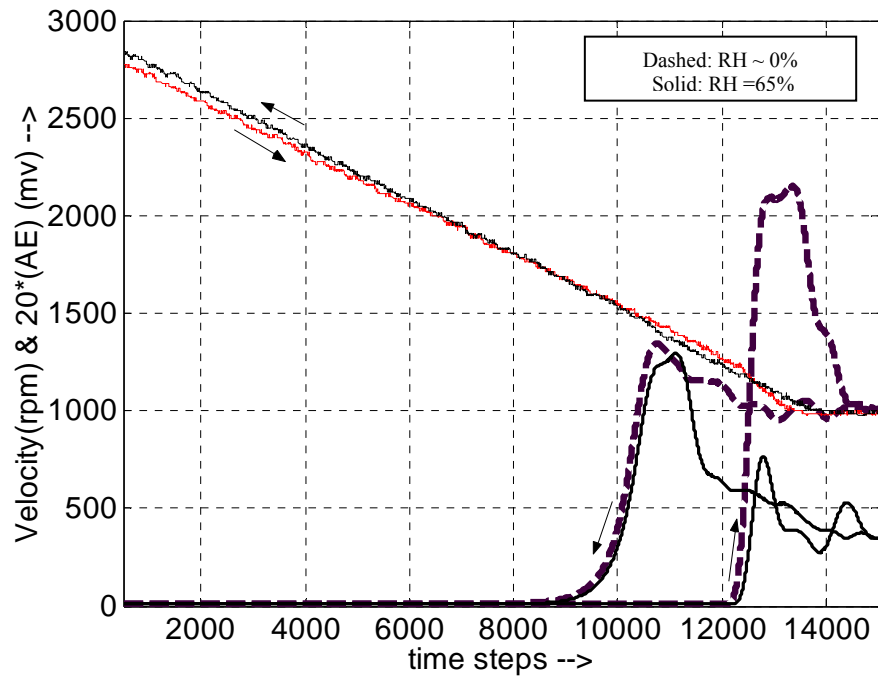


Figure 2.6: Dependence on ambient humidity

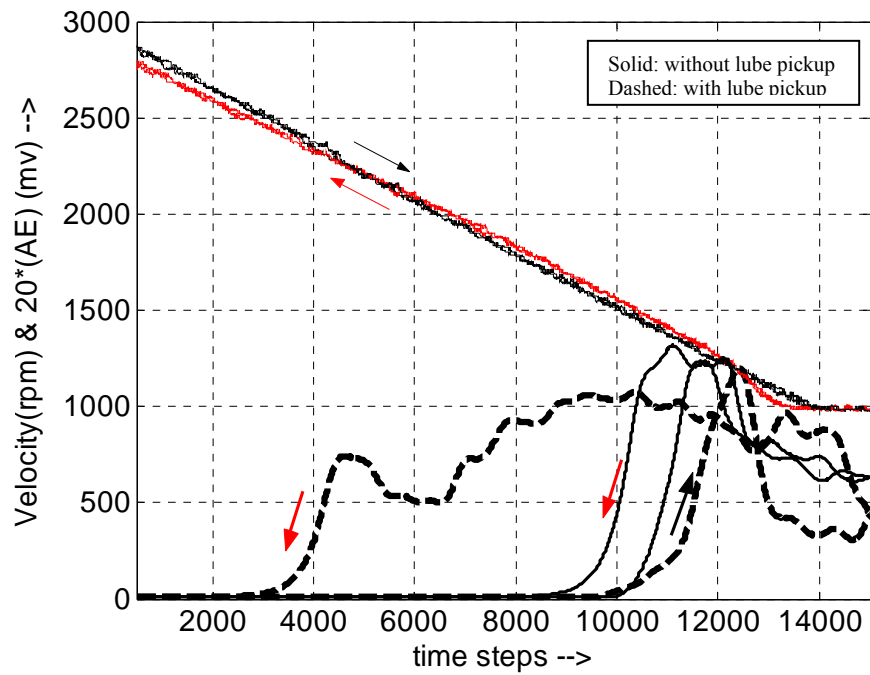


Figure 2.7: High hysteresis at high humidity: Lubricant pickup

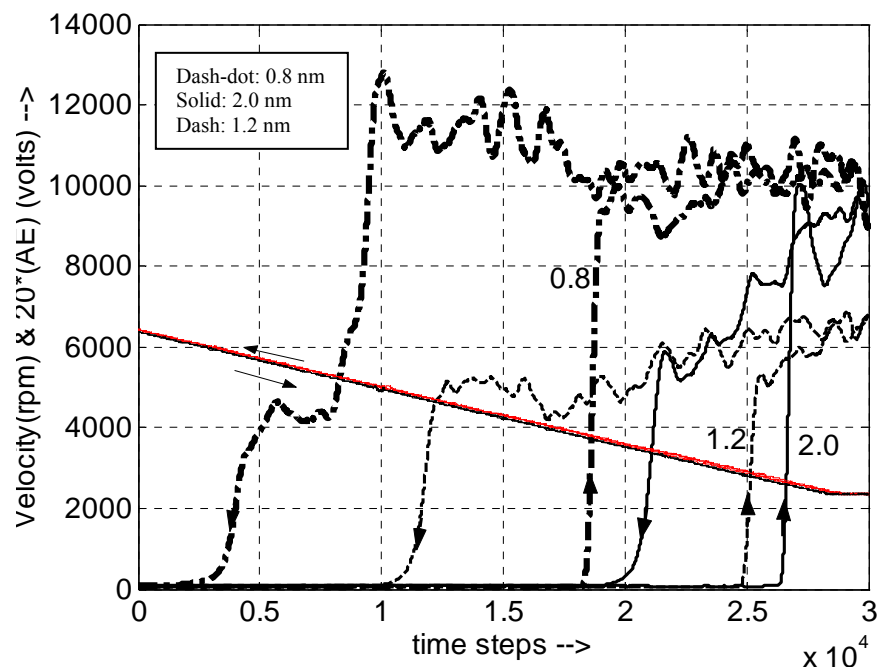


Figure 2.8: Hysteresis observed for various lubricant thicknesses (Red arm of velocity profile is spindown while the black arm corresponds to spin up.)

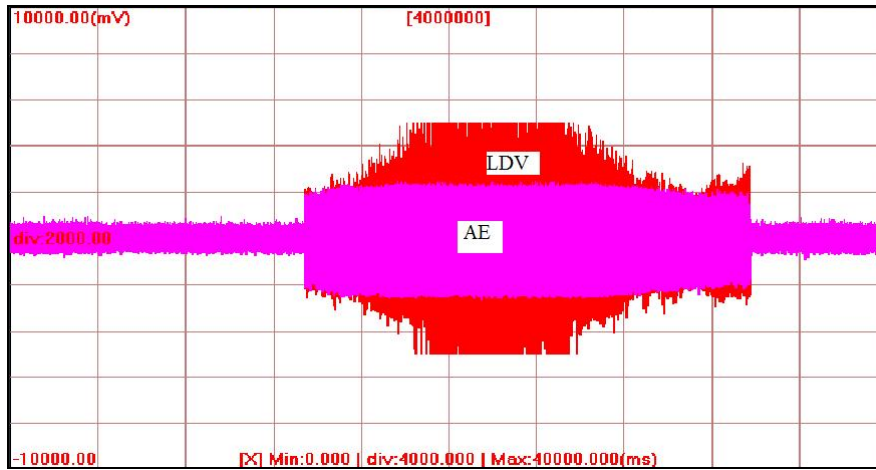


Figure 2.9: Comparison between AE and LDV signals for detection of contact

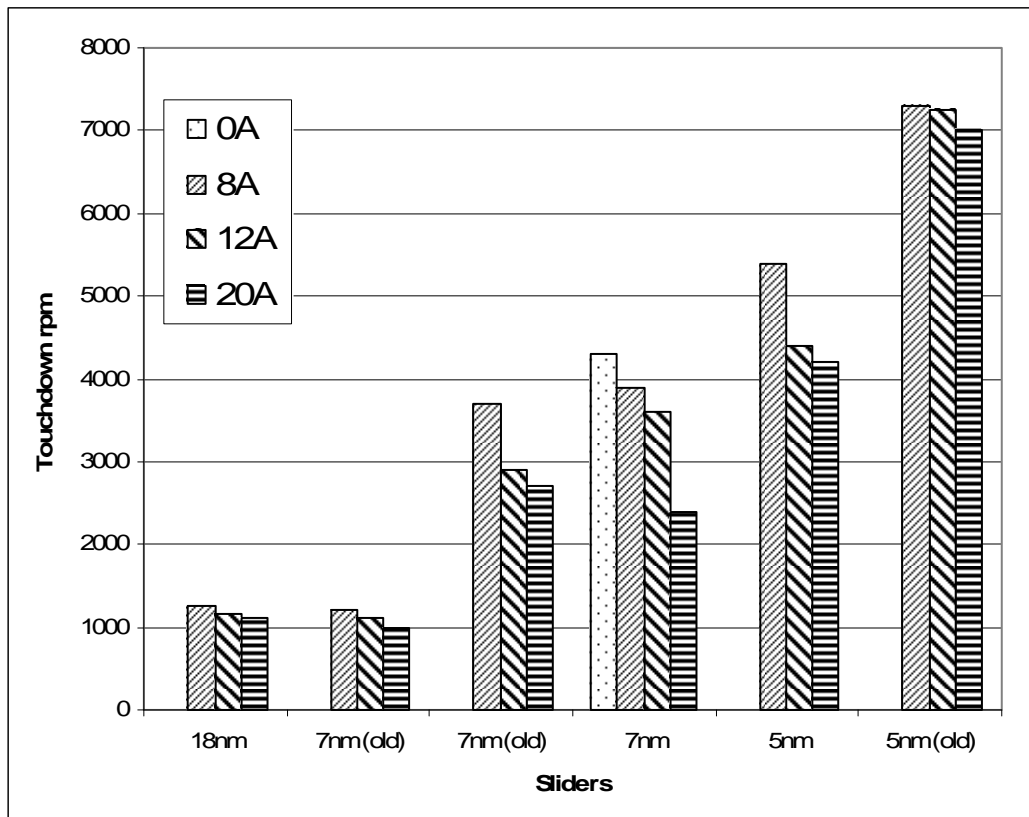


Figure 2.10: Variation of Touchdown rpm as a function of lubricant thickness for various slider designs (Experimental Results).

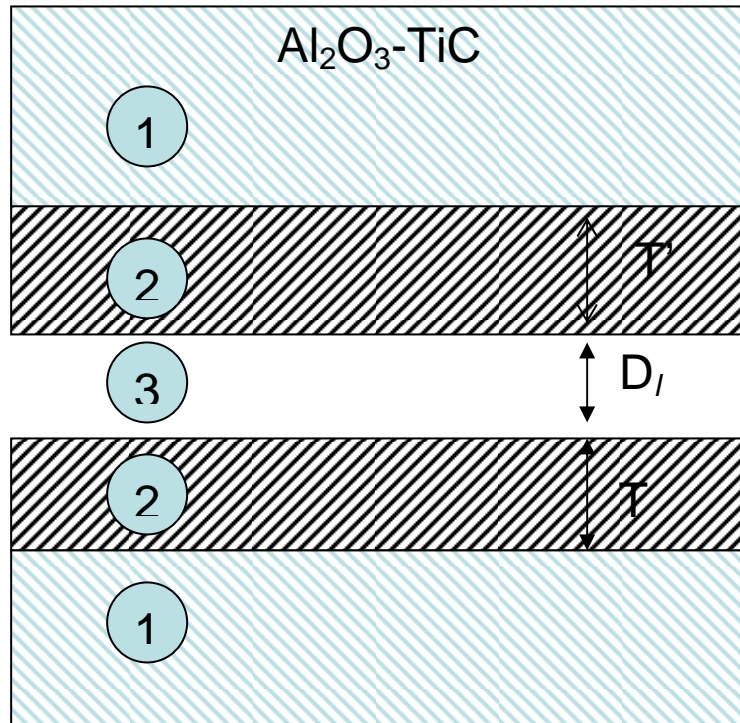


Figure 2.11: Multilayer model for modeling intermolecular forces

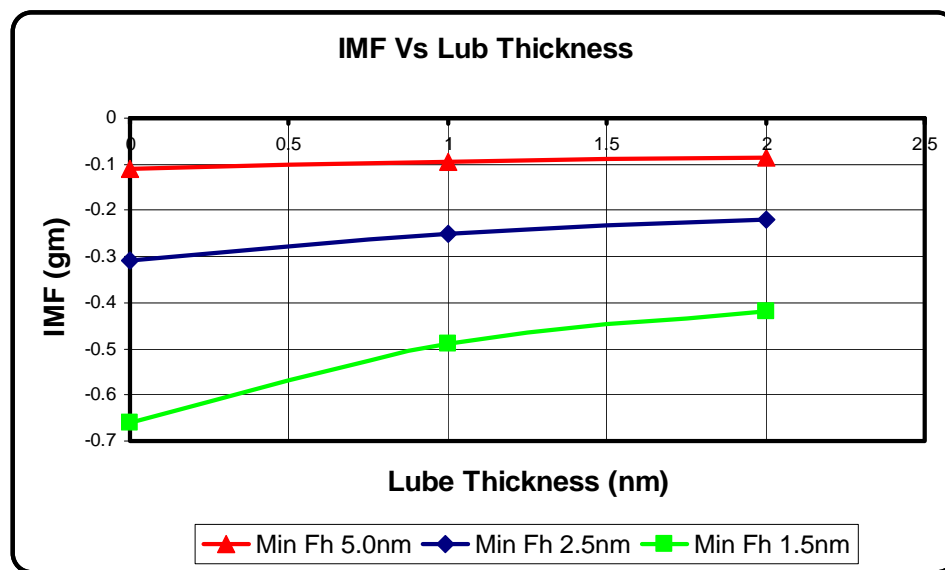


Figure 2.12: Variation of intermolecular forces as a function of lubricant thickness

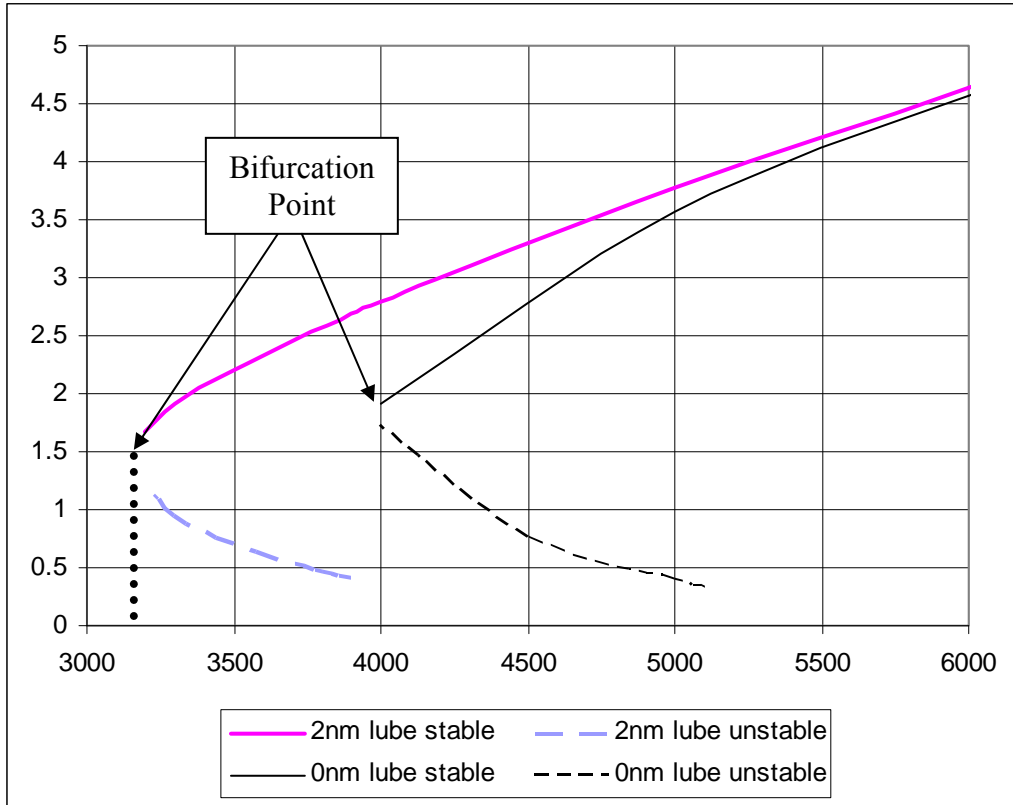


Figure 2.13: Fly height diagram (Simulations)

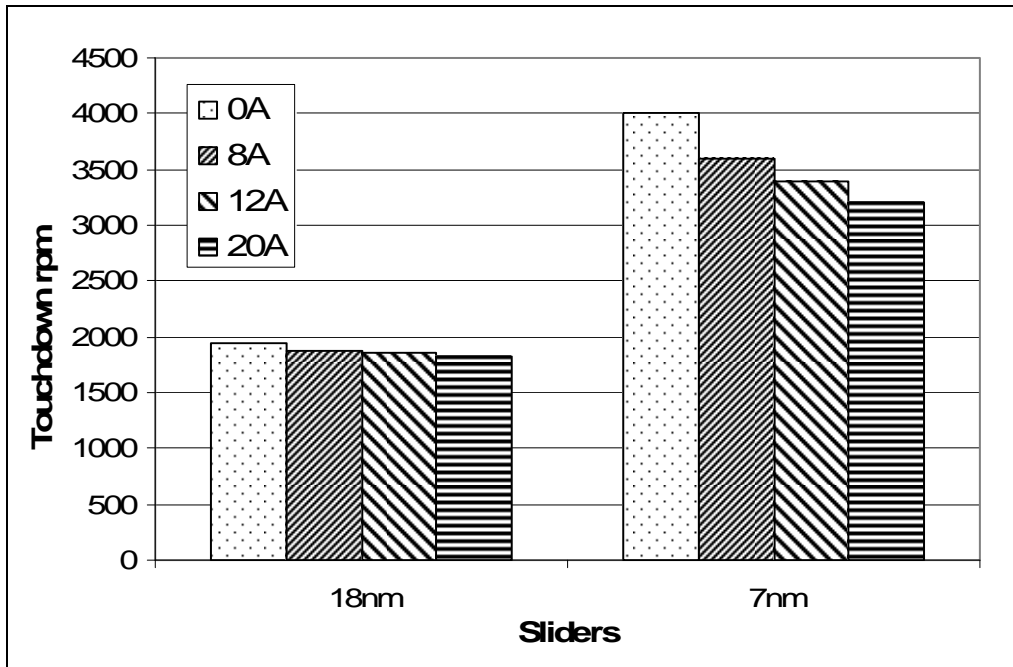


Figure 2.14: Variation of Touchdown rpm as a function of lubricant thickness for various slider designs (Simulation results)

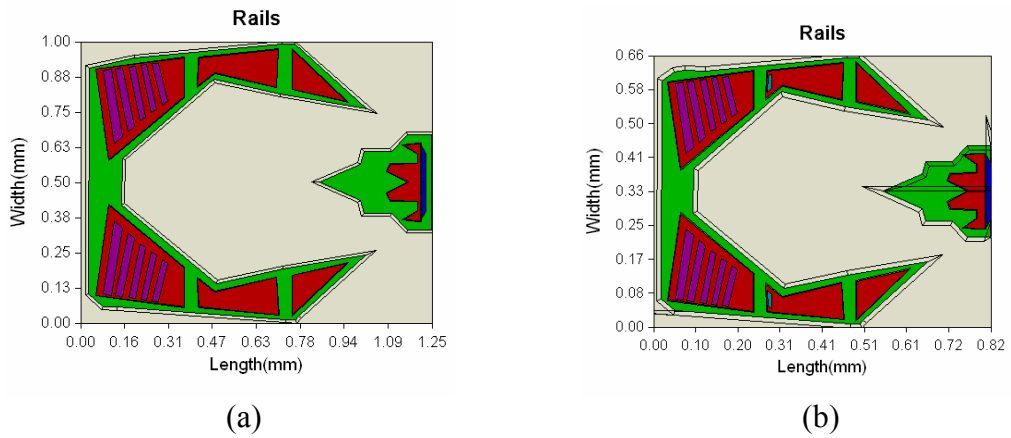


Figure 2.15: Sliders used for simulations – high-damped design: (a) Pico slider and (b) Femto slider

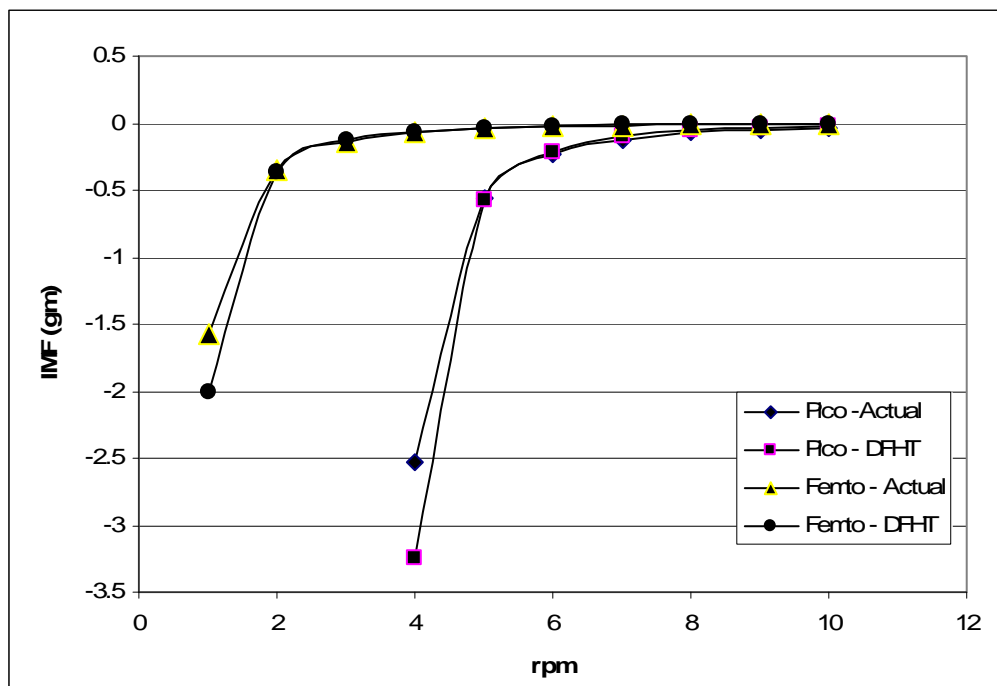


Figure 2.16: IMF between slider and disk for high-damped slider designs when simulated over actual and DFHT interfaces.

CHAPTER 3

FURTHER STUDIES ON THE TOUCHDOWN-TAKEOFF HYSTERESIS

3.1 Introduction:

In the last chapter, we reported on an experimental study of the hysteresis we conducted using touchdown-takeoff tests. From the experimental results and multilayer modeling of IMF we concluded that IMF does affect the dynamic stability of the slider at proximity. In this chapter we present some findings on the dependence of hysteresis on other factors, including meniscus forces and the disk topography using similar experimental techniques and rationale as explained in the previous chapter. The rationale is outlined briefly as follows:

Since there are many HDI phenomena that can affect hysteresis and slider stability, they can only be separated by knowing their “domain of operation”. The touchdown velocity will only be affected by non-contact phenomena such as intermolecular force or external excitation due to lubricant modulation or disk topography. Similarly, the takeoff velocity will be mainly affected by contact interactions which include slider-lubricant interactions causing lubricant pickup by the slider and lubricant depletion and redistribution on the disk as well as the disk burnishing due to slider-disk contact.

3.2 Experiments

3.2.1 Touchdown-takeoff tests

A detailed description of the touchdown-takeoff tests has been provided in Chapter 2 and is briefly described by Figure 3.1. These tests were conducted on a CETR tester using an acoustic emission (AE) sensor to detect contact. The test conditions (humidity, disk lubricant thickness and slider design) were varied and the variation of touchdown speed, takeoff speed and the resultant hysteresis was observed. The slider and the disk were examined using an optical microscope and a Candela Optical Surface Analyzer, respectively, to determine the slider air-bearing surface (ABS) contamination and lubricant profile change on the disk.

3.2.2 Stability tests for effect of lube pickup

From the tests described above, only variations in takeoff velocity could be observed since a clean slider was used for every test. However, in operation, lubricant pickup and contamination occurs continuously. To study the effect of this accumulation, a different set of tests was conducted on a TTi spinstand using a Laser Doppler Vibrometer (LDV) to detect contact. These tests were similar to the tests described above with the exception that the touchdown-takeoff tests were carried out continuously without cleaning of the slider before each test. For all the subsequent tests, a CML-7nm pico slider (Figure 3.2(a)) was used.

In these tests three disks from the same batch (INSIC-IV) but having different lubricant thicknesses (SG Lube) were used. Touchdown-takeoff tests were conducted on each of the disks in the order 1.2 nm, 0.8 nm and 2.0 nm (disks A, B and C respectively)

of lubricant thicknesses of ZDOL and at a constant skew of zero degrees on different tracks in the order 1.5”, 1.1” and 1.4” on each disk. The rpm of the disks were adjusted for different tracks so as to have a constant linear velocity for all the tracks. The slider was carefully cleaned to remove the ABS contamination before beginning a test on each disk.

3.2.3 Stability tests for effect of disk topography

These tests were conducted later on a TTI spindstand using a LDV to study the slider dynamics and an AE sensor to detect contact. A fresh INSIC batch IV disk with 1.2 nm of SG lube was used (Disk D). This disk showed better properties than the disks used in the previous experiment as regards to ABS contamination due to lube pickup. Repeated touchdown-takeoff tests were conducted on a particular track to see the effect of disk burnishing on the touchdown and takeoff velocities. Since the slider ABS was always clean after every touchdown-takeoff cycle, when seen under the optical microscope, these tests discounted the effect of lubricant pickup. The slider dynamics were also observed, and this gave information about the evolution of slider bouncing velocities during contact.

3.2.4 Dependence on velocity profile (experimental bias)

In addition to the different phenomena that contribute to hysteresis, the touchdown and takeoff velocities may also depend on the deceleration or acceleration of the disk during the tests, i.e. the velocity profile (Figure 3.1). Hence, while comparing the effect of different lubricant thicknesses or humidity conditions, the velocity profile was maintained constant across experiments. However, since it was possible to get a repeatable hysteresis for disk D (described in detail in the results section), the

dependence of the touchdown and takeoff velocities on the velocity profile was also studied. The velocity profile used was similar to that shown in Figure 3.1, except that there was no dwell at the minimum rpm in this case.

Two different pico sliders, CML 7nm and 5nm (Figure 3.2) were flown over different tracks (1.1” and 1.0” respectively) on disk D and the disk rpm was varied as 8000→2400→8000 symmetrically and linearly in 10, 15, 20 and 25 secs (called “acc-time” henceforth). In all, 20 runs were conducted (5 runs corresponding to each acc-time) in random order of acc-times to eliminate any procedure-biased errors. The variation of the touchdown and takeoff velocities was studied for the above four different acceleration/deceleration rates.

3.3 Results:

3.3.1 Touchdown-takeoff tests

During the touchdown-takeoff tests it was seen that when the slider picked up lubricant the takeoff velocity was relatively high. This lubricant pickup could be observed on the slider using the optical microscope. Figure 3.3 shows results for tests in which the same slider and disk were used with the same ambient humidity. In this figure the AE signal is plotted against the disk rpm. The time axis folds back on itself so that the hysteresis is evident. The dashed and solid curves show the AE signal corresponding to the cases where there was presence and absence of lubricant on the slider ABS, respectively. The touchdown velocity does not show much variation while there is variation of takeoff rpm associated with lubricant pickup. Based on these and similar

other tests, it is concluded that due to the lubricant pickup and the ABS contamination of the slider during its contact with the disk there is an increase in the takeoff velocity.

3.3.2 Stability tests for the effect of lube pickup

Figure 3.4 shows the experimental results from the stability tests. The time of touchdown in seconds has been plotted for each track on each disk. It should be noted that the later the slider comes into contact with the disk, the more stable is its flying. The labels “cleaned” indicate that the slider was cleaned before conducting that test.

For each of the disks the first bar corresponds to the time of touchdown when the ABS is clean. When the slider comes into contact with the disk the ABS gets contaminated. It is seen that for the 1.2nm (lubricant thickness) disk, when the slider was flown over different tracks successively without cleaning, its stability kept decreasing. This observation can also be made for the 0.8 nm and 2.0 nm disks. However, after the slider was cleaned, it regained its flying stability.

During the tests it was found that the slider ABS was contaminated as a result of contact with the disk. Figure 3.5(a) shows ABS contamination after the slider was flown twice over the 2.0 nm disk without cleaning (corresponding to the lowest stability in Figure 3.4). Figure 3.5(b) shows a magnified image of the trailing pad corner marked by the rectangle in Figure 3.5(a), where a significant lubricant pickup is observed. A consistent lubricant pickup similar to that shown in Figure 3.5(b) was seen during all the tests.

3.3.3 Stability tests for the effect of disk topography

From the tests it was found that the presence of contaminants or asperities on the track destabilizes the slider. For this reason rough or contaminated disks show high

touchdown velocity. The presence of contaminants can also explain the loss of stability in the takeoff zone, as seen in Figure 3.8. However, once in contact, burnishing of the track may occur and the takeoff velocity can become lower than the touchdown velocity causing an “inverse hysteresis” (Figure 3.7(a)). Upon conducting repeated tests on such a burnished track it was seen that the touchdown velocity kept decreasing due to successive burnishing of the disk during subsequent contacts, thus decreasing or eliminating the inverse hysteresis (Figure 3.9) or even the slider-disk contact all together (Figure 3.7 (b)).

It was seen that the hysteresis, in general, was not very repeatable as it depends on a variety of factors which cannot be maintained constant as the slider-disk contact changes the disk topography, redistributes the lubricant and it also contaminates the slider ABS. However, when many tests were conducted on disk D it was possible to achieve a “steady-state” hysteresis (Figure 3.10 and Figure 3.11). When the tests started on a new track, the touchdown and takeoff velocities were relatively high, but they kept dropping as the tests progressed, finally achieving a steady-state.

3.3.4 Dependence on velocity profile

In addition to the above mentioned factors, it is also generally considered that the touchdown and takeoff velocities may also depend on the deceleration or acceleration of disk during the tests. Hence, while comparing the effect of different lubricant thicknesses or humidity conditions, the velocity profile was maintained constant across experiments. Further, the above premise can be tested experimentally only if the hysteresis is a repeatable phenomenon and its variation due to change in the disk acceleration/deceleration can be compared. Since this repeatability of hysteresis was

achieved for disk D experiments were conducted to study the dependence of hysteresis on the disk acceleration/deceleration using that disk. The results are shown in Figure 3.12 and Figure 3.13.

In these figures the mean values of touchdown (shorter bar) and the takeoff (taller bar) velocities are plotted for each of the four times, along with the error bars corresponding to their standard deviation (5 readings). It is seen from the small standard deviation that the touchdown and takeoff velocities show good repeatability. For both sliders it is also seen that the steady-state touchdown and takeoff velocities (and the hysteresis) does not depend on acceleration time within the range of accelerations considered.

3.4 Discussion:

3.4.1 Intermolecular Forces

A detailed account of the nature of intermolecular forces (IMF) and their effect on the head-disk interface has been given in the previous chapter. To summarize, the IMF are modeled using a Lenard-Jones potential, which contains a long range attractive force term and a short range repulsive force term. The repulsive force term comes into play when the distance between the bodies is less than 0.3 nm, which in the case of the slider-disk, is contact. The long range attractive force is responsible for slightly decreasing the fly height of the slider and increasing adhesion between the slider and the disk, which causes the slider to come into contact earlier. A force balance between the airbearing force (providing lift), the IMF and the electrostatic forces [1], reveals multiple

equilibriums for the slider flying height [1]. The slider exhibits a chaotic motion due to the presence of these multiple equilibriums and contributes to instability and hysteresis [2].

The presence of IMF at the head-disk interface was experimentally seen from the effect of lubricant thickness on the touchdown velocity in the previous chapter, a trend which was opposite to that predicted by the meniscus forces. Multilayer modeling of the IMF was carried out to determine the IMF between the slider and the disk. Using the fact that the IMF depends on the refractive indices of the interacting mediums, it was shown that the presence of lubricant reduces the IMF, thus explaining the experimentally observed trend.

Thus, from this study, the contribution of intermolecular forces to instability and hysteresis was determined. We now proceed with a detailed discussion of the other factors influencing hysteresis.

3.4.2 Lubricant Pickup

From the results of the touchdown-takeoff tests we see that the takeoff velocity, which is the measure of the recovery of the slider from contact to stability, is higher in the presence of lubricant pickup. Thus, lubricant pickup decreases the slider's stability. Further, it also causes ABS contamination, which in turn may collect miniscule debris particles as seen in Figure 3.5(b). This would cause accelerated wear at the head-disk interface.

However, due to the high shear rates at the HDI, the contaminants are washed away from the ABS in most cases. From the pictures taken after the tests it is evident that these contaminants accumulate behind the trailing pad of the slider. This

accumulation is especially more near the corner of the trailing pad which flies lower and therefore is the lowest flying point on the slider (in the absence of pole tip protrusion, as in case of the sliders used). Since this part first makes contact with the disk, and there is a consistent lubricant pickup around this area, it is estimated that the lubricant-lubricant adhesion (Figure 3.6) between the slider and the disk affects the interface from this point. These adhesive forces can be termed as meniscus forces as this lubricant-lubricant adhesion is similar to forming a meniscus bridge between the slider and the disk. However, we note that this definition of meniscus forces is a broader definition since it is not known if an actual meniscus bridge can form during a slider-disk contact which typically last for less than $1\mu\text{s}$ [1].

From the stability tests we see that once lubricant pickup occurs, even the touchdown velocity in the subsequent tests increases (i.e. the time taken for touchdown decreases). Thus, lubricant pickup not only hampers the slider's ability to recover from contact but also increases the instability by making the slider go into contact earlier.

Head-disk contact may not be the only way by which lubricant pickup occurs. Many researchers [3]-[5] are studying the problem of disk-to-slider lubricant transfer even in the absence of contact. In any regime, contact or flying, if there is lubricant pickup on the ABS, it is estimated that some of it will be sheared off towards the trailing edge and will accumulate behind it [3]. Thus, there would be lubricant on the low-flying slider area as well as on the disk, causing lubricant-mediated adhesion.

To model the effect of lubricant pickup on adhesion between the slider and disk we used a simplified adhesion model based on surface energy of interacting materials at

the interface [6]-[8]. The work of adhesion between two surfaces a and b in the absence of lubrication is given by

$$\begin{aligned} W_{ab} &= (\gamma_a + \gamma_b - \gamma_{ab}) \\ &= C(\gamma_a + \gamma_b), \quad 0 \leq C \leq 1, \end{aligned} \quad (3.1)$$

where C is the “compatibility index”, the values of which are prescribed for different combinations of surfaces including metals and non-metals of different compatibilities [6]. In the presence of lubrication a parameter c_l is included in (3.1) to incorporate the dependence on lubrication. The combined parameter $c_l C$ is called the “combined compatibility index”. The values of $c_l C$ are provided as a function of the degree of lubrication or contamination for various interfaces like metal-metal, metal-nonmetal and nonmetal-nonmetal and degree of compatibility between these surfaces [6]. Figure 3.14 shows such a plot which was used to obtain the value of the combined compatibility index.

For the head-disk interface DLC overcoat on the slider and the lube on the disk are nonmetallic. They are assumed to be dissimilar nonmetals (other categories being identical and similar) and the air-bearing lubrication is a lubrication equivalent to that in clean air. For such an interface we obtain $c_l C = 0.36$. In case of lube-lube interaction, since the lubes on the disk and slider are identical, $c_l C = 1.0$. In addition, assuming surface energies $\gamma_{\text{lube}} \sim 23 \text{ erg/cm}^2$ and $\gamma_{\text{DLC}} \sim 40 \text{ erg/cm}^2$, we obtain:

$$W_{\text{lube-lube}} = 1(23+23) = 46 \text{ erg/cm}^2 \quad (3.2)$$

(with lubricant pickup)

$$W_{\text{lube-slider}} = 0.36(23+40) = 22.68 \text{ erg/cm}^2 \quad (3.3)$$

(without lubricant pickup)

Thus, lubricant pickup is expected to increase adhesion and enhance wear of the disk as observed experimentally by Li et.al. [9]. Using this same model it is also seen that in the absence of lubricant the work of adhesion will be

$$W_{\text{DLC-DLC}} = 1(40+40) = 80 \text{ erg/cm}^2 \quad (3.4)$$

This implies that the adhesion, and hence instability and wear are maximum in the absence of lubricant. The presence of lubricant helps in reducing the instability. However, lubricant pickup by the slider causes lubricant-mediated adhesion, which increases the instability.

3.4.3 Disk Topography

Disk topography provides external excitation to the flying slider. The rougher the disk, the more excitation the slider gets. There is also more probability of having high asperities on the disk track for a rougher disk. This increases the chance of losing flying stability by hitting an asperity. However, during the steady state operation of the drive, burnishing may take place due to intermittent contact forced by a rough topography or due to contact with an asperity. This in turn will smoothen the topography as well as reduce the glide height. Thus, the slider's stability may increase in the long run. The action of burnishing during contact is being used to explore new slider designs. In order to achieve lower flying heights and insensitivity to manufacturing tolerances, burnishing heads are being used [11].

It should also be noted however, that during the burnishing action debris particles are generated which contaminate the interface. Though these particles can aid in further burnishing, they also might contribute to excessive wear and friction heating if they are stuck in the interface [12]. During contact, there also can be a substantial lubricant

pickup, which, if not sheared away behind the trailing edge or in recesses can causes ABS contamination thereby reducing the slider stability. Thus, the net effect of burnishing may also depend upon the slider ABS design [13],[14] and lubricant at the interface [15].

3.4.4 Inherent Hysteresis

In addition to factors such as intermolecular forces, meniscus forces and disk topography influencing hysteresis, an inherent hysteresis also exists in the touchdown-takeoff process. Observing the slider velocities obtained by the LDV, it was seen that the slider “snapped” into contact showing high velocities and therefore high instability in its dynamics. When the disk velocity started increasing in the takeoff leg, the slider dynamics gradually stabilized showing less velocities before the slider finally lost contact with the disk at the takeoff velocity (Figure 3.15).

During the touchdown-takeoff sequence, the slider loses its fly height during the touchdown leg, as the disk velocity decreases. Due to this, the slider is affected by proximity phenomena as well as the uneven disk topography, thus reducing its stability. When it comes into contact with the disk the slider-suspension system starts vibrating with much higher amplitudes due to the impact forces, which in turn adds more energy into the vibrating system. As a result, there are sustained high amplitude vibrations during contact. When the velocity starts increasing again, the mean fly height of the slider starts increasing and the high vibrations due to impact are resisted by a stiffer air-bearing. This tends to stabilize the system and decrease the vibration as experimentally seen using the LDV. But the stiffer air-bearing now required to curb these vibrations also requires a higher disk velocity; thus, more energy has to be expended now to stabilize an

unstable system as compared with that required to maintain the system stability in the absence of contact or high vibrations which was the case during the touchdown leg. Hence, the slider dynamics during contact may be seen as an inherent reason for the hysteresis observed.

3.5 Conclusions

From the touchdown-takeoff and stability tests conducted to investigate the factors causing the touchdown-takeoff hysteresis, it is concluded that the slider dynamics itself during the touchdown-takeoff process introduces a hysteresis. In addition, intermolecular forces, meniscus forces and disk topography influence the hysteresis. The long range IMF is mainly attractive in nature and causes the slider to have a slightly reduced fly height and to have multiple equilibriums which affect the stability of the slider. Meniscus forces act through lubricant pickup and slider-lubricant interactions, which cause lubricant mediated adhesion as well as contamination. This causes the slider to come into contact with the disk earlier and delays its recovery from contact as well.

Rough and contaminated disks increase the probability of slider-disk contact compromising the slider's stability. However, during slider-disk contact, burnishing takes place which increases the stability of the slider.

In this chapter, we identified various factors influencing the hysteresis. From the experimental results reported in Chapters 2 and 3, it is seen that the effect of the lubricant pickup (caused by slider-lubricant interaction) on the slider's stability is more than IMF (Figure 3.3-Figure 3.4). Hence, in the next few chapters we focus on understanding the physics of the slider-lubricant interactions using various experimental, numerical and theoretical techniques. Since disk topography is also an important factor

affecting slider stability, the effect of radial and circumferential disk topography is studied in Chapter 8. Finally, using previously published research, a causal relationship has been shown between IMF, meniscus and electrostatic forces with the help of an organizational chart in Chapter 9.

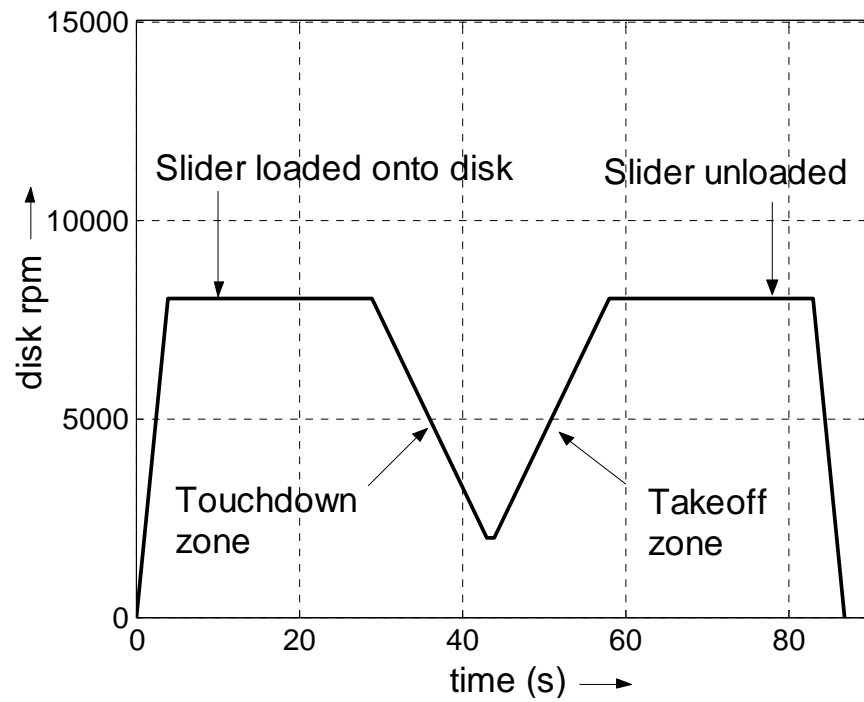


Figure 3.1: Disk velocity profile during touchdown-takeoff tests

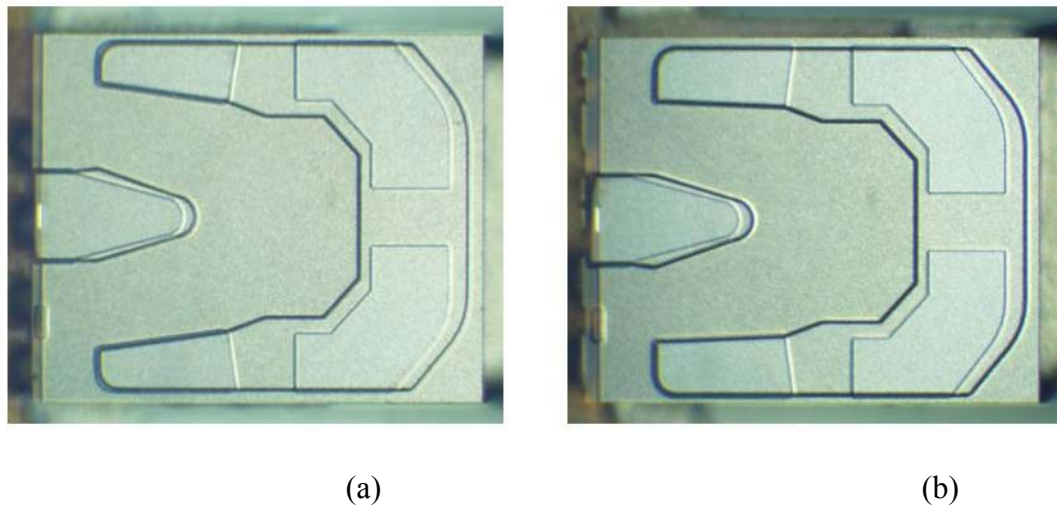


Figure 3.2: Sliders used (a) CML 7nm : For tests A, B, C and D ; (b) CML 5 nm: For test D

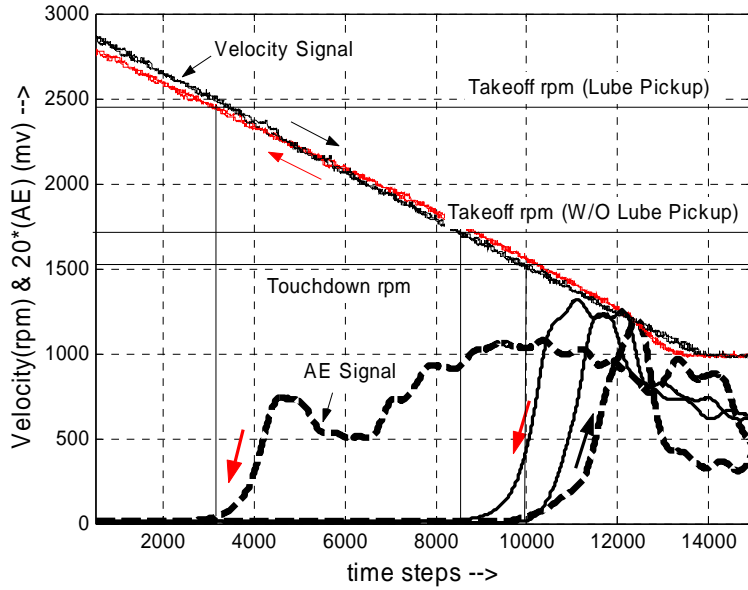


Figure 3.3: Increased takeoff velocity due to lubricant pickup (dashed curve).

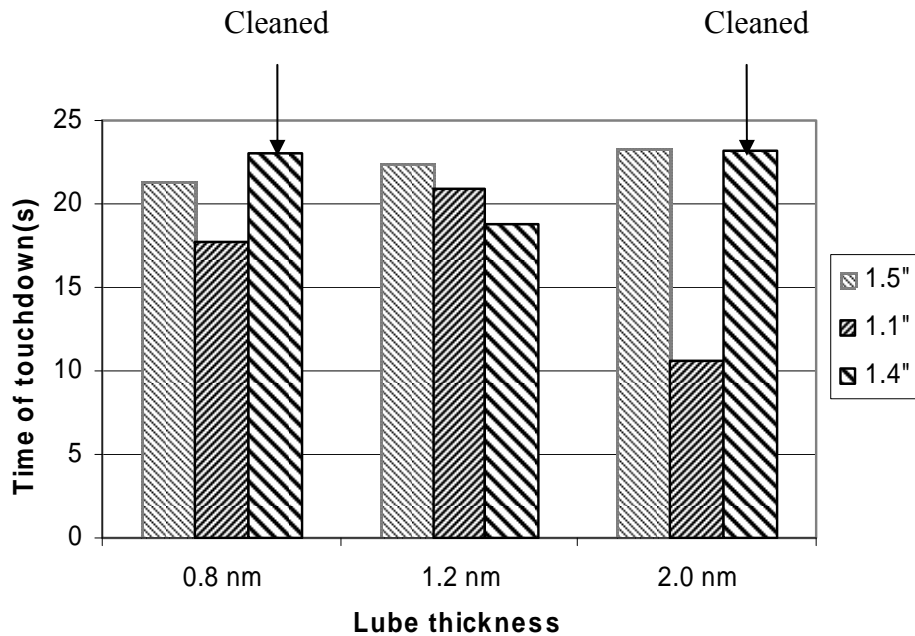


Figure 3.4: Effect of lubricant pickup on stability

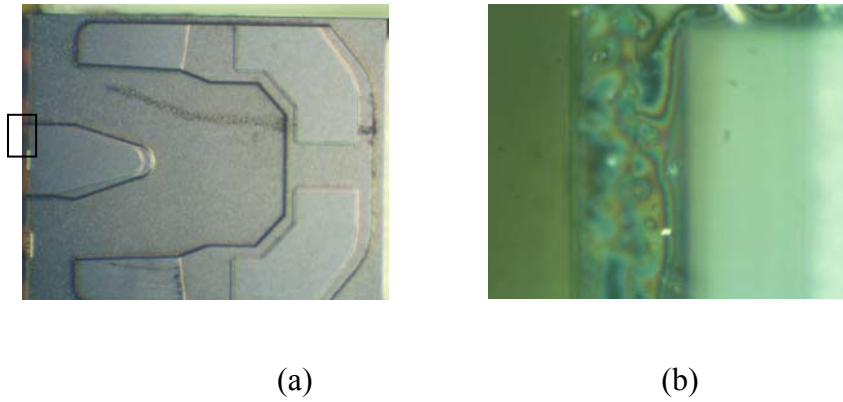


Figure 3.5: (a) ABS contamination during stability tests; (b) Lubricant pickup behind the trailing pad

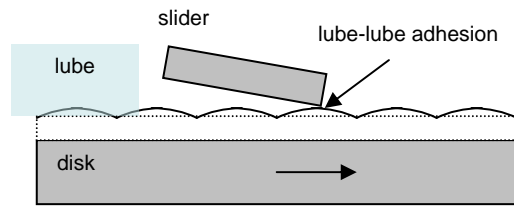


Figure 3.6: Schematic of the lube-lube interaction in the event of lubricant pickup by the slider.

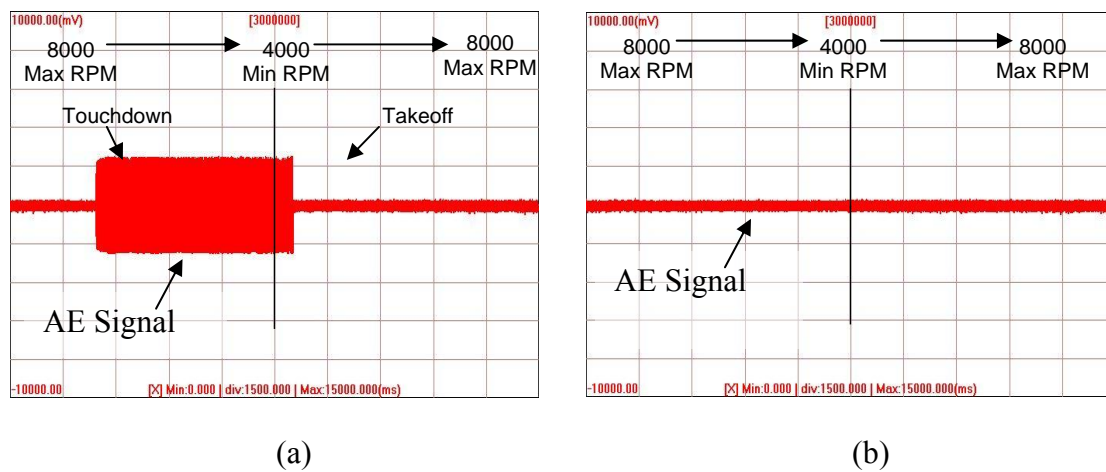


Figure 3.7: (a) Inverse hysteresis; (b) Effect of burnishing

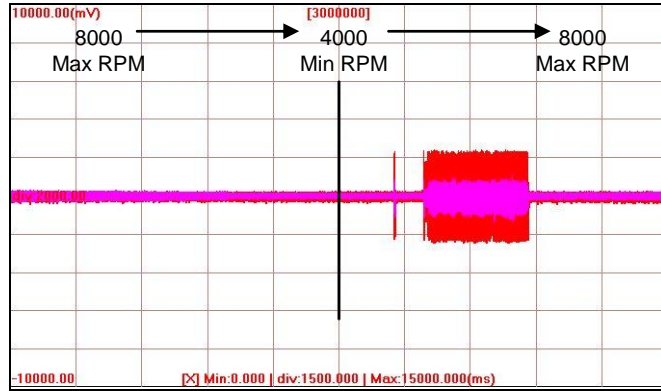
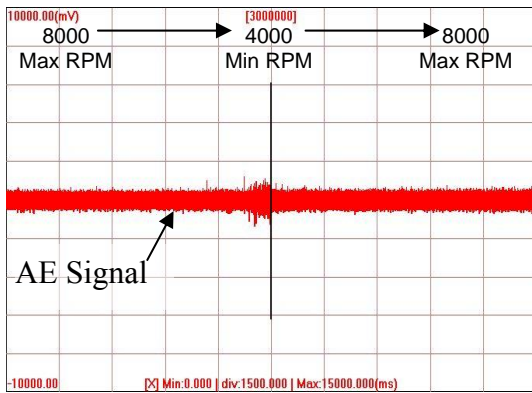
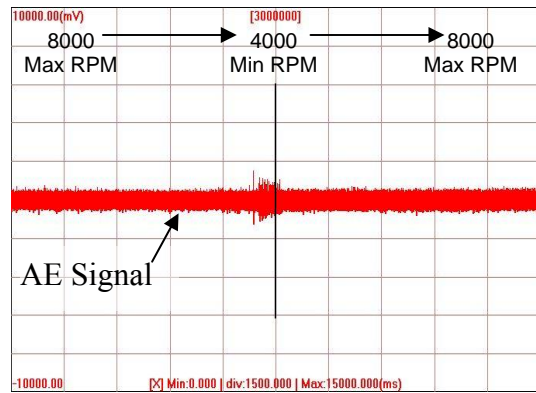


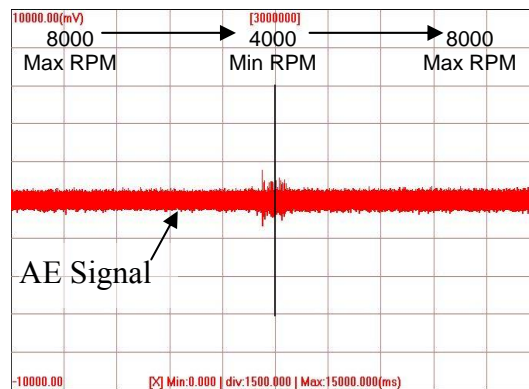
Figure 3.8: Contact in the Takeoff Leg (Effect of contamination)



(a)



(b)



(c)

Figure 3.9: Shifting of the hysteresis to the right

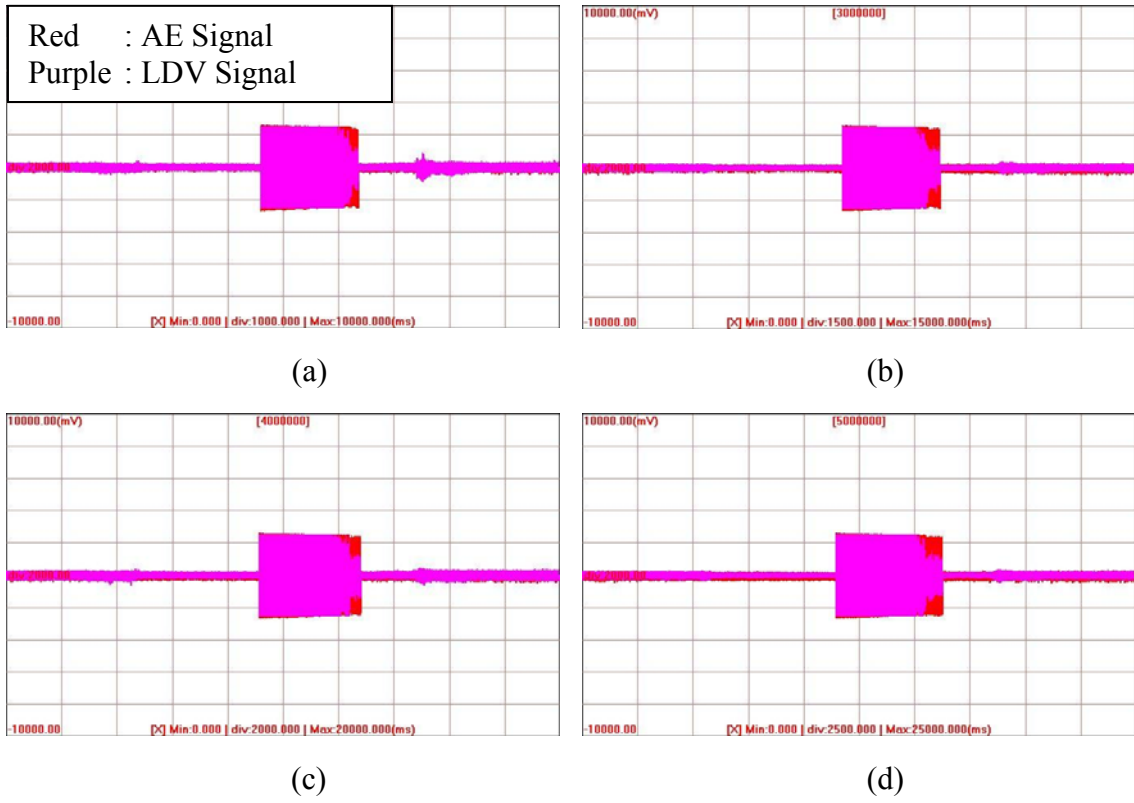


Figure 3.10: Steady State Hysteresis for CML-7nm slider

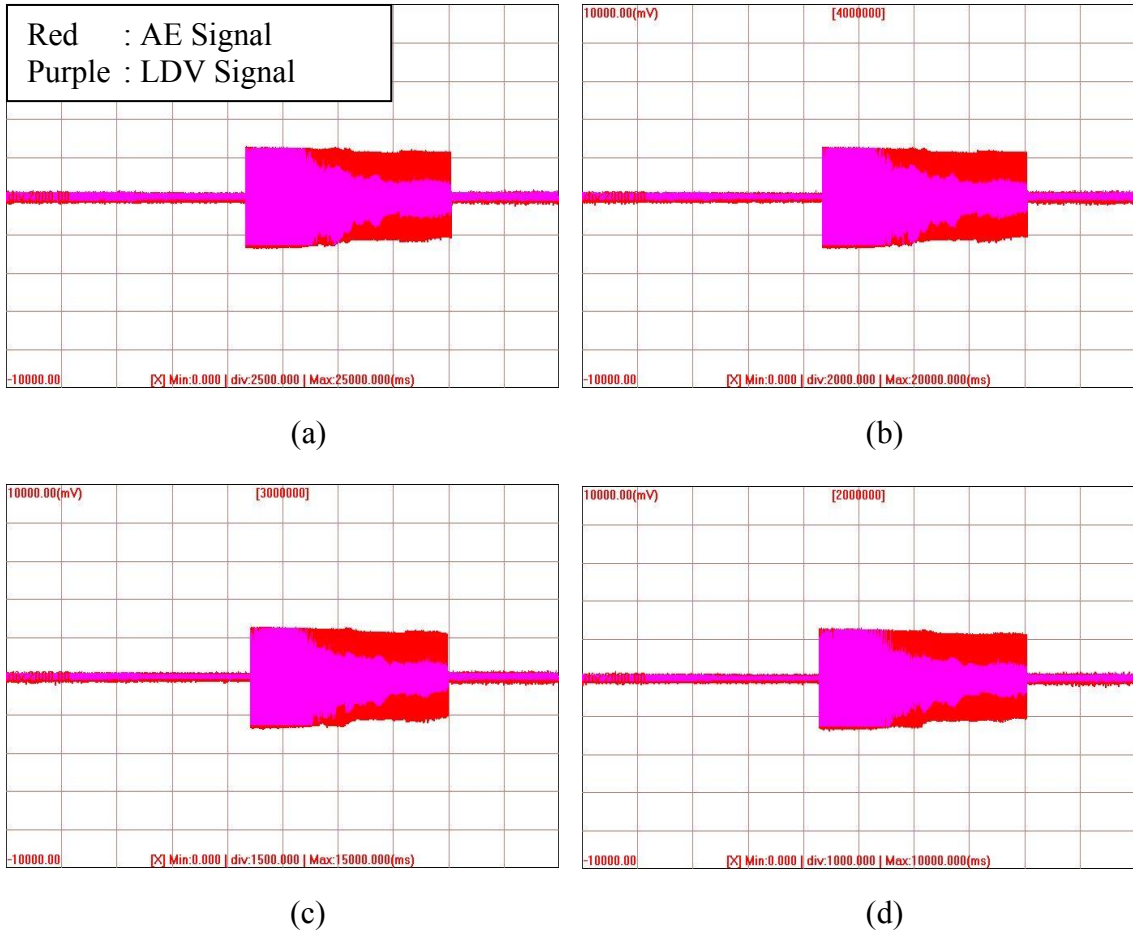


Figure 3.11: Steady State Hysteresis for CML-5nm slider

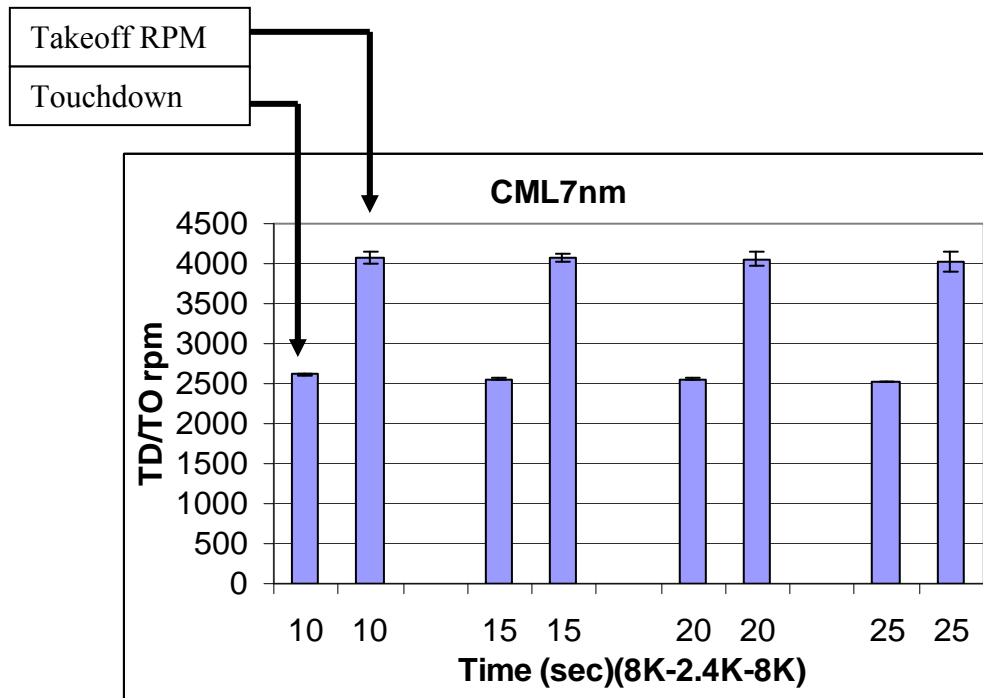


Figure 3.12: Dependence of Acceleration/Deceleration

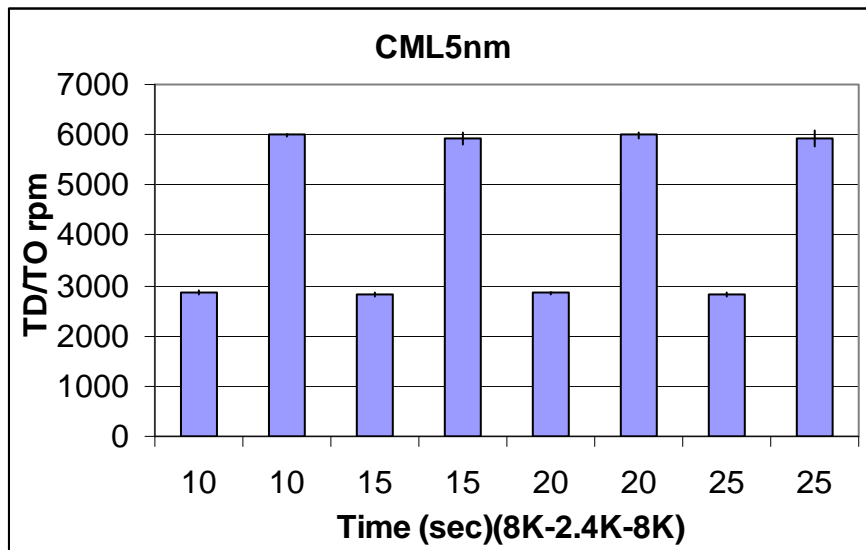


Figure 3.13: Dependence of Acceleration/Deceleration

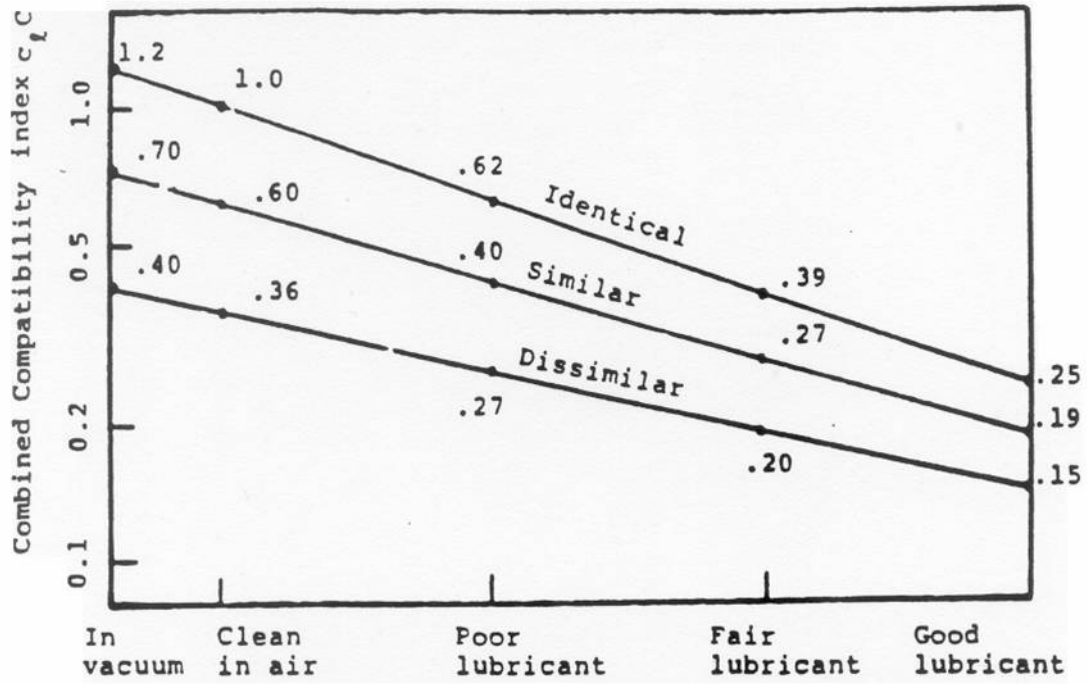


Figure 3.14: Plot of combined compatibility index as a function of the degree of lubrication or contamination, for use when at least one of the two contacting materials is non-metallic.

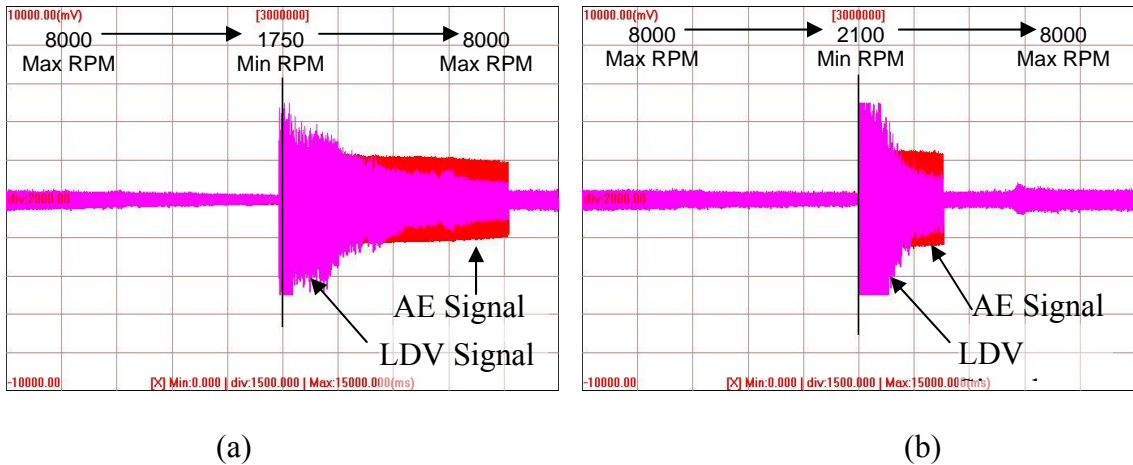


Figure 3.15: Inherent hysteresis

CHAPTER 4

SLIDER-LUBRICANT INTERACTIONS AT THE HEAD-DISK INTERFACE

4.1 Introduction:

In a Hard Disk Drive (HDD), there exist multiple layers on the magnetic disk. On top of the magnetic layer there is a hard diamond-like carbon (DLC) overcoat of about 1-2nm to protect the magnetic layer against head crashes and corrosion. On top of the DLC, there exists a molecularly thin (~0.5-1.5nm) lubricant layer to reduce the friction and wear at the head-disk interface (HDI).

In order to achieve the areal recording density of 1 Tb/in², the physical head-disk spacing has to be reduced to about 2.5 nm. At such a small spacing, the effect of lubricant needs to be considered in simulating the fly height of the slider. Various experimental studies [1]-[4] have been done to investigate lubricant changes under a flying slider and its effect on magnetic spacing. It has been reported that a flying slider modulates [2]-[3] and redistributes [1] the lubricant. Simulations [3] attribute the lubricant modulation to ABS shear effects. This lube modulation can prove detrimental to the dynamic performance of the slider. Further, the ABS air shear and pressure can also contribute to the displacement of the lubricant under the slider. Hence, even in static simulations, this effect needs to be considered in order to predict the correct fly height of the slider.

In this chapter we report on both experimental and numerical studies of lubricant changes under an ABS. In the first section the lubricant distribution profiles under a flying slider were obtained experimentally as well as by conducting simulations.

Subsequently, these profiles were included in the CMLAir static solver to estimate the flying attitude (fly height, pitch, roll, pressure distribution, etc) of the slider after inclusion of the lubricant. Comparison of the flying attitudes with and without the inclusion of the lubricant is made and discussed.

In the second section an experimental study of slider-lubricant interactions in the partial contact regime is presented. As the slider flies in close proximity of the disk, intermittent contacts are unavoidable during operation of the HDD. Not much literature is available concerning how the lubricant is affected during these intermittent contacts as most effort has been concentrated on slider-lubricant interactions in the non-contact regime. Hence, such a study is carried out to understand the effect of intermittent slider-disk contacts on the lubricant distribution.

Section I: Non-contact regime

4.2 Experiments

The Candela Optical Surface Analyzer (OSA) was used to experimentally measure the lubricant profile under a flying slider. The OSA can measure the lubricant thickness with a sub-Å accuracy. Since the OSA gives an output in terms of percentage reflectivity (as measured by the ellipsometer in the OSA), a calibration of percentage reflectivity vs. lubricant thickness was done using ZDOL disks with three different lubricant thicknesses (Figure 4.1) and the calibration constant was determined to be - 0.076%/nm. Sliders of two different ABS designs (CML pico-7nm and CML femto-3.5nm) as shown in Figure 2 were flown over disks with 1.2 nm of Zdol lubricant on the

OSA spinstand for 30 minutes. The linear velocities were 23.37 mps (7.2K rpm @ 31 mm) and 32.46 mps (10K rpm @ 31 mm) for the pico and femto sliders, respectively. The lubricant profile measurements were carried out in-situ. An acoustic emission sensor was used to detect slider-disk contact.

Scans were done after 0, 15 and 30 minutes for each slider-disk combination to confirm that the lubricant profile was reaching a steady state. A very high radial resolution (0.1 μ m) of scan on the OSA was used to measure the lubricant profile with sufficient accuracy. The angular resolution was 2048 points per track. Each scan furnished a two dimensional (radial x angular) reflectivity data. Averaging was done in the angular direction to obtain average percentage reflectivity as a function of radius. This was then converted into average lubricant thickness as a function of radius using the calibration curve. Multiple experiments were conducted for each slider design and the lubricant profile corresponding to maximum depletion was used in simulations for adding onto the slider ABS profile.

4.3 Simulations

4.3.1 Using lubricant profiles from experiments

The lubricant profiles obtained from experiments were used in the CMLAir static simulator to investigate changes in the slider flying attitude due to inclusion of the lubricant. The lubricant profile was mapped onto the existing grid on the slider made in CMLAir. Though the lubricant is on the disk, its profile was added to the slider profile and the disk was assumed flat (Figure 4.3). This was achieved by making suitable

changes to the software. The newer versions of CMLAir (version 6.55 and later) have a suitable User Defined Geometry (UDG) option, which can be used to add the lubricant profile to the slider. Since the UDG assumes that the grid points are regularly spaced, a regular (non-adaptive) grid of 289x289 was used for meshing. The lubricant profile was assumed to be uniform on the disk (Figure 4.5). Hence, adding of lubricant profile to the slider does not change the physics of the problem as the gap height between the slider and the disk remains constant at each grid point, whether the lubricant profile is added on the disk or the slider. Static simulations were carried out with and without adding the lubricant profile. The experimentally measured lubricant profile was assumed not to change due to ABS pressure.

4.3.2 Calculating the lubricant depletion profile

Using the 3-D Navier-Stokes equation, and setting the length scale in the thickness (Z) direction much less than in the lateral (X and Y) directions we can arrive at a lubricant thickness evolution equation considering lubricant flow due to ABS pressure as well as shear. Since the lubricant layer is molecularly thin there will also be velocity slip boundary conditions and existence of a Knudsen layer. Using a Couette flow profile due to shear and a Poiseuille flow profile due to pressure, we can arrive at the following continuum lubricant thickness evolution equation.

$$\frac{\partial h}{\partial t} = \frac{\partial(J_x)}{\partial x} + \frac{\partial(J_y)}{\partial y} \quad \dots \text{continuity equation} \quad (4.1)$$

where,

$$J_x = \frac{1}{\mu} \frac{\partial(p_{ABS} + p_{dis})}{\partial x} \left(\frac{h^3}{6} + \Phi \right) + \frac{\tau_x}{\mu} \left(\frac{h^2}{2} \right) \quad (4.2)$$

$$J_y = \frac{1}{\mu} \frac{\partial(p_{ABS} + P_{dis})}{\partial y} \left(\frac{h^3}{6} + \Phi \right) + \frac{\tau_y}{\mu} \left(\frac{h^2}{2} \right) \quad (4.3)$$

$$\Phi = (2 - \sigma_v) / \sigma_v * Kn \quad (4.4)$$

Here,

$h = h(x,y,t)$ = lubricant film thickness

J_x, J_y = flux in X and Y directions, respectively

μ = viscosity of the lubricant film (different from bulk viscosity [5] and strain-rate dependent, since the lubricant is a non-Newtonian fluid)

τ_x, τ_y = shear stress in the X and Y directions, respectively

σ_v = tangential momentum accommodation coefficient, and

Kn = Knudsen number

p_{dis} = disjoining pressure of the lubricant

p_{ABS} = airbearing pressure from CMLAir

From experimental evidence (Figure 4.5), we see that the lubricant depletion profile is almost uniform in the x (circumferential) direction. The non-uniformity seen is thought to be due to disk runout and other externalities. The profile such as in Figure 4.5 was seen when there was lubricant transfer to the slider or in some cases to some other part of the track, due to which the final lubricant volume was not equal to the initial lubricant volume in that part on the disk. However, after initial loss in lubricant volume, there was almost no lubricant transfer due so that the lubricant volume was conserved.

Thus Eq. (4.1) can still be applied to determine the steady-state solution. Under steady-state, the LHS of Eq. (4.1) is zero at every point (x,y) in the domain. Due to the uniformity of the lubricant profile in the angular direction, it is reasonable to assume that

there is no flow of lubricant in this direction in steady-state. Thus $\partial J_x / \partial x = 0$ and to satisfy the Eq. (4.1) we must require $\partial J_y / \partial y = 0$. For 0° skew, we have $\tau_y \approx 0$ which leaves us to satisfy $\partial(p_{ABS} + p_{dis}) / \partial y = 0$ in order to satisfy the steady-state condition. This is satisfied by $p_{dis} + p_{ABS} = Const$ and this was used to determine the steady-state lubricant depletion due to the flying slider under the above conditions.

The disjoining pressure p_{dis} , is defined as the negative gradient of the surface energy with respect to the film thickness [6],[7]. Since the lubricant on the disk is molecularly thin its surface energy is a strong function of its film thickness and the surface energy of the substrate below, which is the carbon overcoat (COC). Thus, the disjoining pressure is non-zero and significant, especially for our thickness range of the lubricant (0-2nm). Just as for the surface energy, the disjoining pressure has two components: dispersive and polar [7]. The dispersive component is a result of the van der Waals forces and the polar part is a result of polar interactions. The relations can be written as:

$$p_{dis}^d = -\frac{d\gamma^d}{dh} = \frac{A}{6\pi h^3}; \quad (5.5)$$

$$p_{dis}^p = -\frac{d\gamma^p}{dh} = -\frac{\left(\sum_{i=1}^k a_i h^i\right)}{dh} \quad (5.6)$$

where $(.)^d$ is the dispersive component, $(.)^p$ is the polar component and γ is the surface energy. It has been shown that the dispersive disjoining pressure can be written in terms of the film thickness h and the Hamaker constant A [6]-[8]. By comparison, there is no established relation between the polar component and the film thickness, and so a

polynomial fit (coefficients a_i) of the film thickness h is used to fit the experimentally measured polar surface energy [7].

Various studies have measured the total (dispersive + polar) surface energy/disjoining pressure of ZDOL. Fukuzawa et. al. [9] determined the disjoining pressure for PFPE 4000 using fabricated microgrooves (Figure 4.6 (a)). Waltman et. al. [10] determined the dispersive and polar surface energies of Zdol (Figure 4.7(a)), while Smallen et. al. [11] determined the total disjoining pressure of AM3001 as a function of lubricant thickness. Suitable curve fits to these experimentally measured disjoining pressures are shown in Figure 4.6(a) and Figure 4.8(a), and the resulting fit equations for dispersive and polar surface energies as shown in Figure 4.7(a-b) were differentiated to obtain the corresponding disjoining pressure (Figure 4.7(c)). The fits shown in Figure 4.6(a) and Figure 4.7(c) are henceforth referred to as models 1 and 2, respectively. Similarly, the fits corresponding to the thin line and thick line in Figure 4.8 (a) are referred to as models 3A and 3B respectively.

The pressure profile of the CML-7nm slider is used to illustrate the resultant lubricant profiles predicted by each surface energy measurement using $p_{dis} + p_{ABS} = Const$. The condition of volume conservation of the lubricant was not imposed while solving for lubricant depletion as it was not observed experimentally in the absence of lubricant modulation. A single curve fit for the disjoining pressure enabled us to obtain the film thickness h without an iterative procedure when models 1, 3A and 3B were used. However, an iterative procedure had to be used to obtain h with model 2. The resultant lubricant profiles for the cases of 1.0 nm and 2.0 nm lubricant thickness are shown next to each of the models (Figure 4.6-8). In all of the simulations

the disk is assumed to be smooth (no asperities and roughness) and no contact model was used.

As mentioned before, it was seen experimentally that the lubricant depletion profile was uniform in the circumferential direction in the absence of lubricant modulation (Figure 4.5). Hence, the lubricant profiles obtained from the above calculations were modified as shown in Figure 4.9 to closely resemble the experimentally observed ones. The peak pressures corresponding to the width (y) direction were dragged/extruded along the x-direction to form a pressure envelope since the high pressure areas along the slider width are assumed to be responsible for the lubricant depletion. The final lubricant profile obtained satisfies $\partial(p_{ABS(peak)} + p_{dis})/\partial y = 0$, where $p_{ABS(peak)}$ is the peak ABS pressure along the slider width.

4.3.3 Using calculated lubricant profiles

The lubricant profile obtained above was then added to the slider profile and static FH simulations were conducted. It was observed that there was a change in the pressure distribution due to the presence of the lubricant profile. The change in the pressure distribution in turn affects the lubricant profile, although the change is not very significant. In order to obtain the exact pressure and lubricant profiles an iterative procedure, as shown in Figure 4.10, was used. This procedure was tested for convergence, and Figure 4.11(a) and (b) show the convergence results for the CML Pico and Femto sliders, respectively, using model 2 to calculate the lubricant depletion. This simulation procedure was then used on the multiple ABS designs shown in Figure 12 to

study their effect on lubricant depletion and the change in their flying attitude due to the inclusion of the lubricant.

4.4 Results:

4.4.1 Experimental lubricant depletion profile

When the experiments were conducted to determine the lubricant depletion, lubricant modulation was observed in some cases. However, since this phenomenon is dynamic and cannot be modeled in static simulations, only the profiles which showed less or no modulations were considered for simulations. In the absence of modulations it was seen that the lubricant profile was uniform in the circumferential direction as shown in Figure 4.5 (the non-uniformity seen is thought to be an effect of disk runout). Hence, the lubricant profile was averaged in the circumferential direction without losing much information. Such averaged lubricant profile cross-sections have been plotted for CML femto and pico sliders in Figure 4.4(a) and (b), respectively. These profiles were obtained from OSA scans taken after 30 mins after the start of tests, when the lubricant had achieved steady-state depletion as there was not much change in the lubricant profiles between scans at 15 and 30 mins. It is seen from the Figure 4.4(a-b) that the lubricant depletion occurs primarily below the trailing pad where the airbearing pressure and shear are the maximum. These lubricant profiles were added to the corresponding slider profiles and simulations were carried out according to the procedure outlined in the previous section.

4.4.2 Numerical lubricant depletion profile

Different models were used for calculating the lubricant depletion profiles, and the results are shown in Figure 4.6-8. Further, the maximum and minimum height in each of the calculated lubricant profiles is shown in Table 4.1. In these simulations the CML Pico slider pressure profile was used. To simulate excessive lubricant depletion, we divided by 10 the slope of the disjoining pressure in model 3B, and the results are also included in Table 4.1 as model 3B/10. From the simulation procedure used it can be seen that the amount of lubricant depletion or buildup calculated by a model depends on the slope of disjoining pressure. From the table and the figures we see that model 1 overpredicts the lube buildup when thicker lubricant is used. This is because the slope of the corresponding disjoining pressure curve is very small as the lubricant thickness increases, which is always characteristic of a dispersive disjoining pressure. Hence, it is the polar disjoining pressure that restricts the lubricant buildup for higher lubricant thicknesses as shown by the model 2 results. We also note that the slope of the disjoining pressure in model 2 is not constant over all lubricant thicknesses unlike models 3A and 3B. It predicts more depletion for higher lubricant thicknesses (agrees with experiments), while 3A and 3B predict constant depletion. From these characteristics we conclude that model 2 is the most physical model. However, the lubricant height h has to be solved iteratively while using model 2 unlike for the other models, and thus it takes more computational time.

Further, the experiments were also done with Zdol 4000 lubricant which allowed direct comparison between experimental and numerical lubricant profiles (Figure 4.13). It is seen that the model overpredicted the lubricant depletion for the CML pico as well

as the femto designs. However, the experimental profiles show a wider valley compared to the calculated ones.

4.4.3 Comparison of flying attitudes with and without the inclusion of lubricant

Table 4.2 shows the flying attitude without the inclusion of lubricant (before) and with the inclusion of the experimental and calculated profiles. No significant change is seen in the flying attitude of the slider. This is primarily because of the small amount of lubricant depletion. To see the effect of a larger depletion in the flying attitude, we used model 3B/10 with various ABS designs (shown in Figure 4.12). The results are shown in Table 4.3. It is seen that under severe lubricant depletion the flying height drops by 0.1-0.2 nm. Further, the pitch increases slightly in four out of five cases. There is also an increase in pressure of as much as 0.52 atm in the case of the DSI femto slider, while the other designs display only a slight increase.

4.5 Discussion:

From the above experiments and simulations we find that the inclusion of the lubricant in static simulations yields only small changes in the flying characteristics of the slider. It should be noted that the modeling of lubricant depletion used in these simulations is too simplistic for explaining more complex slider-lubricant interactions. However, we see that the lubricant depletion obtained by simulations is of the same order of magnitude as the experimental data. The simple lubricant depletion model seems to fit certain experimental observations better (Figure 4.13(c)), while it is unable to explain others in which there is some lubricant buildup. The model also predicts that

the total steady-state lubricant depletion is a function of the peak ABS pressures, a statement which needs experimental validation.

We note that in equations (4.2-4.3), p_{dis} is a nonlinear function of h . This makes the Eq. (4.1) a non-linear conservative hyperbolic partial differential equation, which has to be solved using iterative schemes such as fixed point iterations or Newton's method and makes the calculation of the lubricant profile time intensive.

Other models for flow in thin films can also be used ([7],[12]) which yield different fluxes than that obtained by the continuum formulation (Eq. (4.2-4.3)). However, the nature of the partial differential equation obtained does not change, although the complexity may vary depending upon the type of nonlinearity introduced in the equation. For better modeling of the observed phenomena such as lubricant modulation these formulations may have to be used and some recent efforts for dynamic lubricant simulations are mentioned in Chapter 10.

Section II: Partial Contact Regime

4.6 Experiments

In this set of experiments a TTi spinstand was used to conduct touchdown-takeoff tests because the spindle rpm of this spinstand could be controlled very accurately. During each test the rpm of the disk was linearly decreased until the slider came into contact with the disk and it was increased again linearly and symmetrically until the slider ceased to be in contact with the disk. A detailed account of these tests can

be found in Chapter 2 and 3 ([13]-[14]). An AE sensor was used to detect the contact and a Laser Doppler Vibrometer (LDV) was used to monitor the slider dynamics.

Touchdown-takeoff tests are a controlled way to study partial contact since the duration of slider-disk contact is restricted to the time between the touchdown and takeoff. These tests were conducted on INSIC disks (rms roughness 0.2 nm) with SG lubricant with 50% bonded ratio.

The CML pico 7nm design slider was flown at 0° skew over disks with three different lubricant thicknesses (0.8nm, 1.2nm and 2.0nm). After the tests the disks were scanned by OSA to determine the change in the disk lubricant due to slider-disk contact. (The calibration constant for the SG lubricant was determined to be -0.063%/nm.)

4.7 Results:

By analyzing the experimental data it was found that slider in contact with the disk could cause lubricant depletion, buildup, redistribution or modulation. It was also seen that the depletion and buildup due to intermittent slider-disk contact was much more than what was observed in the case of no contact. This might be expected as the slider-lubricant interaction is much more intense during slider-disk contact as compared to when the slider is flying on the disk without contact.

Figure 4.14(a) shows a track on a disk with 2.0 nm lubricant on which a touchdown-takeoff test was conducted. The black boxes show the regions where angular averaging was done individually to obtain cross-sections as shown in Figure 4.14(b-*). In all these figures the OSA reflectivity data is shown on the left and the corresponding lubricant profile obtained from calibration is shown on the right. We notice that an increase in reflectivity corresponds to lubricant depletion, while a drop in reflectivity

corresponds to lubricant buildup. It is seen that the profiles are very different from each other even though they correspond to the same track. Such a pronounced difference is not seen in the non-contact case, and is a major difference between slider-lubricant interaction in non-contact vs. the partial contact regime. In the non-contact regime it was seen that the cross-section was fairly uniform for a particular track.

Upon close observation of the profiles in each of the cross-sections we also see the effect of the trailing pad and the side rails on the lubricant. In Figure 4.14(b-1) the trailing pad as well as both the side rails are seen to have caused lubricant depletion. There is also a small lubricant buildup near one edge of the trailing pad. Traversing through the rest of the figures in order, we see that there is also lubricant buildup due to the trailing pad and side rails.

The constant lubricant buildup near the trailing pad is thought to be an effect of slider roll as is explained later. Careful observation of Figure 4.14(b-2) shows a gentler depletion profile due the trailing pad on the side away from the lubricant buildup. Similarly, more depletion can be seen due to the side rail on the same side of lubricant buildup in (b-4). In (b-6), we also see lubricant buildup due to one side rail but lubricant depletion due to the other.

These observations can be explained by the physical model shown in Figure 4.15. Due to bouncing of the slider during intermittent contact depletion and buildup can occur. The bold arrows in subfigures (a), (b) and (c) show the direction of slider motion. Various small arrows in the lubricant film show the direction of lubricant flow in response to the slider motion. The profile on the right shows an estimated lubricant

profile due to the lubricant flow which matches well with the experimentally observed profile.

Figure 4.15(a) shows that when the slider is moving towards the disk and makes a contact the lubricant below the trailing pad and the side rails (low lying areas) is squeezed and moves laterally. It then accumulates in the pockets between the side rails and the trailing pad, causing lubricant buildup in these areas. Further, the effect of slider roll can also be seen. Due to the slider's roll one side of the trailing pad flies lower than the other. When slider-disk contact occurs the lower flying edge squeezes more lubricant causing a deeper ridge and a higher lubricant buildup. Such lubricant profiles can be seen in Figure 4.14(b-2,4 and 5).

In addition to lubricant depletion the trailing pad and the side rails also experience lubricant buildup. Figure 4.15(b) and (c) show two possible explanations of this phenomenon. Figure 4.15(b) shows the possibility of a meniscus bridging the slider and the disk as the slider moves farther from the disk after bouncing. Another possibility is that when the lubricant is squeezed due to the downward slider motion the lubricant also moves in the on-track direction in addition to the lateral direction. Immediately after the contact the slider moves upward without squeezing the newly formed lubricant buildup. This causes a lubricant buildup under the side rails and the trailing pad after the depletion, and it is also a possible mechanism for lubricant modulation, which was observed in addition to lubricant buildup and depletion.

Typically, substantial depletion was observed during severe slider-disk contact which could be inferred from the corresponding AE signal. However, when there was a very light contact (indicated by a slight increase in the magnitude of the AE signal from

the base noise level), lubricant modulation was observed. Figure 4.16 shows OSA scans (left) with the associated AE signal (right; purple and green correspond to AE and LDV signals respectively). It can be seen that the top two OSA scans show lubricant depletion/buildup with a clear increase in the AE signal during contact, while the bottom two OSA scans show lubricant modulation. As noted, we see a slight increase in the associated AE signal while the LDV signal does not show a sustained increase in slider dynamics, which does occur during severe contact. Thus this light contact does not influence the slider dynamics as much as a sustained contact.

Figure 4.17(a-c) show detailed images of such lubricant modulation for 0.8nm, 1.2nm and 2.0nm lubricant thickness disks. In all cases two distinct modulated tracks are seen and they correspond to the trailing edge of the slider. Light tracks were also seen corresponding to the side rails (not seen in Figure 4.17). From Figure 4.17(a-c) substantial lubricant depletion and buildup are seen in the modulation. The peak-to-peak difference was about 0.9nm for a 2.0nm disk (45%). Frequency analysis (FFT) of the lubricant modulation profiles was done and the results are shown in Figure 18. For the data acquisition of the lubricant profile using the OSA, the disk was rotating at a constant speed of 5000 rpm and the sampling frequency was 0.34 MHz. Hence the Nyquist frequency was 170 KHz. In all the FFTs, strong suspension modes were observed, which are between 1-20 KHz. The highest frequency seen is about 35KHz in Figure 4.18(a) and (c). Since the disk rpm was varied during the touchdown-takeoff tests, the rpm at which lubricant modulation occurred is unknown. Hence, it is difficult to determine which of the suspension modes correspond to the observed frequencies. If the modulation rpm is known, then the plotted frequencies could be scaled as:

$$f_{actual} = \frac{RPM_{modulation}}{RPM_{OSA}} \times f_{observed} \quad (7)$$

where, $RPM_{OSA} = 5000$, used for data acquisition of lubricant profile. Alternatively, if the observed frequency can be attributed to some particular modal frequency of the suspension, the modulation rpm can be determined.

Figure 4.19(a) and (b) show the LDV signal and its FFT during light slider-disk contact respectively. We see that only the suspension modes are dominant in the slider dynamics during bouncing as they have much smaller stiffness compared to the slider modes. The dominant frequencies seen are $\sim 77\text{Hz}$, 1.52KHz and 2.15 KHz . 1.52 KHz is the first bending mode of the suspension and matches well with FEM analysis [15]. The lowest mode corresponds to the disk runout and shifts with the disk rpm. Finally, 2.15 KHz is believed to be a bending mode as the high buildup peaks and depletion valleys (dark and golden bands, respectively) in Figure 4.17 under the trailing pad are in phase with each other indicating that the torsion mode of the suspension is not dominant.

4.8 Discussion:

By monitoring the condition of the disk lubricant while conducting touchdown-takeoff tests, we can obtain information about slider-lubricant interactions during partial contact. It is seen that these interactions are more severe than in the non-contact regime. The non-uniformity in lubricant profile along the track direction is also more pronounced in partial contact regime.

Modeling of slider-lubricant interactions during partial contact is challenging as it requires accurate modeling of the lubricant flow along with a good contact model to

predict the slider motion during partial contact and a dynamic slider-disk-suspension model to include the effect of suspension and disk dynamics along with the slider dynamics.

Lastly, it should be noted that although the lubricant is different than Zdol, it is expected that the qualitative results would translate to Zdol or other lubricants since the slider-lubricant interaction is much more intense during slider-disk contact as compared to when the slider is flying on the disk without contact. Because of this, the lubricant properties may not influence the interaction as much as they do in the case of no slider-disk contact. Also, the change in lubricant profile is expected to be more pronounced for untextured disks and for disks with more mobile lubricant since the lubricant can flow more easily in these cases.

4.9 Conclusions

In this chapter, we investigated the slider-lubricant interactions in non-contact and partial contact regimes. The main conclusions are as follows:

- (a) A method is presented to include the effect of lubricant in static ABS simulations. Lubricant depletion under a flying slider was measured using the OSA and also calculated using different disjoining pressure models. Inclusion of such lubricant depletion profiles in static simulations did not change the flying attitude of the slider appreciably. A case of severe lubricant depletion was examined and some change was seen in the slider flying attitude.
- (b) Study of slider-lubricant interactions in the partial contact regime is important as the slider flying height is reduced to achieve the goal of higher areal density. From the

experiments it was concluded that a slider in partial contact with the disk causes lubricant depletion, buildup, modulation or simply redistribution of the lubricant. The slider's trailing pad and side rails have an effect on lubricant depletion and buildup and so does the slider roll. Further, lubricant modulation occurs during light contact while lubricant buildup and depletion is seen when there is considerable slider-disk contact. The frequency analysis of lubricant modulation shows mainly suspension bending modes.

Model	1nm		2nm	
	Max (nm)	Min (nm)	Max (nm)	Min (nm)
1	1.05	0.7	2.8	0.8
2	1.25	0.85	2.02	1.72
3A	1.01	0.88	2.01	1.88
3B	1.02	0.82	2.02	1.82
3B/10	1.2	0	2.2	0.2

Table 4.1: Maximum and minimum lube height predicted by different models for original lube thicknesses of 1nm and 2nm.

		Nominal FH	Pitch	Roll	Peak pressure	Lube Height (below transducer)
		(nm)	(rad)	(rad)	(atm)	(nm)
CML	Before	5.250	289.468	-2.105	8.5243	1.2
Pico	Model2	5.246	289.478	-2.108	8.5243	0.9704
	Expt	5.241	289.453	-2.104	8.5246	1.13
CML	Before	5.930	286.789	5.437	14.1207	1.2
Femto	Model2	5.931	286.789	5.435	14.1213	0.8797
	Expt	5.920	286.671	5.408	14.1102	1.0368

Table 4.2: Comparison between static simulation results with and without the effect of lube depletion

		Nominal FH (nm)	Pitch (rad)	Roll (rad)	Peak pressure (atm)	Lube Height (below transducer) (nm)
CML Pico	Before	6.046	289.478	-2.108	8.5287	2
	After	5.861	289.555	-2.106	8.6767	1.3491
HD Pico	Before	14.752	125.549	1.809	20.6463	2
	After	14.608	125.021	1.821	20.6473	0
CML Femto	Before	6.730	286.789	5.437	14.1207	2
	After	6.628	285.663	5.419	14.3801	0.0393
DSI Femto	Before	8.080	214.798	-11.386	11.7261	2
	After	7.863	213.027	-11.297	12.1436	0.5072
HD Femto	Before	18.431	146.871	2.533	17.8183	2
	After	18.337	146.026	2.549	17.8005	0.1132

Table 4.3: Static simulation results for different ABS designs to show maximum effect of lube depletion on the flying attitude of the slider.

Section I: Non-contact Regime

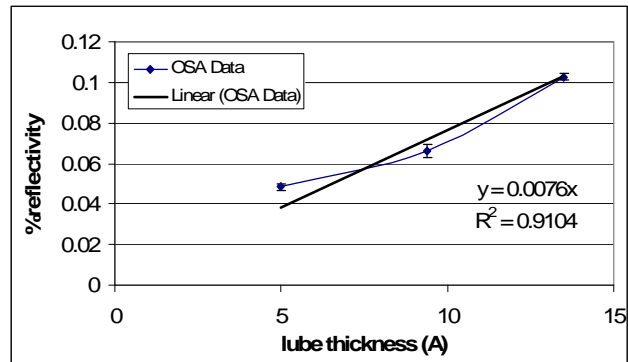


Figure 4.1: OSA Calibration for Zdol 4000

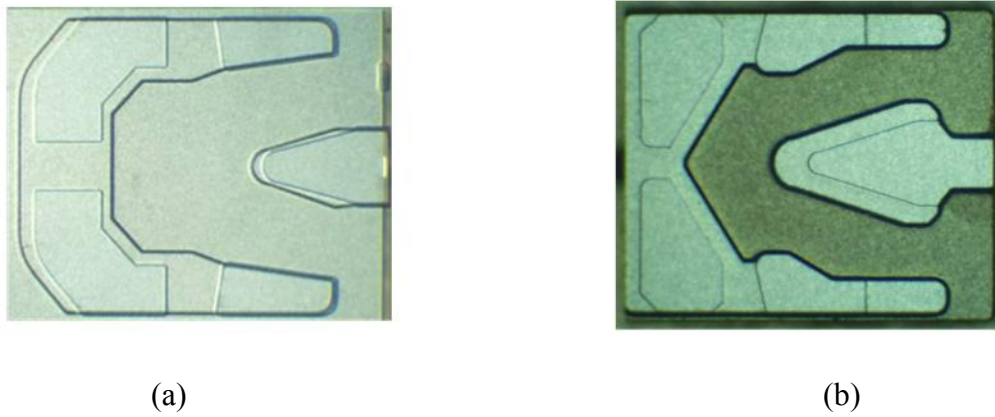


Figure 4.2: ABS designs used for experiments: (a) CML Pico 7nm; (b) CML Femto 3.5nm

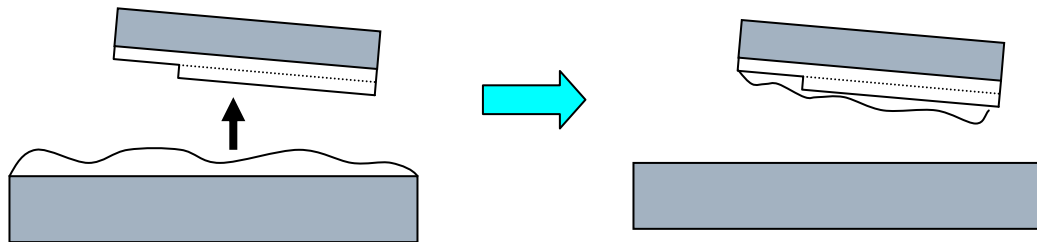


Figure 4.3: Adding the lube profile on the disk to the slider

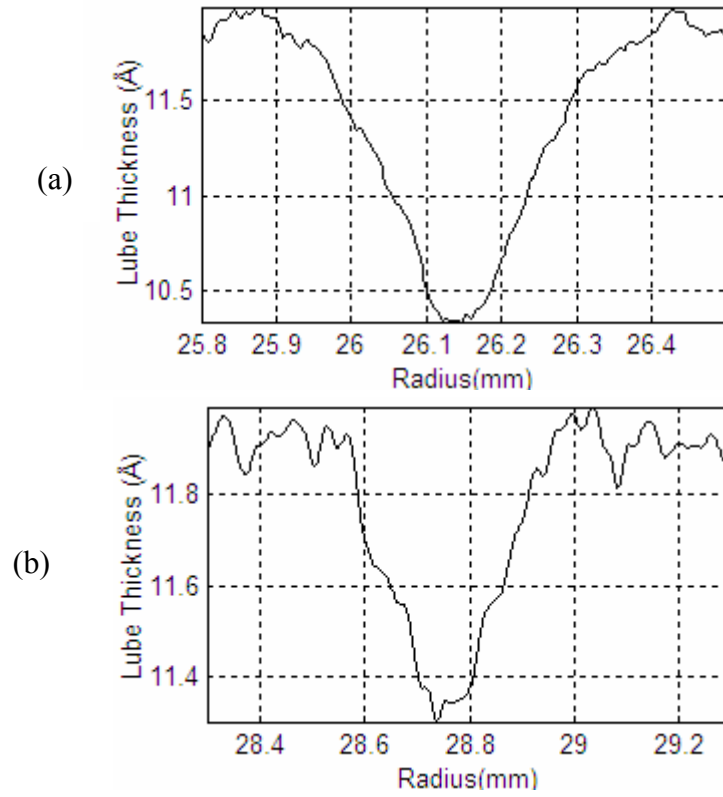
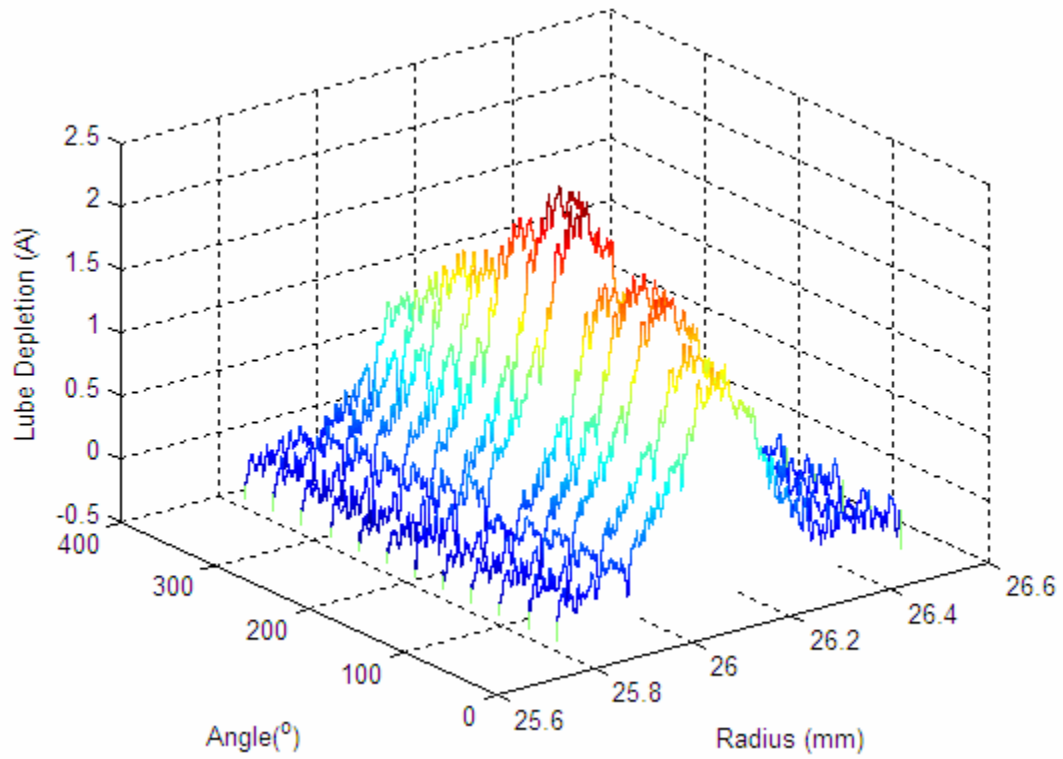
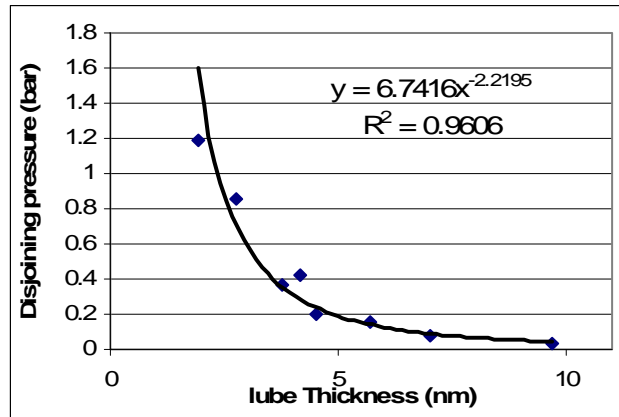


Figure 4.4: Experimentally measured lube profiles at 30 mins after smoothing for (a) CML Femto and (b)CML Pico slider. These profiles were used for static simulations

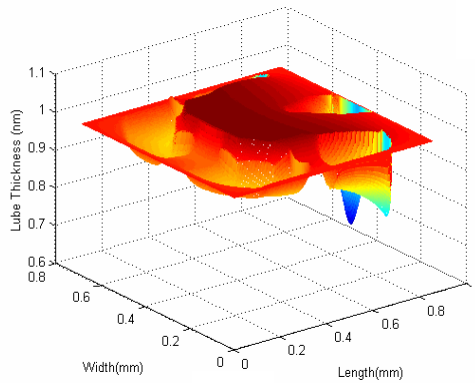


Mean (Peak Depletion) = 1.75 Å
 Stdev (Peak Depletion) = 0.39 Å

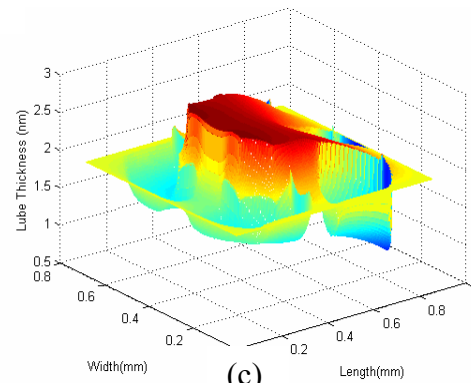
Figure 4.5: Waterfall plot of cross-section of lube profile at various angles along the circumferential direction for showing uniformity in lube depletion.



(a)



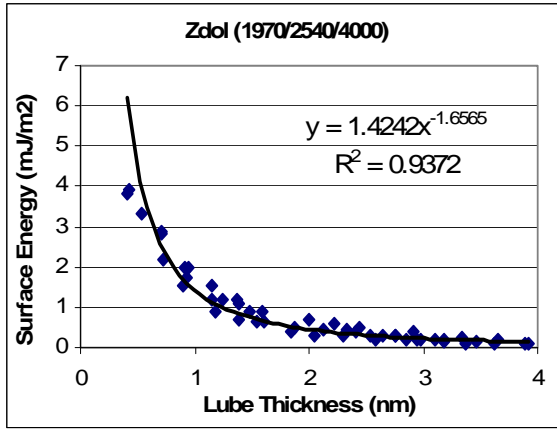
(b)



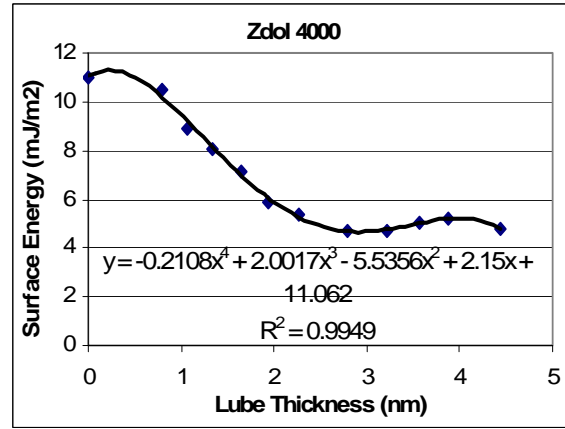
(c)

Figure 4.6: Model 1 used for predicting lube depletion: (a) Data fit to experimental measurements of disjoining pressure [9]; (b) Lube profile for 1nm thick lube with CML Pico slider; (c) Lube profile for 2nm thick lube with CML Pico slider

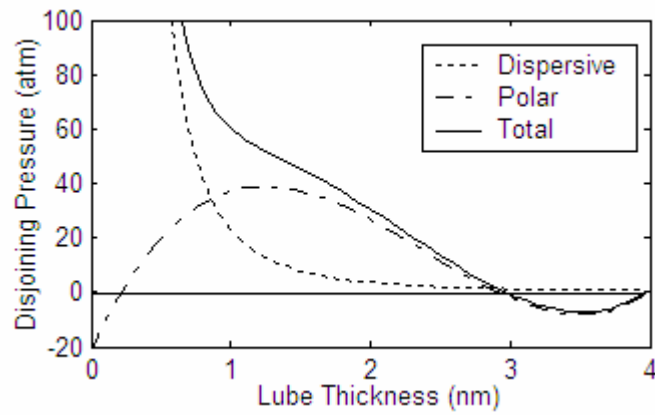
Note: CML Pico slider also used for lube profiles in Figures 8-10.



(a)



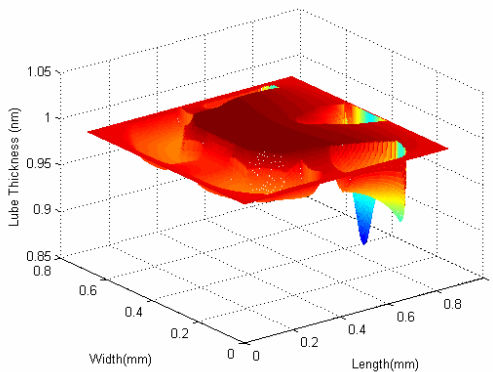
(b)



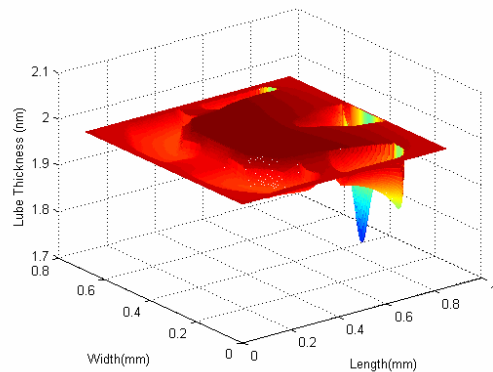
$$p_{dis}^d = 23.24 h^{-2.646} \text{ (atm)}$$

$$p_{dis}^p = 8.31 h^3 - 59.16 h^2 + 109.08 h - 21.1823 \text{ (atm)}$$

(c)

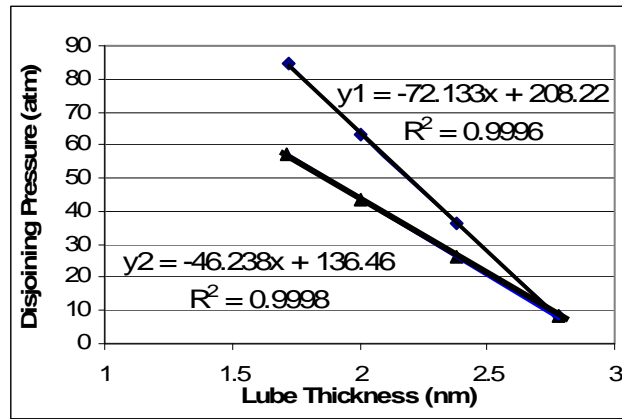


(d)

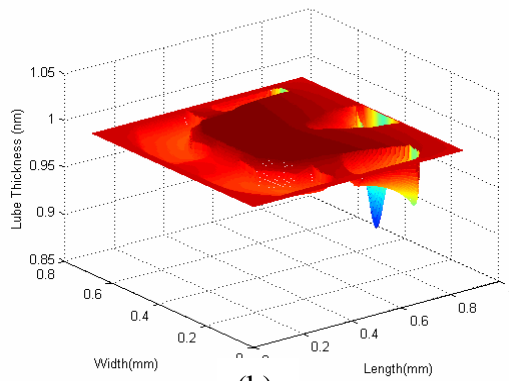


(e)

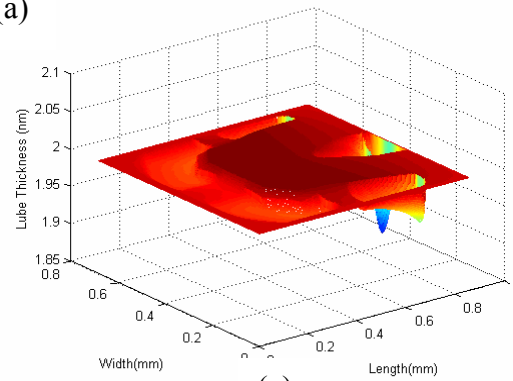
Figure 4.7: Model 2 used for predicting lube depletion: (a) Data fit to experimental measurements of dispersive surface energy [10]; (b) Data fit to experimental measurements of polar surface energy [10]; (c) Plot of polar, dispersive and total disjoining pressure using data fits obtained from (a) and (b); (d) Lube profile for 1nm thick lube; (e) Lube profile for 2nm thick lube



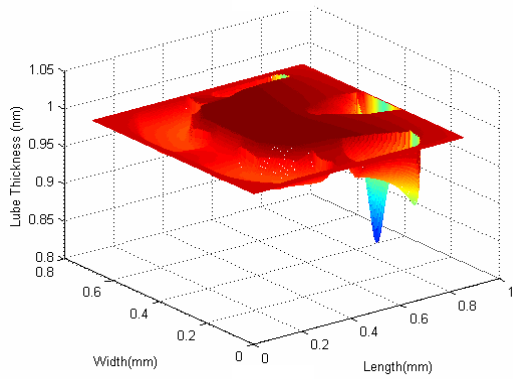
(a)



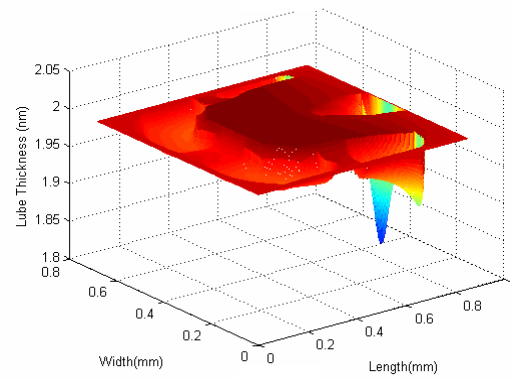
(b)



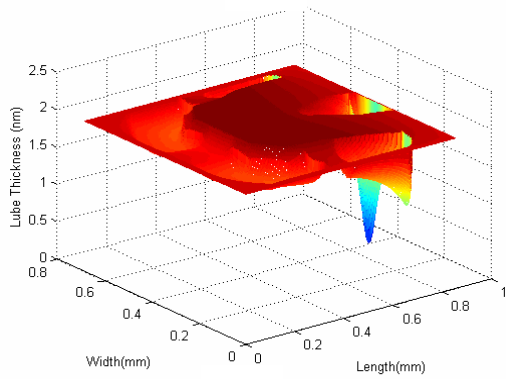
(c)



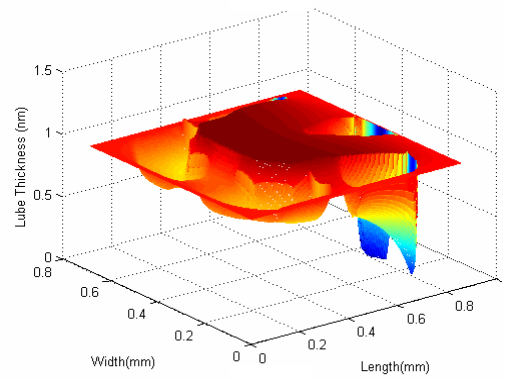
(d)



(e)



(f)



(g)

Figure 4.8: Model 3 used for predicting lube depletion: (a) Data fits to experimental measurements of disjoining pressure [11]. Black and blue lines correspond to models 3A and 3B respectively; (b) Lube profile for 1nm thick lube using model 3A (c) Lube profile for 2nm thick lube using model 3A; (d) Lube profile for 1nm thick lube using model 3B (e) Lube profile for 2nm thick lube using model 3B; (f) Lube profile for 1nm thick lube using model 3B/10; (g) Lube profile for 2nm thick lube using model 3B/10

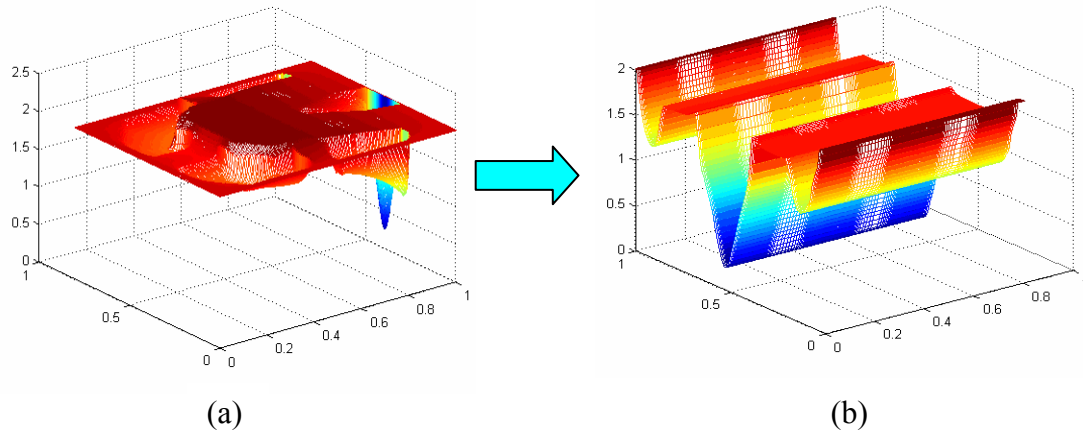


Figure 4.9: Extruding the lube profile: (a) Lube profile estimated by model 2; (b) Extruded lube profile added to slider profile for static simulations

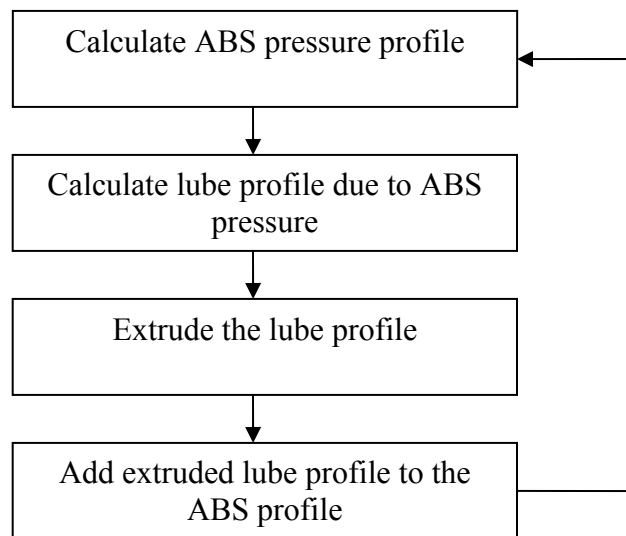


Figure 4.10: Algorithm for static simulations for inclusion of the effect of lube

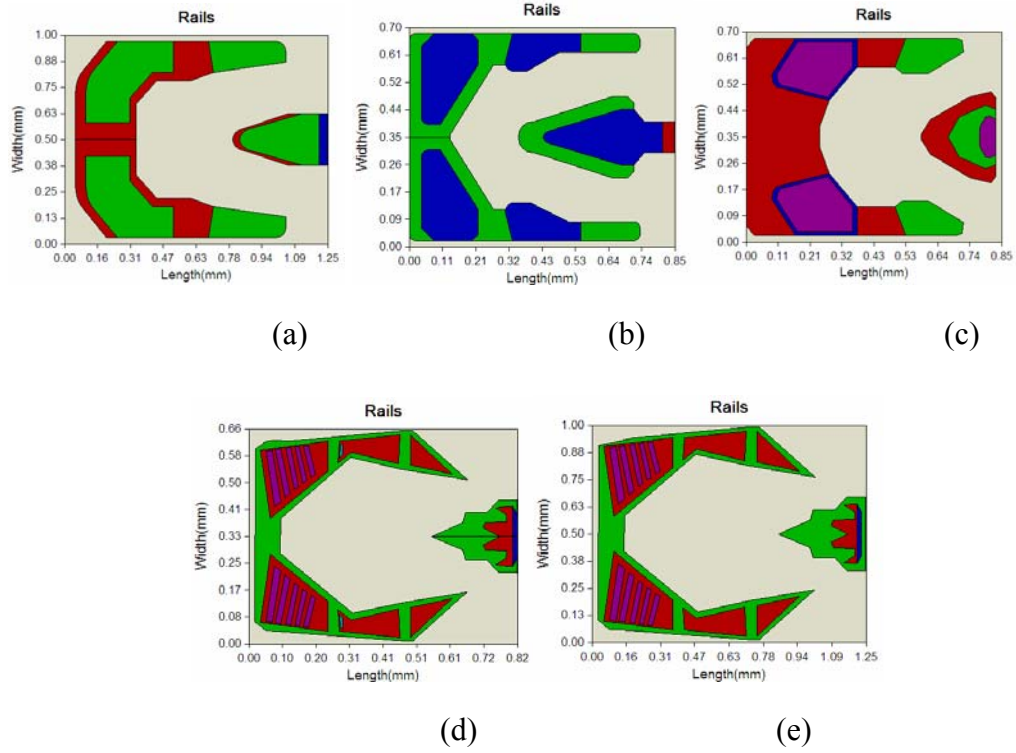


Figure 4.11: ABS designs used for simulations: (a) CML Pico; (b) CML Femto; (c) DSI Femto; (d) High Damped (HD) Pico; (e) HD Femto

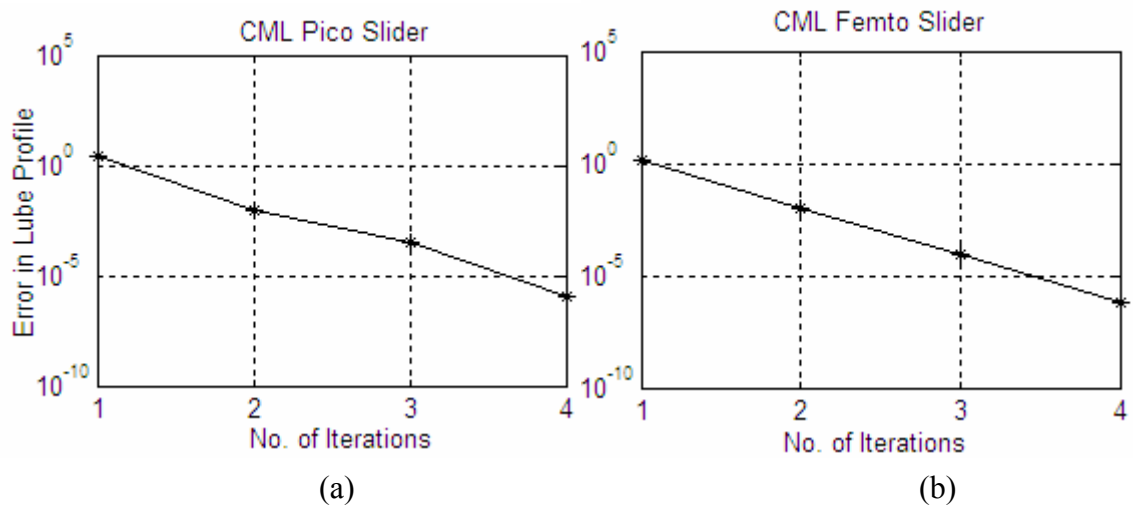


Figure 4.12: Convergence for simulation procedure outlined in Figure 4.10; (a) Convergence for CML Pico slider; (b) Convergence for CML Femto slider

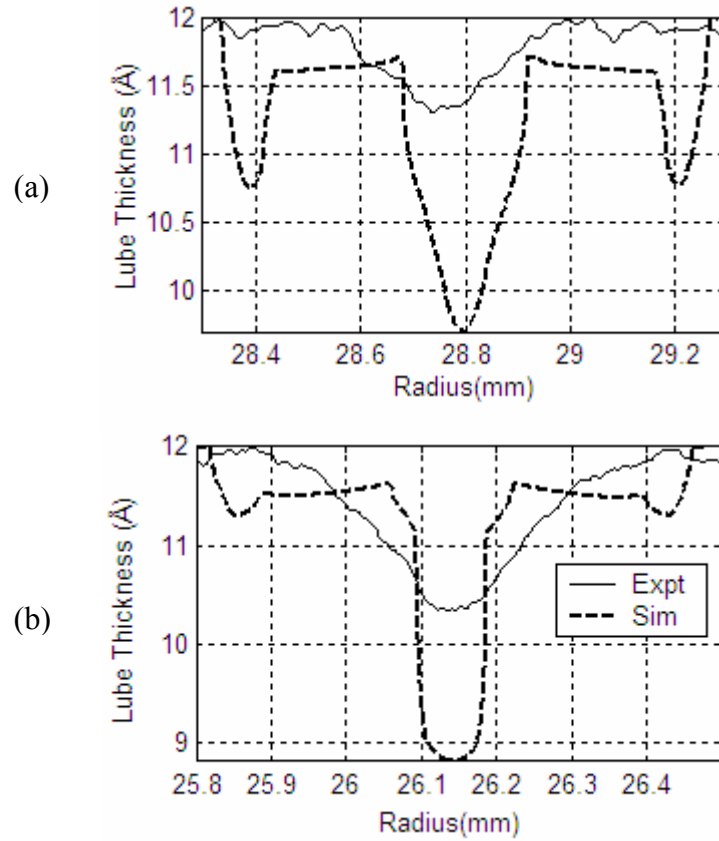
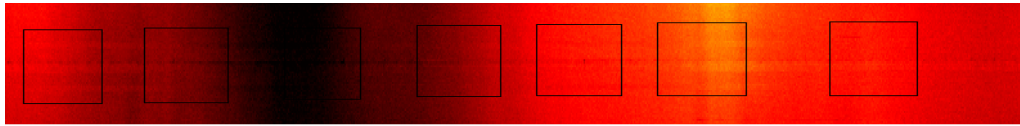
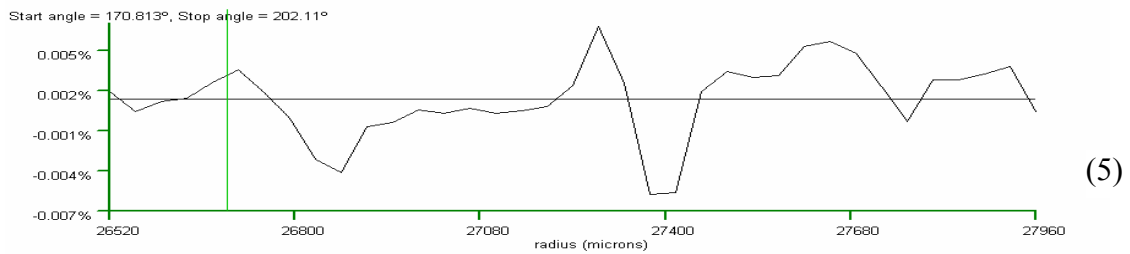
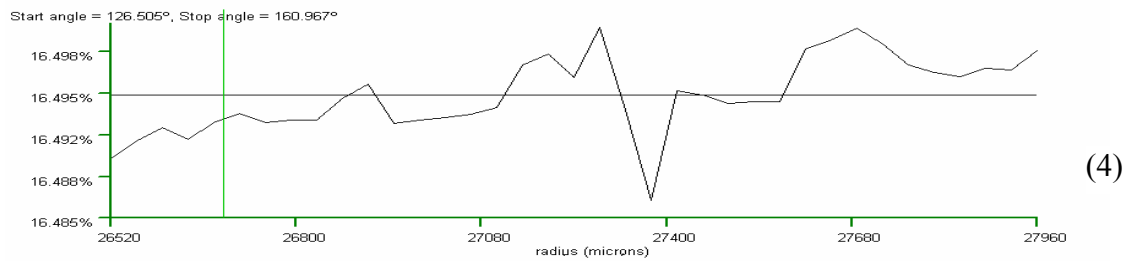
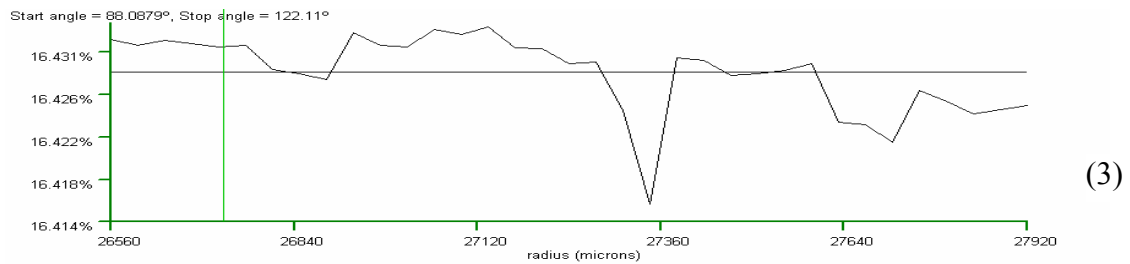
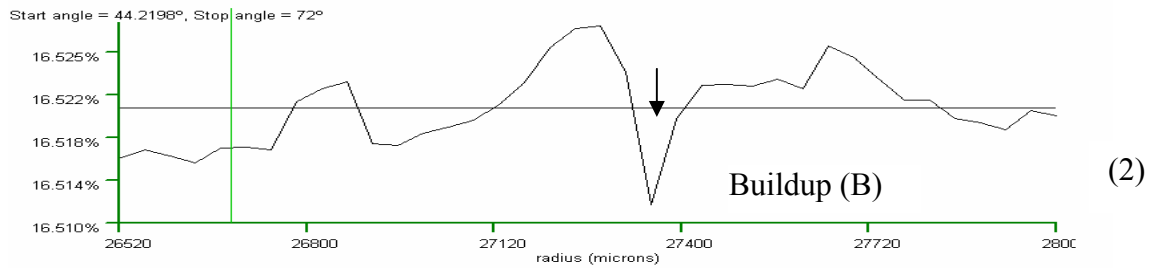
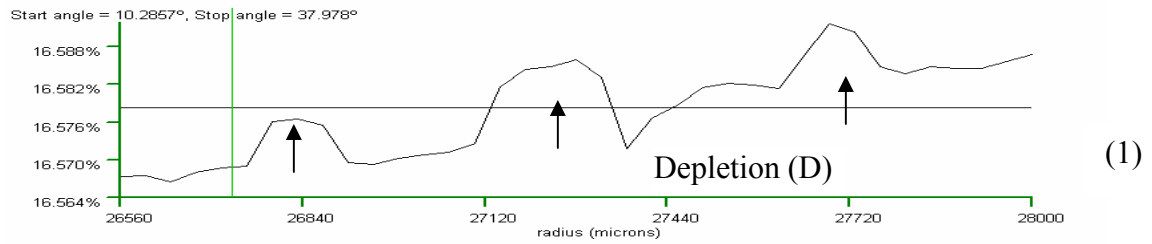


Figure 4.13: Comparison between experimental and numerical lube profile: (a) For CML pico slider ; (b) For CML Femto slider;

Section II: Partial Contact Regime



(a)



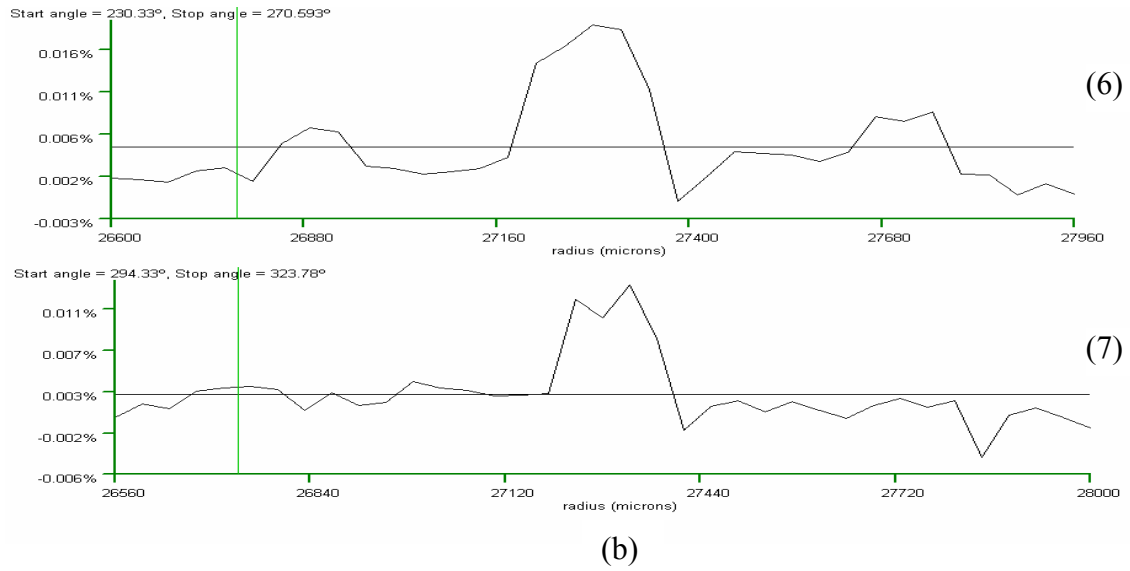


Figure 4.14: Lubricant profile as a result of slider-disk partial contact: (a) OSA scan of the experimental track; (b) Lubricant profiles corresponding to each of the black squares in (a).

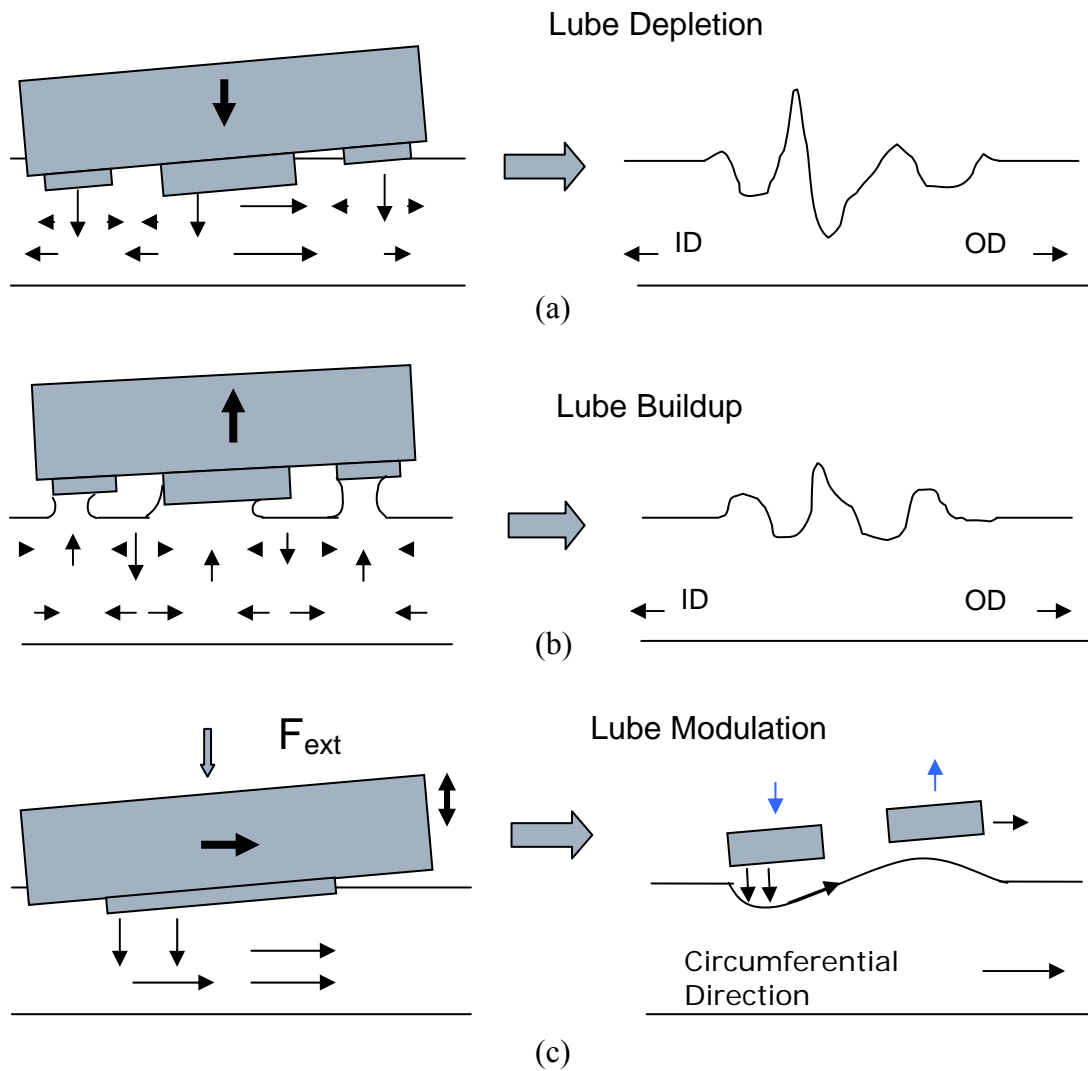


Figure 4.15: Physical explanation for experimentally observed lube profiles during slider-disk partial contact: (a) Lube depletion due to downward motion of the slider; (b) Lube buildup due to upward motion of the slider; (c) Lube modulation due to bouncing of the slider

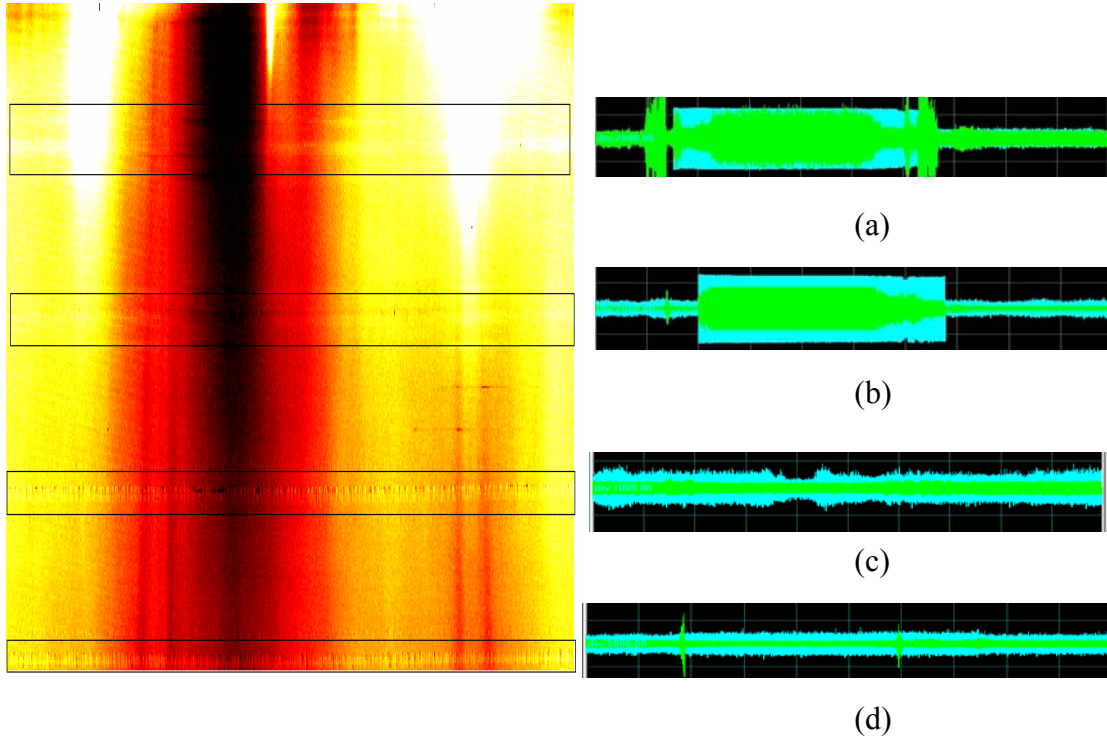
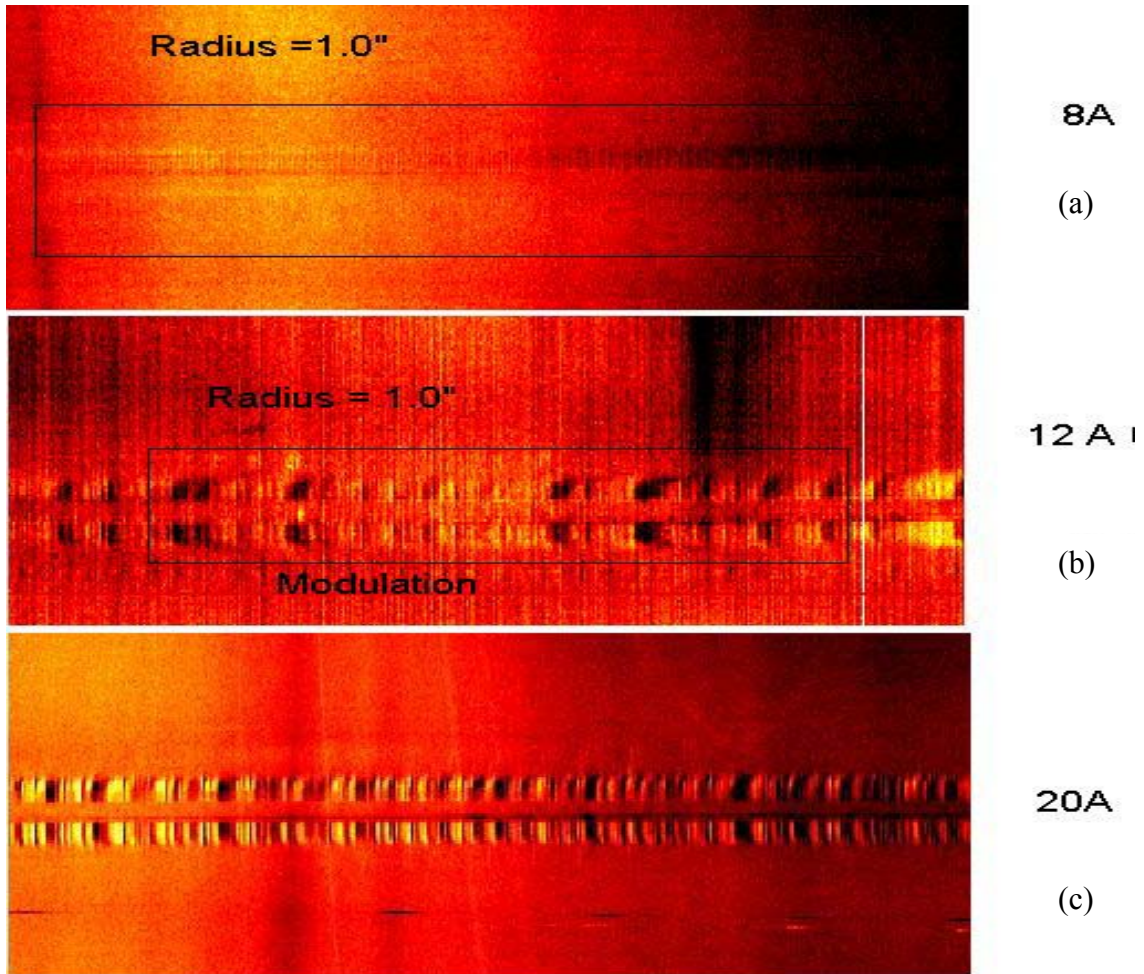


Figure 4.16: AE(blue) and LDV (green) signals with corresponding lube profile observed during experiments: (a) and (b) Lube depletion observed when substantial slider-disk contact; (c) and (d) Lube modulation observed when light slider-disk contact.



Dark bands in modulation correspond to lubricant buildup and light/golden bands correspond to lube depletion

8A: Max P-P buildup/depletion = 0.030% ~ 5 Å

12A: Max P-P buildup/depletion = 0.035% ~ 6 Å

20A: Max P-P buildup/depletion = 0.055% ~ 9 Å

Figure 4.17: Lube modulation under slider trailing pad observed for disks with different lube thicknesses

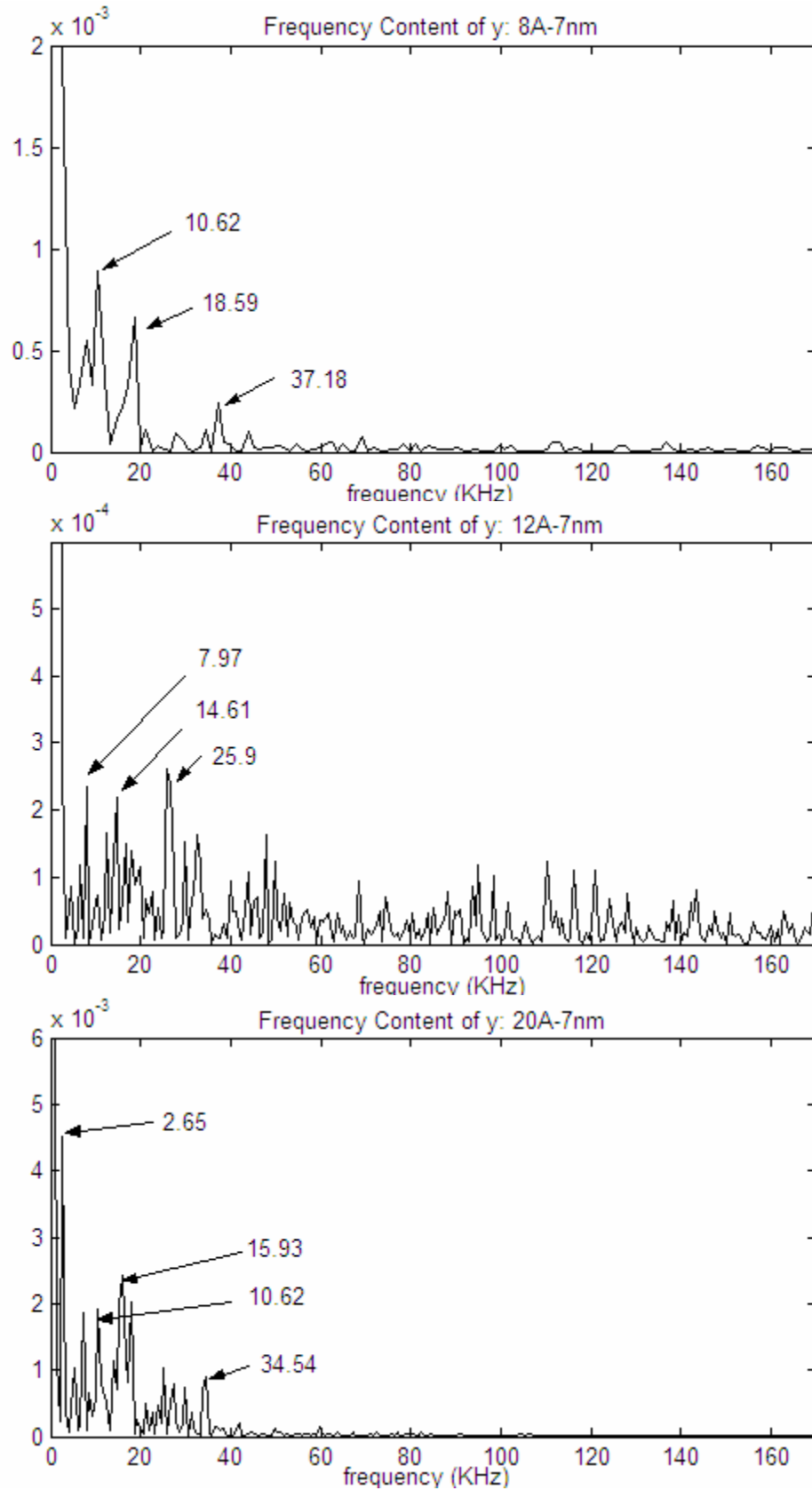


Figure 4.18: Frequency content of lube modulation for (a) 8Å; (b) 12Å and (c) 20Å disks

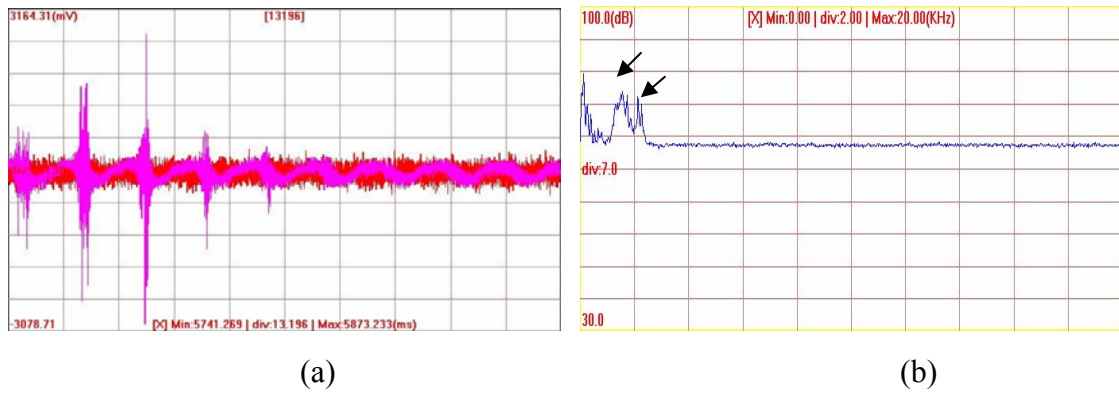


Figure 4.19: Slider dynamics corresponding to observed lube modulations: (a) Time history during light contact; (b) Frequency content during light contact

CHAPTER 5

LUBRICANT DEPLETION AND DISK-TO-SLIDER TRANSFER

5.1 Introduction:

As demonstrated in Chapter 3, lubricant pickup by the slider also substantially reduces the stability of the slider, and it also contributes to ABS contamination. During the lifetime operation of the drive this might become the most important factor affecting stability. The lubricant pickup is predominantly caused by disk-to-slider lubricant transfer (DSLTT), which also causes lubricant depletion on the disk. Retention of lubricant on the disk as well as reduction of lubricant pickup on the slider are critical for HDI reliability, and hence it is important to study DSLTT and its dependence on various parameters.

In the lubricant layer on the disk part of the lubricant is bonded while the remaining is mobile. The bonded fraction helps in providing a permanent cover on the DLC overcoat to reduce friction and corrosion. It also resists catastrophic failures during occasional slider-disk contact. The mobile fraction helps in replenishment of the lubricant at sites on the disk where lubricant depletion has occurred. The mobile fraction is also responsible for the DSLTT, which can be reduced by reducing the mobile fraction. However, it is known that the reliability of the HDI is greatly reduced by reduction in the mobile fraction, and it fails immediately in absence of any mobile lubricant. Hence, DSLTT is unavoidable, and it can be used favorably through proper design of the HDI, as it aids in quick replenishment of lubricant at the depleted sites.

Ma et. al. [1] showed that “negative” (sub-ambient) pressure sliders demonstrate DSLT using a half-delubed disk approach. Marchon et. al. [2] proposed a model based on the Langmuir equation of evaporation-condensation incorporating the airbearing shear force, and they studied the dependence of DSLT on lubricant thickness and molecular weight. Smallen et. al. [3] experimentally studied the dependence of DSLT on the lubricant disjoining pressure. They used the area of lubricant pickup on the slider as a metric for the amount of DSLT and concluded that the amount of lubricant pickup depends on the disjoining pressure and its slope. Since this method does not give the actual volume of transfer (some lubricant may also be sheared off behind the ABS, which is not accounted for) or an insight into the process of transfer, we used the half delubed disk method here to study DSLT.

When a slider is flown on a half delubed disk, the DSLT occurs in the lubed zone, while slider-to-disk lubricant transfer (SDLT) happens in the delubed zone (Figure 5.1). By calculating the volume of lubricant lost/gained by the lubed/delubed zones over time, the DSLT can be studied. In this chapter we describe the experimental investigation of DSLT and its dependence on three factors: lubricant thickness, lubricant type and ABS design. From the resulting quantitative data we arrive at a parametric model to describe the process of lubricant depletion and transfer and we compare the experimental data to the existing model by Marchon et. al.[2]. The study aims to enhance our understanding of this phenomenon and help in designing a better interface with reduced lubricant pickup by the slider and better retention of lubricant on the disk.

5.2 Experimental:

Three disks of different thicknesses of Zdol and Ztetrol were used in the experiments. Table 1 shows the total lubricant thickness for each type of disk along with the bonded and mobile fractions. These disks were half delubed using a delubing apparatus kept under a clean hood. The disks were lowered into a beaker of HFE-7100 solvent until they were half immersed. They were kept immersed for 10 minutes and were then pulled out smoothly and left exposed to the atmosphere for 2 minutes for the HFE to evaporate. The amount of time the disks were immersed was varied initially from 1 to 30 minutes. It was seen that the disk immersed for 5 minutes removed about 95% of the lubricant, if 100% was the amount of lubricant removed when the disk was immersed for 30 minutes. After the preparation of the half delubed disks, calibration of Candela OSA was done for Zdol and Ztetraol disks using half delubed disks of 3 different thicknesses with the results shown in Figure 5.2. As HFE removes only the mobile fraction of lubricant the mobile lubricant thickness was considered to be the same as the lubricant step height.

Subsequently lubricant transfer experiments were conducted on the Candela OSA. Two different femto slider designs, shown in Figure 5.3, were flown on a half delubed disk at constant linear velocity of 32.46 mps (10K@31mm) and the lubricant profiles were measured in-situ. Time histories of the lubricant profiles were obtained, which were further processed to obtain quantitative estimates of the amount of lubricant depleted from the lubed zone and the amount transferred to the delubed zone. Figure 4 outlines the steps in this post-processing, which was carried out using Matlab programs. After background subtraction and radial averaging in the lubed and the delubed zones

(Figure 5.4(a)), the resulting data was smoothed (Figure 5.4(b) and (c)) and the area under the profile corresponding to depletion or transfer was calculated (Figure 5.4(d)). Using a calibration constant of the lubricant and the radius of the track, the area calculated was converted into lubricant volume. Errors in volume calculations exist in this procedure due to the noisy data, radial averaging and post-processing. The errors due to the first two reasons cannot be estimated, but they are systematic errors and hence should be similar for all data. The errors due to post-processing were determined by repeatedly calculating the lubricant volume from the lubricant profile for a few data points. The error (6σ) in post-processing was less than $500\mu\text{m}^3$ (10%) for data close to $5000\mu\text{m}^3$ and decreased to about $200\mu\text{m}^3$ (20%) for data close to $1000\mu\text{m}^3$. Thus the absolute value of the errors decreased, but the percentage value increased.

5.3 Results and Discussion:

5.3.1 Dynamics of Lubricant Transfer

Experiments were conducted on Zdol disks with femto slider A (Figure 5.3 (a)) to study the dynamics of lubricant depletion and transfer. Figure 5.5(a) and (b) show the time history of lubricant depletion and transfer for disks with 13.5\AA of lubricant (mobile fraction). It is seen that the rate of depletion as well as transfer is high initially and gradually reduces. It should be noted that there is a difference between the volumes of lubricant depleted and transferred. This is plotted in Figure 5.5(c), and it was found to be most likely because the lubricant on the slider is sheared away by the airflow to deeper etches on the ABS behind the low flying areas and to the edge of the slider behind the trailing pad. It is seen from Figure 5.5(c) that the net lubricant depletion increases with

time before reaching a steady-state for the thickness of 13.5Å. On re-running the experiment on a disk with 9.4Å of lubricant without cleaning the slider used above, it was observed that there was very little net lubricant depletion (Figure 5.5(c)). This is because the net lubricant depletion had already reached a steady-state in the previous experiment and more lubricant accumulation in the already filled areas of the slider could not be supported. This shows that the lubricant loss due to air shear is bounded and only occurs until the recessing areas behind the trailing pad are filled with lubricant. Hence, in operation, it can be assumed that there is no lubricant loss due to air shear and there exists a balance of lubricant transfer between the slider and the disk (unless lubricant pooling occurs on the slider due to ABS design, which is discussed later).

Figure 5.6 shows the angular distribution of lubricant at various times. Figure 5.6(a) displays the raw data as obtained from the OSA, which shows a background low frequency noise due to disk runout. Hence the raw data was conditioned by subtracting the data obtained at 0 minutes, which gave the net change in the lubricant profile at various time instants, and an idealized lubricant step profile was assumed for 0 minutes as shown in Figure 5.6(b). From the profile at 1 minute (Figure 5.6(b)), we see more depletion at the start of the lubed zone and more transfer at the start of the delubed zone. Shearing of lubricant from the lubed zone to the delubed zone cannot explain this as it would predict more depletion at the end of the lubed zone. Thus, the depletion and transfer observed are a result of DSLT.

The observed angular distribution of the lubricant can be explained in the following way. Upon the start of the test there is not much lubricant on the slider. Hence, when the slider enters the lubed zone from the delubed zone it is in a ‘starved’ regime,

while the disk is in a ‘flooded’ regime. Due to this there is a high rate of lubricant transfer from the disk to the slider. As the slider proceeds through the lubed zone there is more lubricant transfer so the slider approaches the flooded regime. As the lubricant volume on the slider increases the rate of disk-to-slider transfer decreases. Once the slider crosses from the lubed zone to the delubed zone, the slider now is in the flooded regime and the disk is in the starved regime. Thus, a similar process as described previously follows, and there is net lubricant transfer from the slider to the disk. Further, as the lubricant volume on the slider decreases so does the rate of transfer. This explains why there is more transfer at the beginning of the delubed zone at 1 minute in Figure 5.6(b).

The above observations can be formulated into equations for DSLT. If the lubricant volume on the slider and the disk is normalized by the area where the lubricant transfer occurs, the equations can be written in terms of lubricant thickness on the slider and the disk. Figure 5.7 shows a schematic diagram of the lubricant transfer model. Let h_1 , h_2 and h_3 be the disk lubricant thickness, slider lubricant thickness and the lubricant thickness of the sheared-off lubricant on the slider, respectively. If the disk track is discretized and the slider is over node i , then $h_1(i)$ is the disk lubricant thickness below the slider. The simplest relation that can be arrived at from the above observations is one in which the rate of transfer depends on the difference of lubricant thicknesses on the slider and the disk. This is similar to the Langmuir equation, where the evaporation and condensation depend linearly on the concentration. Thus, we arrive at Eq. (5.1), which is the rate of lubricant transfer from the slider to the disk and K_1 is a constant of proportionality. The lubricant sheared off from the slider surface can be assumed to be a

function of h_2 (proportional to h_2^2 if Couette flow is assumed). Hence K_2 , the proportionality constant, is assumed to depend on h_2 . From the experiments we see that as the accumulation (h_3) increases, the rate of accumulation goes down until it becomes zero at a maximum allowable thickness h_3^0 . This yields Eq. (5.2). Finally, Eq. (5.3) represents the mass balance at the HDI.

$$\frac{dh_1(i)}{dt} = K_1(h_2 - h_1(i)) \quad (5.1)$$

$$\frac{dh_2}{dt} = K_1(h_1(i) - h_2) - K_2(h_2) \cdot (h_3^0 - h_3) \quad (5.2)$$

$$\frac{dh_3}{dt} = -\frac{dh_1(i)}{dt} - \frac{dh_2}{dt} \quad (5.3)$$

Neglecting the shearing of the lubricant behind the ABS, as it is only seen at the start and is negligible later, this is a linear system of equations and yields exponential solutions in time of the form $h(1 - e^{-t/\tau})$, where τ is a time constant. If we use such a solution to fit the lubricant depletion history in Figure 5.5(a) we find that only one time constant cannot produce an effective fit, since the rate of depletion is very high at the start. Hence, at least two time scales must be used. A short time scale corresponds to the initial transfer after which a longer time scale sets in. Using two time scales we obtain an effective fit as shown in Figure 5.8 along with the fit equation.

The higher initial transfer rate is believed to be due to a total lack of mobile lubricant in the delubed zone. Thus the disjoining pressure is very high in the delubed zone which facilitates the high slider-to-disk transfer rate (based on the evaporation-condensation model in [2] reproduced here in Eq. (5)). This also leads to a high disk-to-slider transfer rate in the lubed zone as a source of replenishment of the slider lubricant.

Once a small layer of mobile lubricant is formed in the delubed zone the disjoining pressure drastically reduces and so does the transfer rate. Figure 5.6(b) shows the angular distribution of lubricant from 1 to 100 minutes. It is seen that up until 3 minutes there is a large change in h_1 in the lubed and delubed zones. After 3 minutes, there is only a gradual change in h_1 .

If there is a local depletion on the disk during operation of the drive the rate of lubricant replenishment due to the slider is thus expected to be a function of the difference between the average disk lubricant thickness and that in the depleted zone. The higher rate of transfer in the case of total depletion may be responsible for avoiding critical failures in case of total lubricant depletion in some region of the disk.

Equations (5.1-5.3) were simulated using different constants, and the results are shown in Figure 5.9. Runge-Kutta methods of integration (from ODESuite in Matlab) took extremely long times for integration. Since the system of differential equations is linear ($K_2=0$), an implicit Euler method was then used for integration. Since this method is first order accurate as well as stable (hence convergent), reliable results are guaranteed for non-stiff problems, such as the current set of equations.

From the results in Figure 5.9, it is seen that the simulated results qualitatively satisfy the experimental observations of the angular profile as well as the depletion history. A low value of K_1 produced a relatively flat angular profile which matched the experimental observations similar to the lubed zone in Figure 5.6(b). A high value of K_1 produced steeper angular profiles, which matched better with the observations similar to the delubed zone (1 min) in Figure 5.6(b). Lastly, it should be noted that the system of

equations (5.1-5.3) is just a parametric system to understand the dynamics of DSLT, and hence it is not able to explain the observed results quantitatively.

Using the information about the rate of lubricant transferred during the experiments, we can estimate the average lubricant volume on the trailing pad. We assume that the same amount of lubricant is transferred during each rotation of the disk, and all of the lubricant collected on the slider in the lubed zone is transferred to the delubed zone in the first minute when there is no lubricant in the delubed zone. From Figure 5.5(a) we see that the actual lubricant volume transferred in the first minute is $1654\mu\text{m}^3$ for a disk lubricant thickness of 13\AA . The slider passed over the delubed zone 10,000 times in 1 minute (=rpm). Thus, the total lubricant volume transferred per revolution on the slider is estimated to be $1654\mu\text{m}^3/10^4 = 0.1654\mu\text{m}^3$. Further, the trailing pad area of the Femto A slider was determined to be 0.0122mm^2 from image analysis. Thus, the average lubricant thickness on the trailing pad is $0.1654\mu\text{m}^3/0.0122\text{mm}^2 = 0.013\text{nm} = 0.13\text{\AA}$. However, all of the trailing pad would not have been covered by the lubricant, only the low flying areas close to the trailing edge would be covered.

5.3.2 Dependence on Disk Lubricant Thickness

Experiments were conducted on disks with three different lubricant thicknesses of Zdol. The ABS design A was used, shown in Figure 5.2(a). The time histories of lubricant depletion, transfer and net depletion were recorded for 30 minutes for the various lubricant thicknesses and are shown in Figure 5.10(a), (b) and (c).

From Figure 5.10(a) and (b) we see that the rate of depletion and transfer was high initially and decreased later, as explained in the previous section. The net lubricant

depletion is plotted in Figure 5.10(c). It is seen that the net depletion is very close to zero except in case of the 13Å thickness. Since this was the first test conducted there was no lubricant accumulation behind the ABS prior to the test. Hence, the net lubricant depletion became negligible for the subsequent tests after there was enough lubricant accumulation behind the ABS due to air shear, which occurred in the 13Å case.

Figure 5.11(a) and (b) show the lubricant depletion and transfer volumes after 30 mins for various disk lubricant thicknesses for two instances of the same ABS design A along with the data fits. The relation between the disk lubricant thickness and the lubricant depletion/ transfer is observed to be monotonic and non-linear for Zdol. The monotonicity implies that there is more transfer and depletion for higher disk lubricant thickness. Thus, the slider lubricant thickness, which is responsible for the slider-to-disk transfer, is higher for higher disk lubricant thickness. This can aid in meniscus formation and reduction of stability of the slider.

Data fits were performed on the experimentally obtained depletion and transfer volumes in Figure 5.11(a) and (b) to explore their non-linear dependence on the disk lubricant thickness. Since no depletion or transfer is expected for 0Å of mobile lubricant thickness, data was extrapolated to obtain better fits. For four points, a cubic polynomial produced an exact fit for the transfer data as seen in Figure 5.11(a), while only a quadratic polynomial was sufficient to fit the depletion data in Figure 5.11(b).

The reason for the non-linear relation between the disk lubricant thickness and the lubricant depletion and transfer can be determined after identifying the factors that influence these processes. Through experimentation, it is demonstrated in Chapter 8 that DSLT depends on airbearing forces as well as molecular roughness and lubricant-carbon

adhesion and lubricant cohesion. By contrast, the SDLT mainly depends on lubricant evaporation/desorption energy. With increasing disk lubricant thickness the lubricant-carbon adhesion and lubricant cohesion decrease non-linearly leading to non-linear increase in DSLT. This increases the slider lubricant thickness. As the SDLT is an evaporation based process, we can use the lubricant transfer model based on evaporation-condensation [2] to explain its non-linear relationship with lubricant thickness. According to this model in [2] the lubricant condensation flux R_{evap} from slider-to-disk is given by

$$R_{evap} = P_0 \sqrt{\frac{M_n}{2\pi RT}} \cdot \exp\left(-\frac{\Pi(t_s)M_n}{\rho RT}\right) \quad (5.5)$$

where P_0 is the bulk vapor pressure, M_n is the molecular weight, R is the gas constant, T is the absolute temperature, and ρ is the lubricant density. $\Pi(t_s)$ is the disjoining pressure for the slider lubricant thickness t_s . From R_{evap} , the volume flux of lubricant from slider-to-disk can be calculated as $Q_{evap} = R_{evap} A/\rho$, where A is the cross-section area and ρ is the lubricant density. As $\Pi(t_s)$ decreases non-linearly with increasing t_s , it can be seen from the above formulation that Q_{evap} increases non-linearly with increasing t_s , which increases with increasing t_d .

Similar to Q_{evap} , Q_{cond} the condensation flux for disk-to-slider transfer is given by Eq. (5.5) with t_s replaced by t_d . Since disjoining pressure is an indicator of lubricant adhesion and cohesion, given constant airbearing forces, the condensation flux can be a good qualitative indicator of DSLT. Following the analysis in [2] and using the values given for various parameters therein, we plot the dependence of Q_{cond} on t_d in Figure 5.13 for ZDol 4000. It indicates the non-linear dependence of Q_{cond} on t_d . This qualitative

trend also holds for Q_{evap} and t_s . From the figure, we see three regimes: 0-6Å, 6-18Å and above 18Å. Below 6Å, the transfer rate is extremely small because of a very high dispersive disjoining pressure (Π^d). The polar disjoining pressure (Π^p) is small in this range for Zdol 4000. Between 6 and 18Å, Π^p is high and introduces almost a linearity in the transfer rate, which increases rapidly after 18Å due to low Π^d and Π^p .

Thus, if Zdol 4000 is used as a lubricant then the stability of the slider, associated with lubricant pickup, is expected to be best if the disk lubricant thickness t_d is below 6Å and worst if t_d is more than 18Å. Between 6-18Å, a linear decrease in stability is expected. In addition to lubricant properties, Π also depends on the surface energy of the DLC layer. Lowering the surface energy of the slider DLC by chemical modification or coating could lead to less lubricant pickup and hence better stability.

Certain anomalies were also observed in the depletion and transfer data (Figure 5.11(b)). In this figure we see that the lubricant transfer is more than the lubricant depletion in the 5Å Zdol case. Upon investigation it was discovered that the slider is capable of transferring the accumulated lubricant back to the disk at once, especially if the disk lubricant thickness is small. This is because the disjoining pressure is high for less lubricant on the disk and low for the accumulated lubricant on the slider causing large slider-to-disk transfer. This causes lubricant pooling on the particular track, which may be as high as 20Å as observed in one case, and then it diffuses with a diffusion time constant of several minutes. The lubricant pool may lead to meniscus formation and reduced flyability, and it can also result in magnetic spacing loss. Thus, the ABS should be designed to avoid excessive lubricant accumulation.

5.3.3 Dependence on Lubricant Type

Experiments were conducted on disks with three different lubricant thicknesses of Ztetraol, and the results were compared to the Zdol results. The depletion and transfer volumes after 30mins are plotted in Figure 5.14(a) and (b) for both lubricants. It is seen that for the same disk lubricant thickness the depletion and transfer volumes for Ztetraol are less than those for Zdol after considering the error (6σ) in post-processing of the OSA data to be $200\mu\text{m}^2$ for a calculated lubricant volume of about $1000\mu\text{m}^2$. The anomalous data in Figure 5.14(b) is a result of lubricant pooling, which was explained previously.

The difference in the observed rates of depletion and transfer for the two lubricants can be explained on the basis of the structures of Ztetraol and Zdol, as shown in Table 5.2. Ztetraol has four reactive -OH endgroups per chain as compared to Zdol, which has two. Because of this Ztetraol is known to bond stronger to the DLC than Zdol. This is also manifested in the higher viscosity [6] and lower mobility [6],[7] of Ztetraol even at lower molecular weights. Due to this increased adherence of Ztetraol to the substrate it is more difficult for it to transfer to the slider. Also, once Ztetraol is transferred to the slider, it is more difficult to transfer it back to the delubed zone on the disk due to its strong adherence. This can explain the lower depletion and transfer rates for Ztetraol. In addition to the lubricant type, the type of carbon overcoat also determines the bond strength between the lubricant and carbon layer. Hence, it is estimated that the type of carbon overcoat (CH_x , CN_x , etc.) will have an effect on the rate of lubricant transfer. Deoras et. al. [8] reported that Zdol 2000 and 4000 have lower mobility on a CN_x overcoat as compared to CH_x . Lower mobility, being an indicator of higher bond

strength between lubricant and carbon, implies that DSLT will be less for the CN_x overcoat.

5.3.4 Dependence on ABS Design

ABS design is perhaps the most critical component in the HDI design. Different recommendations have been made to achieve small spacings, better load-unload characteristics, less fly height modulation, etc. However, the lubricant performance is also extremely important to ensure reliability of the HDI. Therefore we investigated the dependence of DSLT on the ABS design.

In this set of experiments two different ABS designs, as shown in Figure 5.3(a) and (b), were used. A substantial difference in the amount of lubricant depletion was observed between the two sliders. Figure 5.15(a) and (b) plot the lubricant depletion and transfer for ZDol. A large difference between the depletion and transfer is seen in case of the Femto A. Such a pronounced difference between depletion and transfer is not observed for Femto B. When the ABS designs were observed under an optical microscope after the tests (Figure 5.16(a) and (b)), large lubricant accumulation was seen in the deep etched area behind the trailing pad in case of Femto A. Lubricant accumulation on the slider depletes lubricant on the disk and also causes loss in stability. Further, excessive lubricant accumulation can also lead to lubricant pooling on the disk. Thus, this is an undesirable characteristic of the ABS design, and it should be avoided.

The above observations can be explained on the basis of the mass flow lines from the static simulations of the ABS designs as shown in Figure 5.16(c) and (d). The massflow analysis is based on the velocity field given by a second- order slip model [9]. We experimentally verified that there was a good correlation between the lubricant

traces on the slider and the massflow lines at 70% of the spacing. In the case of Femto A it is seen that the mass is transported from over the sides of the trailing pad into the deep etches behind them. This results in a relatively large lubricant accumulation since the deep etches have a large area and depth. In case of Femto B, only a small area with a low etch-step exists behind the trailing pad. Therefore, it is able to hold much less lubricant and thus does not allow excessive lubricant accumulation. Thus, deep etches behind low flying areas need to be avoided in order to avoid lubricant accumulation on the slider. Designs such as Femto A may be currently attractive as they have less area close to the trailing edge due to which there will also be less influence of intermolecular forces. However, this may also cause excessive lubricant accumulation if the front of the trailing pad is designed as in Femto A. The reduction in area at proximity is achieved in Femto B by the introduction of a “sub-shallow etch step” [10] of 25 nm, the shape of which is such that excessive lubricant accumulation is avoided.

The above analysis only explains lubricant accumulation on the ABS, but it does not explain a more important observation, i.e. the large depletion in case of Femto A. Lubricant flow on the disk due to the slider depends on the airbearing pressure and shear stress and in the continuum formulation is given by equations (4.1-4.4) ([11]). This flow is expected to affect the DSLT. A higher pressure or shear may result in greater depletion and transfer. Static simulations were conducted for both ABS designs at 10K rpm at 31mm with 0° skew. The pressure profiles for both of the designs from these simulations are shown in Figure 5.17(a) and (b). The shear stress was also calculated based on the first order slip model according to Eq. (4) in [12], and it is plotted in Figure 5.17(c) and (d). Further, the total shear experienced by a point on the disk is an

integration of the shear stress along the length of the slider above that point, as the points on the slider along its entire length pass over that point on the disk. This calculated shear is plotted along the slider width in Figure 5.17(e) and (f) for Femto A and B, respectively.

From the pressure profiles of both ABS designs in Figure 5.17(a) and (b), it is observed that design A has a slightly higher peak pressure. While this certainly can lead to more depletion, it cannot explain the large difference in depletion observed between the two designs. Further, the difference in the gradient of pressure is also negligible and cannot be the reason for more depletion in case of Femto A. Due to the higher pitch and roll of design A, it is seen from Figure 5.17(e) and (f) that the shear in design A is actually less than design B. Thus, the pressure and shear profiles by themselves cannot explain the large difference in the depletion.

The only other parameter of the ABS design which is thought to affect the disk-to-slider lube transfer causing lube depletion on the disk is the negative pressure zone on the ABS. Ma et. al. [1] conducted experiments to compare lube interaction of catamaran (positive) and negative pressure sliders. They found that there was lube pickup and transfer by the negative pressure slider only, while the catamaran slider only displaced the lube on the lubed part of the disk. Hence they concluded that “negative pressure ABS may facilitate lubricant accumulation on the slider”[1].

The current ABS designs were characterized for their positive and negative forces using CMLAir software. Femto B was found to have, in fact, a greater negative force because it has a larger negative pressure area. However, the base etch for Femto A is $2.5\mu\text{m}$ while that for Femto B is $1.6\mu\text{m}$. This causes the peak negative pressure for

Femto A to be greater. In order to create a negative pressure area, all ABS designs have front pads followed by a deep etch (typically base etch). When the air enters the air-bearing from the leading edge, it undergoes sudden expansion when it reaches this deep etch, as shown in Figure 5.18, causing sub-ambient pressure. This also causes the air velocity to be finite in the Z (height) direction and is thought to assist the flow from the disk to the slider. It is noted here that the Reynolds' equation, which assumes negligible velocity in the Z-direction (hence two-dimensional equation) is not valid locally where there are large gradients in the Z-direction. Hence, it does not capture the Z-velocity accurately although some efforts have been made to estimate the Z-velocity from a combination of Reynolds' and the continuity equation [13]. To calculate the Z-velocity accurately, a full Navier-Stokes equation needs to be solved in the local zone. However, here we just estimate the Z-velocity (denoted by W) dependence on key ABS parameters. We assume the sudden expansion to be isothermal, i.e. the time scale of heat conduction is orders of magnitude smaller than the time scale for air expansion. Under such conditions, the rate of expansion and hence W is proportional to the expansion ratio and the disk velocity and inversely proportional to the lateral distance over which the expansion takes place, which in turn depends on the local wall angle α . Using the Buckingham II theorem in Fluid Mechanics and non-dimensionalizing variables, we get the dependence as indicated in Eq. (5).

$$\frac{W}{U} = f\left(\frac{h_1 + h_2}{h_1}, \alpha\right) \quad (5.5)$$

Here, h_1 is the spacing of point on inner edge of leading pad and h_2 is the etch depth of the recess, while U is the disk velocity.

It is noted that h_1 depends on the slider pitch. The slider attitude changes as the disk velocity U changes, changing h_1 and in turn the expansion ratio. Parameters h_2 and α are design parameters and remain constant. The etch depth h_2 is $1.5\mu\text{m}$ and $0.95\mu\text{m}$ for femto A and B, respectively. From AFM measurements, α was determined as 35° and 40° for femto A and B, respectively. With these measurements and simulated flying attitudes, the maximum expansion ratios for femto A and B are plotted in Figure 5.19. The ratio is seen to be less for femto A for high rpms, so even if the etch depth is more the fly heights are similar. This is due to a much higher pitch for femto A. As the rpm reduces, the pitch and fly height for femto A as well as femto B reduce and hence the expansion ratios increase. However, the pitch reduction is much faster for femto A due to which the expansion ratio for femto A increases faster than for femto B and is much more at lower rpms. We note that the actual sliders may have considerably different flying attitudes due to possible pitch and roll static attitudes (PSA and RSA). Hence, if femto A is assumed to have the same attitude as femto B, the expansion ratio is much greater for femto A for all rpms, as plotted in Figure 5.19.

These results indicate that lubricant pickup by the sliders due to sub-ambient pressure zone is expected to increase with reducing rpm as the expansion ratios increase. Also, assuming that the actual flying attitude of femto A is slightly different, it is possible that its maximum expansion ratio is more than that for femto B and this can be one of the major reasons for the increased lubricant pickup for femto A. In such a case, the longer trailing pad of femto A can also be responsible for increased lubricant pickup as a longer trailing pad with low slider pitch increases the total shear experienced by lubricant [14]. Further, the slider roughness can also play a significant role, but is not

considered here since the roughnesses are assumed to be comparable as the sliders were manufactured from the same batch of wafers.

Although more experimental data involving more ABS designs is needed to determine which of the above factor(s) is/are dominant, from the above analysis we can also prescribe some recommendations for ABS parameters to reduce the DSLT and accumulation:

(a) To reduce the expansion ratio, higher pitch angle and lower recess depth are helpful.

It is also noted that typically a small reduction in the base recess depth does not change the pressure profile significantly although it might change with altitude, skew and other sensitivities. We also estimate that gentler wall profiles of ABS features near the expansion zone can be useful in reducing the DSLT.

(b) To reduce airbearing shear of the lubricant, higher pitch angle and shorter length of the trailing pad are recommended [14].

(c) To prevent accumulation of lubricant, avoiding stagnation zones in massflow is recommended.

Further experimental investigation was carried out for both designs by monitoring the lubricant depletion and transfer after 5 minutes for each design at a particular fly height. The fly height of the sliders was varied by changing the rpm, which was reduced until the sliders went into contact with the disk. The AE sensor was set to a high gain to accurately monitor contact. The LDV was used to monitor the slider dynamics to determine if there was any change in the slider dynamics in the event of light contact not detected by AE.

When these experiments were conducted on the Zdol disks for each ABS design from a high rpm to low rpm, it was found that almost no lubricant depletion/transfer occurred at high rpm. The depletion/transfer rate did not increase significantly as the rpm was lowered to a point where there was a sudden increase in the depletion and transfer rates. This behavior was demonstrated by both ABS designs. There was no change in the root mean square (RMS) level of AE signal until at a much lower rpm where the slider went into contact (touchdown rpm). When the rpm is lowered beyond this point the depletion and transfer rates are expected to remain high and keep increasing with decreasing rpm due to the reduction in fly height as well as the pitch and roll.

Figure 5.20(a) and (b) show the lubricant depletion volume after 5 minutes for designs A and B, respectively, using a bar plot. The RMS AE signal is also plotted along with the depletion volume. From these figures is seen a “critical” rpm at which the rate of lubricant transfer is high and above which the rate is small. Further, the corresponding AE signal shows no change at the critical rpm, indicating no contact of the slider with the disk at that rpm. The FFT of the slider dynamics at various rpms is shown in Figure 5.21, where it is seen that the frequency content of the slider dynamics did not change until there was slider-disk contact, which was also detected by AE. (The contact slider dynamics were not recorded for the Femto A slider due to severe slider-disk contact.) Thus, AE and LDV measurements confirm that there is no physical slider-disk contact at the critical rpm leading to a higher transfer rate. (Even a light contact of the slider with the lubricant is detected by an AE sensor.) This implies that the observed DSLT occurs without contact.

The touchdown rpm corresponds to the glide height of the disk, which was 3.5 nm on the disks used in the experiments. By means of static simulations (radius= 26 mm used for experiments), the change in the flying attitude was calculated as a function of rpm. From this we can calculate the minimum fly height of the sliders as a function of rpm. This is plotted in Figure 5.22(a). The fly height corresponding to the critical rpm can be considered as the critical flying height for the lubricant transfer from disk to the slider. The difference between the critical flying height and the glide height is defined as the critical clearance. More experimental and theoretical analysis of critical clearance is done in the next chapter.

It is seen that this critical clearance is higher for design A ($6.95 - 3.5 = 3.45$ nm) than B ($4.12 - 3.5 = 0.62$ nm). Thus, slider B can fly lower without causing large lubricant depletion and therefore has a better reliability. The existence of a critical clearance also explains the large difference in the depletion occurring with designs A and B as the lubricant depletion and transfer volumes plotted in Figure 5.15 correspond to an rpm of 12.1K @26 mm (=10K@31mm). This rpm is clearly above the critical rpm of design B, but it is lower than the critical rpm of design A. Thus we observe high depletion for design A and low depletion for design B.

Figure 5.23(a) and (b) show the OSA scans of depletion and transfer above and below the critical rpm respectively for design A. Similar scans are shown in Figure 5.23(c) and (d) for design B. The golden color corresponds to lubricant depletion while the black color corresponds to lubricant accumulation. A large amount of depletion and transfer is seen below the critical rpm for both of the designs on the track corresponding to the location of the trailing pad.

From the experiments we conclude that the rate of DSLT from the lubed part of the disk as well as the rate of SDLT to the delubed part of the disk is dependent on the head-disk clearance. The rates are expected to increase as the clearance decreases. This has not been included in the evaporation-condensation model in [5], and it is a direction for future work.

5.4 Conclusions

In this chapter we experimentally and numerically investigated the process of DSLT using a half-delubed disk and a parametric model based on the experimental results. We also compared some of the experimental results with a physical model based on evaporation-condensation. Further, the dependence on DSLT on the disk lubricant thickness, lubricant type and the slider ABS design was investigated. From the study we conclude the following:

- (a) Substantial DSLT can occur without slider-disk contact and more than one timescale can be associated with the transfer. While DSLT aids in lubricant replenishment in areas where lubricant depletion occurs, it also leads to lubricant pickup by the slider leading to meniscus forces and contamination at the HDI causing reduced stability.
- (b) The DSLT increases non-linearly with increasing disk lubricant thickness, and this can be explained on the basis of disjoining pressure of the lubricant.
- (c) The DSLT depends on the type of lubricant used and is less for Ztetraol than for Zdol. This is because Ztetraol adheres more strongly to the substrate than Zdol.
- (d) The DSLT also depends on the ABS design. The sudden expansion of air in the sub-ambient pressure zone under the slider can be one of the factors. High pitch, lower

base etch and gentler wall profiles in the sub-ambient pressure zone can reduce the transfer. Further, high pitch and shorter length of trailing pad can reduce the total airbearing shear on the lubricant, possibly reducing transfer.

- (e) Certain ABS features can lead to excessive lubricant accumulation on the slider. This in turn leads to lubricant pooling on the disk as the slider is capable of transferring some of the accumulated lubricant back to the disk. Lubricant pooling on the disk is undesirable as it can lead to magnetic spacing loss as well as a reduction in stability.
- (f) Good correlation exists between the lubricant traces on the slider and the 70% spacing massflow lines, which are calculated in CMLAir based on velocity field given by second-order slip model. The stagnation zones in the massflow field correspond to the lubricant accumulation zones. Thus, the ABS features causing larger stagnation zones should be avoided.
- (g) A critical clearance exists for each ABS design at which the transfer rate is high and above which the transfer rate is small. For better lubricant performance the ABS should be designed such that this critical clearance is as small as possible, i.e. the critical rpm is as close to the touchdown rpm as possible.

	Bonded (Å)	Mobile (Å)	Total (Å)
Zdol	2.9	5.0	7.9
	2.9	9.4	12.3
	3	13.5	16.5
Ztetraol	5.8	2.2	7.9
	5.9	5.1	11.0
	8.1	5.9	14.0

Table 5.1: Lubricant thicknesses of various disks used for experiments

Zdol	$\text{HO-CH}_2\text{CF}_2[(\text{OCF}_2\text{CF}_2)_p(\text{OCF}_2)_q]\text{OCF}_2\text{CH}_2\text{-OH}$
Ztetraol	$\begin{array}{c} \text{HO-CH}_2\text{CHCH}_2\text{OCH}_2\text{CF}_2[(\text{OCF}_2\text{CF}_2)_p(\text{OCF}_2)_q]\text{OCF}_2\text{CH}_2\text{CHCH}_2\text{-OH} \\ \qquad \qquad \qquad \\ \text{OH} \qquad \qquad \qquad \text{OH} \end{array}$

Table 5.2: Chemical structures of Zdol and Ztetraol

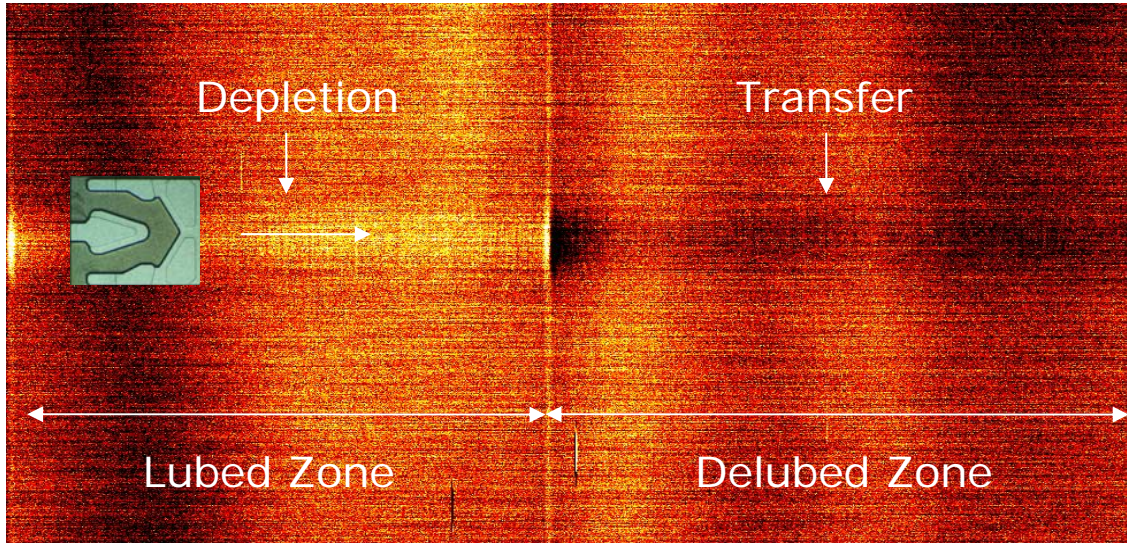


Figure 5.1: OSA trace showing depletion and transfer in lubed and delubed zones respectively

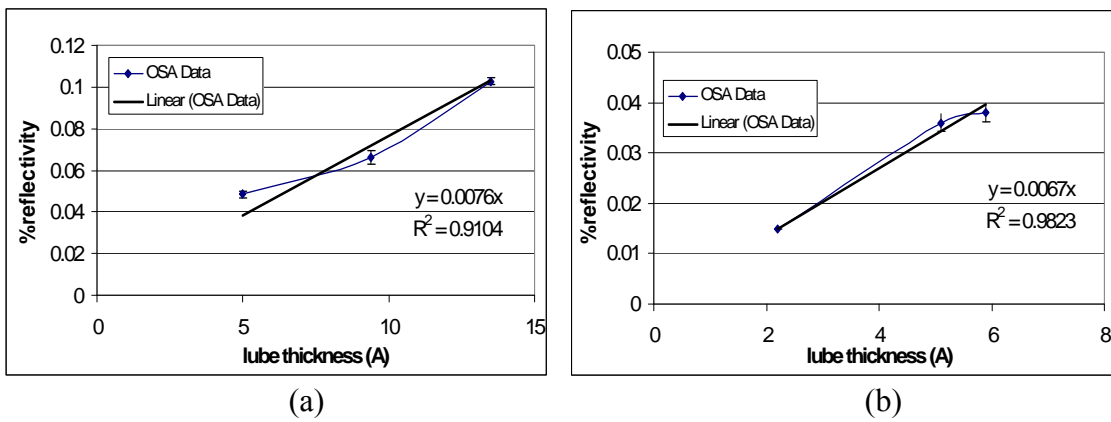


Figure 5.2: OSA Calibration: (a) Zdol and (b) Ztetrol

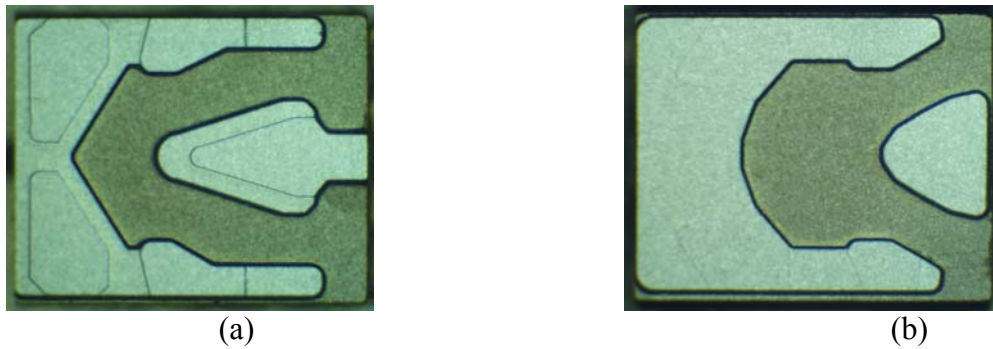


Figure 5.3: ABS designs used for experiments: (a) Femto A; (b) Femto B

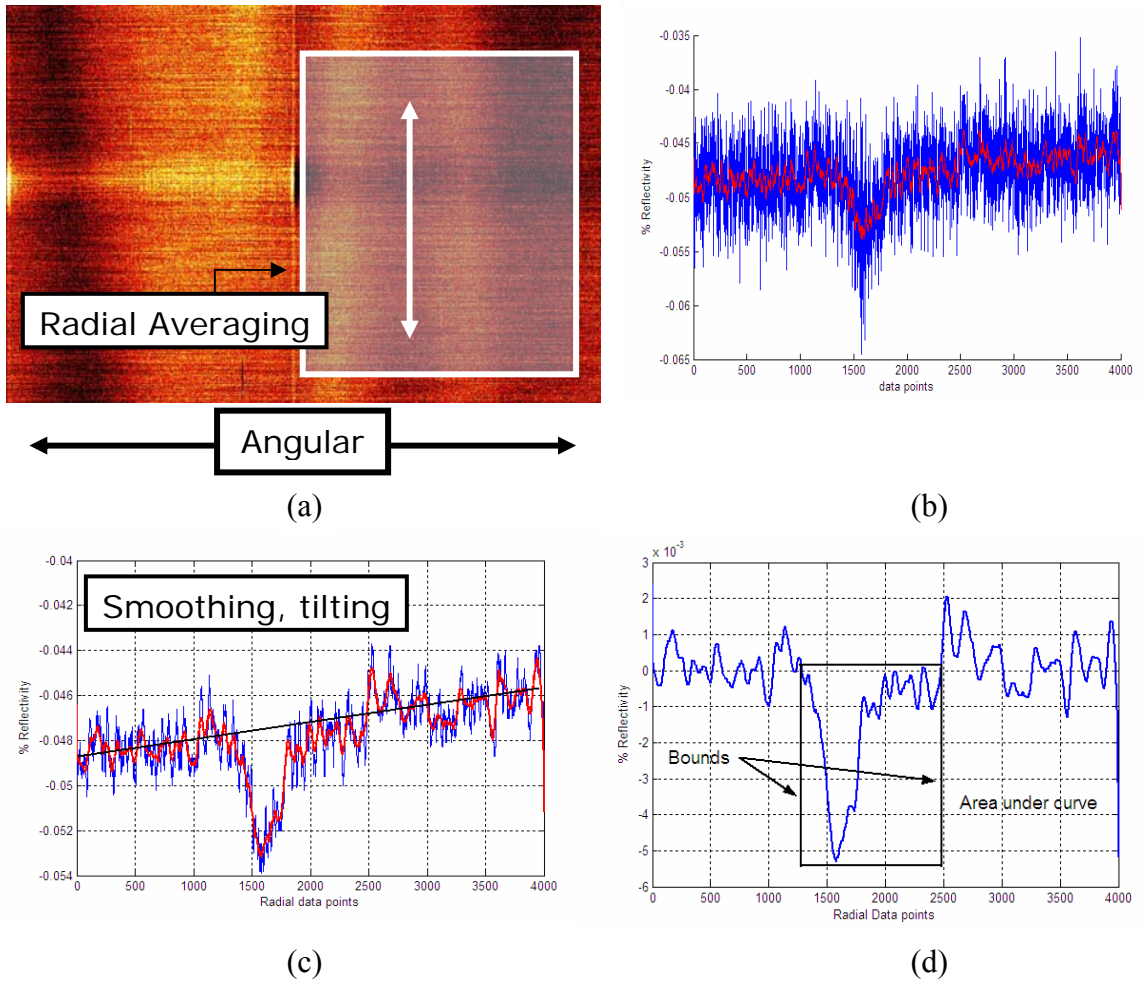


Figure 5.4: Successive operations on the OSA trace to obtain lubricant transfer volume: (a) Radial averaging to OSA trace; (b) Filtering the data (blue) obtained from (a) to get smooth data (red); (c) Further smoothing and changing the background reflectivity to zero by tilting; (d) Integrating area under the reflectivity curve

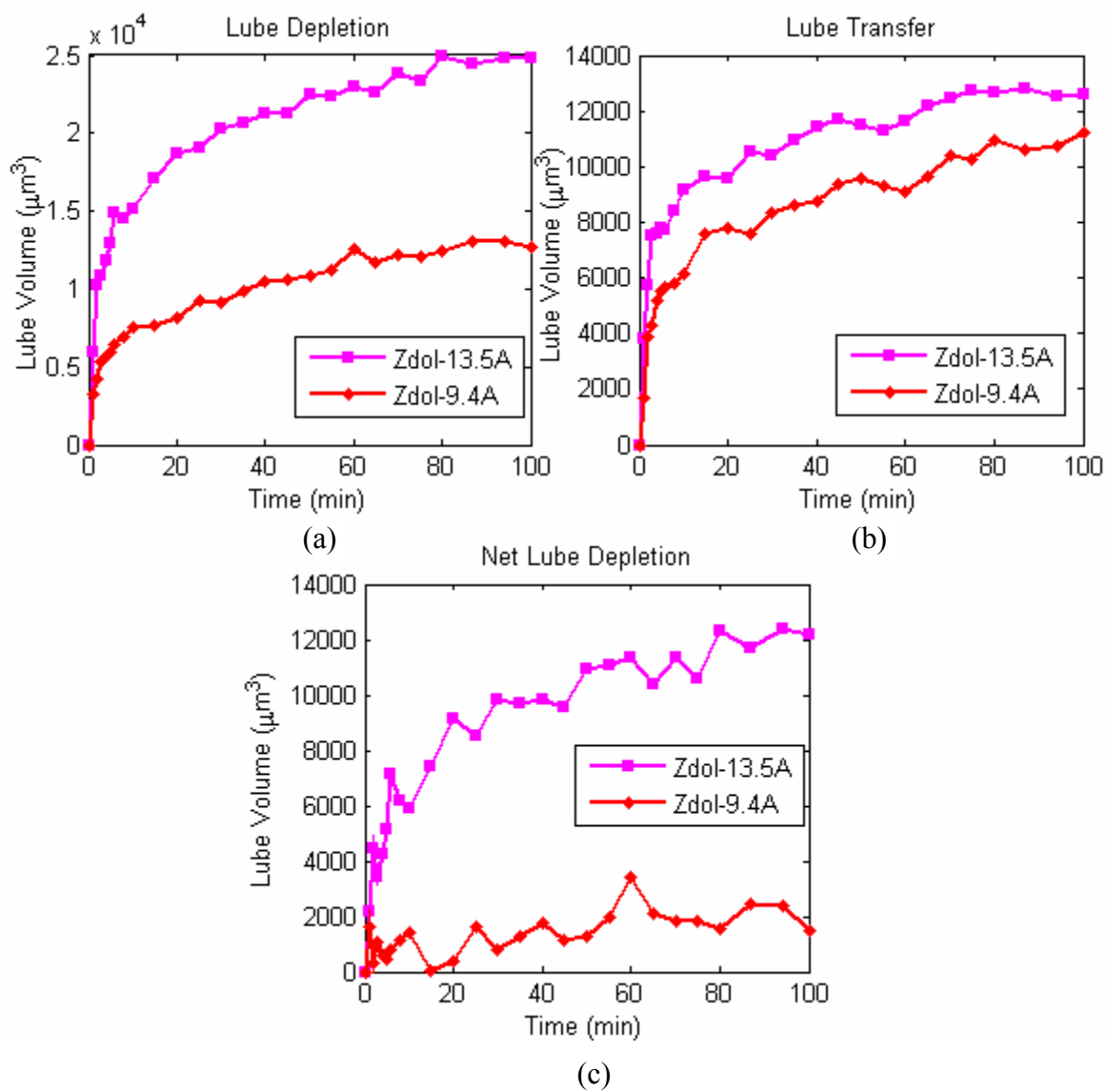
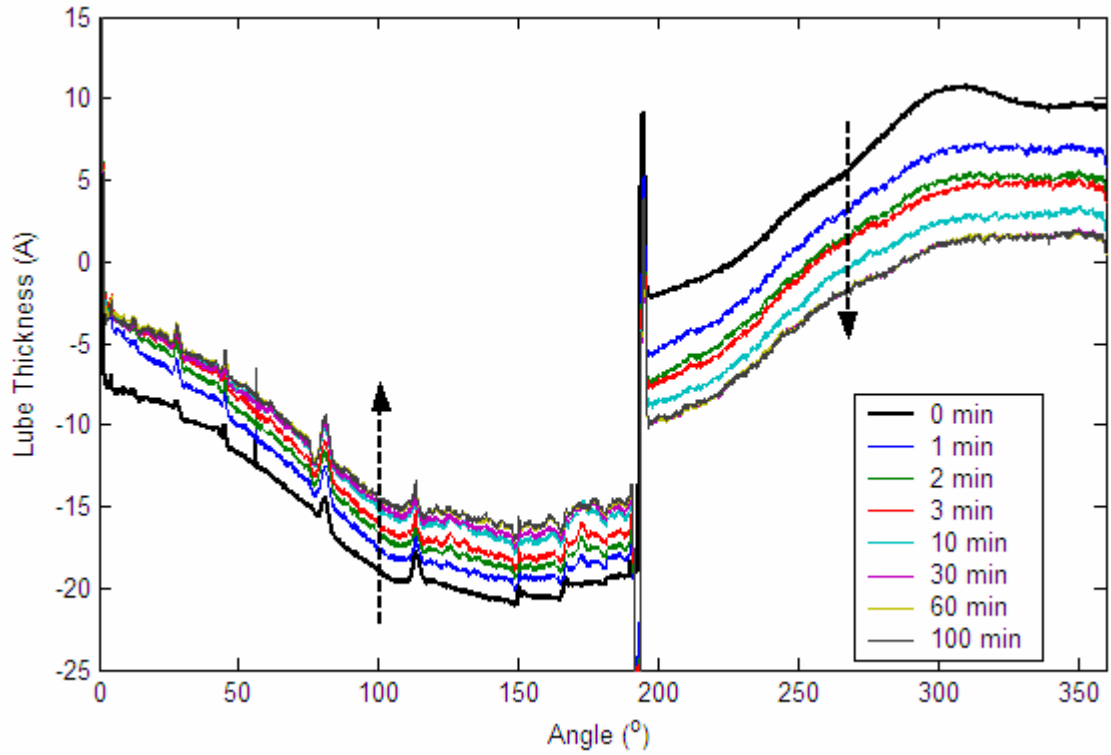
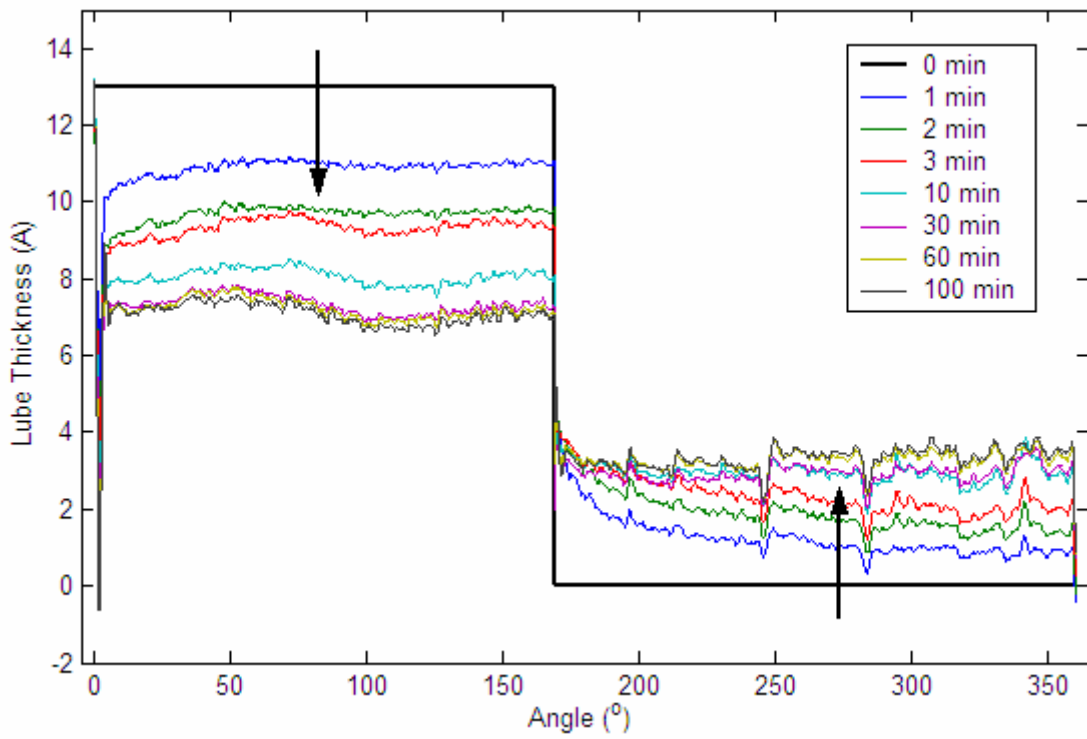


Figure 5.5: Time history of (a) Lubricant depletion volume; (b) Lubricant transfer volume; (c) Net depletion volume for Femto A with Zdol lubricant



(a)



(b)

Figure 5.6: Angular distribution of the lubricant (a) Original data from OSA; (b) Conditioned data of (a)

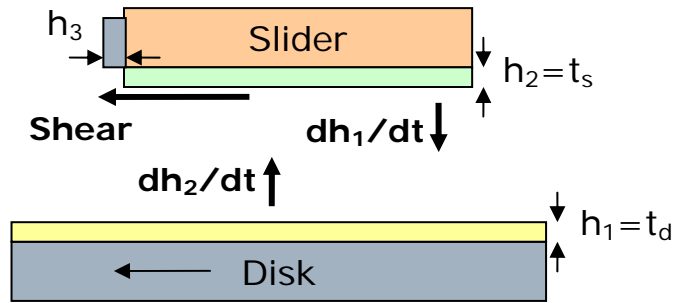


Figure 5.7: Schematic of lubricant flow between the slider and the disk

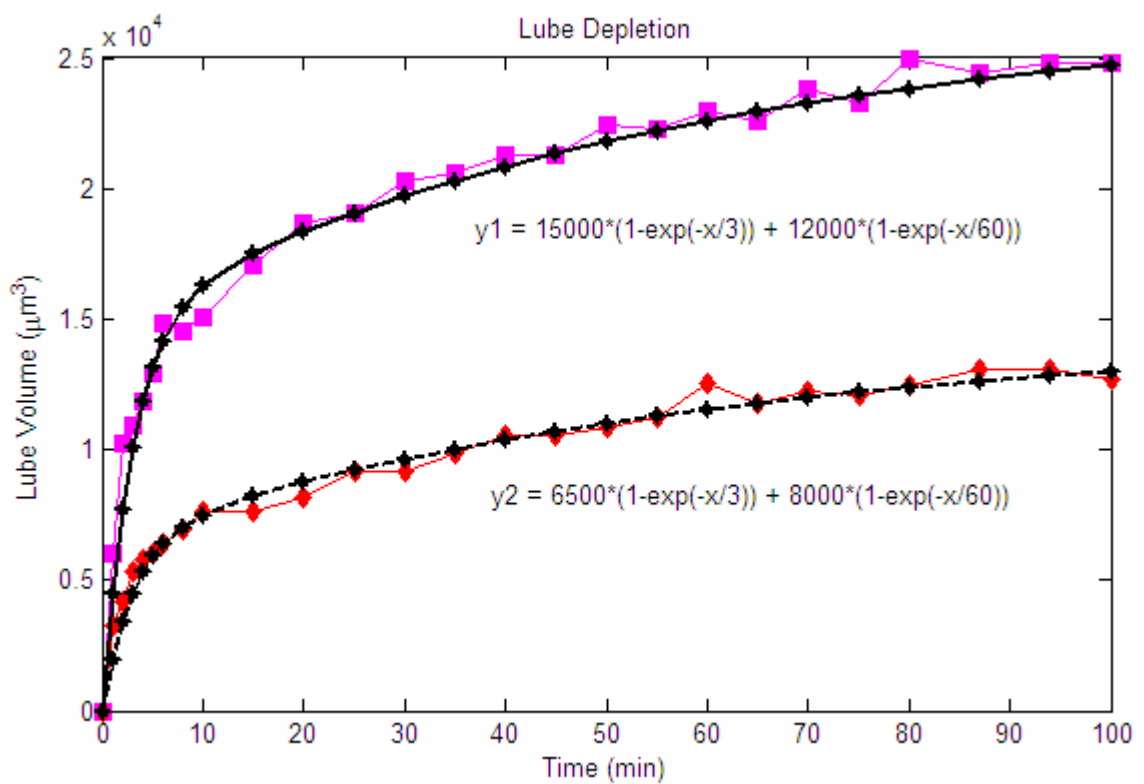


Figure 5.8: Data fit to lubricant depletion volume showing two time scales

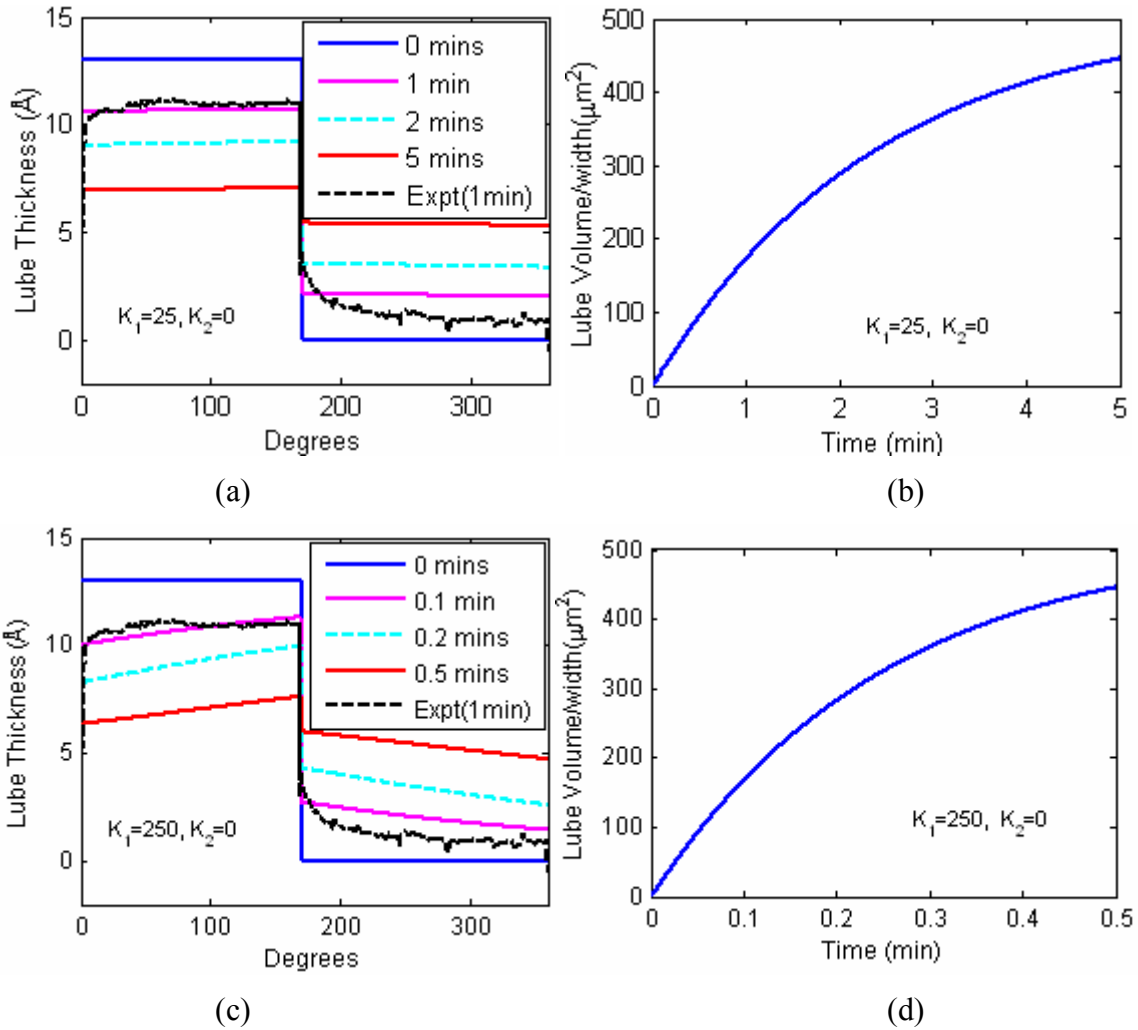
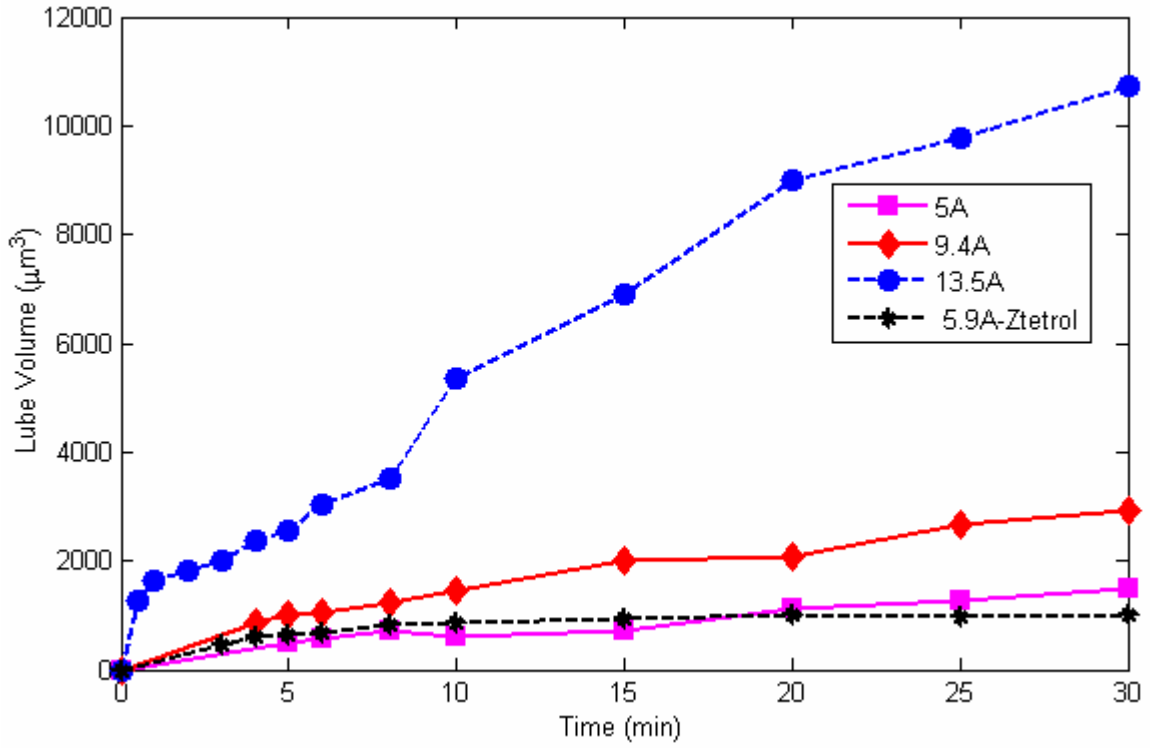
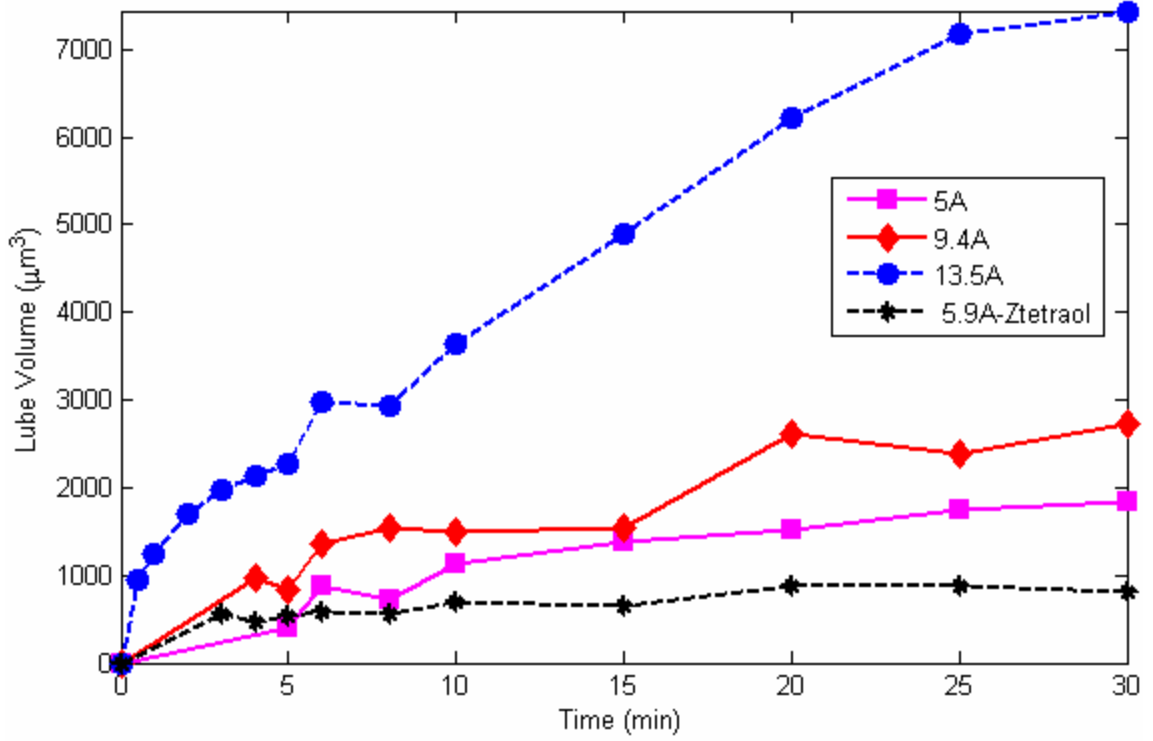


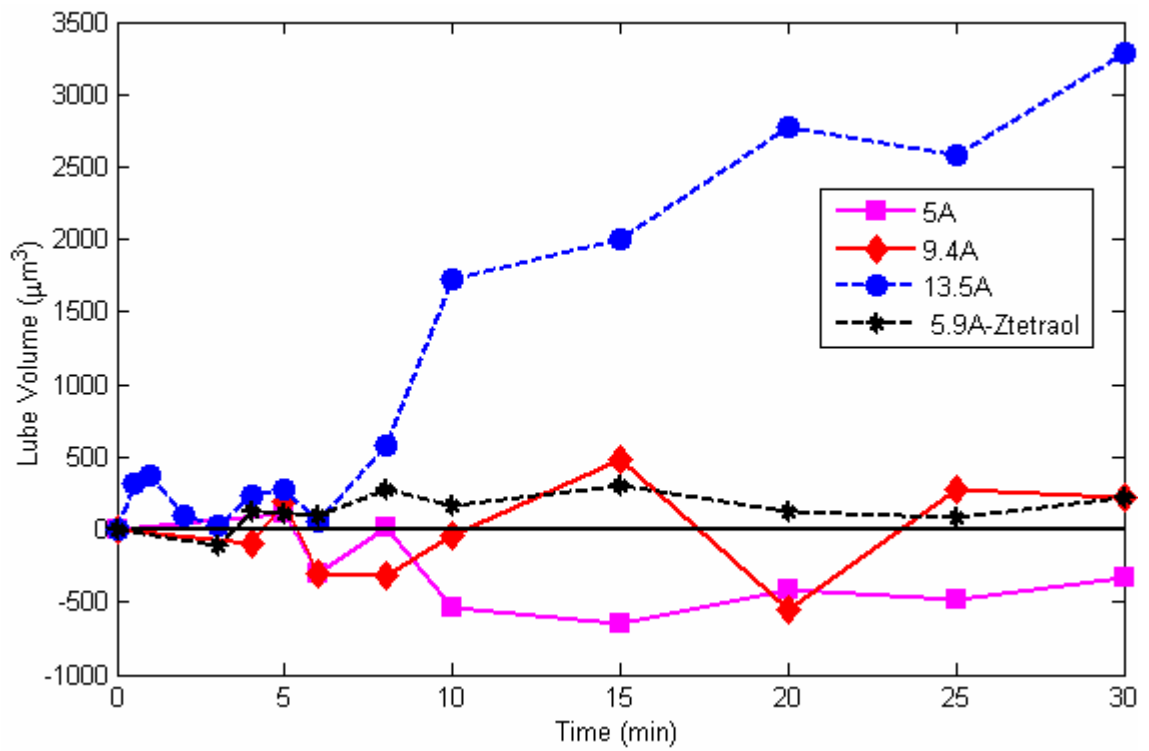
Figure 5.9: (a),(b) Angular distribution and transfer history for low value of K_1 , respectively; (c),(d) Angular distribution and transfer history for high value of K_1 , respectively



(a)



(b)



(c)

Figure 5.10: Lubricant depletion and transfer for different thicknesses of Zdol:

(a) Lubricant depletion in the lubed zone; (b) Lubricant transfer to the delubed zone; (c) Net lubricant depletion

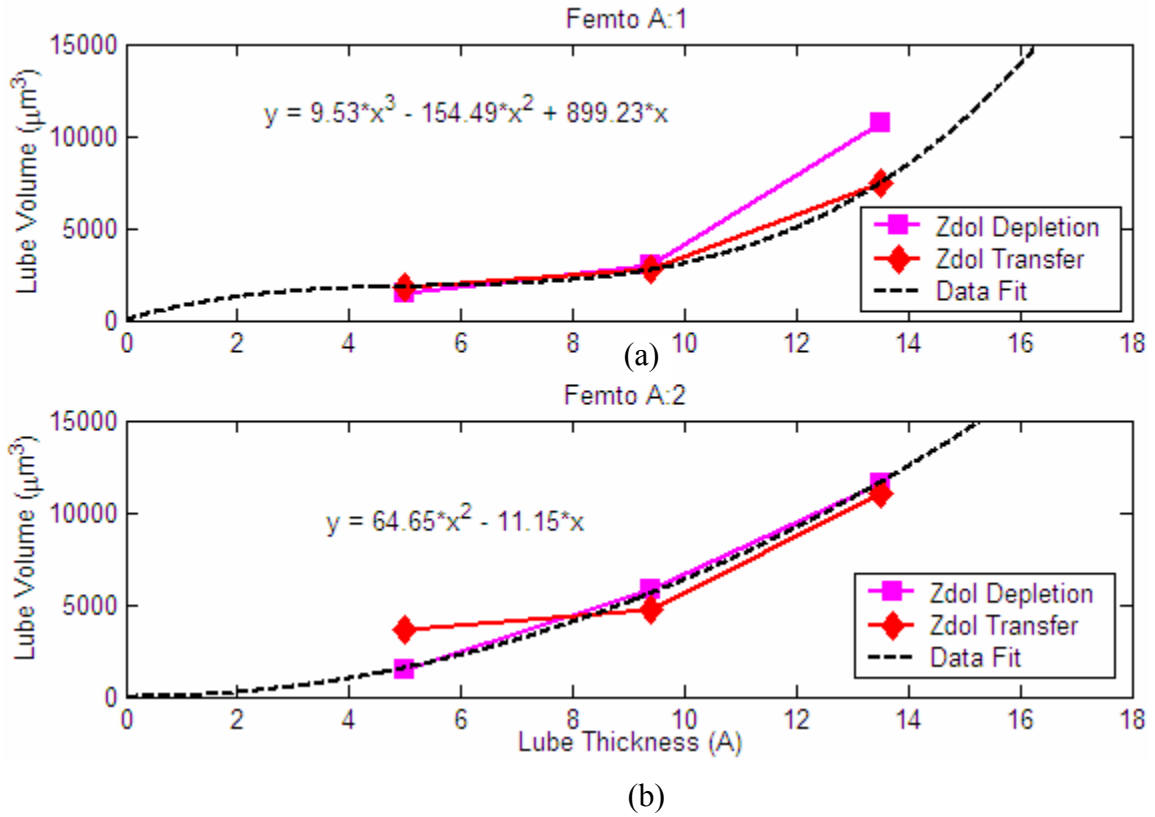


Figure 5.11: Total lubricant depletion and transfer after 30 minutes along with data fits

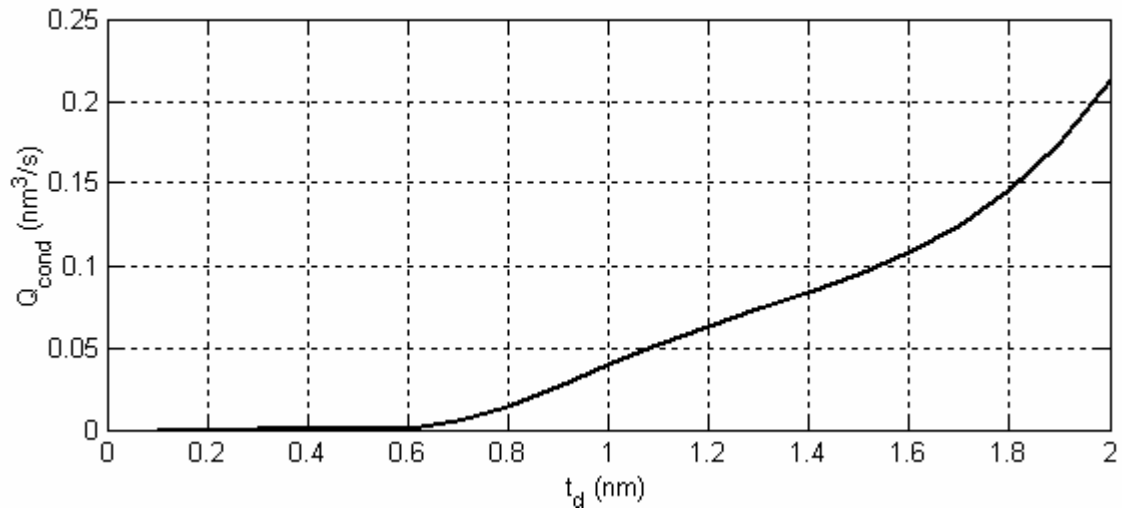


Figure 5.12: Volume rate of lube transfer as a function of disk lubricant thickness as predicted by evaporation model of [5]

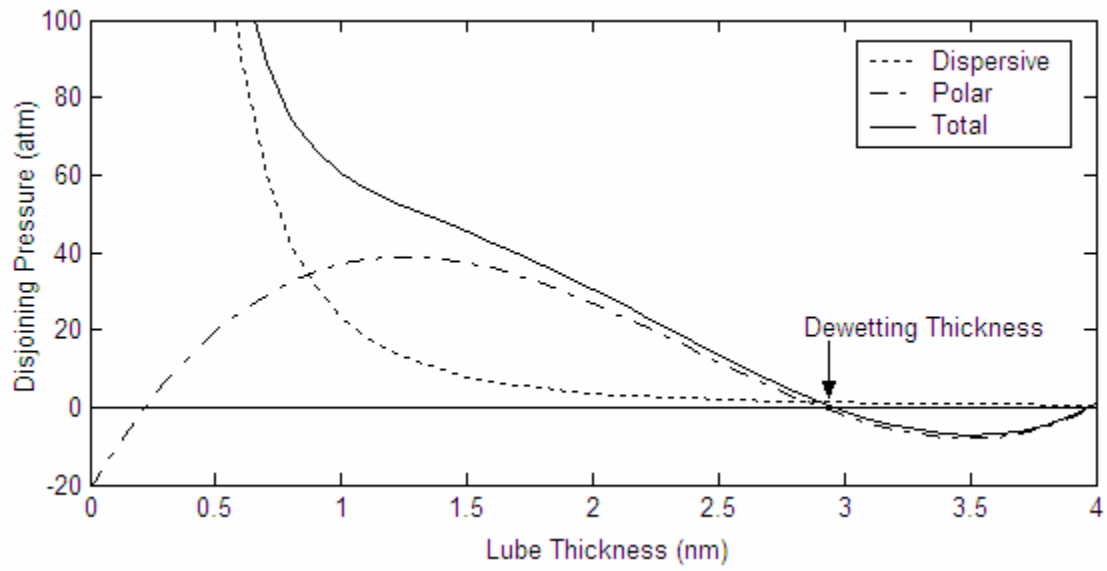


Figure 5.13: Dependence of disjoining pressure lubricant thickness for Zdol 4000 [8] and the disk lubricant thickness (t_d)

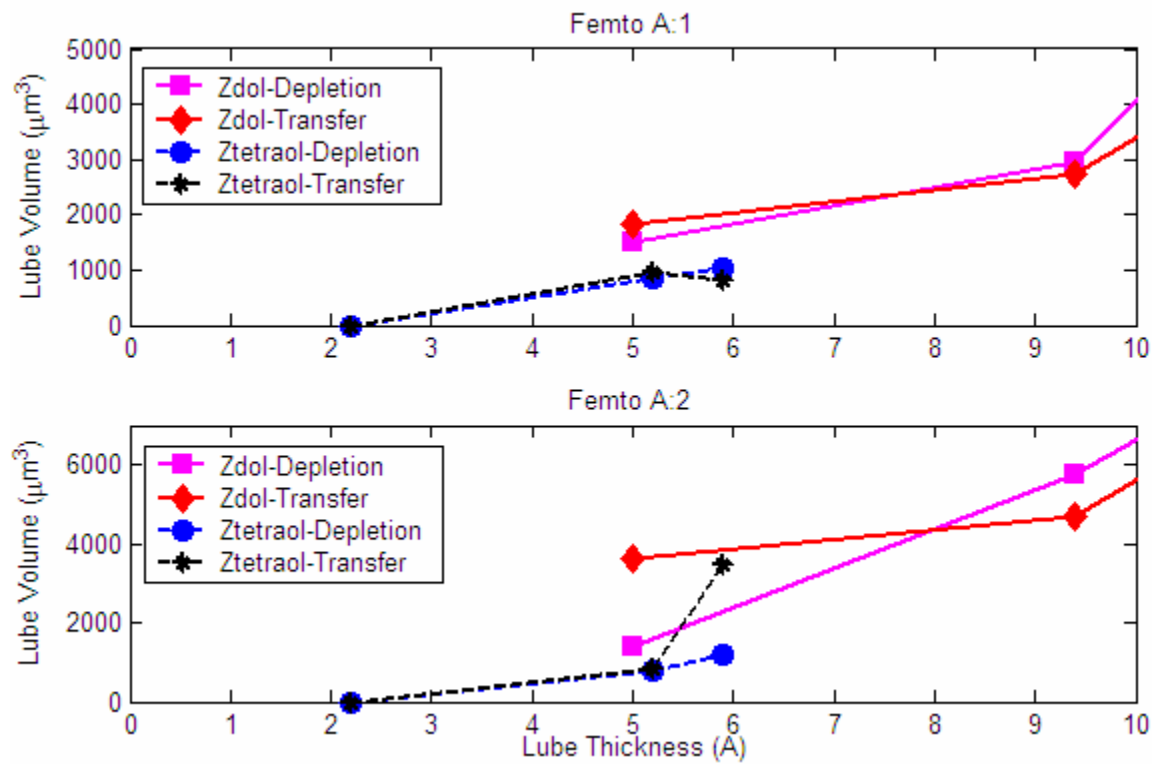


Figure 5.14: Effect of lubricant type on the lubricant depletion and transfer

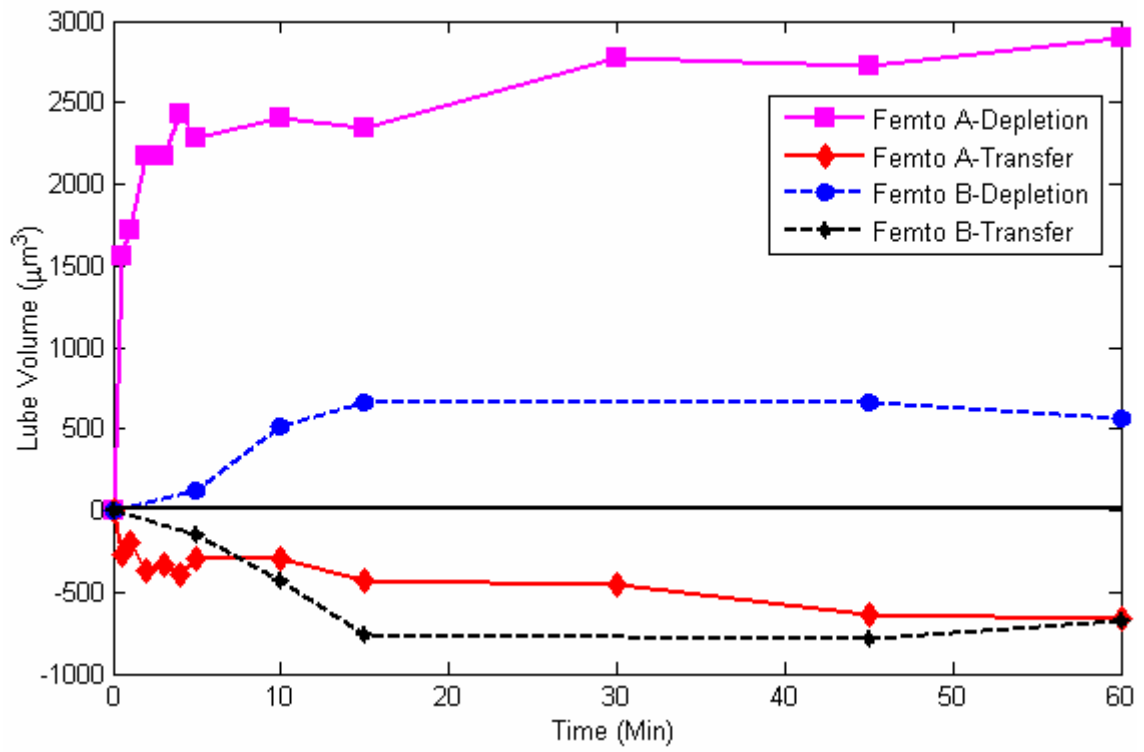
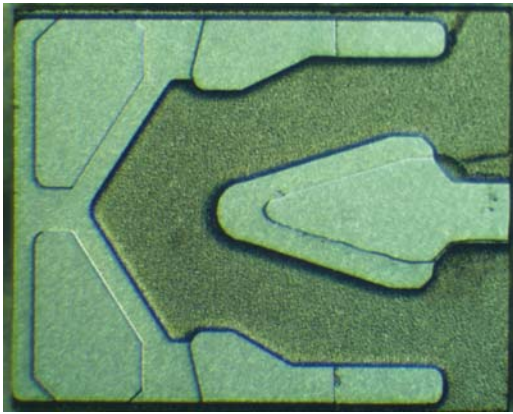
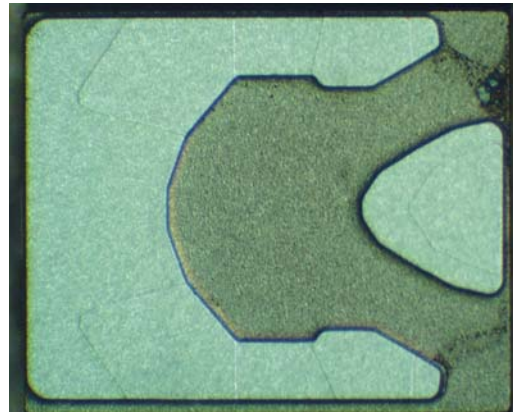


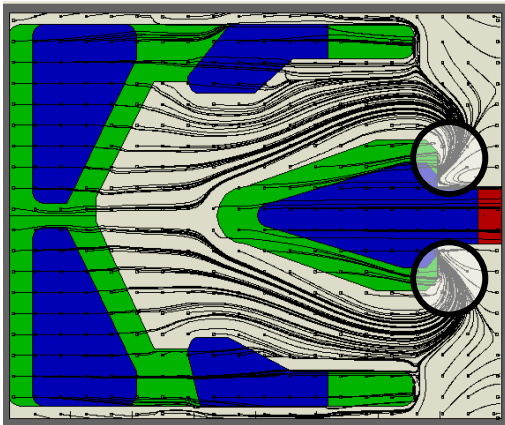
Figure 5.15: Effect of ABS design on the lubricant depletion and transfer



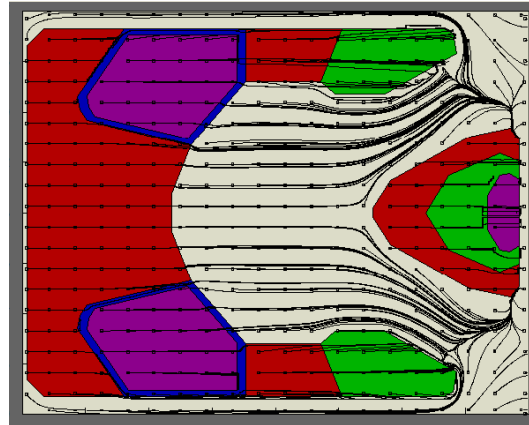
(a)



(b)



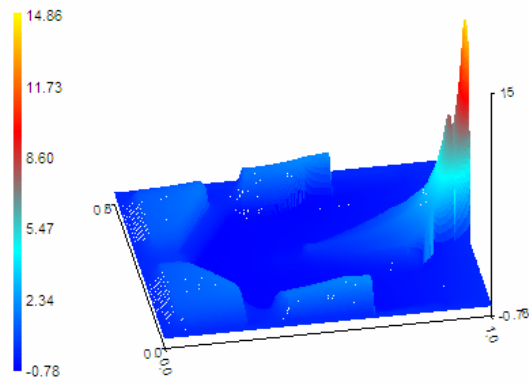
(c)



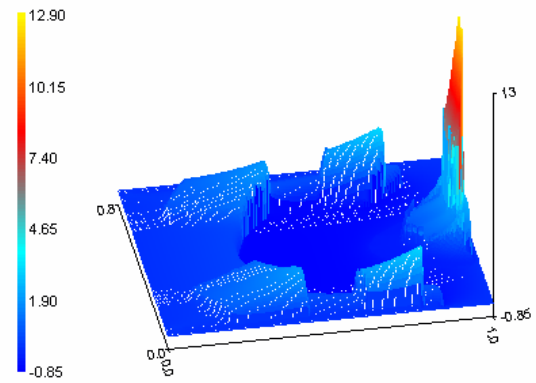
(d)

Figure 5.16: (a), (b): ABS of Femto A and B, respectively, as seen under optical microscope after experiments;

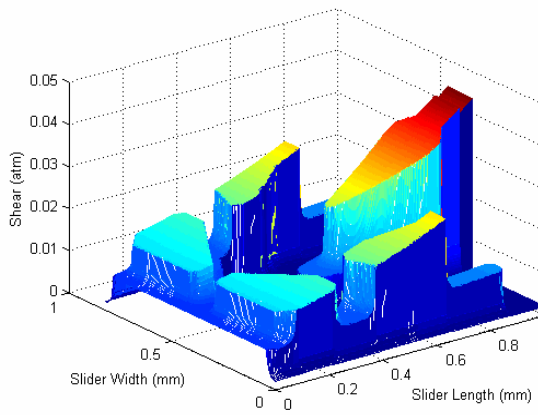
(c), (d): Mass flow lines at 70% spacing across ABS for Femto A and B, respectively, as obtained from static simulations in CMLAir.



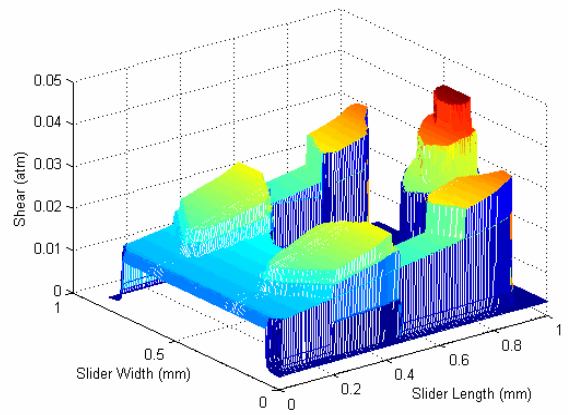
(a)



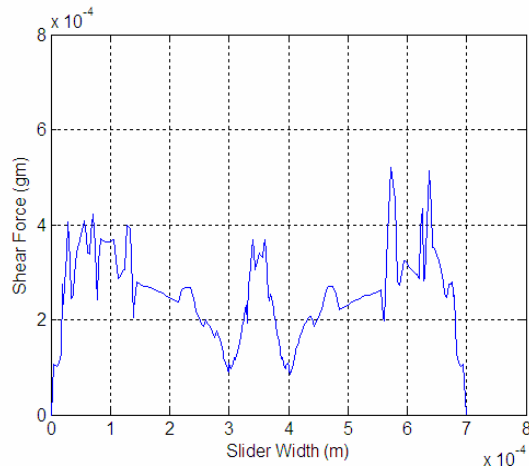
(b)



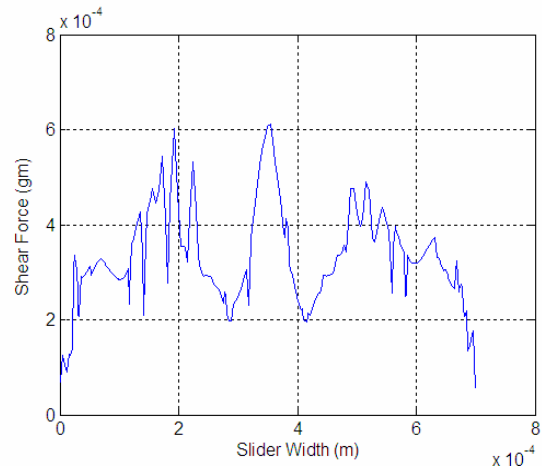
(c)



(d)



(e)



(f)

Figure 5.17: (a),(c),(e) Pressure distribution, shear stress and shear/unit width for Femto A, respectively; (b),(d),(f) Pressure distribution, shear stress and shear/unit width for Femto B, respectively

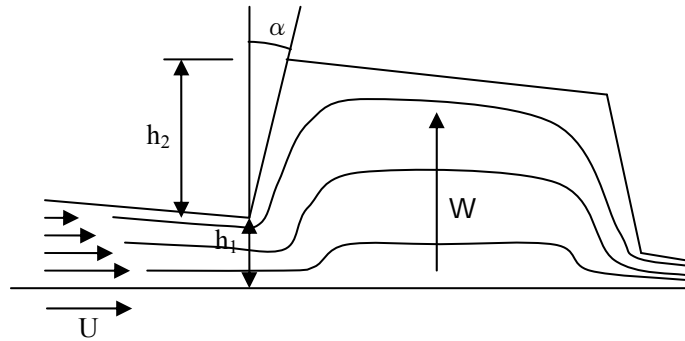


Figure 5.18: Schematic of sudden expansion of air under the airbearing

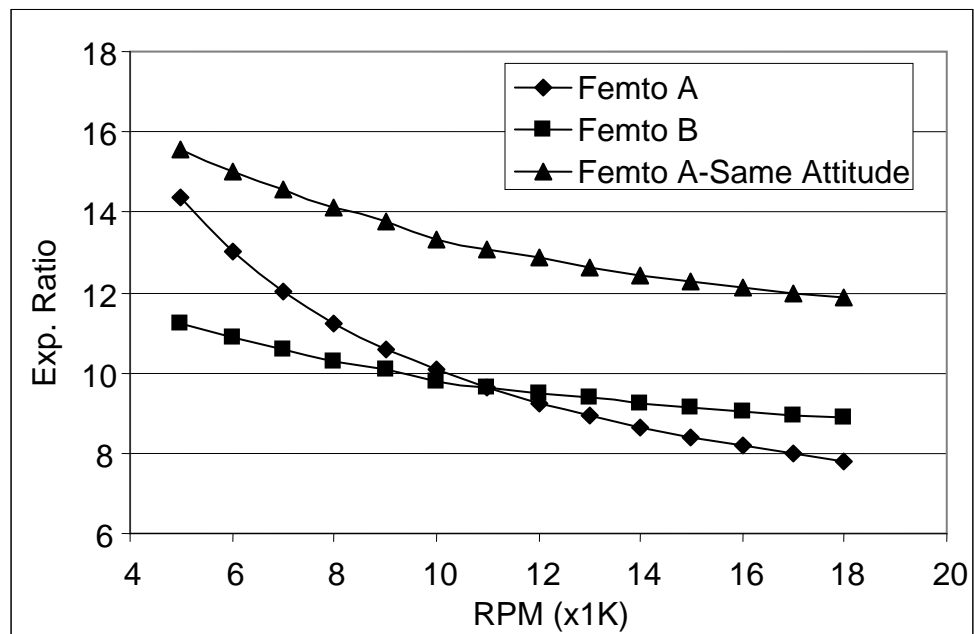
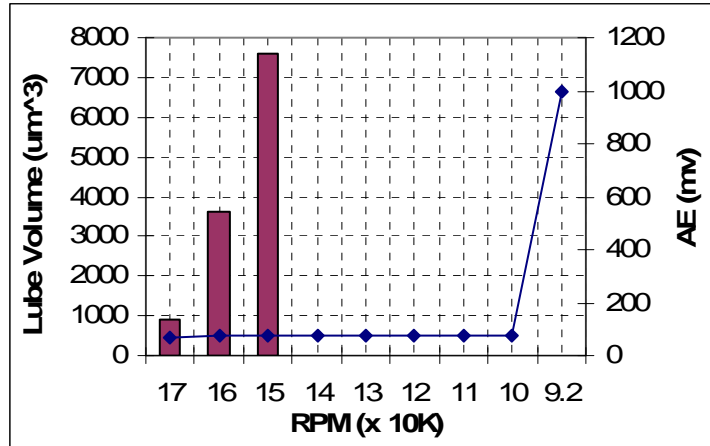
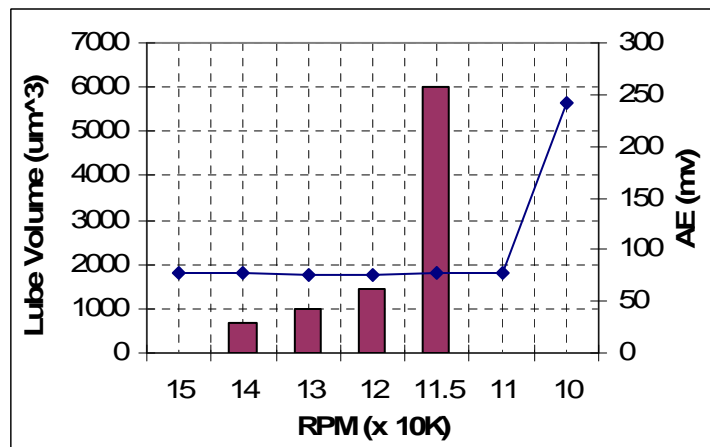


Figure 5.19: Maximum expansion ratios for Femto A and B

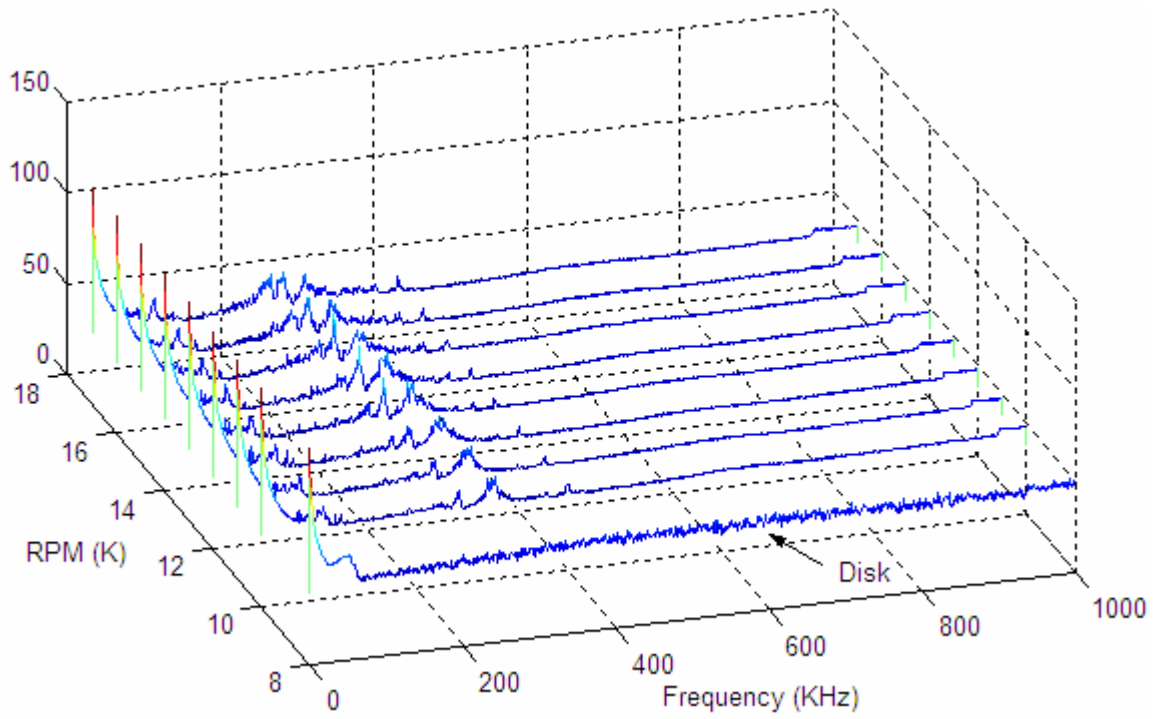


(a)

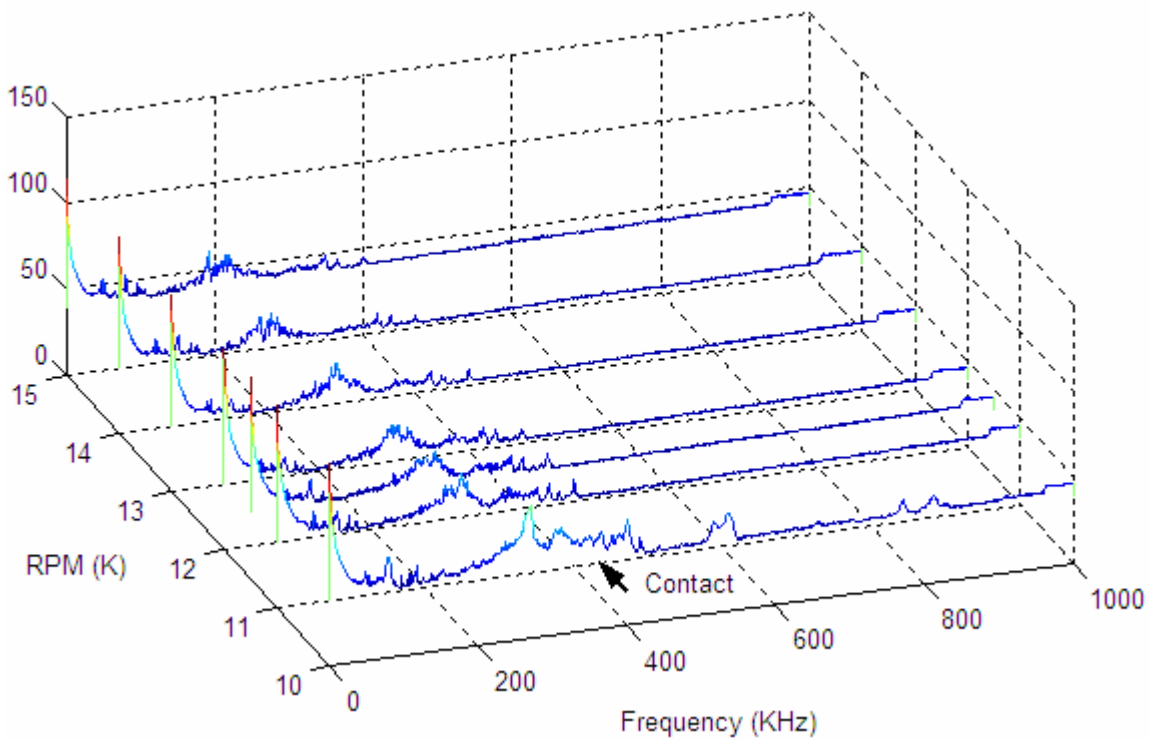


(b)

Figure 5.20: Lubricant depletion volume and RMS AE signal at different rpms : (a) Femto A ; (b) Femto B

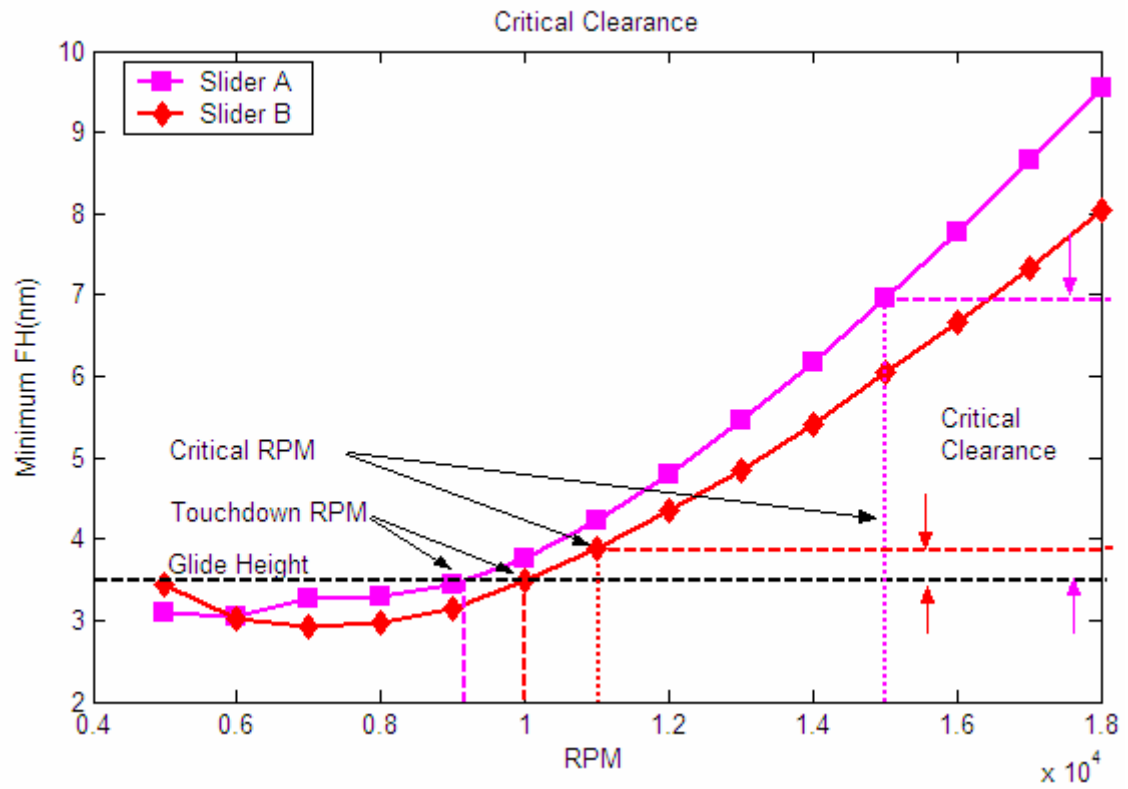


(a)

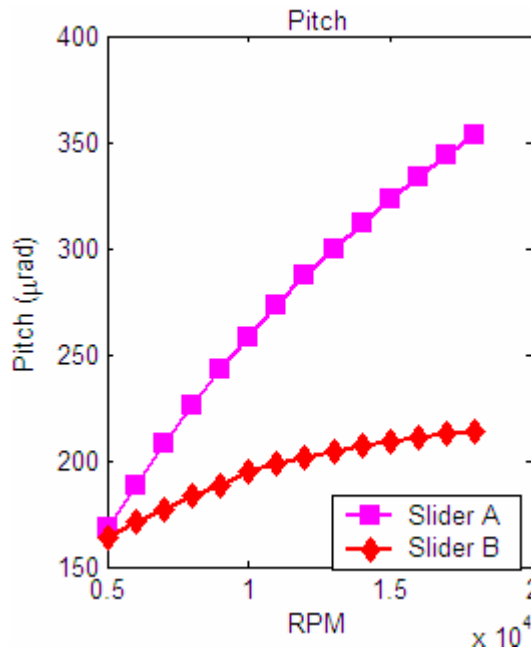


(b)

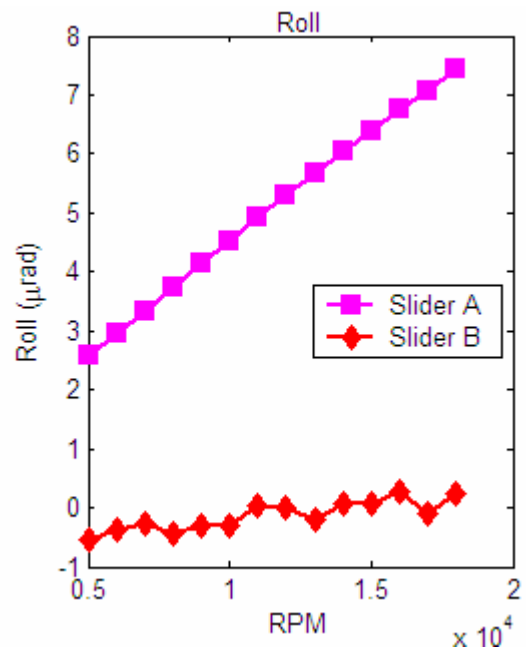
Figure 5.21: Frequency content of slider dynamics as measured by LDV at different rpms for (a) Femto A and (b) Femto B



(a)



(b)



(c)

Figure 5.22: (a): Critical clearance and Minimum fly height for Femto A and B;

(b), (c): Pitch and Roll of Femto A and B, respectively

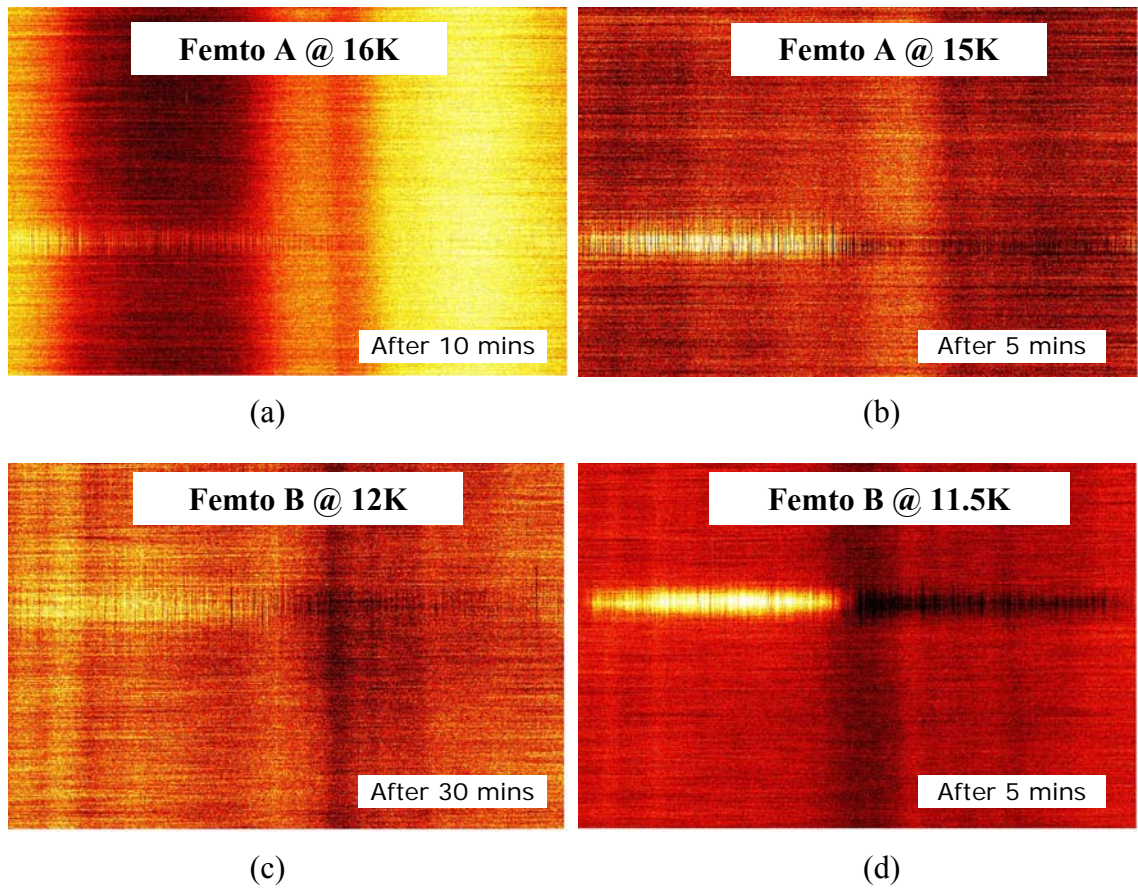


**Figure 5.23: (a) ,(c): Femto A and B above critical rpm showing less depletion and transfer, respectively;
 (b), (d): Femto A and B at critical rpm showing greater depletion and transfer, respectively**

CHAPTER 6

CRITICAL CLEARANCE FOR SLIDER-LUBRICANT INTERACTIONS

6.1 Introduction:

In the last section of the previous chapter, we saw some experimental demonstration of critical clearance. In this chapter, a more in-depth analysis of the critical clearance is carried out. Using shear stress simulations and previously published work we propose two related mechanisms of slider-lubricant interaction to explain the experimental observations and trends. Various slider and media properties that affect the critical clearance have been identified using the theory developed.

6.2 Experimental:

To study slider-lubricant interactions we used half-delubed disks following Ma et. al. [1] as shown in Figure 6.1. When the slider is flown over such a disk on any track, it spends equal time on the lubed and delubed parts of the disk during each revolution. This helps in studying slider-lubricant interactions as the slider picks up lubricant from the lubed part and deposits it on the delubed part. The process dynamics are discussed in Chapter 5. The lubricant used in the experiments was Zdol, with varying thickness, bonded ratio and molecular weight. The carbon overcoat was 2.7 nm thick and of the type CH_xN_y with x:y = 1:1.4. The base substrate for the disks was AlMg, 50 mils (1.27mm) thick and 95 mm in diameter. Various ABS designs were used for the experiments (one design is shown in Figure 6.2), which were conducted in-situ on a Candela Optical Surface Analyzer (OSA) equipped with an ellipsometer to measure the

change in the disk lubricant with a sub-Å accuracy. A sensitive acoustic emission (AE) sensor was mounted near the suspension base plate to monitor head-disk contact. In addition, a Polytec Laser Doppler Vibrometer (LDV) was focused on the slider to monitor its dynamics, which also provided an additional method of detecting contact. Very good correlation was observed in the AE and LDV contact detection.

The experimental procedure was as follows. The disk was mounted on the OSA spinstand and spun at a high rpm (17K), and then the slider was loaded onto a track and moved to a different fresh track. The disk rpm was maintained for a certain period and then reduced by increments of 1000 rpm to 11000 rpm, after which it was reduced by 500 rpm increments to 9000 rpm followed by 100-200 rpm reductions until substantial slider-lubricant interaction was observed. The rpm was then further reduced until the AE and LDV detected head-disk contacts to determine the touchdown rpm/velocity.

6.3 Results

There was no change in the lubricant at high rpms even when the tests were monitored for a long time, as shown in Figure 6.2(a-d). Only when the rpm was reduced to a particular value was there some change, such as depletion and modulation (Figure 6.2(e)), which kept increasing with time (Figure 6.2(f)). We refer to this rpm/velocity as the critical velocity and the associated head-disk clearance as the critical clearance. Upon conducting multiple runs, we found a good repeatability (3σ of error $\sim 600\text{rpm}=0.30\text{nm}$) in the value of critical clearance, determined from the difference between the critical velocity and the touchdown velocity. The values of critical clearances observed were in the range of 0.5 -3.5 nm depending on the slider and disk designs, as shown in Figure 6.3, which shows critical clearances for Zdol lubricant with different molecular weights,

different carbon substrates (CHx and CHxNy) and with inclusion of an additive X-1P or A20H. It is seen that the critical clearance increases with increasing lubricant molecular weight, the inclusion of additives and for CHx.

6.4 Simulations:

To understand the physics of the process and explain the observed trends, we conducted airbearing simulations for models of the experimental sliders using CMLAir, a finite-volume based software developed at CML to solve the Reynolds equation. Steady-state fly heights of sliders and pressures were obtained at various rpms and radial positions that matched the experiments. Using this data, we obtained the shear stress (γ_x) for the first-order slip model (Equation 6.1), which has been shown to give results close to those obtained by Kang's model using kinetic theory [2],[3].

In Equation 6.1, μ_{air} is the viscosity of air, U is the disk velocity, a is the accommodation coefficient while h and P are the slider-disk clearance and airbearing pressure at a particular point on the slider, respectively, and λ is the mean-free path of the air molecules. Equation 6.2 shows the dependence of λ on pressure, where $\lambda_0=63.5$ nm is the mean free path of air molecule at STP. Using this formulation, we calculated the shear rate($\dot{\gamma}_x$) and total shear force (F_x^{shear}) as shown in Equations 6.3 and 6.4, respectively.

$$\gamma_x = \mu_{air} \frac{U}{(2a\lambda + h)} - \frac{\partial P}{\partial x} \frac{h}{2} \quad (6.1)$$

where, $\lambda = \lambda_0 / P$ (6.2)

Further, $\dot{\gamma}_x = \frac{d\gamma_x}{dt} = \frac{d\gamma_x}{dx} \frac{dx}{dt} = \frac{d\gamma_x}{dx} \times U$ (6.3)

and
$$F_x^{shear} = \sum \gamma_x(dx \cdot dy) \quad (6.4)$$

The total shear force and maximum shear rate are plotted in Figure 6.4 for the ABS design shown in Figure 6.2. It is seen that both of these quantities decrease with decreasing rpm/velocity even if the decreasing disk velocity leads to lower slider fly height and pitch. This presents somewhat of a paradox as shear force has been shown to be the most important factor affecting the lubricant by various researchers [4],[5] and we see increased head-disk interaction at lower disk velocity. Further, the total vertical positive and negative force also decrease with decreasing disk rpm/velocity. Thus, the decrease in pressure as well as shear with decreasing rpm is unable to explain the increased slider-lubricant interaction observed at lower clearances unless the lubricant is of shear-thickening type, i.e. behaving more like a fluid at lower shear and shear-rates. However, some experiments in the literature show PFPE lubricants to be of Newtonian type [6] or a shear-thinning type (as are most polymers) in the thickness range of 5-10 nm [7]. But it still remains to be proven for the thickness range used in the current experiments.

6.5 Discussion:

Various external non-contact forces like airbearing pressure, shear, intermolecular force (IMF) and electrostatic force (ESF) act on the lubricant. Only IMF and ESF increase with decreasing head-disk clearance under decreasing disk velocity and can explain the experimental observations. Since disk was well grounded in the experiments conducted, we assume the effect of ESF was negligible. Even in presence of

ESF, the following analysis will still hold since there is monotonic increase in the force with decreasing head-disk clearance.

Dagatine et. al. [8] investigated the effect of van der Waals forces (IMF) on disk lubricant using Lifshitz theory to calculate the disjoining pressure of the disk lubricant in the presence of the slider. They found that the lubricant disjoining pressure decreases with decreasing head-disk spacing and becomes negative at a particular spacing. Because negative disjoining pressure implies instability/dewetting, their calculations also suggest the existence of a critical clearance, below which the lubricant is affected by the slider due to the increase in the IMF although the interaction only sets up lubricant modulations and does not explain the lubricant transfer to the slider. Further, in their calculations, the lubricant layer was considered to be a continuum, and other forces such as airbearing shear and pressure were not considered, which may accelerate or delay the destabilization process. Nevertheless, the magnitude of the IMF at low clearance is relatively high and so the prediction of these calculations may still be valid. We build on their theory here and present two related physical mechanisms to explain the observed phenomenon. It is first noted that the thin lubricant layer (close to a monolayer) is only approximated by a continuum. Thus, a look at the molecular level is essential to understand and explain the possible mechanisms.

Figure 6.5 shows a schematic of lubricant polymer molecules adhered to the carbon layer. A rich literature exists on the interaction between the active sites in carbon and the lubricant. It has been shown that active polymer endgroups bind to the active carbon sites responsible for lube-carbon adhesion, while their backbones remain coiled and extend upwards contributing to “molecular roughness.” [9]. The lower lubricant

layer bonds well with the carbon layer to form the ‘bonded’ layer while the upper layer is a ‘mobile’ layer having more mobility. Cohesion between lubricant molecules plays a much more important role in the mobile layer than the adhesion between lube-carbon in the bonded layer. Based on this concept, we propose that the combined action of shear, pressure and IMF leads to increased slider-lubricant interaction even if the shear reduces with the reduction in fly height under reduced rpm.

To calculate the IMF more precisely, a multilayer model introduced in Chapter 2 could be employed using a ‘lube centered approach’ [8]. However, the qualitative trend in IMF (increase with decreasing clearance) is enough to explain the mechanisms. At low clearances, the topmost layer of lube is pulled to the slider by the IMF along with suction pressure in case of negative pressure sliders, and it is kept on the disk by cohesion between the lube molecules and IMF from the disk, as shown in Figure 6.5. At the (critical) clearance where the IMF from the slider becomes greater than the forces holding the lubricant molecule on the disk viz. cohesion and IMF from the disk, the lubricant molecule is loosened or pulled away from the disk surface to be atomized. This is one physical mechanism explaining the observed phenomenon. The second mechanism is the secondary effect of the increased IMF. There might be preferential pulling of the lubricant backbone, which stretches the molecule in the vertical direction. This increases its normal surface area subject to the airbearing shear. Hence, even if the magnitude of the shear stress decreases, the total shear force experienced by the stretched lubricant molecule could increase. Also, increased molecular roughness increases the surface area of the molecule to the airbearing shear. Thus, we can estimate by using this theory that destabilization of the lubricant layer [8], which increases the

molecular roughness, aids increased slider-lubricant interaction and increases the critical clearance. When experiments were conducted on tracks where the lubricant was already modulated, this was indeed seen to be the case.

By the mechanisms described above, higher molecular roughness and lower cohesion/adhesion increase the critical clearance as they decrease the forces holding the lubricant molecules to the disk. Since higher molecular weights have higher molecular roughness [9] and lower bond density, they should have higher critical clearance. Additives X-1P and A20H have a relatively large phosphazene ring [10] which increases their molecular roughness. Further, X-1P is also reported to preferably occupy bonding sites thus decreasing the adhesion of Zdol [11]. On the other hand, in A20H the phosphazine ring, which is one endgroup of the chain, does not adhere to the carbon. This leaves only the other active OH endgroup to adhere, which decreases the overall adhesion of the lubricant [10]. This explains the increased critical clearance with inclusion of these additives. Finally, research on CH_x and CN_x overcoats [12] suggests that the inclusion of nitrogen leads to better lubricant coverage, stronger adhesion with carbon and possibly more lubricant entanglement due to repulsion of the basic lubricant backbone by nitrogen moieties, which exposes more active sites on carbon. This explains the decrease in critical clearance on CH_xN_y as compared to CH_x.

6.6 Conclusions

A critical head-disk clearance exists above which there is negligible slider-lubricant interaction. Using shear stress simulations and previously published work two related mechanisms of slider-lubricant interaction are proposed: IMF between slider and lubricant may ‘loosen’ a lubricant chain on the disk surface directly or increase its

normal area to the airbearing shear by preferentially pulling the chain backbone which lies closer to the slider and farther from the disk. This can explain the increase in slider-lubricant interaction in spite of lower shear at lower clearance and lower disk velocity and also explain the criticality associated with the slider-lubricant interactions and the trends shown in Figure 6.3.

From this theory, it can be concluded that IMF influences slider-lubricant interactions. This implies that IMF also affects the slider stability through slider-lubricant interactions, a secondary effect, which might be more important than the primary one, viz. slider instability due to attractive IMF between disk and the slider.

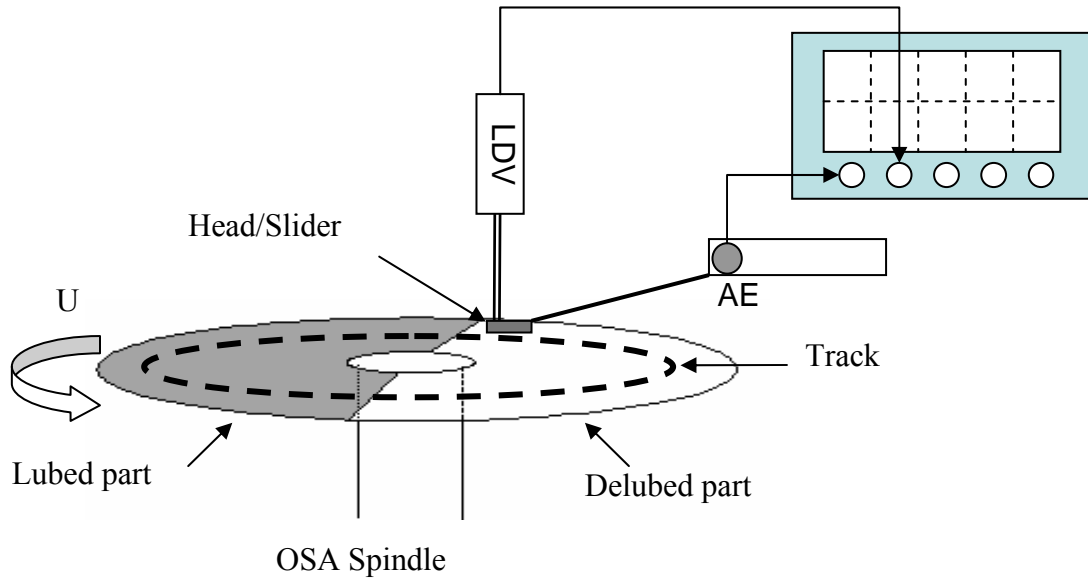


Figure 6.1: Experimental setup for studying slider-lubricant interaction

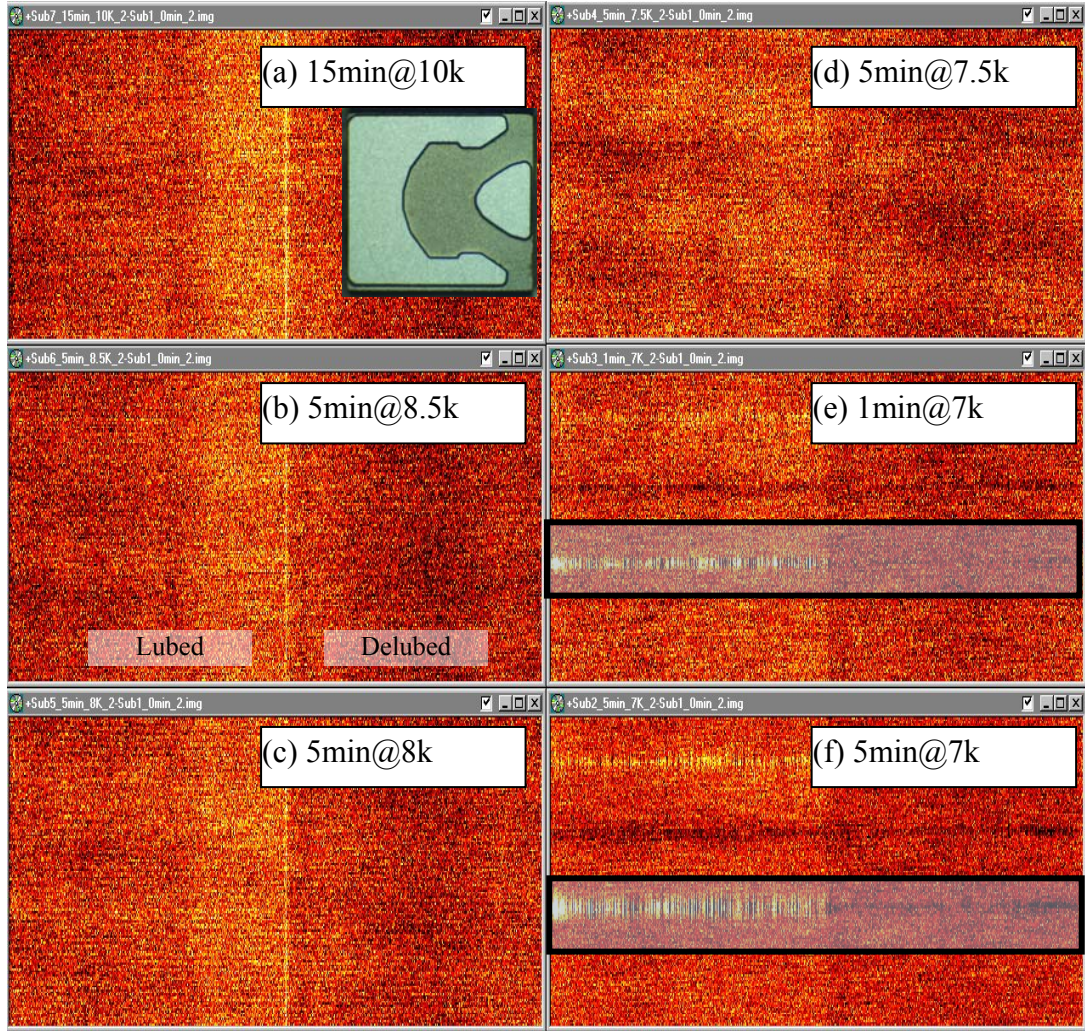


Figure 6.2: OSA images showing lube change at various rpms

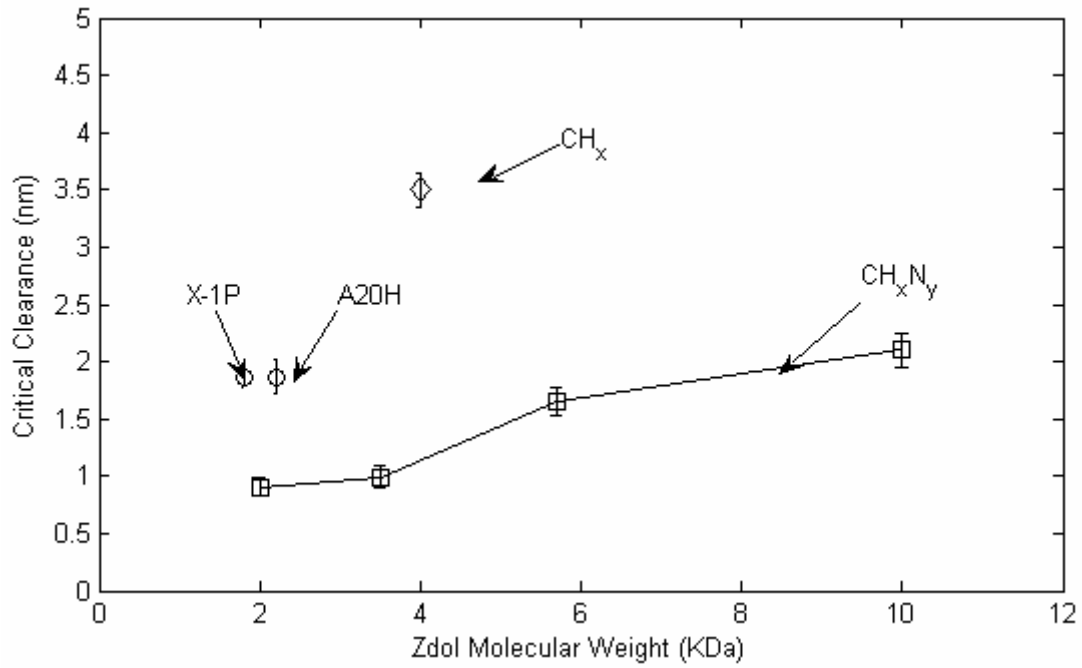


Figure 6.3: Critical clearance as a function of lubricant molecular weight, additives and carbon overcoat type.

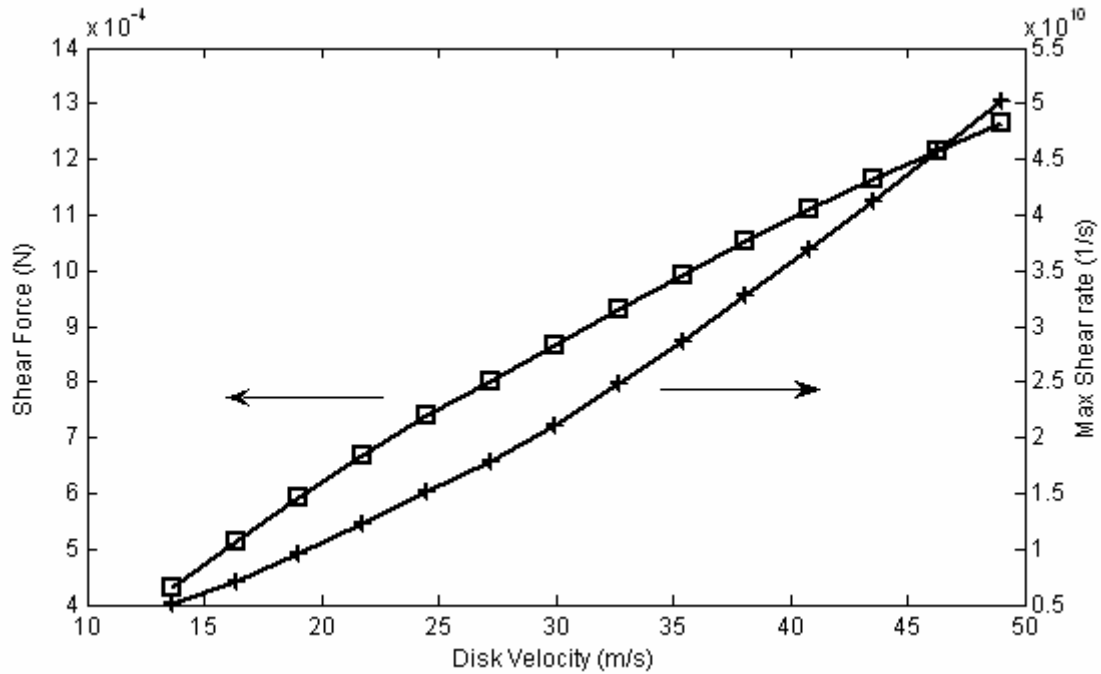


Figure 6.4: Variation of shear force and maximum shear rate with disk velocity

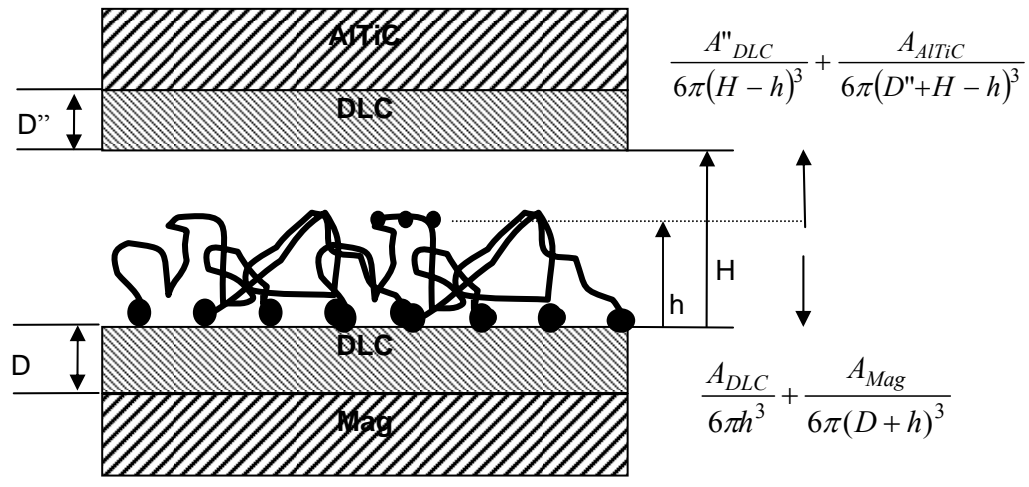


Figure 6.5: Molecular view of disk lubricant

CHAPTER 7

SLIDER-LUBRICANT INTERACTIONS: EFFECT OF MEDIA-TYPE, LUBRICANT MOLECULAR WEIGHT AND ADDITIVES

7.1 Introduction:

In the previous chapters, we saw that the disk-to-slider lubricant transfer (DSLTT) depends on various HDI parameters. Dependence on lubricant thickness, type and ABS design was described in Chapter 5. In this chapter, the dependence on three more factors, media type (CH_x, CH_xN_y), lubricant molecular weight and inclusion of additives (X-1P, A20H), is described.

7.2 Experimental:

The experimental setup is described in detail previously in chapters 5 and 6. The experiments were conducted in-situ on a Candela Optical Surface Analyzer (OSA) equipped with an ellipsometer to measure the change in the disk lubricant with sub-Å accuracy. A sensitive acoustic emission (AE) sensor was mounted near the suspension base plate to monitor slider-disk contact. In addition, a Polytec Laser Doppler Vibrometer (LDV) was focused on the slider to monitor its dynamics, which also provided an additional method of detecting contact. Very good correlation was observed in the AE and LDV contact detections. Two slider ABS designs, shown in Figure 7.1, were used for the experiments.

7.2.1 Determination of Critical Clearance:

The experimental procedure for determining critical clearance has been described in the previous chapter. To summarize, a disk was mounted on the OSA spinstand and spun at a high rpm. The slider was then loaded onto a track and moved to a different fresh track. Subsequently, the disk rpm was reduced by small increments until substantial slider-lubricant interaction was observed. Then the rpm was further reduced until the AE and LDV detected head-disk contact to determine the touchdown rpm/velocity. There was no change in the lubricant at high rpms even when the tests were monitored for a long time as seen in Figure 6.2(a-d). Only when the rpm was reduced to a particular value did it show some change such as depletion and modulation (Figure 6.2(e)), which increased as time progressed (Figure 6.2(f)). This rpm/velocity is referred to as the critical velocity. The associated head-disk clearance determined from the difference between the critical and the touchdown velocity is the critical clearance.

It is shown in the previous chapter that the shear force and maximum shear rate actually decrease with decreasing disk rpm/velocity and the increase in the slider-lubricant interaction can be attributed to an increase in intermolecular forces as well as higher probability of ‘light’ contacts which might not be detected by AE/LDV.

7.2.2 Fixed Clearance tests:

These were carried out in addition to the experiments to determine the critical clearance for a particular head-disk interface. In these tests, the sliders were flown for 15 minutes over disks with different properties (such as different molecular weight or presence of additives) and the head-disk clearance was maintained constant. From the

OSA data, the lubricant depletion and transfer volumes were determined using the procedure described in Chapter 5.

7.2.3 Parametric Dependence

Tests A and B were conducted for three different sets of experiments:

(a) Dependence on Media type:

In these tests, disks from different sources were used. Various properties of these media are shown in Table 7.1. Media A had a glass substrate, 3.0 nm CHx (hydrogenated) type of overcoat and 1.7 nm of Zdol 4000 lubricant (1.2 nm mobile). Media B had an AlMg substrate, 2.7 nm of CHxNy (hydrogenated and nitrogenated) type of overcoat with x:y = 1:1.4, and 1.6 nm of Zdol 4000 lubricant (1.2 nm mobile). The disk topography and the measured slider dynamics over these media are shown in Figure 7.2. It is seen that media A has a better microwaviness control while media B has a better roughness control. The flyability of the slider (Femto A) was better for media B as the media topography features did not excite the ABS modes as much as media A. However, due to better microwaviness control on media A, the fly height modulation (3σ) was less in the case of media A. The touchdown height was determined to be ~ 3.2 nm for both media, while the glide height of media B was better than that of media A. However, since the experimental tracks did not contain any asperities (no AE or LDV contact detection due to asperities), the touchdown rpm/velocity is assumed to correspond to the touchdown height.

(b) Dependence on Lubricant Molecular Weight:

In these tests, media B was used with different molecular weights of Zdol (2000, 3500, 5700 and 10000) with thicknesses as shown in Table 7.2. All properties of the

disks except the lubricant molecular weight were considered to be the same as the disks were manufactured in the same batch.

(c) Dependence on Additives:

In these tests, media B was used with different lubricants as shown in Table 7.3. The structure of Zdol, X-1P and A20H are shown in Table 7.4. For disk B1, Zdol with chain length 2000 was used. For disk B2, Zdol 2000 mixed with X-1P of molecular weight 1000 with thickness 0.6 nm was used. For disk B3, A20H 3000 – a product of Zdol 2000 and X-1P 1000 was used. It is noted that both additives (X-1P and A20H) contain cyclophosphazene molecules as shown in Table 7.4.

7.3 Results and Discussion:

7.3.1 Dependence on media type:

Figure 7.3(a) and Figure 7.3(b) show the lubricant depletion volumes after 5 minutes at each rpm when a slider (Femto A) was flown over media A and B at a radius of 26 mm, respectively, using a bar plot. The RMS AE signal is also plotted along with the depletion volume. From these figures it is seen that the rate of lubricant depletion is higher for media A as compared to media B. Also, the lubricant depletion takes place on media A at higher rpms when none or very little depletion takes place in the case of media B. We clearly see a transition to a high depletion rate at 10600 rpm (critical rpm) for media B. The critical rpm for media A is much higher, at 15000 rpm.

Since there is significant lube depletion at the critical rpm, lube volume was not measured below the critical rpm, but it is expected to increase with decreasing rpm and

spacing. Further, the corresponding AE signal shows no change at the critical rpm for either of the media, indicating no contact of the slider with the disk at the critical rpm. The slider dynamics monitored by LDV showed no change in amplitude or frequency content at the various rpms until there was slider-disk contact, which was also detected by AE at 9200 rpm. From simulations the flying attitude of the slider was found and adjusted assuming that the experimentally observed touchdown rpm (9200 rpm) corresponds to the disk touchdown height 3.5 nm. From this corrected fly height diagram, as shown in Figure 7.4, the critical clearance for media A and B was determined to be 3.5 nm and 1 nm, respectively. Given that the fly height characteristics of the slider were similar for both the media, the difference in the lubricant performance is attributed to the difference in the lubricant – carbon chemistry in the two media.

A rich literature exists on the lubricant-carbon chemistry. Research on CH_x and CN_x overcoats [1] suggests that the inclusion of nitrogen produces up to 50% less surface coverage of lubricant. The main reason for this is the repulsion of the basic acetal backbone of the PFPE lubricant by nitrogen moieties present in the carbon surface. This repulsion keeps the lubricant backbone away from the carbon surface thus exposing more active sites on carbon. Thus, more Zdol endgroups bond to the carbon leading to better lube-carbon adhesion and also a possibility of better entanglement of lubricant molecules on CN_x as the lubricant backbones are bent and endgroups of more chains try to adhere to the active sites. This increases the lubricant retention on the disk surface. By comparison, the lubricant chains lie flat in the case of CH_x [2]. Due to these factors, the lubricant mobility is lower [3] and the lubricant monolayer thickness is higher [1] for CN_x than for CH_x.

Various forces are exerted by the slider on the lubricant. These forces are the positive and negative pressure, shear and intermolecular forces as shown in Figure 7.5(a). The lubricant depletion due to the slider occurs when these forces exceed the retention forces on the lubricant, which are adhesion to the carbon overcoat, cohesion between lubricant molecules and the IMF from the substrate. The previous research noted above indicates better lubricant adhesion and cohesion in the presence of nitrogen in the case of CH_xN_y. The IMF from the substrate is estimated to be similar for both cases as the underlying magnetic layer (thickness > 5nm) is assumed to have similar material characteristics. The substrate materials, glass and AlMg, are more than 7-8 nm away from the lubricant and therefore do not have a strong influence on the IMF on the lubricant.

The above discussion explains why, in the presence of similar airbearing forces, there is more lubricant depletion as well as a higher critical clearance for CH_x as compared to CH_xN_y as observed in Figure 7.4.

7.3.2 Dependence on lubricant molecular weight:

Figure 7.6 shows the dependence of the critical clearance on the lubricant molecular weight. Experiments 1 and 2 correspond to two different sliders of design Femto B while the error bars show 3σ of three experiments conducted with each slider-disk combination for determining the critical clearance. We note that the standard deviations associated with experiment 1 are smaller than for experiment 2. The trend in experiment 1 suggests that the critical clearance monotonically increases with lubricant molecular weight, while in experiment 2 it appears that the critical clearance increases initially with lubricant molecular weight, achieves a maximum and then decreases.

However, due to higher standard deviations for experiment 2, the trend in experiment 1 is more believable.

We next review past literature to explain the observed trend. Many studies have been done on the dependence of lubricant properties on its molecular weight. With increasing molecular weight, the activation energy [4] and viscosity of a lubricant increase, while the lubricant mobility decreases [5]. Thus, lower molecular weight increases the rate of recovery but increases lubricant loss due to evaporation. The lower viscosity associated with lower molecular weight also decreases the shear at the interface during slider-disk contact sliding [5]. Khurshudov et. al. [6] report a higher touchdown velocity for higher molecular weight. They attribute this to the greater “molecular roughness” of longer molecules as shown in Figure 7.7. The backbone of the lubricant molecule is coiled and its end groups adhere to the carbon layer. Further, in the presence of nitrogen in the carbon overcoat, the basic lubricant backbone is repelled. Due to this, the molecular roughness may be pronounced. Also, the endgroup density and hence the “bond density” is lower for higher molecular weight, which may reduce its adhesion with the carbon layer.

Higher molecular roughness and lower adhesion for higher molecular weight can explain the observed experimental trend in Figure 7.6. When the slider flies close to the disk, higher molecular roughness implies more IMF between the slider and the molecular roughness peaks. This roughness also provides a greater area to the airbearing shear. This combined with less lubricant-carbon adhesion implies that the higher molecular weight lubricant is affected more by a slider at proximity. This explains why the critical clearance is higher for higher molecular weight.

Next experiments were conducted to determine the volume of lubricant depletion and transfer over 15 minutes at a constant clearance. This clearance was chosen to be the critical clearance of Zdol 2000. Thus, for the higher molecular weights the chosen fixed clearance was below their respective critical clearances. Accordingly a relatively large amount of lubricant depletion and transfer was seen. Figure 7.8 shows plots of the lubricant depletion from the lubed disk region, lubricant transfer to the delubed disk region and the net lubricant depletion assumed to be equal to the amount of lubricant accumulated on the slider. From this figure it is seen that depletion increases with the lubricant molecular weight. This is because the slider flies increasingly below the respective critical clearances as the molecular weight increases. Thus, we see that when the head-disk clearance continues reducing below the critical clearance of the lubricant, increasingly more slider-lubricant interaction takes place. We also note that lubricant transfer to the delubed portion of the disk does not increase at the rate of increase in depletion. In fact, as seen in Figure 7.9, when the transfer volume is plotted as a percentage of the depletion volume, we see that the transfer rate actually decreases with increasing molecular weight, from about 54% for Zdol 2000 to about 18% for Zdol 10000. Due to the increasing depletion rate and decreasing transfer rate with increasing molecular weight, the net lubricant accumulation on the slider increases and thereby affects the stability of the slider. Hence, from these trends we conclude that lower molecular weight is better for low flying heights.

The above trends in depletion and transfer give some insight into the physics of slider-lubricant interactions. Lubricant depletion on the lubed part of the disk is caused by DSLT whereas lubricant transfer to the delubed part of the disk is caused by SDLT.

The lubricant on the disk (at point A in Figure 7.5(a)) experiences high airbearing forces since the pads towards the trailing edge of the slider fly very close to the disk. These forces are instrumental in the DSLT. A majority of this lubricant transferred to the slider resides in the deep etches as suggested from the ABS photographs after the experiments. It either gets transferred directly from the disk to the deep etches of the ABS owing to the sub-ambient pressure created there or is sheared off to the deep etches from the ABS pads due to higher airbearing shear on the pads, since they fly closer to the disk. Thus, the airbearing forces acting on the lubricant transferred to the slider (at point B in Figure 7.5(b)) are much weaker since the deep etches are much farther from the disk. Hence, the SDLT is mainly governed by the inherent lubricant properties such as its desorption or evaporation energy rather than the airbearing forces. With increasing molecular weight, the desorption energy also increases [5]. This explains why the slider-to-disk transfer rate decreases with increasing molecular weight.

From the above analysis we concluded that the governing mechanisms of disk-to-slider and SDLT are different. The DSLT is mainly influenced by airbearing forces and lubricant properties such as molecular roughness and cohesion because they have an influence on the magnitude of airbearing forces acting on the lubricant. By contrast, the SDLT is mainly governed by the inherent lubricant properties such as its desorption or evaporation energy rather than the airbearing forces.

Marchon et. al. [7] developed a model of lubricant transfer based on evaporation-condensation of lubricant, which does not consider the effects of airbearing forces. According to this model the lubricant condensation flux R_{cond} from disk-to-slider is given by

$$R_{cond} = P_0 \sqrt{\frac{M_n}{2\pi RT}} \cdot \exp\left(-\frac{\Pi(t_d)M_n}{\rho RT}\right) \quad (7.1)$$

where P_0 is the bulk vapor pressure, M_n is the molecular weight, R is the gas constant, T is the absolute temperature, and ρ is the lubricant density. $\Pi(t_d)$ is the disjoining pressure for the disk lubricant thickness t_d . From R_{cond} , the volume flux of lubricant from disk-to-slider or can be calculated as $Q_{cond} = R_{cond} A/\rho$, where A is the cross-section area and ρ is the lubricant density. Similarly, the evaporation flux R_{evap} of lubricant from the slider-to-disk can be calculated from Eq. (7.1) by replacing t_d by t_s , the slider lubricant thickness. As seen from Eq. (7.1), this model predicts an exponential decrease in the transfer rate with increasing molecular weight given the same lubricant volume or thickness on the slider, and therefore it can explain the transfer rate trend in Figure 7.9. Therefore we have an experimental verification of this model and also support for the current argument that the DSLT is mainly influenced by the lubricant evaporation energy rather than the airbearing forces.

The above model, however, does not explain the trend of the DSLT manifesting as lubricant depletion on the disk. This is because the airbearing forces influence the DSLT more than does the lubricant evaporation energy. Thus, a DSLT model based on airbearing forces, lubricant molecular roughness, cohesion and adhesion energy needs to be developed based on the current experimental data. Such a model will also be able to estimate the influence of all the airbearing forces as well as the lubricant and media type on the DSLT.

7.3.3 Dependence on additives:

Additives are employed in the lubricant because they can enhance the tribological performance and thus the reliability of the head-disk interface. X-1P is the most commonly used additive as it possesses excellent lubricity, low vapor pressure, high thermal stability and good solubility in non-CFC solvents [5]. In addition, Chen et. al. [5] also found that X-1P, when used as an additive, prevents catalytic degradation of the lubricant and improves the lubricant mobility thereby improving the overall tribological performance. Mate et. al. [8] proved through ESCA measurements that X-1P forms an underlayer in case of Zdol lubricant. The chemical structure of X-1P is shown in Table 7.4. It contains a cyclophosphazene molecule, which is large in size compared to the Zdol chain, with a radius of gyration of 5Å. Therefore, it could add to the molecular roughness of the lubricant when used as an additive. Further, from higher mobility of AM3001 lubricant in the presence of X-1P, Chen et. al. [5] “believe(d) that X-1P molecules preferably occupied the bonding sites on the carbon surface,” thereby reducing the bonding fraction and adhesion of Zdol molecules with the carbon surface.

A20H is obtained when X-1P is chemically reacted with Zdol. The resultant chemical structure of A20H is shown in Table 7.4. One endgroup for A20H is the –OH group (from Zdol) while the other is the cyclophosphazene. Similar to X-1P, A20H is predicted to have more molecular roughness than Zdol due to the cyclophosphazene moiety. Waltman et. al. [9] report a lower mobility for A20H as compared to Zdol with comparable molecular weight. Their further analysis indicates that there is actually an increased adhesion provided by the adsorbed film structure of A20H on the carbon surface.

Figure 7.10 shows the measured critical clearance for the Femto B slider for Zdol, Zdol+X-1P and A20H lubricated disks with lubricant thicknesses as shown in Table 7.4. It is seen that the critical clearance is greater for the Zdol+X-1P mixture and A20H as compared to Zdol. This increase in the critical clearance can be attributed mainly to increased molecular roughness due to the cyclophosphazene moiety present in X-1P and A20H.

Finally experiments were conducted to determine the volume of lubricant depletion and transfer over 15 minutes at a constant clearance. The results of these experiments are shown in Figure 7.11. The first set of experiments was done maintaining the slider-disk minimum clearance at 1.5 nm, which is above the critical clearance of Zdol, but below the critical clearances of Zdol+X-1P and A20H. Hence, no lubricant depletion and transfer was seen for Zdol. However, comparable amounts of depletion and transfer were seen for Zdol+X-1P and A20H. For the second set of experiments, the slider-disk minimum clearance was decreased to about 0.7 nm by reducing the disk rpm/velocity. In this case, the clearance was just below the critical clearance for Zdol, but much below that for Zdol+X-1P and A20H. Hence, some depletion and transfer was observed in case of Zdol while much more depletion and transfer was observed in case of Zdol+X-1P and A20H as compared to the first set of experiments. From Figure 7.11 we also see that much more depletion and transfer is seen in case of Zdol+X-1P as compared to A20H even if the critical clearances are similar. This is attributed to the different lubricant adhesion. As mentioned before, previous research concluded that X-1P tends to form an underlayer for Zdol and preferentially binds to active sites in carbon resulting in lower lubricant-carbon adhesion and hence, increased lubricant mobility. By

contrast, A20H is reported to have decreased mobility as compared to Zdol due to better lubricant-carbon adhesion. Thus, due to poorer adhesion, there is more lubricant depletion and transfer for Zdol+X-1P as compared to A20H.

From the above results we conclude that negligible slider-lubricant interaction takes place when the slider-disk minimum clearance is above the critical clearance; the interaction starts at the critical clearance and keeps increasing as the slider-disk clearance reduces below the critical clearance. Further, the critical clearance appears to depend on the lubricant molecular roughness more than the lubricant-carbon adhesion, which apparently influences the intensity of slider-lubricant interaction below the critical clearance. However, more experiments regarding this observation are needed to validate this conclusion.

7.4 Conclusions:

In this chapter we report on an experimental investigation of the effect of media type, lubricant molecular weight and the inclusion of X-1P and A20H on the slider-lubricant interactions using a half-delubed disk. Based on the experimental results and the following analysis, we conclude that:

- (a) There is a critical slider-disk clearance above which negligible slider-lubricant interaction occurs. As the minimum slider-disk clearance is reduced the interaction starts at this critical clearance (CC) and increases in intensity below the CC, which depends on various HDI parameters.
- (b) Media-type: Comparison of the CC on CH_x and CH_xN_y media indicates that the presence of nitrogen is better for the HDI as it reduces the CC primarily due to better lubricant-carbon adhesion and possibly better entanglement of lubricant chains.

Further, the contribution of disk microwaviness to the slider-lubricant interaction needs to be examined as it affects slider flyability.

- (c) Lubricant Molecular Weight: The CC was found to increase with increasing lubricant molecular weight for Zdol. This is attributed to the increased molecular roughness and lower bond density at higher molecular weights. Fixed clearance experiments revealed that different mechanisms dominate disk-to-slider and SDLT. Airbearing forces appear to dominate the DSLT while inherent lubricant properties such as evaporation energy are more important in SDLT.
- (d) Additives: The CC was found to increase in the presence of additives X-1P and A20H. This is mainly attributed to an increase in the lubricant molecular roughness due to the presence of the large cyclophosphazene molecule. Fixed clearance experiments suggested that lubricant-carbon adhesion significantly influences the amount of lubricant depletion and transfer when the minimum slider-disk clearance is below the CC.

In Chapters 4-7, we studied various aspects of slider-lubricant interaction as we believe it is the most important factor affecting the slider stability at low flying heights. The next chapter investigates the effect of disk topography on the slider dynamics.

Properties	Media A	Media B
Substrate	Glass (39 mils)	Al-Mg (50 mils)
COC type	CHx	CHxNy
COC thickness	3.0 nm	2.7 nm
Lubricant type	Zdol 4000	Zdol 4000
Lubricant thickness	1.6 nm 0.4 nm bonded, 1.2 nm mobile	1.7 nm 0.5 nm bonded, 1.2 nm mobile

Table 7.1: Media properties

Disk No.	Molecular Weight (Da)	Lubricant Thickness [Mostly mobile] (nm)
ZD1	2000	1.49
ZD2	3500	1.62
ZD3	5700	1.51
ZD4	10000	1.68

Table 7.2: Lubricant thickness for disks corresponding to different lubricant molecular weight used in the experiments

Disk No.	Disk Type	Lubricant Thickness (nm)		
		Total	Zdol	Additive
B1	Zdol 2000	1.49	1.49	0
B2	Mixture: Zdol 2000 + X-1P 1000	1.56	1.50	0.06
B3	Product: A20H 3000 = Zdol 2000 + X-1P 1000	1.73	1.43	0.3

Table 7.3: Lubricant thickness for disks corresponding to different additives used in the experiments

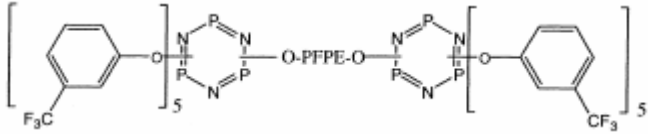
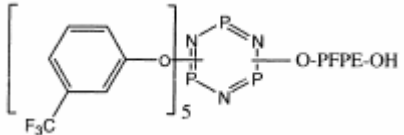
Lube Type	Structure
Zdol	$\text{HO-CH}_2\text{CF}_2[(\text{OCF}_2\text{CF}_2)_p(\text{OCF}_2)_q]\text{OCF}_2\text{CH}_2\text{-OH}$
X-1P [9]	
A20H [9]	

Table 7.4: Chemical structures of Zdol, X-1P and A20H



Figure 7.1: ABS designs used for experiments: (a) Femto A; (b) Femto B

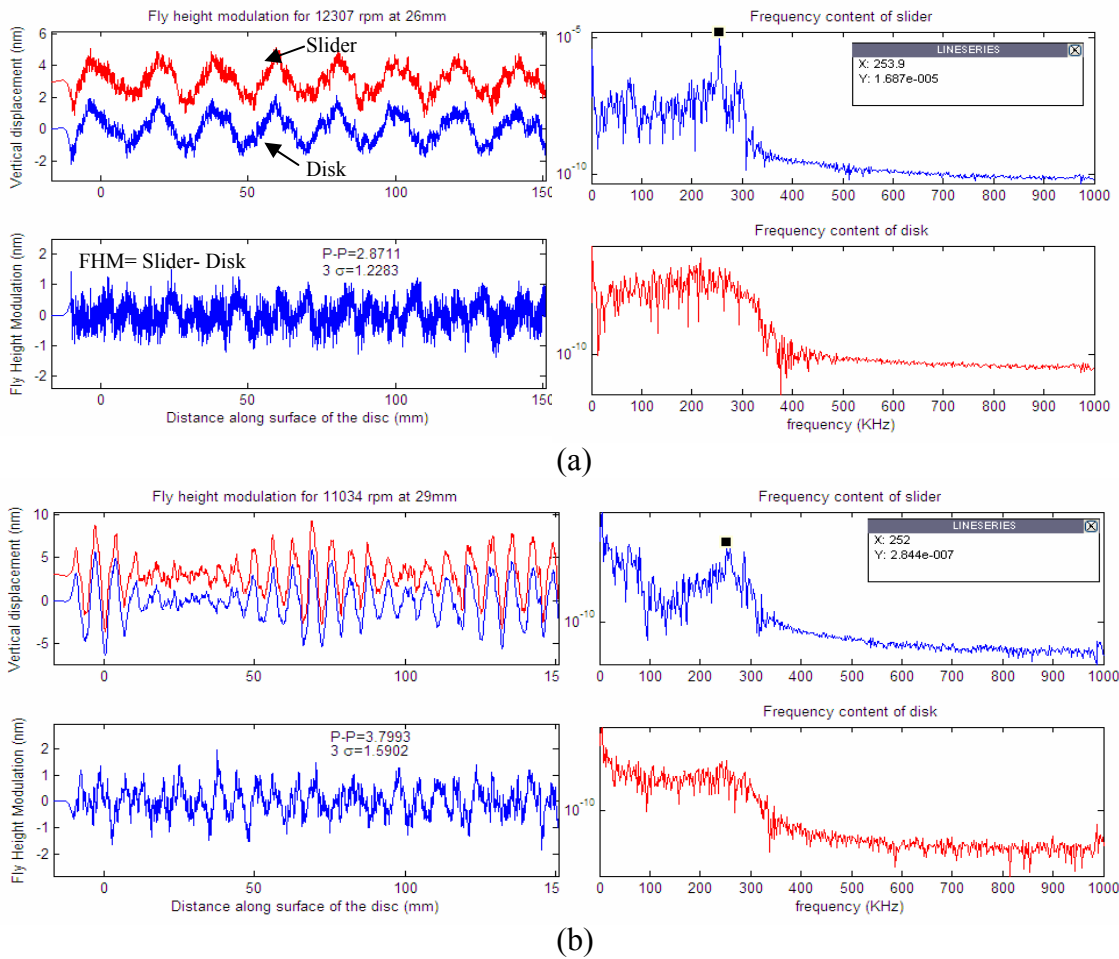


Figure 7.2: Slider (Femto A) response to disk topography, FHM and frequency spectra for slider and disk for (a) Media A and (b) Media B.

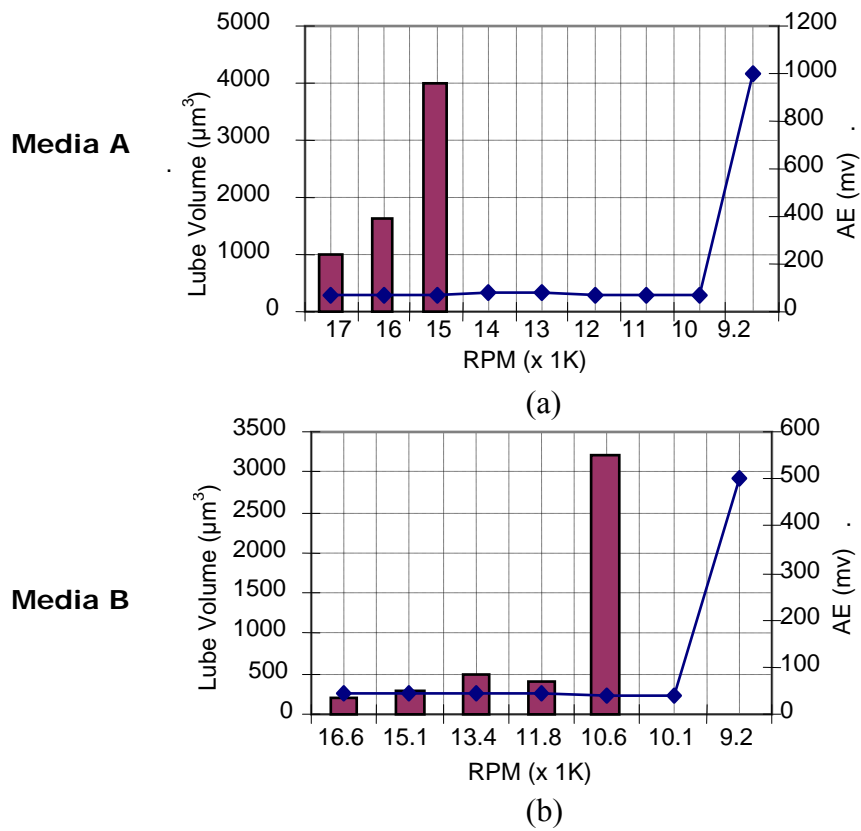


Figure 7.3: Lubricant volume depleted in 5 minutes at various rpms along with corresponding AE signal with Femto A slider for (a) Media A and (b) Media B.

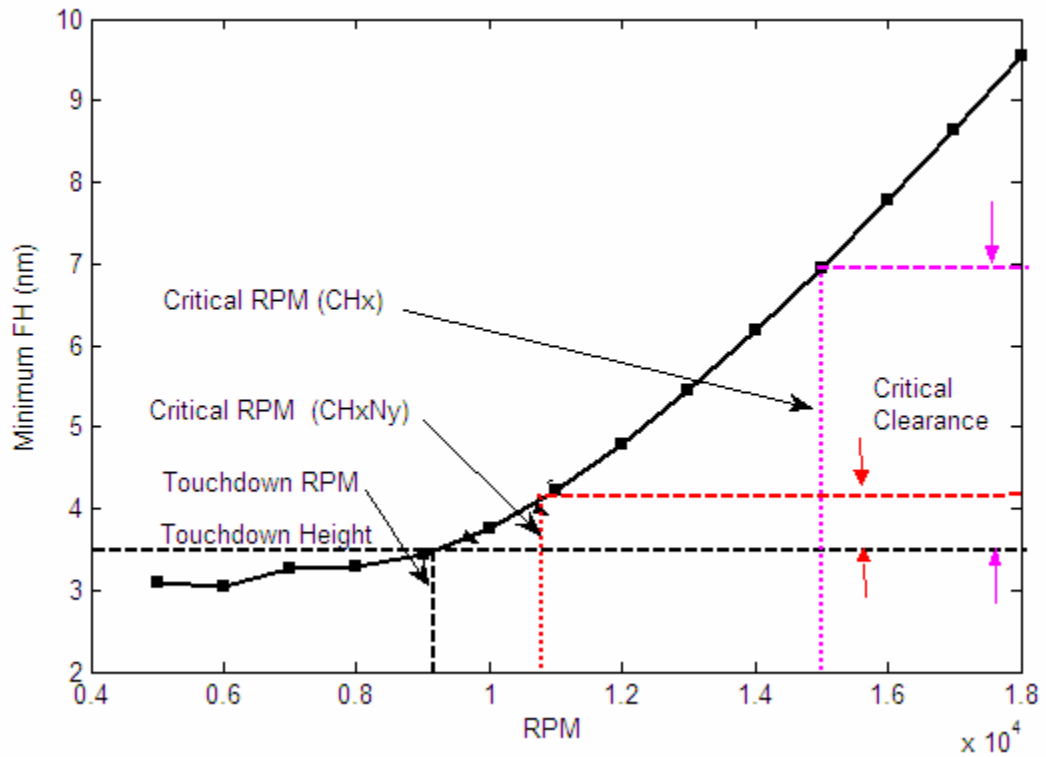


Figure 7.4: Determination of critical clearance from critical rpm and touchdown rpm for Media A (CHx) and Media B (CHxNy) for Femto B slider.

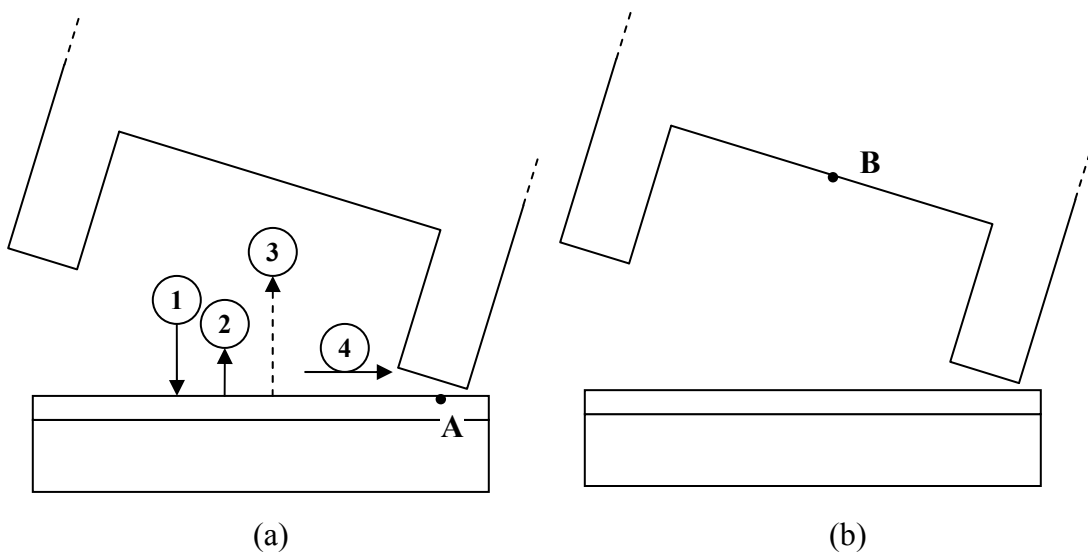


Figure 7.5: (a) Different airbearing forces acting on lubricant at point A on the disk: (1) Positive airbearing pressure, (2) Negative airbearing pressure, (3) Intermolecular force and (4) airbearing shear;

(b) No significant airbearing forces on lubricant placed at point B in the deep etch level on the slider.

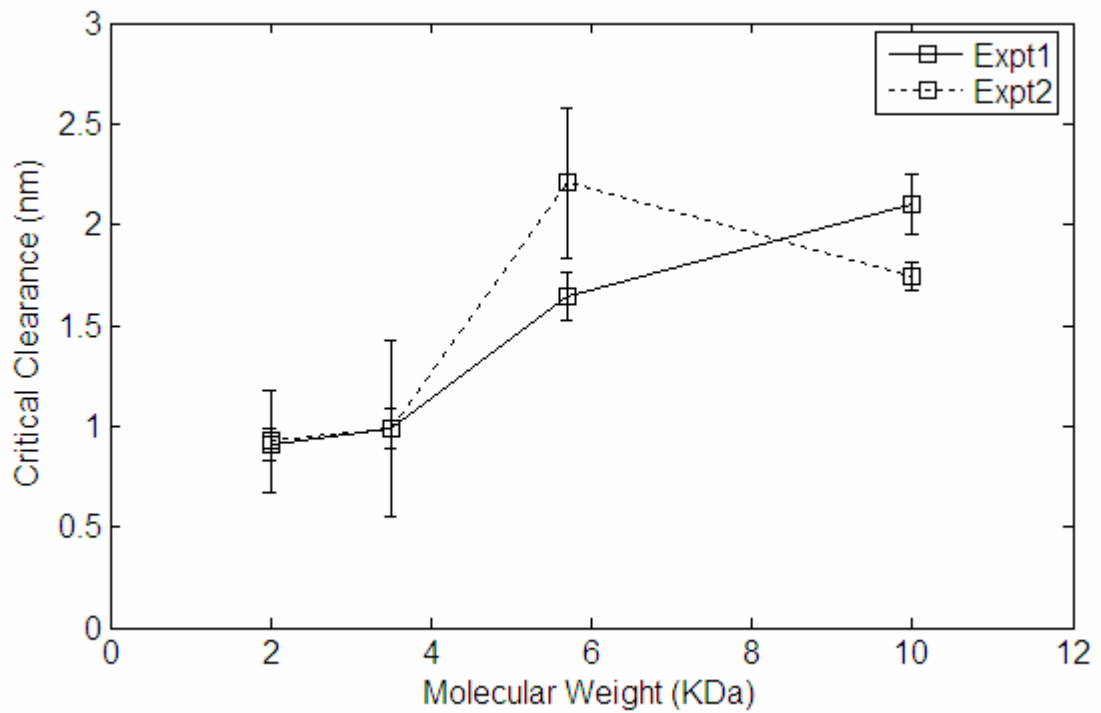


Figure 7.6: Dependence of critical clearance on lubricant molecular weight for Zdol for Femto B slider.

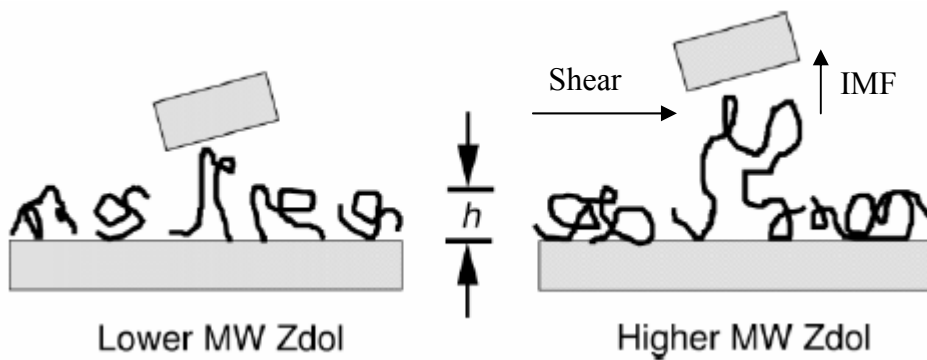


Figure 7.7: Depiction of molecular roughness for lower and higher lubricant molecular weights [14]. Directions of airbearing shear and intermolecular forces due to slider are also shown.

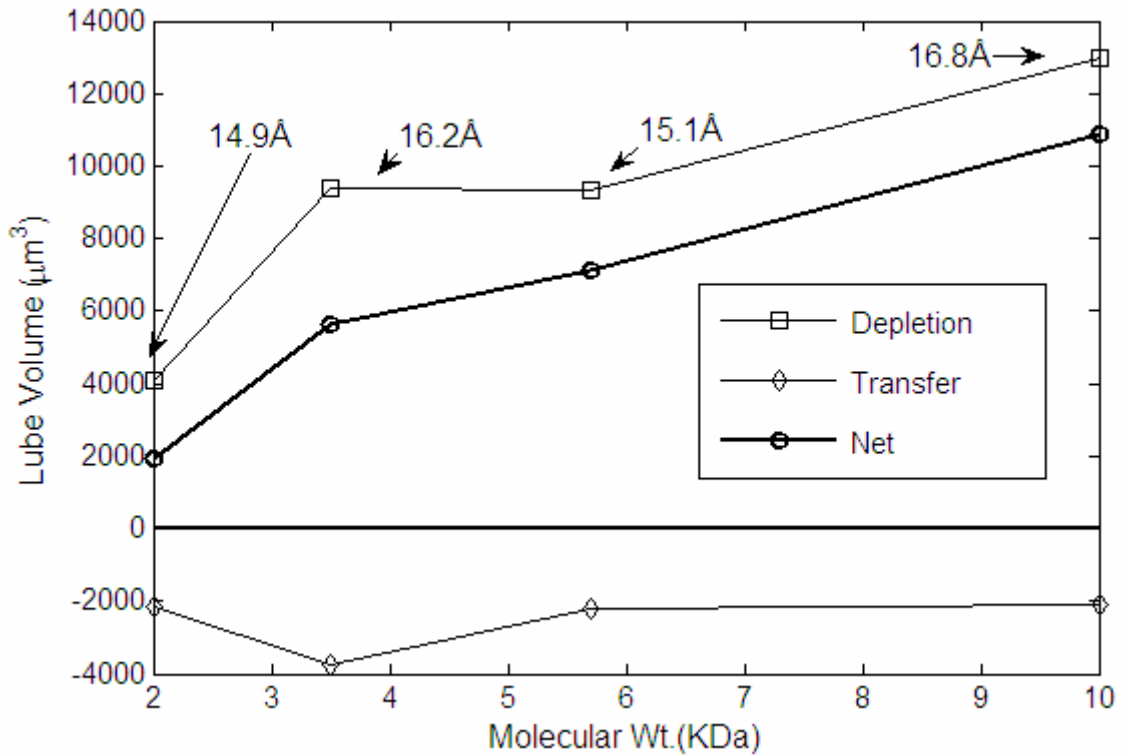


Figure 7.8: Fixed clearance tests: Dependence of lubricant volume depleted, transferred and the net lubricant accumulation on slider on lubricant molecular weight for Zdol with Femto B slider.

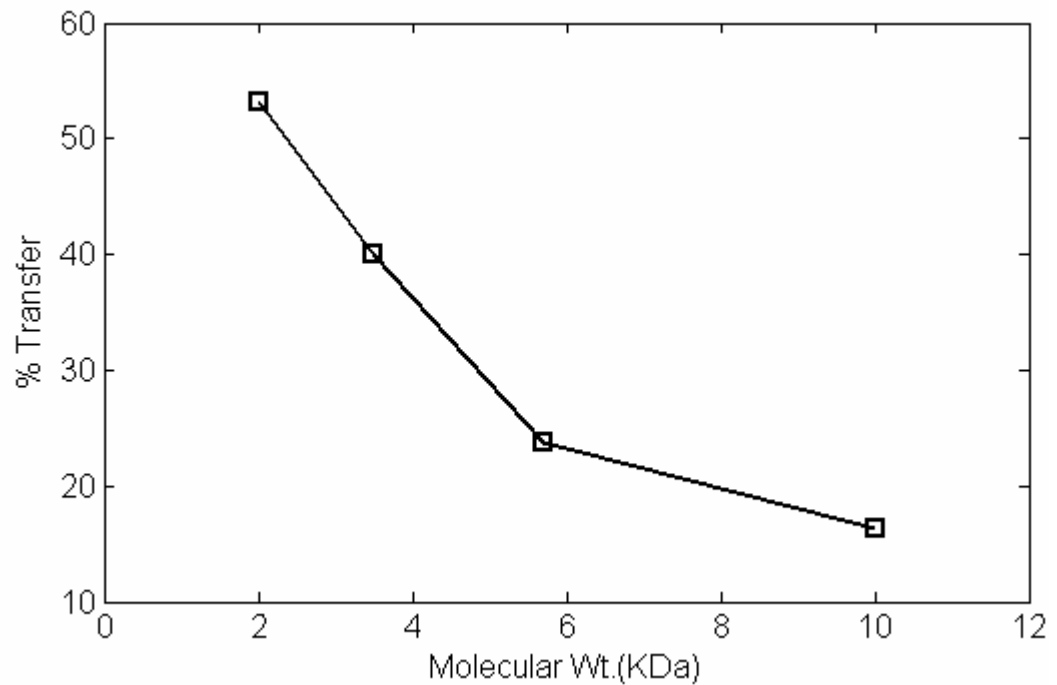


Figure 7.9: Lubricant transfer volume as a percentage of the lubricant depletion volume (Figure 7.8) for different molecular weights of Zdol for Femto B slider.

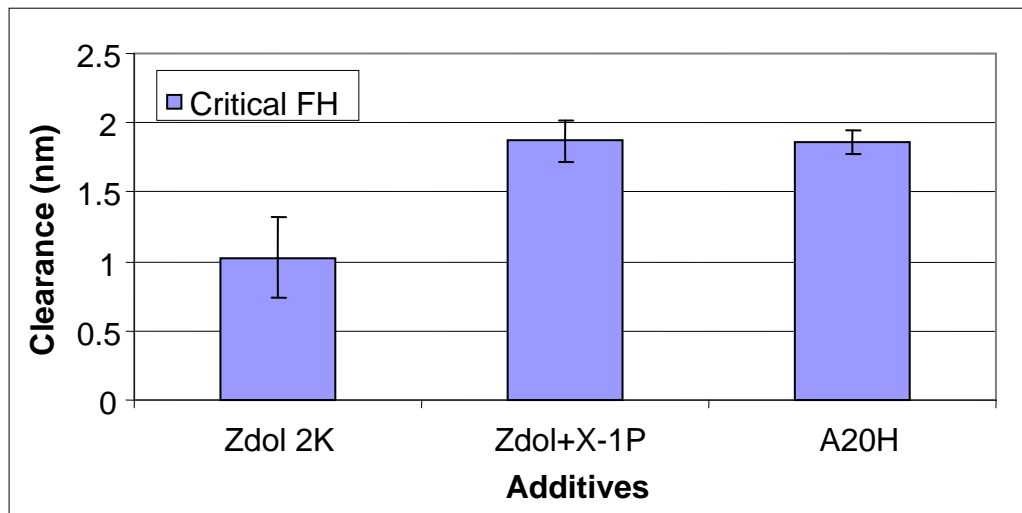


Figure 7.10: Dependence of critical clearance on inclusion of additives X-1P and A20H in Zdol 2000 for Femto B slider.

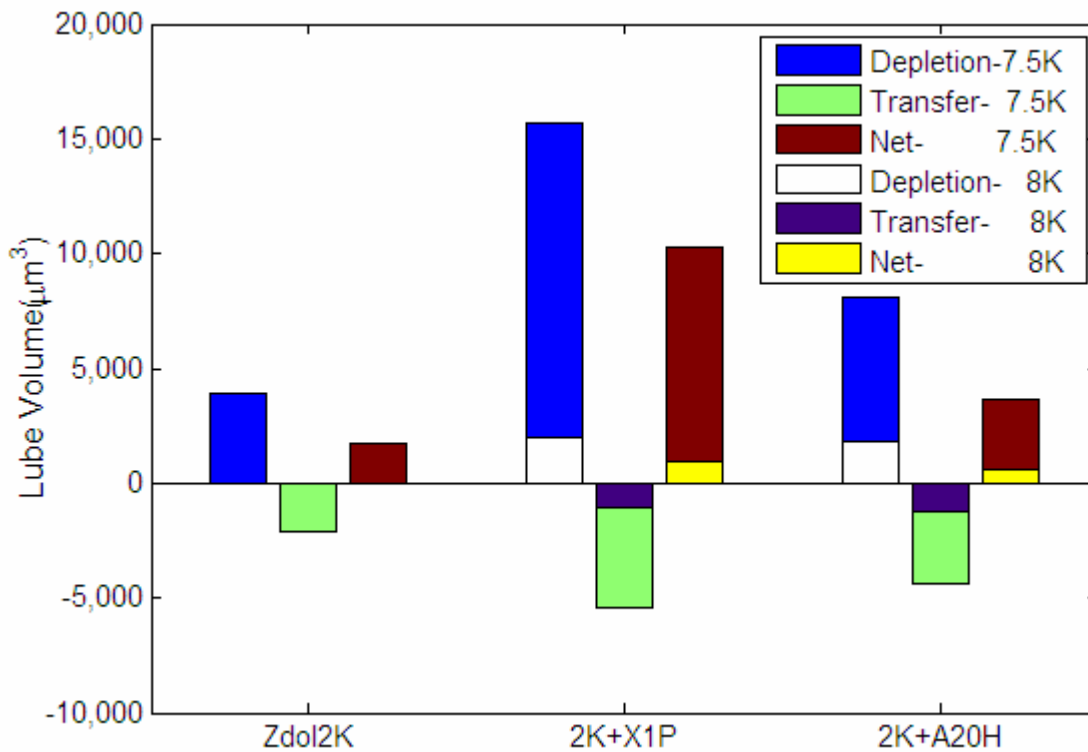


Figure 7.11: Fixed clearance tests: Dependence of lubricant volume depleted, transferred and the net lubricant accumulation on slider on inclusion of additives in Zdol with Femto B slider.

CHAPTER 8

EFFECTS OF RADIAL AND CIRCUMFERENTIAL DISK FEATURES ON SLIDER DYNAMICS

8.1 Introduction:

The study of the dynamics of sliders flying over disks is important to achieve better readback signal in current products, and is also critical for achieving stability at low flying heights essential for increasing the areal density. Various experimental and numerical studies have been carried out on slider dynamics. Some researchers have used Laser Doppler Vibrometer (LDV) to measure track topography and the resulting dynamics of the slider flying over the track [1]-[2], while others [3] have used the read back channel to measure the fly height modulation. Thornton et. al. [2] measured the disk track profiles with an LDV and used them as an input to the CML dynamics airbearing simulator to numerically determine the slider dynamics. They showed a good correlation between the experimental and numerical fly height modulation. However, all of the previous studies concerning the numerical fly height modulation simulation used measurements of only one track on the disk and simulate its effect on the slider dynamics. In reality, when a slider flies over the disk, its motion is influenced by the actual disk surface topography, which is two dimensional (lateral dimensions; third dimension is the height). Such a two dimensional topography also includes roughness and waviness features in the radial direction, the effect of which is not captured in the slider dynamics simulations conducted by using only a one dimensional track topography. Further, to measure the low amplitude - high frequency disk topography

features such as roughness and microwaviness, we need to use the velocity channel of the analog LDV since the low frequency noise floor overwhelms the actual topography if the displacement channel is used. The resulting velocity data is integrated to obtain the disk topography. In this approach, the constant of integration (DC part) of the profile is set arbitrarily as only the changes in the profile (AC part) are important. Hence, this approach cannot be used to create a true two dimensional map of the disk topography because of the inability to determine the constant of integration. So a digital LDV or heterodyne interferometers with low noise floors are required to measure the 2-D disk topography, as their displacement channels can be used directly. In this work the disk topographies are measured using a Candela 6300 system (Figure 8.1), which employs two independent low-noise laser channels to measure the slopes in the radial and circumferential directions [4]. The radial and circumferential information is combined to obtain the 2-D disk topography. The CMLAir dynamic simulator is used to simulate the slider dynamics of two different sliders over the measured 1-D and 2-D disk topographies to study the effect of the circumferential and radial disk features on the slider dynamics.

8.2 Experimental and Numerical Procedure:

In this study two different slider designs were used. Slider A (pico) is shown in Figure 8.2(a), while slider B (femto) is shown in Figure 8.2(b). In the first part of the study we examine the effect of 1-D circumferential features on slider dynamics using three 95 mm disks with different microwaviness features. Disk A is the roughest, while disk C is the smoothest, as measured by an LDV. The MD track (32 mm) of each of these disks was measured using the Candela 6300 system, and Figure 8.3(a) shows part

of the measured track, after it has been filtered through a high-pass filter of 3KHz to remove the disk runout and major clamping distortions. Figure 8.3(b) shows the frequency content of the disk topographies shown in Figure 8.3(a).

The measured circumferential (1-D) disk topographies were input to the CMLAir dynamic simulator, and simulations were conducted for both slider designs. A time step of $0.1\mu\text{s}$ with a total simulation time of 2ms (20,000 time steps) and disk rpm of 5400 was used. In this case no variation in the disk topography along the width of the slider (radial direction) is incorporated.

Since disk A was the roughest and had the most circumferential and radial variations, it was chosen for the second part of the study, viz. the investigation of the effect of radial features on the slider dynamics. Using the Candela 6300 system we obtained the radial as well as circumferential slope information around the MD (32 mm) track. A total of 351 tracks were measured with a radial spacing of $2\mu\text{m}$, from 31.65 mm to 32.35 mm, maintaining 32 mm as the center track. The slope information for the center track was integrated in the circumferential direction to obtain the 1-D disk topography, which is the same as that used in the previous section. In addition, the radial slope information was integrated from 31.65 mm to 32.35 mm for each measurement point along the center track. The DC shift between the radial tracks was provided by the value already known on the center track. Thus, by “weaving” together the radial and circumferential slope information we created a two dimensional (2-D) disk surface. Figure 8.4(a) and (b) show the 1-D and 2-D disk topographies. It should be noted that in Figure 8.4(b) the circumferential length (35 mm) is much larger than the radial width

(0.7 mm) of the track. Hence, the radial features are not as prominent as the circumferential features.

In preparation for performing the simulations we revived a previous capability of the CMLAir dynamic simulator to accept 2-D disk topography as input with a better format for the input file than it had previously (details in appendix A) and a faster implementation. Using this new simulator we conducted simulations with the 1-D and 2-D disk topographies of disk A for both slider designs. A time step of $0.1\mu\text{s}$ with a total simulation time of 2ms (20,000 time steps) was used. For the 2-D disk topography simulations, a large input file (128MB) and additional processing for determining the disk floor heights was required as 351 tracks (high resolution) were used. Even so, the simulation time increased only 30% compared to the 1-D disk topography simulations.

Finally, to identify the ABS modes of vibration observed in the power spectra and to aid further analysis, the CML Parameter Identification Program (CMLPIP) was used (Appendix B). This software utilizes the CMLAir dynamic solver to numerically perturb a steady state and provide the impulse response of an ABS in the vertical, pitch and roll directions. From the impulse response, the ABS modes are extracted along with their axes and damping. This information is shown in the modal diagrams in Figure 8.5 and Figure 8.6 for sliders A and B, respectively.

8.3 Results and Discussion:

To determine the steady state flying attitude of the sliders we used the CML static simulator, and the results are shown in Table 8.1. As seen there, slider B flies slightly higher than slider A, and it has lower pitch and roll. Using these steady state values as the initial conditions for the dynamic simulations, we obtained the response of

the sliders to the measured 1-D disk topographies. Figure 8.3(a) shows that disk A is the roughest while disk C is the smoothest disk as measured by the Candela 6300 system. The frequency content of the disks (Figure 8.3(b)) can be further divided based on the wavelengths of their features. In general, wavelengths greater than 100 μm are considered as micro-waviness (μW), those between 20 and 100 μm as nano-waviness (nW) and those less than 20 μm as roughness (R). For the disk rpm of 5400, these wavelengths correspond to less than 200 KHz, 200-900 KHz and greater than 900 KHz, respectively and these regions are marked in Figure 8.3(b). Based on this, it is seen that disk C has the lowest values of micro and nano-waviness and roughness. Disk A has the greatest micro and nano-waviness, while the roughness of disks A and B are comparable.

After characterizing the disks, the ABSs were also characterized for their modal frequencies using the CML PIP program. The result Tables along with the nodal lines are shown in Figure 8.5 and Figure 8.6 for slider A and B, respectively. From Figure 8.5, it is seen that Slider A has the dominant ABS frequencies at 75.8, 113.7 and 142.4 KHz. From the nodal lines (and modal animations included in the program), it is seen that the lowest mode is a coupled vertical – first pitch mode, the second is the roll mode while the third is the second pitch mode. Similarly, Figure 8.6 shows 166.3, 184.3 and 360.3 KHz as the roll, first pitch and second pitch modes, respectively, for slider B. The damping for all the modes is about 1-3% for both sliders.

As seen in Figure 8.7(a), the sliders followed the low frequency (large wavelength) disk features closely. However, high frequency features were not closely followed, resulting in modulations in the slider's flying height. The modulation in the slider flying height, or the fly height modulation (FHM), corresponding to Figure 8.7(a)

is plotted in Figure 8.7(b). It is indeed seen that only the high frequency components are present in this fly height modulation.

Figure 8.8(a) and Figure 8.9(a) plot the FHM and Figure 8.8(b) and Figure 8.9(b) plot the frequency content of the sliders' response for sliders A and B, respectively, on the disks A-C. For both sliders, the FHM correlates with the waviness of the disks i.e. the FHM is the greatest for disk A and the least for disk C. Table 8.2 indicates the standard deviation (3σ) values of the FHM for all of the slider-disk combinations. The simulations indicate that in order to have less fly height modulation, which directly correlates with the magnetic signal modulation, smoother disk topography is required.

From the power spectra the slider responses peaks are seen to correspond to the ABS modes, and they are marked by arrows. It is also seen that the modes of slider A are lower in amplitude than those of slider B. Further, the disk topographies mainly excite the coupled vertical – first pitch mode of slider A and the second pitch mode of slider B. Since there is not much difference in the high frequency features of disks A and B, the corresponding FHM frequencies are also similar for both the slider designs. However, lower frequencies are associated with higher amplitudes, and thus we see a large difference in the FHM on disks A and B. From Figure 8.8(a) it is seen that disk A excites the ABS frequencies of slider A much more than disk B. Disk C distinctly excites the coupled vertical-first pitch mode, but the overall amplitude for all frequencies for disk C is an order of magnitude lower than for disk A. This is in agreement with the FHM also being an order of magnitude smaller, as seen in Table 8.2.

We can do a similar analysis for slider B using Figure 8.9(b). It is seen there that all of the disks excite the second pitch mode as it is the most compliant. Only disk A

distinctly excites a low frequency ABS mode indicated in Figure 8.9(b) by an arrow. This is a coupled pitch mode, as the 1-D topography does not have any radial features to excite the roll mode of the slider. In general, the frequency spectrum is of higher amplitude for disk A than disk B below the second pitch mode frequency after which the spectrum for disk B is higher. However, lower frequencies (longer wavelengths) correspond to higher amplitudes due to which the overall FHM for disk A is much greater than that for disk B. The FHM for disk C is an order of magnitude lower than for disk A even in this case.

From the above analysis it is clear that disk C is the best choice for both ABS designs. The ABS modes of slider B are at higher frequencies, which help to reduce the FHM (3σ) on disk A as compared to slider A, but they are responsible for increasing the FHM for disk B. This suggests that the choice of the slider ABS design and disk should be correlated to obtain the best FHM performance. Thus, given a disk, the dynamic characteristics (ABS modes) of the slider need to be optimized for minimizing the FHM. Alternatively, if an ABS design is finalized, the disk choice can be made by studying the disk waviness spectrum. Transfer functions [2] can also be used to avoid separate dynamic simulations for each disk topography.

Many researchers have analyzed different aspects of FHM using 1-D disk topography, both numerically and experimentally. However, as the slider flies on an actual disk surface which is 2-D, its dynamics can be captured more accurately using 2-D disk topography as an input to the simulator. Also, these numerical dynamics simulations using 2-D disk topography should be closer to the experimentally observed slider dynamics. Thornton et. al. [2] did a comparison between numerical slider

dynamics using 1-D disk topography and experimental slider dynamics. They found good correlation between the two. However, the dynamics do not exactly match. In this study, similar observations were made when simulations were conducted with 1-D and 2-D disk topographies. As mentioned in the previous section, the topography of disk A was used as an input because it exhibited maximum variation. The FHM for sliders A and B are plotted in Figure 8.10(a) and Figure 8.11(a), respectively. The corresponding frequency spectra are plotted in Figure 8.10(b) and Figure 8.11(b). Table 8.3 shows the standard deviation (3σ) of the FHM.

Table 8.3 shows about 15% and 22% increase in the FHM of slider A and B, respectively, when the 2-D disk topography is used. Upon analyzing the frequency spectra in Figure 8.10(b), we see that the 2-D disk topography excites the first pitch mode of slider A about 2.5 times more than does the 1-D topography. Further, the second pitch mode is only excited by the 2-D topography. These increases are responsible for the increase in the FHM. We did a similar analysis for slider B from Figure 8.11(b). In this case a general increase is seen in the spectrum corresponding to the 2-D topography, notably the second pitch mode. This leads to a greater percentage increase in the FHM of slider B for 2-D disk topography.

Thus, the simulations indicate the slider B is affected by 2-D topography more than slider A. One of the reasons for this is the pressure distribution under the sliders. This is plotted in Figure 8.12(a) and (b) for sliders A and B, respectively. Depending on this pressure distribution and hence the pitch and roll of the slider, different tracks affect the slider dynamics to different extents. The higher the ABS pressure on a track, the more the slider dynamics are affected by that track. In 1-D topography, this aspect is

missed since we only consider the central track. Figure 8.12(a) and (b) show that the high pressure points are not exactly along the center track for sliders A and B. Therefore, the center track is not the track affecting the slider dynamics the most. From the analysis of the pressure plot in Figure 8.12(b), we see that the pressure peak is about $10\ \mu\text{m}$ towards the ID from the center line of slider A and about $58\ \mu\text{m}$ towards the ID from the center line of slider B. Since the tracks corresponding to the maximum pressure affect the slider dynamics the most, we consider the difference between the topographies of these tracks and the center track for the two sliders. This difference is plotted in Figure 8.13(a) and (b) for sliders A and B, respectively. The standard deviation (3σ) of the difference for slider A was $2.68\ \text{nm}$ while that for slider B was $7.62\ \text{nm}$. The difference for slider B is much greater because the maximum pressure track is farther away from the center track as compared to slider A. Due to this, the net increase in FHM is much more in slider B when 2-D disk topography is included.

The effect of 2-D disk topography can be even more important at high skew angles, where the slider dynamics are influenced by more tracks as compared to the zero skew case considered in all the previous simulations. Figure 8.14(a) shows the FHM for slider A at a skew of 17.6° ($32\ \text{mm}$, $5400\ \text{rpm}$) in response to 1-D and 2-D disk topographies. From the figure, it is seen that slider A has multiple contacts with the disk when 2-D disk topography is considered but not with 1-D topography. The main reason for this is the relatively large roll (-1.54°) and high skew together cause more interaction with tracks farther away. The FHM (3σ) for 1-D and 2-D topographies were calculated to be $15.07\ \text{nm}$ and $23.98\ \text{nm}$. Thus, there is an increase of 59.1% in the FHM when the 2-D disk topography is used. This increase in the FHM is mainly caused by multiple

contacts, which excite the pitch modes of the ABS (Figure 8.14(b)). Thus, the 2-D disk topography also gives a more accurate picture of the flyability of an ABS design.

From the above analysis it is clearly seen that the slider dynamics is affected by all of the tracks under the slider and not just the center track. Further, the influence of the center track on the slider dynamics depends significantly on the ABS design. Due to the radial disk features there is a difference between the topographies of adjacent tracks and this difference increases as the tracks become farther apart. Thus, FHM due to radial features is reduced when the maximum pressure is concentrated on the center track. FHM due to circumferential features is reduced when maximum pressure is concentrated near the transducer, which reduces the lag between disk topography and the slider response [5]. By combining these observations, we conclude that FHM is reduced when the pressure is concentrated under the transducer along the center track. However, this may have other consequences such as reduced pitch and roll stiffnesses which may also affect the dynamic performance and contact recovery of the slider. Nonetheless, it is a design parameter to be considered in ABS design.

8.4 Conclusions:

- (a) In this chapter we investigated the effects of circumferential and radial disk features on the slider dynamics. Two slider designs and three disk types were used for this study. The CMLAir dynamics simulator was used as the simulation tool, while the new Candela 6300 system was used for obtaining the 2-D disk topography.
- (b) From the first part of the study we conclude that circumferential features of micro and nano waviness affect the fly height modulation as they excite

different ABS modes. Further, the ABS design and disk features need to be correlated to obtain the best FHM performance.

- (c) Inclusion of 2-D disk topography in the dynamic simulations is more realistic since the slider actually flies over a 2-D surface. Based on the slider's design and its pressure profile, we found that different tracks have a varying influence over its dynamics. The center track, which is typically used in simulations as 1-D disk topography, may have less influence than its adjacent tracks. Hence, 2-D disk topography should be included in the dynamic simulations.
- (d) Higher skew angles are associated with higher roll, and the slider dynamics are influenced by even more tracks than at lower skew. Under these conditions, 2-D disk topography can prove useful in providing the correct picture about the flyability of an ABS design.
- (e) Simulations with CMLAir using 2-D disk topography increased the simulation time by only 30% as compared to 1-D disk topography as input, even with quite high resolution along the radial direction for the 2-D disk topography.

	FH (nm)	Pitch (μrad)	Roll (μrad)
Slider A	11.35	263.8	1.27
Slider B	14.59	126.4	-0.15

Table 8.1: State state flying attitude of sliders

	Disk A	Disk B	Disk C
Slider A	10.28	2.96	0.77
Slider B	9.66	3.50	1.27

Table 8.2: Standard deviation (3σ) values of FHM for different slider disk combinations (in nm)

	1-D	2-D
Slider A	10.28	11.84
Slider B	9.66	11.81

Table 8.3: Standard deviation (3σ) values of FHM corresponding to 1-D and 2-D disk topographies (in nm)

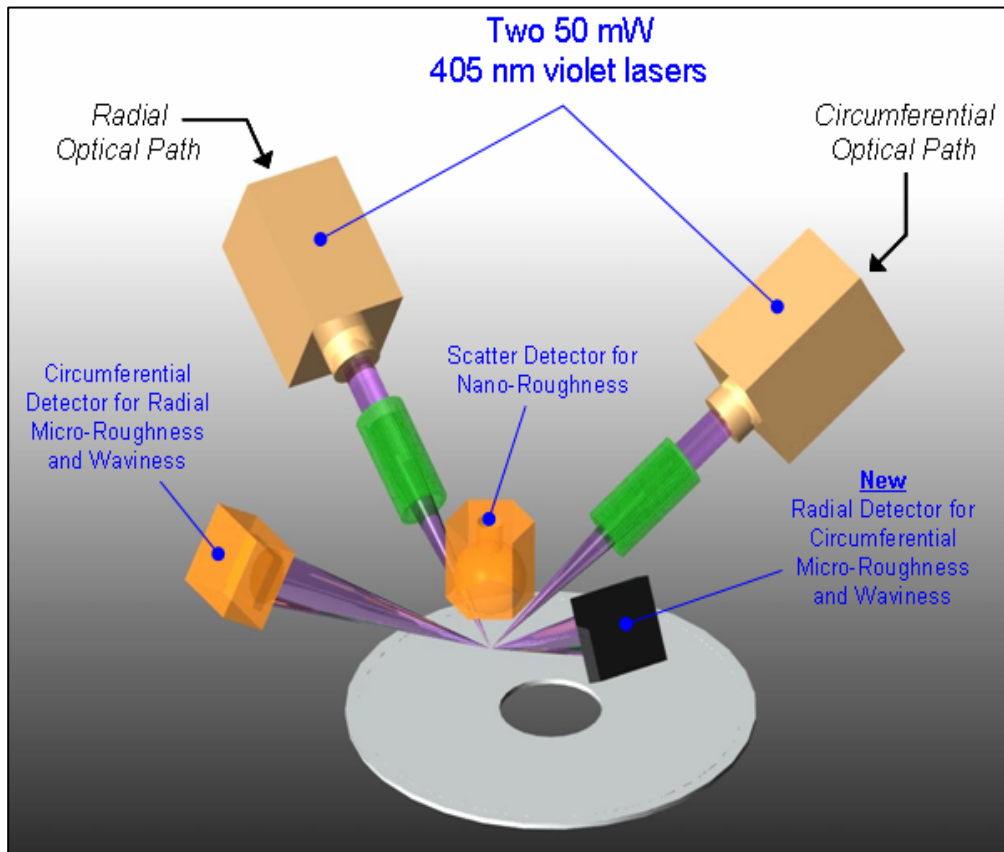


Figure 8.1: Candela 6300 surface topography measurement technique (Source: KLA-Tencor /Candela)

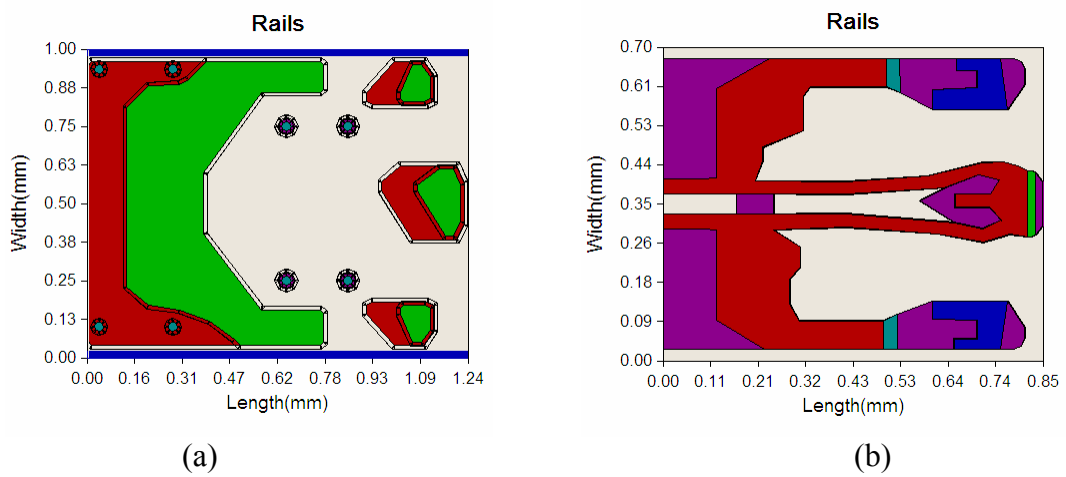


Figure 8.2: ABS Designs used for simulations; (a) Slider A (Pico) and (b) Slider B (Femto) design

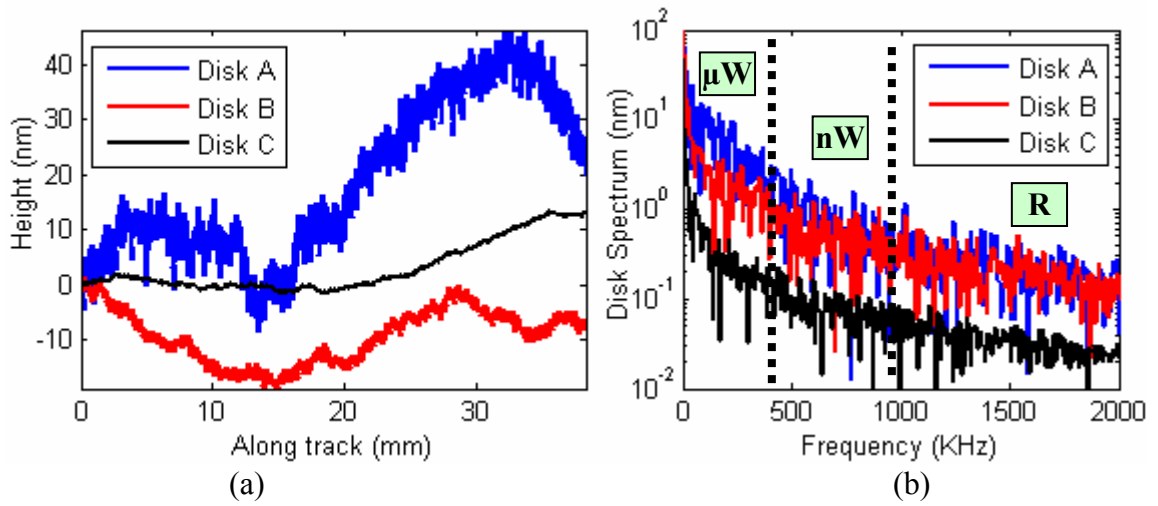


Figure 8.3: Circumferential topography (1-D) of three disks measured at MD by Candela 6300

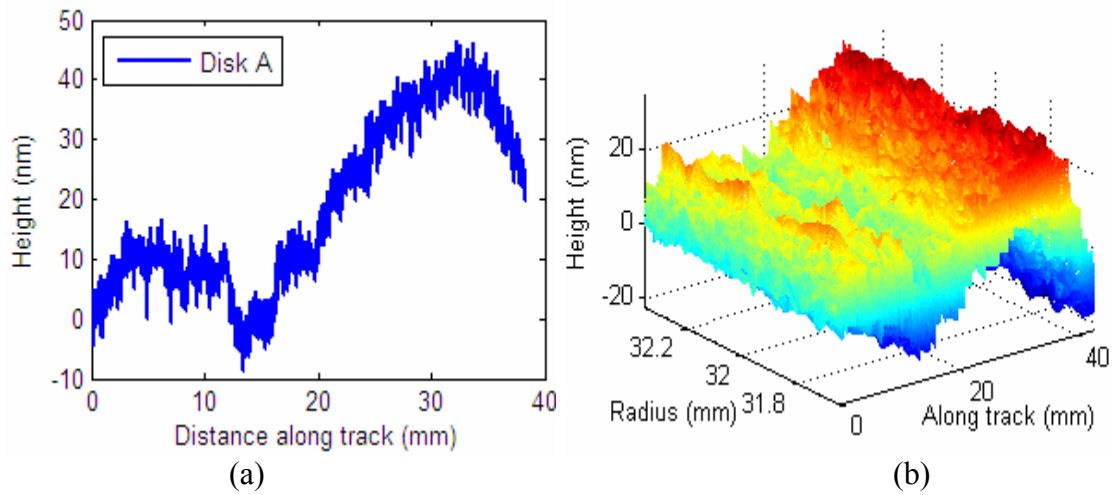


Figure 8.4: (a) 1-D disk topography of the center track; (b) 2-D disk topography obtained from integrating the slope in radial direction and “weaving” it with the center track profile.

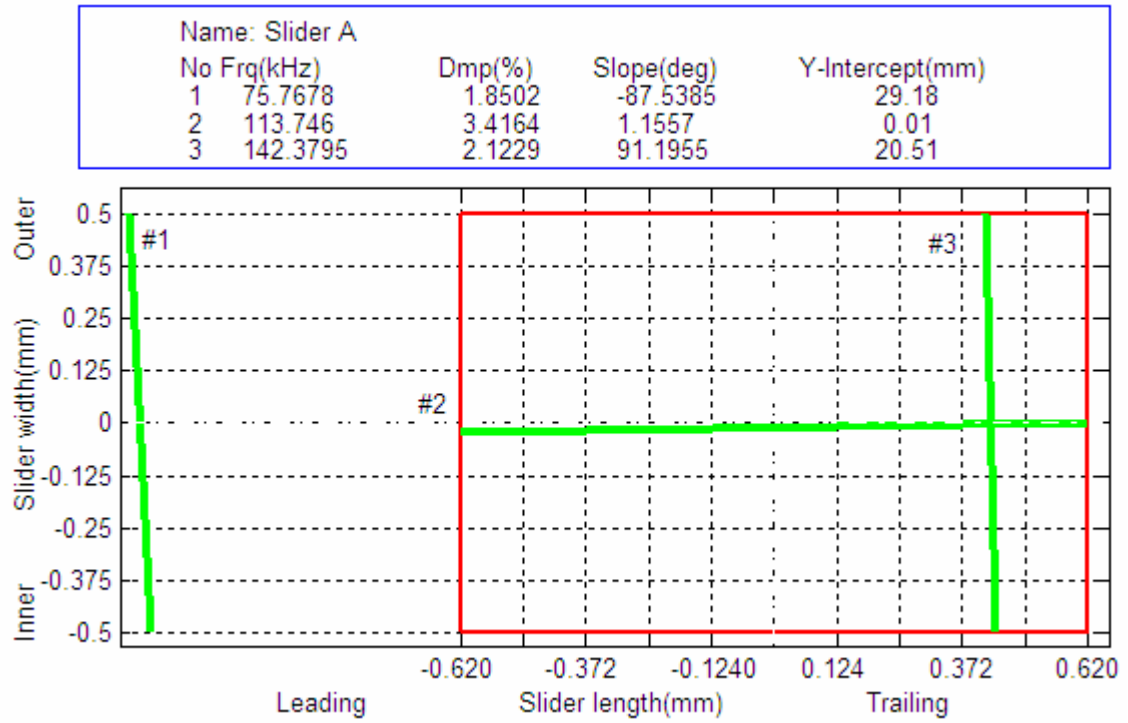


Figure 8.5: Modal diagram for Slider A

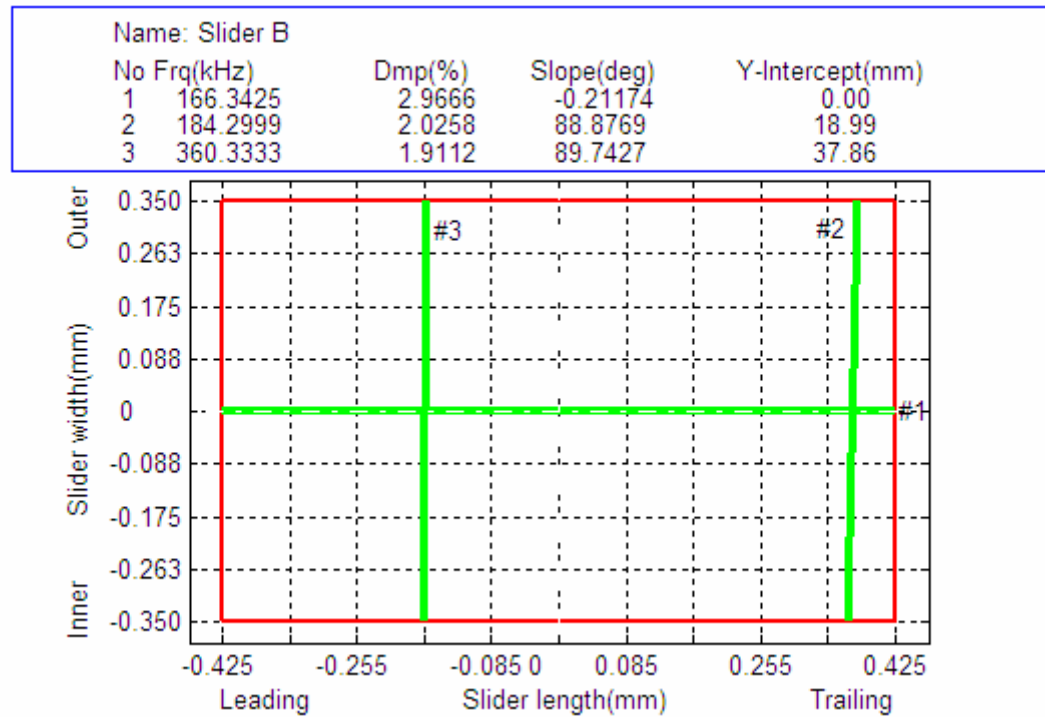


Figure 8.6: Modal diagram for Slider B

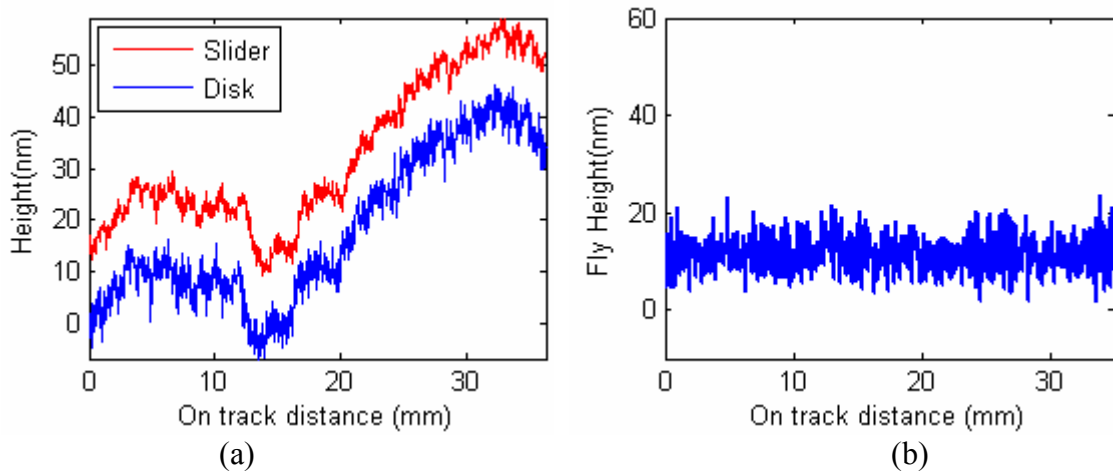


Figure 8.7: (a) Slider following the disk profile; (b) Net fly height of the slider above the disk

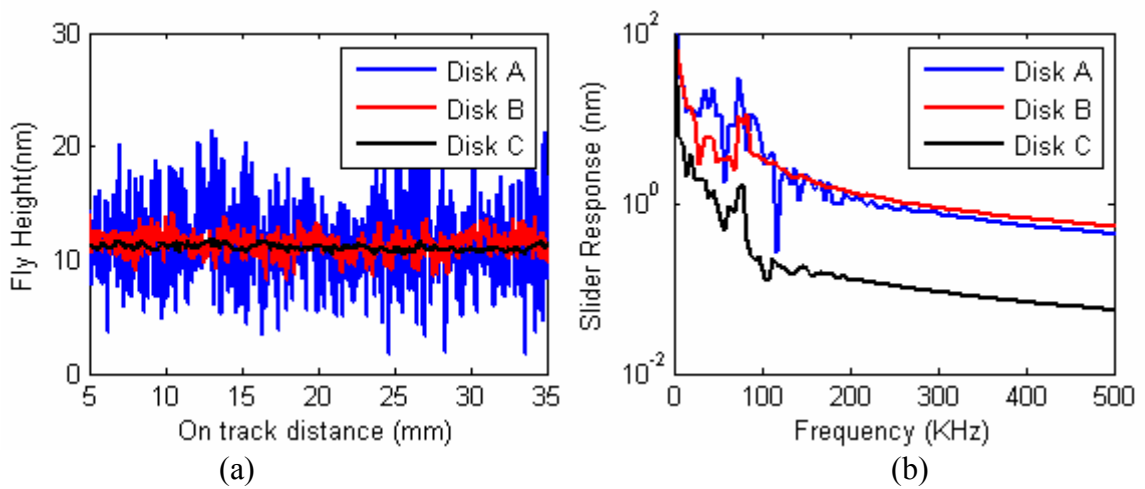


Figure 8.8: (a) Fly height modulation of Slider A relative to 1-D disk topographies; (b) Frequency content of the response of Slider A

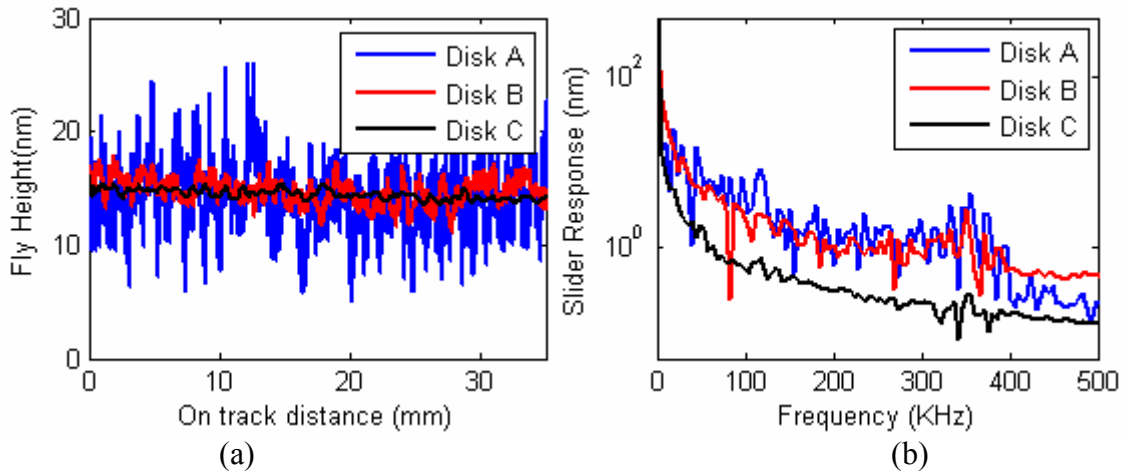


Figure 8.9: (a) Fly height modulation of Slider B relative to 1-D disk topographies; (b) Frequency content of the response of Slider B

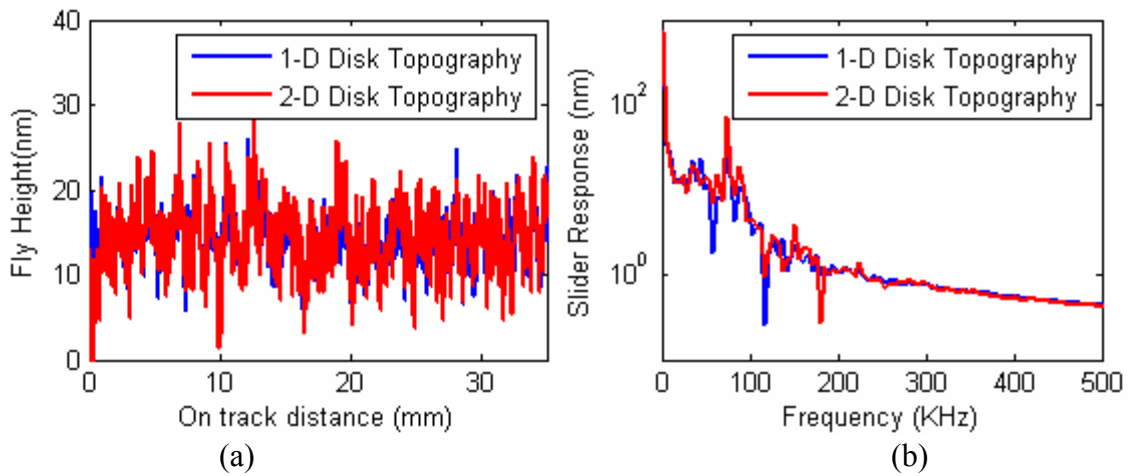


Figure 8.10: (a) Fly height modulation of Slider A relative to 1-D and 2-D disk topographies; (b) Frequency content of the response of Slider A

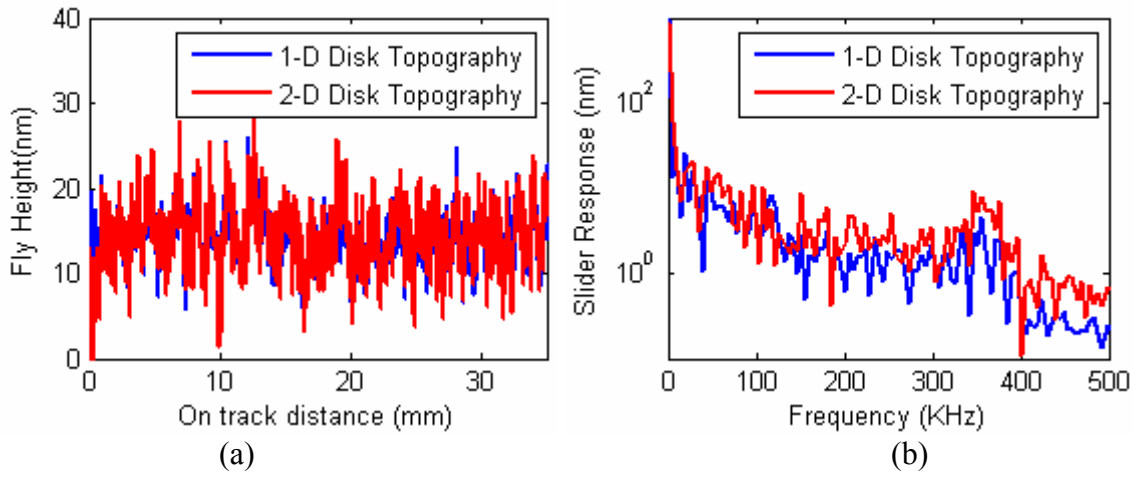


Figure 8.11: (a) Fly height modulation of Slider B relative to 1-D and 2-D disk topographies; (b) Frequency content of the response of Slider B

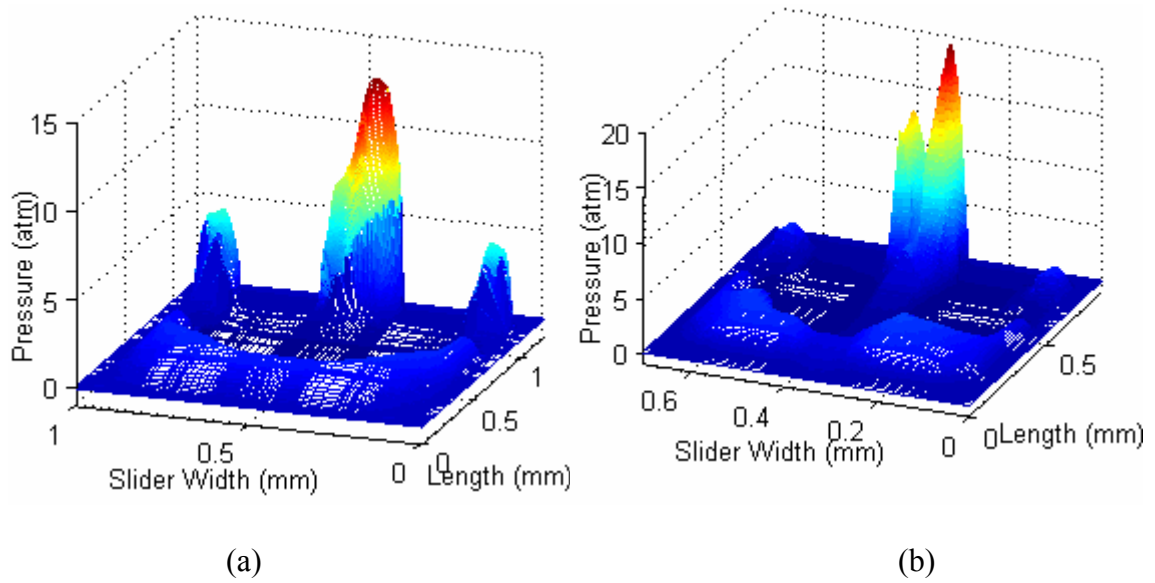


Figure 8.12: (a) Pressure distribution of Slider A; (b) Pressure distribution of Slider B.

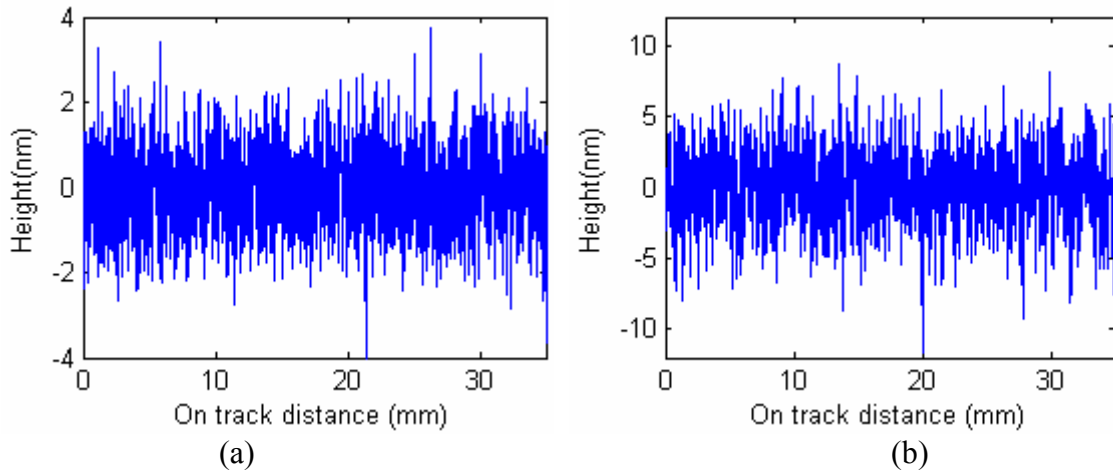


Figure 8.13: Difference in topography of the track corresponding to maximum airbearing pressure and the center track for (a) Slider A and (b) Slider B.

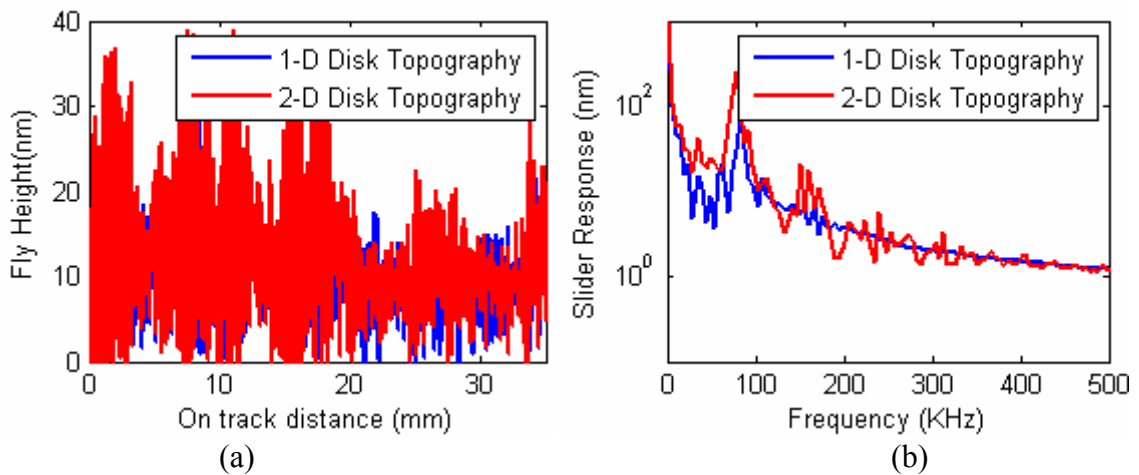


Figure 8.14: At skew angle of 17.6° : (a) Fly height modulation of Slider A relative to 1-D and 2-D disk topographies; (b) Frequency content of the response of Slider A

CHAPTER 9

CORRELATIONS BETWEEN DIFFERENT PHENOMENA AT THE HEAD DISK INTERFACE

9.1 Introduction:

To achieve a recording density of 1 Tb/in², the head-disk mechanical spacing has to be reduced to 2-3 nm. At this spacing, different proximity interactions such as intermolecular forces, meniscus forces and electrostatic forces influence the ability of the slider to fly stably over the disk. Reduction of or compensation for these forces is desired for better HDI reliability and the realization of this recording density goal. Hence, much research has been carried out in the recent past to study these proximity interactions. Different studies (either experimentation or modeling) attribute the loss of stability to one or some of these factors.

However, in this chapter, we attempt to show that there is a causal relationship between intermolecular, meniscus and electrostatic forces, and hence, though apparently different in their macroscopic manifestation, they have common origins and so at some level they may not be separate interactions. This is especially relevant as atomic length scales are approached where the connections between these interactions are realized. Hence, a chart has been organized to show some connections between the various interactions and phenomena that affect the HDI. The relevant literature where studies have been reported regarding particular interactions, phenomena or connections are cited along with the description or explanation of the phenomena/connections. The goal here is to give an overview or a perspective of the various efforts made to develop different

theories or increase the reliability of the HDI. However, the details, such as descriptions of the studies, figures etc. from each reference are not included for the sake of continuity and focus.

The general surface phenomena/interactions as well as those specific to the HDI are included in the same chart, and connections are made between the two sets. This enables the description of some HDI phenomena in terms of the general models used. Also, there are some phenomena, such as disk-to-slider lube transfer, which have not been studied completely. The organization of the chart and the relative placement of some of the interactions suggest some approaches to modeling such phenomena. Note that the words ‘interactions’ and ‘phenomena’ are used almost interchangeably and really mean ‘interactions or phenomena’, since both are included in the chart.

9.2 Chart Organization:

Different interactions or phenomena are put in boxes and joined by arrows, which show a causal relationship. The phenomenon to which an arrow is pointing is caused by the phenomenon from which the arrow emanates. Further, the phenomena are arranged from bottom to top as going in scale from microscopic to macroscopic phenomena. Since microscopic phenomena are dealt with by discrete theories and the macroscopic phenomena are dealt with by continuum theories, there is a natural progression from the discrete to the continuum theories as the chart is traversed from the bottom to the top. Each arrow, which indicates the relation between two phenomena, is labeled. These connections are described and explained in the next section in the alphabetical order of their corresponding labels. Solid arrows are used for the connections between phenomena

not necessarily restricted to HDI, while dashed arrows signify connections specific to HDI.

9.3 Correlations:

A brief account of each correlation indicated by a label is given below:

- A. Thermodynamic and Chemical Phenomena are based on atomic interactions. Thus they form a theoretical basis for describing the atomic interactions within a material or between different materials and form the basis of all theories. Thermodynamics is concerned with the physical parameters of temperature, pressure, volume and entropy, while chemistry deals with the transfer of electrons, ions, etc. and the associated energies and potentials.
- B. The presence of electrostatic forces at the atomic level is a result of the interactions between the charged atomic particles (A1) as negatively charged electrons revolve in specific orbits about the positively charged nucleus in an atom. Specific to the HDI, the presence of electrostatic forces at the macroscopic level is a result of tribocharging [1]-[3], the magnitude of which depends primarily on the electrochemical potential (A2) (thermo-chemical parameter) of the head and the disk surfaces [4]. Recurrent head-disk contact leads to this tribocharging. At this point, no distinction is made between the microscopic and macroscopic manifestation of electrostatic forces, but this will be done later.
- C. Since tribocharging is very pertinent to the study of the HDI a short explanation of how it occurs is presented: When two different materials come into contact there is an electron transfer from one material to the other depending upon the work functions of the materials [4]. This transfer occurs until the electrochemical potential

of both materials is equalized, which results in an equilibrium of this electron transfer process. Materials have been classified into a “triboelectric” series depending upon the amount of charge they acquire when touched by another material [5].

D. At the HDI, electrostatic force (due to tribocharging) affects the stability of the slider at proximity[6]. It influences the flying dynamics of the slider [2] and the lubricant migration on the disk [7]. Thus, it is detrimental to the reliability of the HDI. Further, tribocharging may cause electrostatic discharge (ESD), due to which the magnetic transducers are damaged [3].

E. Intermolecular forces have their origin in electrostatic forces according to the *Hellman-Feynman theorem*, which states that once the spatial distribution of electron clouds has been determined by solving the Schrödinger equation, the intermolecular forces can be calculated on the basis of straightforward classical electrostatics [8].

In a material, individual molecules may be permanently polarized or may have induced polarization, which produces a dipole moment. This dipole-dipole interaction between different molecules leads to intermolecular forces [8]. There are primarily three components of intermolecular forces, depending on the nature of the dipole-interaction.

Keesom force - Permanent dipole – Permanent dipole. This force can be attractive or repulsive.

Debye force – Permanent dipole – Induced dipole. If there is a molecule with a permanent dipole the electric field due to it induces a dipole in an otherwise unpolarized molecule.

Dispersion force – Induced dipole – Induced dipole. In a non-polar atom the electron cloud is not perfectly homogeneous, which produces a dipole moment. Although the time average of this charge imbalance is zero the instantaneous dipole induces a dipole in other atoms in proximity to it, and the time average of this interaction is not zero and is responsible for dispersion force [8].

The Debye and dispersion forces are always attractive in nature. The Keesom and Debye forces only exist when there are permanently polarized molecules, while the dispersion forces are *always* present. In the above discussion of intermolecular forces only the contribution of the microscopic electrostatic forces has been considered. Additionally, when tribocharging occurs at the HDI the electric field at the surface of the head or disk is changed due to which intermolecular force will also change. The spatial distribution of all charges under the changed electric field needs to be calculated in order to determine if this change is significant.

- F. Surface tension is a direct measurement of intermolecular forces [9]. In a bulk material, an individual molecule is surrounded by other molecules on all sides, and it experiences forces from these molecules. However, for a molecule on the surface of the material other molecules of that material only lie to one side and thus there is an imbalance in the force it experiences, and consequently there is a tension at the interface due to this unbalanced force. This is the basis of surface tension of the material [10]. The surface energy is the amount of energy stored when a surface with surface tension σ is expanded by a unit area. Since the numerical value and the units of both quantities are the same surface tension is also considered as surface energy.

Surface energy for a material has two components – polar and dispersive. The dispersive component is always present and is due to dispersive intermolecular forces.

G. The polar component of the surface energy is a result of polar molecules, and thus it can be perceived as a result of Keesom and Debye intermolecular forces. This contributes to most of the observed surface energy in metals. The presence of surface charges also changes the surface energy of materials [11]. Hence, the polar component of the surface energy may change significantly due to tribocharging at the HDI.

H. Friction and wear theories based on adhesion use surface energy [12]-[13] to calculate the work of adhesion, which is a measure of energy required to form a particular interface. Both friction and wear are dependent on the combined effect of hardness and surface energy. Generally, a high surface energy is indicative of more friction and wear. Metals generally have a very high surface energy while non-metals have low surface energy. Surface energy relations are also used to determine the wetting/dewetting thickness of lubricants, which has a direct bearing on HDI reliability.

The disjoining pressure is the negative of the derivative of the surface energy with respect to the film thickness. It appears in lube depletion and transfer models and also in equations governing thin fluid films due to the dependence of their surface energy on the film thickness [14].

I. Surface energies of different phases/materials dictate wetting or dewetting of a liquid on a substrate and the formation of specific contact angles. Hence, surface energy can be determined from contact angle measurements [14]-[16]. Modeling of a meniscus

uses surface energy as a basis along with other continuum mechanics relations [17]-[19]. The meniscus force depends on the surface energy of the meniscus fluid (lubricant or adsorbed water). It should be noted here that the surface energy itself depends on intermolecular and electrostatic forces.

- J. Various studies ([17]-[19]) have shown meniscus force to be the main cause of stiction at the HDI. Further, it is also thought to be a major factor contributing to dynamic friction and loss of stability by increasing the touchdown-takeoff hysteresis [17].
- K. Just as surface energy of a material is a result of its interatomic interactions, the strength of which is given by the IMF, so is the hardness [12]. Hence, if the IMF is very strong in the material, it is dense and/or hard. It should also be noted that denser materials generally have a high refractive index, which is used to calculate the Hamaker constants used in the IMF calculation. It is found from these calculations that across the same interface denser materials typically have more IMF interaction. Thus the magnitudes of IMF and density/hardness/refractive index are related to each other.
- L. Friction and wear are intimately related to hardness of the material. Continuum theories of adhesion and abrasion include hardness as a parameter [12]-[13]. Absolute and relative hardness of the various layers at the HDI have a direct bearing on its reliability.
- M. IMF is the basis for properties such as surface energy and hardness on which the friction and wear depends. Thus, IMF indirectly affects the HDI reliability. However, as the head-disk spacing is reduced below 5 nm various studies have shown that IMF

directly affects the stability of the air bearing slider [20]-[21]. Multilayer models are used to calculate the Hamaker constants used in the calculation of IMF [20],[22] between the slider and the disk. It has been shown that the magnitude of the IMF is significant as compared to the airbearing forces and the external ‘gramload’ applied to the slider.

By traversing the chart from labels A – K, we have been able to relate electrostatic forces, intermolecular forces, surface energy and meniscus forces and to appreciate the causal relationship between them. Hence the question of whether electrostatic, intermolecular and meniscus forces independently influence the HDI should be examined closely.

N. Recently, the phenomenon of disk-to-slider lubricant transfer has gained some attention, but it has not yet been modeled completely. Some experimental studies [2] of the effect of the disjoining pressure and surface energy of the lubricant on the lubricant transfer (M2) have been reported. Airbearing pressure has also been shown to influence the lubricant transfer [24]. Based on the chart a few more possible contributions to this phenomenon are described.

Atomic distances between the slider and the disk present the possibility of physical transfer of lubricant between the slider and the disk surfaces, which may be modeled on the basis of IMF attraction (L2) of the atoms of the polymer molecules by the slider and disk surfaces using statistical mechanics. Such an approach can calculate the probability of a molecule landing on the slider’s surface based on parameters such

as activation energy/ bond energy of polymer molecule (L3) and air shear. Electrostatic force may be another cause of the lubricant transfer (L4). There is a charge on the slider and disk surfaces including the polymer film due to tribocharging. Further, head-disk contact, catalytic degradation etc. may lead to the breaking of long chain lubricant molecules into short fragments with unsatisfied bonds, giving them a charge. Thus, this lubricant molecule or fragment may be attracted to the charged slider contributing to the lubricant transfer.

- O. Besides the above approach of physical transfer of lubricant by different forces evaporation and condensation (thermo-chemical phenomena) (M1) are used in modeling or explaining the transfer of lubricant from disk to slider [24]-[2]. This model [2] also considers the contribution of disjoining pressure of the lubricant (M2). We note that evaporation or condensation is also a physical transfer, but instead of the above mentioned discrete/ probabilistic approach of lube transfer, it is based on a continuum approach.
- P. Lube transfer/pickup is often sighted as one of the factors causing the meniscus (N1) [17]-[18]. However, since the duration of slider-disk contact is usually much less as compared to the time scale estimated to form a lube meniscus (using continuum theory) [21], a continuum lube meniscus picture may not be an accurate visualization of the actual phenomenon. Nevertheless, it has been observed that lube pickup affects the slider stability [26], which may be alternatively explained on the basis of surface energy (N2) since the equilibrium time scale for surface energy is the same as that of intermolecular forces, which is instantaneous even compared to the time scale of

slider-disk contact. However, this is a macroscopic empirical theory [13] and a more accurate discrete theory for meniscus force calculation is necessary.

- Q. Water adsorption on the surface of the disk from ambient humidity is another reason sighted for meniscus formation [17]-[18]. The adsorption can be explained in terms of thermo-chemical phenomena by describing the affinity of water molecules towards the active sites on the carbon overcoat.
- R. The effect of water adsorption on the HDI can be modeled in a similar way as the lube transfer (N) as: due to meniscus formation (P1) or as due to the increase in the surface energy (P2). The adsorbed water occupies the active sites on the carbon overcoat ([14],[27]) thus loosening the lube bonds with the carbon overcoat, and thereby decreasing its viscosity and aiding in lube transfer (P3).
- S. Water adsorption is responsible for passivating the catalytic centers responsible for the chemical degradation of the lube [28]. However, it also assists in corrosion of the carbon and magnetic layers.
- T. The reactions responsible for disintegration of the lubricant at the HDI can be explained by thermo-chemical phenomena, such as hydrogen bonding, electron transfer etc. [29]-[30](S1). In addition to such mechanisms, the lubricants also degrade under electric fields [31] (S2).
- U. The chemical degradation of the carbon overcoat aids in faster degradation of the magnetic layer thereby leading to the loss of data stored [29]-[30] and compromising the HDI reliability.

9.4 Discussion:

From this chart it can be seen that electrostatic, intermolecular and meniscus forces are related. The meniscus formation is modeled in terms of a continuum theory and the meniscus force depends on the surface tension of the meniscus fluid. This surface energy has two components: polar and dispersive, the origins of which can be traced to electrostatic and intermolecular forces. We further note that the HDI spacing is being reduced to atomic length scales and the period of head-disk contact is much smaller than the time required to form an equilibrium meniscus. Thus we may no longer be able to use the continuum concept of meniscus and instead have to use a more basic theory (which occupies a lower position in the chart) to calculate this force. The chart suggests that the meniscus force can be modeled directly in terms of intermolecular and electrostatic forces. The mechanisms proposed in Chapter 6 for slider-lubricant interaction (which causes meniscus force) are based on the effect of intermolecular and electrostatic forces and also support this. Further, the time scales for IMF and ESF are far less than the duration of the head-disk contact and the equilibrium theories for these interactions could be used. However, since the intermolecular and electrostatic forces depend on the position of individual atoms and molecules (of DLC and lube) at the interface and the distance between them, the calculation of the exact force can be commensurately difficult, and a statistical mechanics/Monte-Carlo type approach may need to be considered. It can be appreciated that the meniscus force is a direct result of intermolecular and electrostatic forces, and hence as the length and time scales become smaller it can be calculated directly in terms of these interactions.

The “mesoscopic” length scales lie between the microscopic and macroscopic ones and in these there is an inter-relation of the microscopic and macroscopic theories. The HDI length scales lie in this region as we are simultaneously using macroscopic theories such as the continuum Reynolds equation with modified parameters derived from microscopic theories like the Boltzmann equation (F-K model). From the chart it can be seen that the macroscopic concepts like surface energy and hardness have their roots in microscopic phenomena, and thus it can be said that any theory which can calculate these macroscopic parameters from the microscopic phenomena is mesoscopic in nature. Hence, theories for disk-to-slider lube transfer, water adsorption and chemical degradation, which can be explained in terms of intermolecular attraction or ion/electron exchange etc., occupy the place in the chart corresponding to mesoscopic theories.

9.5 Conclusions:

A chart has been organized to show the connections between different interactions or phenomena occurring at the HDI. Such an organization, in addition to providing an overview of the work in HDI reliability, also acts as an instrument to help understand the relationship between different phenomena, and it can be used to suggest modeling approaches to those phenomena that have not yet been modeled completely.

The chart has been organized with microscopic phenomena at the bottom proceeding towards macroscopic phenomena at the top showing the causal relationships between different phenomena. By observing this causal relationship it can be appreciated that meniscus force depends upon the intermolecular and electrostatic forces, and as the time and length scales at the HDI reduce, the meniscus force can be calculated directly in terms of the intermolecular and electrostatic forces. The disk-to-slider lube transfer has

not yet been modeled completely. Possible approaches for modeling this phenomenon are suggested by the chart.

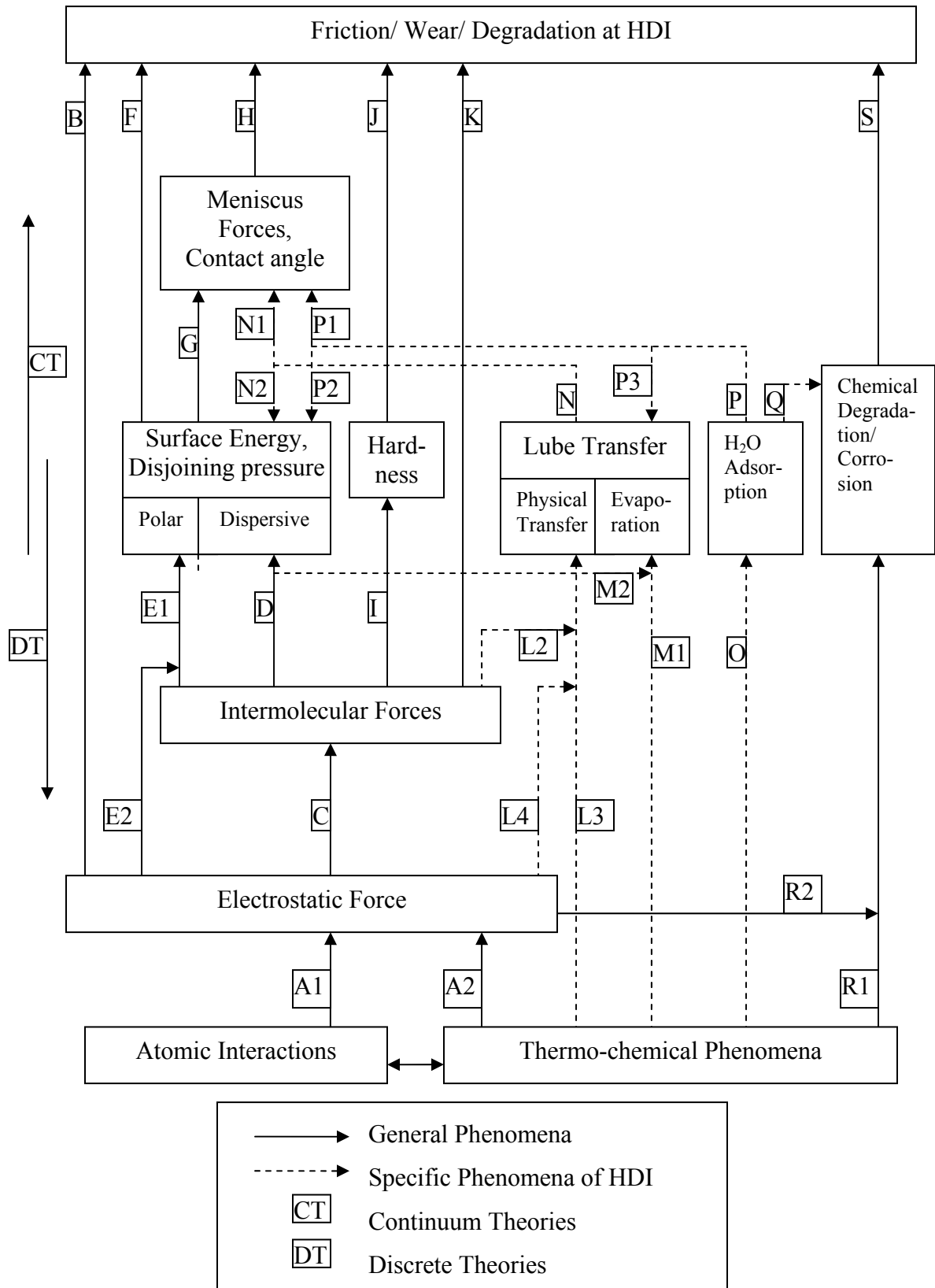


Figure 9.1: Chart for correlation between different phenomena at the head-disk interface

CHAPTER 10

CONCLUSIONS AND FUTURE WORK

10.1 Conclusions

The current information explosion has placed new requirements on the storage capacity and reliability of hard disk drives (HDDs). While there has been great progress in the HDD technology over the past fifty years since its inception, there is a necessity for increasing areal density of storage as well as the reliability of the HDD. To achieve the current areal density goal of $1\text{Tb}/\text{in.}^2$, the flying height of the airbearing slider has to be reduced below 3 nm. At this ultra-low spacing, different proximity forces and interactions influence the slider resulting in fly height modulation and instability. Identifying and characterizing these forces or interactions has become important for achieving a stable fly height at proximity and realize the goals of areal density and reliability.

Several proximity forces or interactions influencing the slider were identified through the study of touchdown-takeoff hysteresis. The difference in the touchdown and takeoff rpm (hysteresis) was monitored for different slider designs, varying the humidity and lubricant thickness of the disks, and the sliders were monitored for lubricant pickup while the disks were examined for lubricant depletion and modulation. Correlation was established between the observed hysteresis and different possible constituent phenomena based on their “domain of operation”. The intermolecular force (IMF) was identified as a factor from the correlation between the lubricant thickness and the touchdown velocity. The long range IMF is mainly attractive in nature and increases the adhesion between the

slider and disk. The IMF simulations using a multilayer model explained the experimental trends.

Meniscus force acts through lubricant mediated adhesion which occurs when a flying slider or a slider in partial contact picks up lubricant from the disk. Meniscus force was identified as a factor from the correlation between the lubricant pickup by the slider and the increased takeoff velocity. Slider-lubricant interactions which cause meniscus force between a slider and disk as well as airbearing surface contamination are thought to be the most important factors affecting stability and reliability at proximity. Hence, slider-lubricant interactions were studied in greater detail.

A flying slider affects the lubricant due to the airbearing forces it creates. A static model of lubricant depletion was presented. Since the changed lubricant profile may in turn cause changes in the flying condition of the slider, iterative simulation of CMLAir and lubricant static simulators was conducted. From the simulation results it was concluded that the flying attitude of the slider does not change significantly unless there is substantial lubricant depletion.

Due to small head-disk spacing, an intermittent contact between the slider and the disk during operation is unavoidable. Hence, an experimental study of slider-lubricant interactions during partial contact was done. It was concluded that under partial contact the slider affects the lubricant on the disk much more than when it is flying. Certain characteristics of the slider such as its roll and position of side rails affect the lubricant and it was observed that a slider in partial contact depletes, redistributes and modulates the lubricant.

Experimental and numerical investigation of the process of disk-to-slider lubricant transfer (DSL_T) was using a half-delubed disk, and a parametric model based on the experimental results was proposed. It is concluded that DSL_T can occur without slider-disk contact and there can be more than one timescale associated with the transfer. Subsequently, a parametric study of the dependence of DSL_T on various HDI parameters was done. In the first part of this parametric study, dependence on the disk lubricant thickness, lubricant type and slider ABS design was investigated. It was concluded that the DSL_T increases non-linearly with increasing disk lubricant thickness, and this was explained on the basis of disjoining pressure of the lubricant. The DSL_T also depends on the type of lubricant used and was less for Ztetraol than for Zdol as Ztetraol adheres more strongly to the substrate than Zdol. The DSL_T also depends on the ABS design. The sudden expansion of air in the sub-ambient pressure zone under the slider is thought to be one of the factors. High pitch, lower base etch and gentler wall profiles in the sub-ambient pressure zone can reduce the transfer. Further, high pitch and shorter length of the trailing pad can reduce the total airbearing shear on the lubricant, possibly reducing transfer.

Good correlation was shown to exist between the lubricant traces on the slider and the 70% spacing massflow lines, which were calculated in CMLAir based on the velocity field given by second-order slip model. The stagnation zones in the massflow field corresponded to the lubricant accumulation zones. Thus, the ABS features causing larger stagnation zones should be avoided.

In the second part of the parametric study, the effect of media-type (carbon overcoat), lubricant molecular weight and inclusion of X-1P and A20H on the slider-

lubricant interactions is investigated using a half-delubed disk approach. Based on the experimental results and following analysis, it is concluded that there exists a critical head-disk clearance above which there is negligible slider-lubricant interaction. The interaction starts at this critical clearance (CC) and increases in intensity as the head-disk clearance is further reduced below the CC. Using shear stress simulations and previously published work a theory was developed to support the experimental observations according to which, higher molecular roughness and lower cohesion/adhesion increase the critical clearance as they decrease the forces holding the lubricant molecules to the disk. Further, the theory proposed that IMF between slider and lubricant may 'loosen' a lubricant chain on the disk surface directly or increase its normal area exposed to the airbearing shear by preferentially pulling the chain backbone which lies closer to the slider and farther from the disk. From this theory, it can be concluded that IMF influences slider-lubricant interactions. This implies that IMF also affects the slider stability through slider-lubricant interactions, a secondary effect, which might be more important than the primary one.

Comparison of the CC on CH_x and CH_xN_y media indicated that the presence of nitrogen is better for HDI as it reduces the CC. This was attributed to better adhesion and chain entangling of the lubricant in presence of nitrogen. The CC was also found to increase with increasing lubricant molecular weight and in the presence of additives X-1P and A20H as was attributed to the increase in molecular roughness as well as a reduction in bond density. Further experiments maintaining a fixed slider-disk clearance suggested that two different mechanisms dominate the disk-to-slider and slider-to-disk lubricant transfers. Airbearing forces appear to dominate the disk-to-slider lubricant transfer while

inherent lubricant properties such as evaporation energy are more important in slider-to-disk lubricant transfer. Fixed clearance experiments in the presence of additives X-1P and A20H suggested that lubricant-carbon adhesion significantly influences the amount of lubricant depletion and transfer when the minimum slider-disk clearance is below the CC.

The disk topography was identified as one of the key factors influencing the slider stability at proximity, since it provides dynamic excitation to the low-flying sliders and strongly influences its dynamics. The effect of circumferential as well as the radial disk topography was investigated and a new method (Candela 6300) was used to measure the 2-D (true) disk topography. The CMLAir dynamic airbearing simulator was used to simulate the slider dynamics over the measured topographies. Simulations indicated a strong dependence on the circumferential roughness and waviness features and also on the radial features, which have not been studied intensively till now. The simulations with 2-D disk topography were also viewed as more realistic than the 1-D simulations since the slider actually flies over a 2-D surface. It was found that different tracks have a varying influence over slider dynamics based on the slider's design and its pressure profile. Based on the simulation results, it was suggested that high pressure areas under the slider should be concentrated near the transducer to reduce the fly height modulation due to circumferential as well as radial disk topography features. Also, under high-skew conditions, it was demonstrated that 2-D disk topography could prove useful in providing the correct picture about the flyability of an ABS design. Further, simulations with CMLAir using 2-D disk topography increased the simulation time by only 30% as compared to 1-D disk topography as input, even with quite high resolution along the radial direction for the 2-D disk topography.

. Finally, an attempt was made to establish correlations between some of the proximity interactions as well as others which may affect the HDI reliability by creating a relational chart. From this chart, a causal relationship was suggested between the electrostatic, intermolecular and meniscus forces.

10.2 Current and Future Work

Detailed experimental and numerical studies regarding all of the proximity interactions are the need of the hour. The work concerning slider-lubricant interactions presented in this dissertation has mainly been an experimental effort. Only simple static simulations have been done in Chapter 4 and accurate modeling of the slider-lubricant interactions remains challenging because of its complex nature. As a continuation of simulation efforts, a dynamic solver for slider-lubricant interactions is currently being worked on. This involves combining of the lubricant dynamic solver (LDS) by Kubotera and Bogy [1] and the CMLAir dynamic solver (CDS) in an iterative scheme outlined in Figure 10.1. In this scheme, the CDS solves for the slider dynamics at every time step. The airbearing data relevant to lubricant evolution airbearing pressure and shear are then used by LDS to solve for the dynamic lubricant evolution at that time step. Due to the change in the lubricant profile on the disk, the disk floor that the slider sees at the next time step also changes. Hence, the change in the lubricant profile is incorporated back in the 2-D disk topography, and the resultant slider dynamics are solved for the next time step. This can be considered as a first step towards simulating the dynamic interaction between the slider and lubricant and has a good scope for future research along the lines indicated below:

- Development of a rich theoretical model for the lubricant which captures its polymer, thin-film and possibly visco-elastic nature. This is not captured effectively by treating the lubricant as a continuum, as is done in the current models.
- Development of a macroscopic/ theoretical model for disk-to-slider lubricant transfer or more generally slider-lubricant interactions which explains many experimental results regarding the critical clearance and the parametric dependence presented in this dissertation.
- Molecular level study of the slider-lubricant interactions using Molecular Dynamics or Monte Carlo methods.

In addition to the above avenues, some other possible directions are:

- Simulation of lubricant conformation on patterned media.
- Experimental and numerical study of lubricant flow under conditions experienced in a heat assisted magnetic recording (HAMR) interface.
- Experimental and numerical investigation into the dynamics and stability of thermal fly-height control (TFC) sliders, which are being used in the latest HDDs.

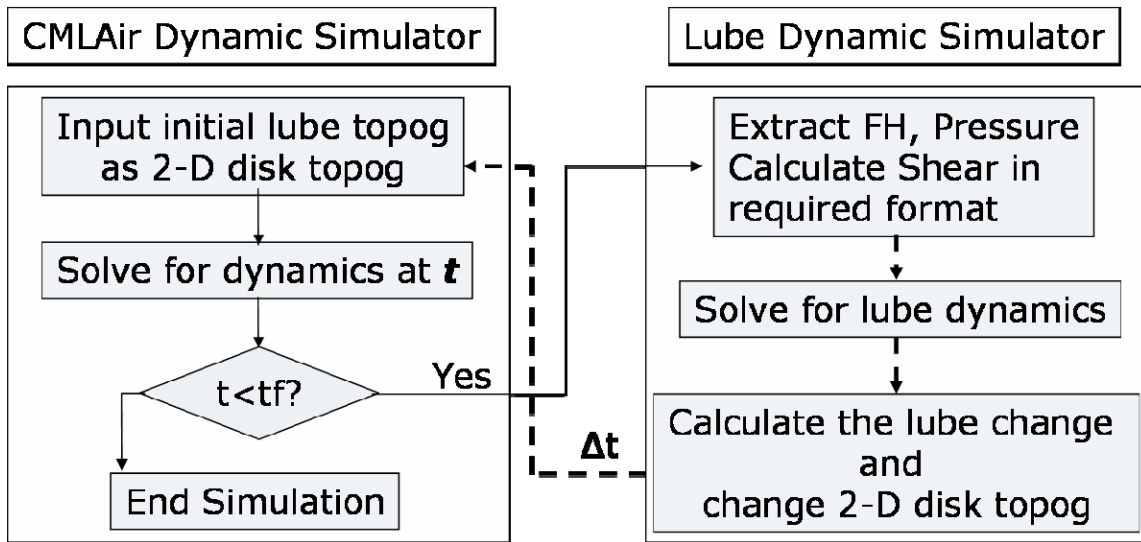


Figure 10.1: Dynamic coupling scheme between CML and lube dynamic simulators

REFERENCES

Chapter 1

- [1] http://en.wikipedia.org/wiki/IBM_305
- [2] <http://www.hitachigst.com> – press release
- [3] E. D. Daniel, C.D. Mee and M.H. Clark, *Magnetic Recording -The First 100 Years*, IEEE Press, New York, 1999.
- [4] C. D.Mee and E.D. Daniel, *Magnetic Recording Handbook*, McGraw-Hill, New York, 1996

Chapter 2

- [1] R. Wood, “The Feasibility of Magnetic Recording at 1 Terabit per Square Inch,” *IEEE Trans. Magn.*, Vol. 36, January, pp. 36-42, 2002.
- [2] L. Wu, and D.B. Bogy, “Effect of the Intermolecular Forces on the Flying Attitude of Sub- 5 NM Flying Height Air Bearing Sliders in Hard Disk Drives,” *ASME J. Tribol.*, Vol. 124, pp. 562-567, July 2002.
- [3] B.H. Thornton, and D.B. Bogy, “Head-Disk Interface Dynamic Instability due to Intermolecular Forces,” *IEEE Trans. Magn.*, Vol. 39, No. 5, pp.2420-2422, Sept. 2003.
- [4] B. Bhushan, C.A. Kotwal, and S.K. Chilamakuri, “Kinetic Meniscus Model for Prediction of Rest Stiction,” *ASME J. Tribol.*, Vol. 120, pp. 42-50, Jan. 1998.
- [5] T. Kato, S. Watanabe, and H. Matsuoka, “Dynamic Characteristics of an In-Contact Headslider Considering Meniscus Force: Part 1—Formulation and Application to

- the Disk with Sinusoidal Undulation,” *ASME J. Tribol.*, Vol. 122, pp. 633-638, July 2000.
- [6] T. Kato, S. Watanabe, and H. Matsuoka, “Dynamic Characteristics of an In-Contact Headslider Considering Meniscus Force: Part 2 – Application to the Disk with Random Undulation and Design Conditions,” *ASME J. Tribol.*, Vol. 123, pp. 168-174, Jan. 2001.
- [7] T. Kato, S. Watanabe, and H. Matsuoka, “Dynamic Characteristics of an In-Contact Headslider Considering Meniscus Force: Part 3 – Formulation and Application to the Disk with Sinusoidal Undulation,” *ASME J. Tribol.*, Vol. 124, pp. 801-810, Oct. 2002.
- [8] K. Iida and K. Ono, “Design Consideration of Contact/Near-Contact Sliders based on a Rough Surface Contact Model,” *ASME J. Tribol.*, Vol. 125, No. 3, pp. 562-70, July 2003.
- [9] L. Zitzler, S. Herminghaus and F. Mugele, “Capillary Forces in Tapping Mode Atomic Force Microscopy,” *Physical Review B-Condensed Matter*, Vol. 66, No. 15, pp.1554361-8, Oct 2002.
- [10] T. Watanabe, and D.B. Bogy, “A Study of the Lubricant Displacement Under a Flying Head Slider Caused by Slider-Disk Interaction,” *IEEE Trans. Magn.*, Vol. 39, No. 5, pp.2477-9, Sept. 2003.
- [11] T.G. Jeong, *Slider-Disk Interactions during Dynamic Load-Unload in Magnetic Recording Disk Drives*, Ph.D. Thesis, University of California at Berkeley, 1991.

- [12] N. Shukla, E. Svedberg, R.J.M van de Veerdonk, X. Ma, J. Gui and A.J. Gellman, "Water Adsorption on Lubricated α -CH_x in Humid Environments," *Tribology Letters*, Vol. 15, No. 1, pp.9-14, 2003.
- [13] Q. Dai, G. Vurens, M. Luna and M. Salmeron, "Lubricant Distribution on Hard Disk Surfaces: Effect of Humidity and Terminal Group Reactivity," *Langmuir*, Vol. 13, pp.4401-4406, 1997.
- [14] R.Z. Lei and A.J. Gellman, "Humidity Effects on PFPE Lubricant Bonding to α -CH_x Overcoats," *Langmuir*, Vol. 16, pp. 6628-6635, 2000.
- [15] B. Knigge and F.E. Talke, "Nonlinear Dynamic Effects at the Head Disk Interface", *IEEE Trans. Magn.*, Vol. 37, pp. 900-905, Mar. 2001.
- [16] J.N. Israelachvili, *Intermolecular and surface forces*, 2nd edition, San Diego, Academic Press, 1992.
- [17] H. Matsuoka, S. Ohkubo and S. Fukui, "Dynamic Characteristics of flying Head Slider considering Van der Waals Forces (Analyses based on the Corrected Van der Waals Force Equation for Multilayers)," *Proceedings of 2003 STLA/ASME Joint International Tribology Conference*, Florida, pp. 51-57, Oct. 2003.
- [18] B. Zhang and A. Nakajima, "Possibility of Surface Force Effect in Slider Air Bearings of 100 Gbit/in² Hard Disks," *Tribology International*, Vol. 36, pp. 291-296, 2003.
- [19] N. Gitis and L. Volpe, "Nature of Static Friction Time Dependence," *J. Phys. D: Appl. Phys.*, Vol. 25, pp. 605-612, 1992.

Chapter 3

- [1] V. Gupta and D. B. Bogy, "Dynamics of Sub-5nm Air Bearing Sliders in the Presence of Electrostatic and Intermolecular Forces at the Head Disk Interface," *IEEE Trans. Magn.*, vol. 41, no. 2, pp. 610-15, Feb 2005.
- [2] B.H. Thornton and D.B. Bogy., "Head-disk interface dynamic instability due to intermolecular forces," *IEEE Trans. Magn.*, vol. 39, no. 5, pp.2420-2422, Sept. 2003.
- [3] B. Marchon, T. Karis, Q..Dai and R. Pit, "A model for lubricant flow from disk to slider," *IEEE Trans. Magn.*, vol. 39, no. 5, pp.2447-2449, Sept. 2003.
- [4] M. J. Smallen and H. W. Huang, "Effect of disjoining pressure on disk-to-head lubricant transfer," *IEEE Trans. Magn.*, vol. 39, no. 5, pp.2495-2497, Sept. 2003.
- [5] X. Ma, H. Tang, M. Stirniman and J. Gui, "The effect of slider on lubricant loss and redistribution," *IEEE Trans. Magn.*, vol. 38, no. 5, pp. 2144–2146, Sept. 1998.
- [6] K. Komvopoulos, *Fundamentals of tribology and contact mechanics*, prepared for Tribology Research Program, University of California at Berkeley, Jan. 1998.
- [7] E. Rabinowicz, "Dependence of adhesive wear coefficient on surface energy of adhesion," *Wear of materials*, 1977.
- [8] E. Rabinowicz, "The wear coefficient – magnitude, scatter, uses," *J. Lub. Tech, ASME Trans.*, vol. 103, no. 2, pp. 188-194, Apr. 1981.
- [9] Z.F. Li, C.Y. Chen and J.J. Liu, "Study of head-disk interference at low-flying height," *IEEE Trans. Magn.*, vol. 39, no. 5, pp.2462-2464, Sept. 2003.
- [10] K. Iida and K. Ono, "Design Consideration of Contact/Near-Contact Sliders based on a Rough Surface Contact Model," *ASME J. Tribol.*, Vol. 125, no. 3, pp. 562-70, July 2003.

- [11] B. Strom, S. Deits, C. Gerber, D. Krajnovich, D. Ohlsen and R. Turner, "Burnishing Heads In-Drive for Higher Density Recording," *IEEE Trans. Magn.*, vol. 40, no. 1, pp.345-348, Jan. 2004.
- [12] X. Shen and D. B. Bogy, "Contact Force and Frictional Heating due to "Large" Particles in the Head Disk Interface," Mar. 2004 (CML Blue Report 2004-04).
- [13] S. Miyazawa, Y. Kawakubo, K. Nagata and S. Kobatake, "Contact burnishing for head wear reduction," *Digest of INTERMAG*, pp.GP-07. Piscataway, NJ, USA, 2003.
- [14] X. Shen, M. Suk and D.B. Bogy, "Reduction of Particle Contamination on Air Bearing Sliders Part I: Wall Profile and Crown Effects," Aug. 2003 (CML Blue Report 2003-07).
- [15] Z.F. Li, C.Y. Chen, J.J. Liu, A.Chekanov, J. Gao and B.G. Demczyk, "Effects of Media Burnish Capability to Head-Disk Clearance," *IEEE Trans. Magn.*, vol. 40, no. 4, pp.3153-3155, July 2004.
- [16] H. Matsuoka, S. Fukui and T. Kato, "Dynamic Characteristics of an In-Contact Head Slider Considering Meniscus Force: Part 3—Wear Durability and Optimization of Surface Energy of Liquid Lubricant Under Perfect Contact Condition," *ASME J. Tribology*, vol. 124, pp. 801-810, Oct. 2002.

Chapter 4

- [1] X. Ma, J. Chen, H. J. Richter, H. Tang and J. Gui, "Contribution of Lubricant Thickness to Head-Media Spacing," *IEEE Trans. Magn*, Vol. 37, Vol. 4,1824-26, July 2001.

- [2] T. Watanabe, D.B. Bogy, "A study of the lubricant displacement under a flying head slider caused by slider-disk interaction," *IEEE Trans. Magn.*, vol.39, no.5, pt.2, pp. 2477-9, Sept. 2003.
- [3] Q. Dai, F. Hendriks and B. Marchon, "Modeling the Washboard Effect at the Head/Disk Interface," *IEEE Trans. Magn.*, Vol. 39, No. 5, pp. 2459-61, Sept. 2003.
- [4] A. Khurshudov and R.J. Waltman, "The contribution of thin PFPE lubricants to slider-disk spacing," *Tribol. Lett.*, vol. 11, pp. 143-49, 2001.
- [5] B. Marchon, T. Karis, Q. Dai and R. Pit, "A Model for Lubricant Flow from Disk to Slider," *IEEE Trans. Magn.*, Vol. 39, No. 5, 2447-49, Sept. 2003.
- [6] B. V. Derjaguin and N. V. Churaev, "On the Question of Determining the Concept of Disjoining Pressure and its Role in the Equilibrium and Flow of Thin Films," *J. Coll. Interface Sci.*, Vol. 66, No. 3, Oct. 1978.
- [7] T.E. Karis and G.W. Tyndall, "Calculation of Spreading Profiles for Molecularly-Thin Films from Surface Energy Gradients," *J. Non-Newtonian Flu. Mech.*, Vol. 82, pp. 287-302, 1999.
- [8] J. Israelachvili, *Intermolecular and Surface Forces*, Academic Press, San Diego, 1992.
- [9] K. Fukuzawa, J. Kawamura, T. Deguchi, H. Zhang and Y. Mitsuya, "Measurement of Disjoining Pressure of a Molecularly Thin Lubricant Film by Using a Microfabricated Groove," *IEEE Trans. Magn.*, Vol. 40, No. 4, July 2004.
- [10] R.J. Waltman, A. Khurshudov and G.W. Tyndall, "Autophobic Dewetting of Perfluoropolyether Films on Amorphous Nitrogenated Carbon Surfaces," *Trib. Lett.*, Vol. 12, No. 3, pp. 163-69, Apr. 2002.

- [11] M. Smallen and H.W. Huang, "Effect of Disjoining Pressure on Disk-to-Head Lubricant Transfer," *IEEE Trans. Magn.*, Vol. 39, No. 5, 2495-97, Sept 2003.
- [12] A. Oron, S.H. Davis, S.G. Bankoff, "Long Scale Evolution of Thin Liquid Films," *Rev. Modern Phys.*, Vol. 69, No. 3, pp. 1-50, July 1997.
- [13] R.P. Ambekar, V.Gupta and D.B. Bogy, "Experimental and numerical investigation of the dynamic instability in the head-disk interface at proximity," *ASME J. Tribol.*, vol. 127, no. 3, pp. 530-36, July 2005.
- [14] R.P. Ambekar and D.B. Bogy, "Effect of Slider Lubricant Pickup on Stability at the Head-Disk Interface," *IEEE Trans. Magn.*, vol.41, no.10, Oct. 2005, pp. 3028-30.
- [15] H.M. Gross, *Off-Track Vibrations of the Read-Write Heads in Hard Disk Drives*, Ph.D. dissertation, University of California-Berkeley, Spring 2003.

Chapter 5

- [1] X. Ma, H. Tang, M. Stirniman and J. Gui, "Effect of Slider on Lubricant Loss and Redistribution," *IEEE Trans. Magn.*, Vol. 38, Vol. 5, 2144-46, Sept. 2002.
- [2] B. Marchon, T. Karis, Q..Dai and R. Pit, "A model for lubricant flow from disk to slider," *IEEE Trans. Magn.*, vol. 39, no. 5, pp.2447-2449, Sept. 2003.
- [3] M. J. Smallen and H. W. Huang, "Effect of disjoining pressure on disk-to-head lubricant transfer," *IEEE Trans. Magn.*, vol. 39, no. 5, pp.2495-2497, Sept. 2003.
- [4] R.J. Waltman, A. Khurshudov and G.W. Tyndall, "Autophobic Dewetting of Perfluoropolyether Films on Amorphous Nitrogenated Carbon Surfaces," *Trib. Lett.*, Vol. 12, No. 3, pp. 163-69, Apr. 2002.

- [5] H. Chiba, T. Musashi, Y. Kasamatsu, J. Watanabe, T. Watanabe, K. Watanabe, "Chemically modified air-bearing surface for the near-contact regime," *IEEE Trans. Magn.*, vol.41, no.10, pp. 3049-51, Oct. 2005.
- [6] B.G. Min, J.W. Choi, H.R. Brown, D.Y. Yoon, T.M. O'Connor and M.S. Jhon, "Spreading characteristics of thin liquid films of perfluoropolyalkylethers on solid surfaces. Effects of chain-end functionality and humidity," *Trib. Lett.*, Vol. 1, No. 3, pp. 225-32, Nov. 1995.
- [7] T.E. Karis, W.T. Kim and M.S. Jhon, "Spreading and Dewetting in Nanoscale Lubrication," *Trib. Lett.*, Vol. 18, No. 1, pp. 27-41, Jan. 2005.
- [8] S.K. Deoras, S-W. Chun, G. Vurens and F.E. Talke, "Spreading and Mobility Analysis of PFPE Lubricants using Surface Reflectance Analyzer (SRA)," *Tribol. Int.*, Vol. 36, No. 4-6, pp. 241-46, Apr.-Jun. 2002.
- [9] L. Wu, *Physical Modeling and Numerical Simulations of the Slider Air Bearing Problem of Hard Disk Drives*, Ph.D. dissertation, University of California-Berkeley, Spring 2001.
- [10] L. Gonzaga and B. Liu, "Fabrication and Evaluation of Panda II design," INSIC Research Presentation.
- [11] R.P. Ambekar and D.B. Bogy, "Slider-Lubricant Interactions at the Head-Disk Interface," CML Report 2006-07, May 2006.
- [12] D. Chen and D.B. Bogy, "A Comparison of Two Rarefaction Models in the Compressible Reynolds Equation Used in Air Bearing Design for Hard Disk Drives," CML Report 2005-10, Sept. 2005.

- [13] X. Shen, *The Effect of Contamination Particles on the Dynamics of Ultra-Low Flying Air Bearing Sliders*, Ph.D. dissertation, University of California-Berkeley, Spring 2001.
- [14] B. Marchon, Q. Dai, V. Nayak and R. Pit, "The Physics of Disk Lubricant in the Continuum Picture," *IEEE Trans. Magn.*, Vol. 41, No. 2, pp. 616-620, Feb. 2005.

Chapter 6

- [1] X. Ma, H. Tang, M. Stirniman and J. Gui, "Effect of Slider on Lubricant Loss and Redistribution," *IEEE Trans. Magn.*, Vol. 38, Vol. 5, pp.2144-46, Sept. 2002.
- [2] S.-C. Kang, *A Kinetic Theory Description for Molecular Lubrication*, Ph.D. Dissertation, Carnegie-Mellon University, 1997.
- [3] D. Chen and D.B. Bogy, "A Comparison of Two Rarefaction Models in the Compressible Reynolds Equation used in air bearing design for hard disk drives" CML Tech Report 2005-10.
- [4] Q. Dai, F. Hendriks and B. Marchon, "Modeling the washboard effect at the head-disk interface," *J. Appl. Phys.* Vol. 96, pp.696-703, July 2004.
- [5] H. Kubotera and D.B. Bogy, "Numerical Simulation of Molecularly Thin Lubricant Film Flow Due to the Air Bearing Slider in Hard Disk Drives," CML Tech Report 2006-11.
- [6] C.M. Mate and B. Marchon, "Shear Response of Molecularly Thin Liquid Films to an Applied Air Stress," *Phys. Rev. Lett.*, Vol. 85, pp.3902-3905, Oct. 2000.
- [7] M. Ruths and S. Granick, "Tribology of confined Fomblin-Z perfluoropolyalkylethers molecular weight dependence and comparison between unfunctionalized and telechelic chains," *Trib. Lett.*, Vol. 7, pp.161-172, 1999.

- [8] R.R. Dagastine, L.R. White, P.M. Jones and Y.-T. Hsia, "Effect of van der Waals forces on molecularly thin lubricant in the magnetic storage head-disk interface," *J. Appl. Phys.*, Vol. 98, pp.124906:1-6, Dec. 2005.
- [9] A. Khurshudov and R. J. Waltman, "The contribution of thin PFPE lubricants to slider-disk spacing" *Trib. Lett.*, Vol. 11, No. 3-4, pp.143-149, 2001.
- [10] R.J. Waltman, N. Kobayashi, N. Shirai, A. Khurshudov and H. Deng, "The tribological properties of a new cyclotriphosphazene-terminated pfpe lube," *Trib. Lett.*, Vol. 16, No. 1-2, pp. 153-162 , Feb. 2004.
- [11] C.-Y. Chen, D.B. Bogy, T. Cheng and C.S. Bhatia, "Effect of the additive X-1P on the tribological performance and migration behavior of PFPE lubricant at the head-disk interface," *IEEE Trans. Magn.*, Vol. 36 pp.2708-10, 2000.
- [12] .G.W. Tyndall, R.J. Waltman and D.J. Pocker, "Concerning the Interactions between Zdol Perfluoropolyether Lubricant and an Amorphous-Nitrogenated Carbon Surface," *Langmuir*, Vol.14, pp. 7527-7536, 1998.

Chapter 7

- [1] G.W. Tyndall, R.J. Waltman and D.J. Pocker, "Concerning the Interactions between Zdol Perfluoropolyether Lubricant and an Amorphous-Nitrogenated Carbon Surface," *Langmuir*, vol. 14, pp. 7527-7536, 1998.
- [2] R.J. Waltman, G.W. Tyndall and Pacansky, "Computer-Modeling Study of the Interactions of ZDOL with Amorphous Carbon Surfaces", *Langmuir*, Vol. 15, pp. 6470-6483, 1999.

- [3] S.K. Deoras, S.-W. Chun, G. Vurens and F.E. Talke, "Spreading and mobility analysis of PFPE lubricants using a Surface Reflectance Analyzer," *Trib. Intl.*, Vol. 36, No. 4-6, pp. 241-246, Apr-Jun 2003.
- [4] R.J. Waltman, and G.W. Tyndall, "The evaporation and bonding of ZDOL polyperfluorinated Ether lubricants on CH_x carbon overcoated rigid magnetic media. 1Effect of Molecular Weight.", *J. Phys. Chem. B*, No. 104, pp. 7085-7095, 2000.
- [5] C.-Y. Chen, *Tribochemistry of the Decomposition Mechanisms of Perfluoropolyether Lubricants at the Head-Disk Interface of Hard Disk Drives in UHV*, Ph. D. Dissertation, University of California Berkeley, 1999.
- [6] A. Khurshudov and R. J. Waltman, "The contribution of thin PFPE lubricants to slider-disk spacing," *Trib. Lett.*, Vol. 11, no. 3-4, pp. 143-149, 2001.
- [7] B. Marchon, T. Karis, Q..Dai and R. Pit, "A model for lubricant flow from disk to slider," *IEEE Trans. Magn.*, vol. 39, no. 5, pp.2447-2449, Sept. 2003.
- [8] C.M. Mate, P.H. Kasai, G.W. Tyndall, C.H. Lee, V. Raman, D.J.Pocker and R.J. Waltman, *IEEE Trans. Magn.*, Vol. 34, pp. 1744-1746, 1998.
- [9] R.J. Waltman, N. Kobayashi, N. Shirai, A. Khurshudov and H. Deng, "The tribological properties of a new cyclotriphosphazene-terminated perfluoropolyether lubricant," *Trib. Lett.*, vol. 16, no. 1-2, pp. 151- 162, Feb. 2004.

Chapter 8

- [1] Q.H. Zeng, B.H. Thornton, D.B. Bogy and C.S. Bhatia, "Flyability and flying height modulation measurement of sliders with sub-10 nm flying heights," *IEEE Transactions on Magnetics*, vol.37, no.2, pt.1, March 2001, pp. 894-9.

- [2] B.H. Thornton, D.B. Bogy, C.S. Bhatia, "The effects of disk morphology on flying-height modulation: experiment and simulation," *IEEE Transactions on Magnetics*, vol.38, no.1, pt.1, Jan. 2002, pp. 107-111.
- [3] Y. Shimizu and J. Xu, "Two-dimensional flying-height modulation mapping at HDD drive level," *IEEE Transactions on Magnetics*, vol.42, no.10, Oct. 2006, pp. 2516-18.
- [4] P. Tribhuvan, V. Velidandla and S. Venkataram, "Disk Topography Metrology for Addressing Head-Disk Interface Challenges," *Asia-Pacific Magnetic Recording Conference (APMRC)*, Nov. 2006, Singapore.
- [5] B.H. Thornton, A. Nayak and D.B. Bogy, "Flying Height Modulation Due to Disk Waviness of Sub-5nm flying Height Air Bearing Sliders," *ASME Journal of Tribology*, vol. 124, Oct. 2002, pp. 762-70.
- [6] J.F. Xu and B. Liu, "ABS design and fly height modulation of femto sliders," *International Magnetics Conference*, 2003, pp. AB-10. Piscataway, NJ, USA.

Chapter 9

- [1] J.D. Kiely and Y.-T. Hsia, "Tribocharging of the magnetic hard disk drive head-disk interface," *J. Appl. Phys.*, Vol. 91, no. 7, pp. 4631-36, Apr. 2002.
- [2] M. Suk, R. Kroeker and D. Gills, "Investigation of slider dynamics under electrostatic force," *Microsystem Technologies*, vol.9, no.4, pp.256-65, March 2003.
- [3] A.J. Wallash, "Electrostatic Discharge and Electrical Breakdown Study of the Head-Disk Interface in a Hard Disk Drive," *IEEE Trans. Magn.*, vol. 40, no. 3, pp. 1751-55, May 2004.

- [4] A.F. Diaz and J. Guay, "Contact charging of organic materials: ion vs. electron transfer," *IBM Journal of Research & Development*, vol. 37, no. 2, pp. 249-59, March 1993.
- [5] http://en.wikipedia.org/wiki/Triboelectric_series
- [6] V. Gupta and D.B. Bogy, "Dynamics of sub-5-nm air-bearing sliders in the presence of electrostatic and intermolecular forces at the head-disk interface," *IEEE Trans. Magn.*, vol. 41, no. 2, pp. 610-15, Feb 2005.
- [7] M. Suk, "Effect of tribocharging on lubricant redistribution," *IEEE Trans. Magn.*, vol. 41, no. 2, pp. 831-35, Feb 2005.
- [8] J. Israelachvili, *Intermolecular and Surface Forces*, Academic Press, San Diego, 1992.
- [9] A.J. Kinloch, *Adhesion and Adhesives*, Chapman and Hall Ltd., London, 1987.
- [10] A.V. Pocius, *Adhesion and adhesives technology: An Introduction*, Hanser Publishers, 1997
- [11] M.D. Rouhani and R. Schuttler, "Influence of the surface charge on the metal surface energy," *Surface Science*, vol.38, no.2, pp.499-502, July 1973.
- [12] K. Komvopolous, *Fundamentals of tribology and contact mechanics*, prepared for Tribology Research Program, University of California at Berkeley, Jan. 1998.
- [13] E. Rabinowicz, "Dependence of adhesive wear coefficient on surface energy of adhesion," *Wear of materials*, ASME – New York, pp.36-40, 1977.
- [14] G.W. Tyndall, R.J. Waltman and J. Packinsky, "Effect of adsorbed water on perfluoropolyether-lubricated magnetic recording disks," *J. Appl. Phys.*, Vol. 90, No. 12, pp. 6287-6295, Dec. 2001.

- [15] R.J. Waltman, D.J. Pocker and G.W. Tyndall, "Studies on the interactions between ZDOL perfluoropolyether lubricant and the carbon overcoat of ridged magnetic media," *Trib. Lett.*, Vol. 4, pp. 267-75, 1998.
- [16] W.R. Good, "A comparison of contact angle interpretations," *J. Coll. Int. Sci.*, Vol. 44, No. 1, pp. 63-71, July 1973.
- [17] K. Iida and K. Ono, "Design Consideration of Contact/Near-Contact Sliders based on a Rough Surface Contact Model," *ASME J. of Tribology*, Vol. 125, no. 3, pp. 562-70, July 2003.
- [18] H. Matsuoka, S. Fukui and T. Kato, "Dynamic Characteristics of an In-Contact Head Slider Considering Meniscus Force: Part 3—Wear Durability and Optimization of Surface Energy of Liquid Lubricant Under Perfect Contact Condition," *ASME J. Tribology*, vol. 124, pp. 801-810, Oct. 2002.
- [19] S.K. Chilamakuri and B. Bhushan, "A comprehensive kinetic meniscus model for prediction of long-term static friction," *J. Appl. Phys.*, vol.86, no.8, pp.4649-56, Oct. 1999.
- [20] R.P. Ambekar, V.Gupta and D.B. Bogy, "Experimental and numerical investigation of the dynamic instability in the head-disk interface at proximity," *ASME J. Tribology*, vol. 127, no. 3, pp. 530-36, July 2005.
- [21] B.H. Thornton and D.B. Bogy., "Head-disk interface dynamic instability due to intermolecular forces," *IEEE Trans. Magn*, vol. 39, no. 5, pp.2420-22, Sept. 2003.
- [22] H. Matsuoka, S. Ohkubo and S. Fukui, "Dynamic Characteristics of flying Head Slider considering Van der Waals Forces (Analyses based on the Corrected Van der

- Waals Force Equation for Multilayers),” *Proc. 2003 STLE/ASME Int. Joint Trib. Conference*, pp. 51-57, Florida, Oct. 2003
- [23] M. J. Smallen and H. W. Huang, “Effect of disjoining pressure on disk-to-head lubricant transfer,” *IEEE Trans. Magn.*, vol. 39, no. 5, pp.2495-2497, Sept. 2003.
- [24] X. Ma, H. Tang, M. Stirniman and J. Gui, “The effect of slider on lubricant loss and redistribution,” *IEEE Trans. Magn.*, vol. 38, no. 5, pp. 2144–2146, Sept. 2002.
- [25] B. Marchon, T. Karis, Q..Dai and R. Pit, “A model for lubricant flow from disk to slider,” *IEEE Trans. Magn.*, vol. 39, no. 5, pp.2447-2449, Sept. 2003.
- [26] R.P. Ambekar and D.B. Bogy, “Effect of Slider Lubricant Pickup on the Stability at the Head-Disk Interface,” FS-13, *IEEE-Intermag*, Nagoya, Japan, Apr.2005 (Details in CML Blue Report 2005-04).
- [27] R.Z. Lei and A.J. Gellman, “Humidity effects on PFPE lubricant bonding to a-CH/sub x/ overcoats,” *Langmuir*, vol.16, no.16, pp.6628-35, Aug. 2000.
- [28] P.H. Kasai and V. Raman, “Z-dol versus Z-tetraol: bonding and durability in magnetic hard disk application,” *Tribology Letters*, vol.16, no.1-2, 2004, pp.29-36.
- [29] S. Jung and T.M. Devine, “Influence of nanothick layers of DLC on the rates of electrochemical reduction reactions on magnetic hard disks,” *J. Electrochemical Soc.*, vol.151, no.3, pp.B195-205, March 2004.
- [30] B. Tomcik, S.C. Seng, B. Balakrisnan and J.Y.Lee, “Electrochemical tests on the carbon protective layer of a hard disk,” *Diamond & Related Materials*, vol.11, no.7, pp.1409-15, July 2002.

- [31] J.V. Wasem, B.L. LaMarche, S.C. Langford and J.T. Dickinson, "Triboelectric Charging of a Perfluoropolyether Lubricant," *J. Appl. Phys.*, vol. 93, no. 4, pp. 2202-07, Feb. 2003.


Chapter 10

- [1] H. Kubotera and D.B. Bogy, "Numerical Simulation of Molecularly Thin Lubricant Film Flow due to the Air Bearing Slider in Hard Disk Drives," CML Report 2006-11.

APPENDIX A

2-D disk topography input in CMLAir Dynamic Simulator

To use the 2-D disk topography input, the following change (highlighted by the box) needs to be made in the dynamic simulator input file **dynamics.def**. Variable *nfy* indicates the number of tracks to be given as input while *nfx* indicates the number of points per track. Variable **ims** activates the point-by-point disk profile when set to 1 while **dinit** indicates the distance of the first point of simulation from the starting of the track.

```
...
*****Grid Control*****
iadapt  isymmetry ioldgrid nx ny nsx nsy
...
1
difmax  decay  ipmax
100.000000 100.000000 0
*****Point by Point Disk Track Profile*****
ims      nfx      dinit      nfy      
1        20001    0.000000    351
*****Numerical Generation of Disk Surface Topography*****
nwave nzone nasper
0 0 0
iwtype wamp(m) wang(dg) wthx(m) wthy(m) wpx(m) wpy(m) wrs(m) wre(m)
```

```

zr1(m)  zh1(m)  zr2(m)  zh2(m)  zr3(m)  zh3(m)

iatype aamp(m)  aang(dg)  alocx(m)  alocy(m)  asizx(m)  asizy(m)

****Numerical Generation of Slider Surface Topography****

nswave nsasper

0    0

istype swamp(m)  swng(dg)  swthx(m)  swthy(m)  swpdx(m)  swpdy(m)

isatype saamp(m)  saang(dg)  salocx(m)  salocy(m)  sasizx(m)  sasizy(m)

*****Track Accessing Motion*****

...

```

The disk topography file **wave.def** should be included in other dynamic input files such as **dynamics.def** and **rail.dat**. It is in the following format:

```

y(1)  y(2)  y(3)          ...  y(nfy)
x(1)  h(1,1) h(1,2) h(1,3)  ...  h(1,nfy-1)  h(1,nfy)
x(2)  h(2,1) h(2,2) h(2,3)  ...  h(2,nfy-1)  h(2,nfy)
x(3)  h(3,1) h(3,2) h(3,3)  ...  h(3,nfy-1)  h(3,nfy)
.
.
.
x(nfx) h(nfx,1)          ...  h(nfx,nfy-1)  h(nfx,nfy)

```

APPENDIX B

Guidelines to use CML – Parameter Identification Program (PIP) 2.0:

The PIP version 2.0 is compatible with Matlab 6.0+ and the newest version (v 4.037) of the dynamic solver. The program might not run satisfactorily for older versions of CML files however these files can be easily converted to version 4.037.

Steps for use of PIP:

1. Open Matlab, select current directory as CMLPIP and type “pip” at the prompt.
2. The PIP main window will open up, with the default “insicml” file loaded. (To see the analysis for this slider, various options are provided in the menubar above)
3. To run PIP for a new CML case, select *File ->Open or Create a new job*. In the pop-up window, enter the job name.
4. A folder with the given job name will be created in the folder CMLPIP. Copy the required CML file in this folder and open it. Set the dynamic properties:
 - a. Initial guess for fly height, pitch and roll and disk rpm
 - b. Grid size
 - c. **Important:** For good results, the convergence parameters should be set for high accuracy.
 - i. Error for Reynolds Equation solver $< 10^{-10}$
 - ii. Load error $< 10^{-4}$
5. After setting the properties, use *File->Export Ascii* on the CML console to export the CML input files to the folder.

6. For starting dynamic simulations, double-click *RunPIP.exe* in the current folder or select *Getdata-> Calculate Responses by the Simulator* from PIP console.
7. Once this program starts, the user will be prompted to enter impulse velocities in the z (height), p(pitch) and r(roll) directions and the time for simulations. The default values are given and form a good guideline for choosing these values.
8. After choosing the values and clicking OK, the dynamic simulations will start and the output files will be written to the current folder.
9. After the simulations are done, select *Getdata-> Get Data from the Simulator*
10. Select *Getdata-> Calculate IRFs and FRFs* and select Frequency range.
11. After obtaining the IRFs and FRFs, select *Estimate-> Automatic Estimate* for automated estimation of modes, or *Estimate->Interactive Estimate* for more flexibility in mode identification. After this step, the required modes have been identified and the mode identification is complete. Results can be viewed by selecting *DisplayCurves* or *Results*.
12. *DisplayCurves* displays the impulse response of the slider to the impulse in z/p/r directions along with their IRFs and FRFs.
13. *Results* tab has options for displaying stiffness matrices, nodal lines and mode animations.
14. The results obtained can be stored by selecting *File->Save Current Job* for easy retrieval.